



HAL
open science

Using image-based large-eddy simulations to investigate the intracardiac flow and its turbulent nature

Christophe Chnafa

► **To cite this version:**

Christophe Chnafa. Using image-based large-eddy simulations to investigate the intracardiac flow and its turbulent nature. Modeling and Simulation. Université Montpellier II - Sciences et Techniques du Languedoc, 2014. English. NNT : 2014MON20112 . tel-01537721v3

HAL Id: tel-01537721

<https://theses.hal.science/tel-01537721v3>

Submitted on 12 Jun 2017

HAL is a multi-disciplinary open access archive for the deposit and dissemination of scientific research documents, whether they are published or not. The documents may come from teaching and research institutions in France or abroad, or from public or private research centers.

L'archive ouverte pluridisciplinaire **HAL**, est destinée au dépôt et à la diffusion de documents scientifiques de niveau recherche, publiés ou non, émanant des établissements d'enseignement et de recherche français ou étrangers, des laboratoires publics ou privés.

THÈSE

Pour obtenir le grade de
Docteur

Délivré par l'**Université Montpellier II**

Préparée au sein de l'école doctorale **I2S**
Et de l'unité de recherche **I3M**

Spécialité: **Mathématiques et modélisation**

Présentée par **Christophe Chnafa**

Using image-based large-eddy
simulations to investigate the
intracardiac flow and its
turbulent nature

Soutenue le 21 novembre 2014 devant le jury composé de

Franck NICOUD	Université Montpellier II	Directeur
Simon MENDEZ	Université Montpellier II	Co-encadrant
Jean-Frédéric GERBEAU	INRIA Paris-Rocquencourt	Rapporteur
Pascal VERDONCK	Ghent University	Rapporteur
Pierre SGAUT	Université Pierre et Marie Curie	Examinateur
Damien COISNE	CHU Poitiers	Examinateur

USING IMAGE-BASED LARGE-EDDY SIMULATIONS TO INVESTIGATE THE
INTRACARDIAC FLOW AND ITS TURBULENT NATURE

Abstract:

The first objective of this thesis is to generate and analyse CFD-based databases for the intracardiac flow in realistic geometries. To this aim, an image-based CFD strategy is applied to both a pathological and a healthy human left hearts. The second objective is to illustrate how the numerical database can be analysed in order to gain insight about the intracardiac flow, mainly focusing on the unsteady and turbulent features.

A numerical framework allowing insight in fluid dynamics inside patient-specific human hearts is first presented. The heart cavities and their wall dynamics are extracted from medical images, with the help of an image registration algorithm, in order to obtain a patient-specific moving numerical domain. Flow equations are written on a conformal moving computational domain, using an Arbitrary Lagrangian-Eulerian framework. Valves are modelled using immersed boundaries.

Application of this framework to compute flow and turbulence statistics in both a realistic pathological and a realistic healthy human left hearts is presented. The blood flow is characterized by its transitional nature, resulting in a complex cyclic flow. Flow dynamics is analysed in order to reveal the main fluid phenomena and to obtain insights into the physiological patterns commonly detected. It is demonstrated that the flow is neither laminar nor fully turbulent, thus justifying a posteriori the use of Large Eddy Simulation.

The unsteady development of turbulence is analysed from the phase averaged flow, flow statistics, the turbulent stresses, the turbulent kinetic energy, its production and through spectral analysis. A Lagrangian analysis is also presented using Lagrangian particles to gather statistical flow data.

In addition to a number of classically reported features on the left heart flow, this work reveals how disturbed and transitional the flow is and describes the mechanisms of turbulence production.

Keywords: Arbitrary Lagrangian-Eulerian, Immersed Boundary Method, Image registration, Hemodynamics, Heart, Patient-specific, Turbulence, Lagrangian particles.

UTILISATION DE SIMULATIONS AUX GRANDES ÉCHELLES À PARTIR D'IMAGES
MÉDICALES POUR L'ÉTUDE DE L'ÉCOULEMENT INTRACARDIAQUE ET DE SA NATURE
TURBULENTE

Résumé :

Le premier objectif de cette thèse est de générer et d'analyser une base de données pour l'écoulement intracardiaque dans des géométries réalistes. Dans ce but, une stratégie couplant simulation numérique et imagerie médicale est appliquée à un cœur gauche pathologique et à un cœur gauche sain. Le second objectif est d'illustrer comment cette base de données peut être analysée afin de mieux comprendre l'écoulement intracardiaque, en portant une attention particulière aux caractéristiques instationnaires de l'écoulement et à sa nature turbulente.

Une chaîne numérique pour simuler l'écoulement dans des géométries spécifiques au patient est tout d'abord présentée. La cavité cardiaque et ses mouvements sont extraits à partir d'images médicales à l'aide d'un algorithme de recalage d'image afin d'obtenir le domaine de calcul. Les équations qui régissent l'écoulement sont écrites dans le cadre d'un maillage se déformant au cours du temps (approche arbitrairement Lagrangienne ou Eulérienne). Les valves cardiaques sont modélisées à l'aide de frontières immergées.

L'application de cette chaîne numérique à deux cœurs gauches, l'un pathologique, l'autre sain est ensuite détaillée. L'écoulement sanguin est caractérisé par sa nature transitoire, donnant un écoulement complexe et cyclique. Il est montré que l'écoulement n'est ni laminaire, ni pleinement turbulent, justifiant a posteriori l'utilisation de simulation aux grandes échelles.

Le développement instationnaire de la turbulence est analysé à l'aide de l'écoulement moyenné sur un nombre suffisant de cycles cardiaques. Les statistiques de l'écoulement, l'énergie turbulente, la production de turbulence et une analyse spectrale sont notamment présentées. Une étude Lagrangienne est aussi effectuée en utilisant des statistiques calculées à l'aide de particules ensemencées dans l'écoulement.

En plus des caractéristiques habituellement rapportées, ce travail met en évidence le caractère perturbé et transitoire de l'écoulement, tout en identifiant les mécanismes de production de la turbulence.

Keywords: Approche Arbitrairement Lagrangienne ou Eulérienne, Frontières Immergées, Recalage d'Image, Hémodynamique, Cœur, Simulation spécifique au patient, Turbulence, Description Lagrangienne.

Remerciements

En premier lieu, je tiens à exprimer toute ma reconnaissance à mes deux encadrants de thèse : Franck et Simon. Merci de m'avoir proposé un sujet de recherche aussi intéressant et merci de votre soutien durant ces quatre années. J'ai énormément appris à vos côtés et vous ne vous êtes jamais échappés face à mes questions ou mes doutes de jeune thésard. Merci aussi pour la bonne ambiance qui a toujours régné. Nos réunions, cafés ou voyages en conférences ont toujours été l'occasion de travailler ET de rire.

Simon, je tiens particulièrement à te remercier pour le temps que tu as passé à m'écouter, à prendre le temps de comprendre ce que je voulais dire et à toujours m'apporter des réponses bien plus claires que mes questions. Mais outre tout ce que j'ai appris à ton contact, ton soutien a réellement compté.

Je remercie aussi tous ceux sans qui cette thèse ne serait pas ce qu'elle est, aussi bien par les discussions que j'ai eu la chance d'avoir avec eux, leurs suggestions ou contributions. Je pense ici en particulier à Vincent Moureau, Ramiro Moreno et Ming Chau.

Je tiens aussi à exprimer ma gratitude envers notre pays et son système de bourse d'enseignement supérieur. Je tiens à remercier notre état français pour avoir financé ces années de thèse, mais aussi pour m'avoir permis de suivre des études supérieures dans de bonnes conditions en m'offrant une bourse et un toit durant mes cinq années d'études avant la thèse. Il est facile d'oublier à quel point nous sommes chanceux de non seulement pouvoir accéder librement à la connaissance, mais en plus de pouvoir être aidé financièrement dans ce but.

J'ai ici une pensée pour tous les étudiants auprès desquels j'ai eu l'occasion d'enseigner durant ces trois dernières années, que ce soit au sein de Polytech' Montpellier ou de l'université. Ça a réellement été une bouffée d'air frais durant ma thèse. Je garderai un excellent souvenir de mes classes et de leurs attentions ! Vous ne lirez sûrement jamais ce message, mais merci à vous !

Une pensée affectueuse pour le crew de l'IMFT avec qui j'ai partagé du temps au début de ma thèse. Grâce à vous, l'aquarium de Barcelone ou les concepts de cal'sschage et de moit-moit' n'ont plus de secrets ! Je ne peux évoquer l'IMFT sans avoir une pensée particulière pour toi Lou, merci pour tous les bons moments.

Un grand merci aussi aux personnels administratifs et techniques du laboratoire : Bernadette pour ta gentillesse et ton efficacité, Myriam, Sophie, Nathalie, Baptiste, ainsi qu'à Éric pour nos sorties courses à pied et nos discussions.

Je tiens évidemment à remercier les doctorants, permanents et matheux de Montpellier que j'ai pu côtoyer, que ce soit pour les discussions autour et au-delà de la thèse, les soirées, les sorties et les événements fêtés ensemble. Ça a été un plaisir d'avoir fait un bout de chemin avec vous. Señor Camilo (tu ne me referas jamais tester ton truc de body combat ;)), Carine, Olivier, Afaf (la jeune), Vava (eeeet l'autre hé), Boris, Ioan, Rémi, Pierre, Youssri Ze King a.k.a. l'homme qui pouvait se dribbler lui-même, Anthony pour nos discussions et nos franches rigolades (c'est ça les maths !), la Cathal', Nunus (Copaing !), Fifou l'homme qui murmurait à l'oreille des chiens, Alaeddine et sa patience légendaire, Sofiane, Benjamin et Lucy (dont je garderai littéralement une trace à vie), Elsa l'organisatrice de soirée jeux, Coach Tutu, Julianna, Claudia, Matthieu S. (Prof' Ibrahim, c'est vous ?), Zaza (épave !), Pacchus, Junior, Christian (soirée Réptiliens demain ?), Taron, Mister Bérard et Juanito avec qui aller manger une pizza à 19h peut dérapier sur une soirée anniversaire jusqu'au lendemain matin, Marco R. (le masochiste du travail !), Damien, Anis, Julien, Samuel, Joub (RDV l'été prochain, même table ?), Coralie, Guillaume G. (j'ai trop de conneries à écrire pour toi, je vais juste te qualifier de dolphin lover), Mymy pour toutes tes attentions et nos discussions, Mymy pipot (tant qu'y'a d'la div ?), Micka, Camarade Gauthière (attends-moi pour terminer le GR !), Jerem', David (Zbla !), Antoine (à tous les coups, je te croiserai par hasard en soirée à Toronto), Francesco, Emmanuelle, Quentin, Thomas et Björn.

Un grand merci à mes co-bureaux ! Angelina, ça a vraiment été un plaisir de partager le bureau avec toi ! Jojo le teufeur, merci pour nos discussions de geeks ;), la Sig' (dire que tu étais mon étudiant et maintenant on fait de grandes soirées ensemble) et enfin Étienne pour nos soirées papote sur la vie et nos fous rires (U wot m8?).

Pour terminer, une pensée pour ces personnes formidables qui m'accompagnent depuis pas mal d'années maintenant et sans qui ma vie aurait été bien différente. Vous avez toujours été là que ce soit en cas de coups durs ou pour faire la fête. Je pense à vous, Chon (j'ai évité le "Camille", note l'effort !), Raph', Ghunter, Milou, Déb et Ninou.

Contents

Contents	viii
I Introduction	1
Chapter 1 Thesis introduction	3
1.1 Thesis general introduction	3
1.1.1 Motivations	3
1.1.2 In vivo blood flow visualization	4
1.1.3 CFD: a complementary and comprehensive method?	6
1.1.4 About turbulence	7
1.2 Thesis aims	9
1.3 Thesis outline	10
1.3.1 Part I - Introduction	10
1.3.2 Part II - Image-based CFD method	10
1.3.3 Part III - Eulerian analysis	11
1.3.4 Part IV - Lagrangian analysis	12
1.3.5 Conclusion	12
Chapter 2 Physiological overview	13
2.1 The cardiovascular system	13
2.1.1 The circulatory loop	13
2.1.2 The cardiac cycle	15
2.1.3 The human heart	16
II Image-based CFD method	19
Chapter 3 Numerical methods for blood simulations	21
3.1 Governing equations	22
3.2 Fluid equations in moving domains	23
3.2.1 Conceptual aspects	23
3.2.2 ALE formulation	23
3.3 Design of the time advancement scheme	26
3.3.1 Runge-Kutta scheme	26
3.3.2 Pressure treatment	28
3.4 Large Eddy Simulation	28
3.5 Immersed boundary method	30

3.6	Numerical test cases	32
3.6.1	ALE test cases	32
3.6.2	Immersed boundary test cases	41
Chapter 4 From medical images to numerical simulations		45
4.1	Methodology overview	46
4.1.1	First major step: measurements and images treatments	47
4.1.2	Second major step: image registration.	47
4.1.3	Third major step: CFD preparation	48
4.2	Mathematical setting	50
4.3	Model extraction from the <i>template</i> image	50
4.4	Image registration	54
4.4.1	Mathematical problem	54
4.4.2	Regularisation	54
4.4.3	Pyramidal strategy	56
4.4.4	Final formulation	57
4.4.5	Optimization	57
4.5	Numerical domain deformation	58
4.5.1	Application of the patient-specific deformation	58
4.5.2	Volumetric grid	59
4.6	Valves model	61
4.7	Inlet and outlet boundary conditions	65
4.8	Discussions	66
III Eulerian analysis		71
Chapter 5 First insights in a left heart flow		73
5.1	Introduction	74
5.2	Numerical simulation setup	74
5.2.1	Heart model and extraction of the deformation	74
5.2.2	Computational mesh and simulation details	75
5.2.3	Phase-averaged and fluctuating velocity definitions	79
5.2.4	LES quality assessment	79
5.2.5	Data convergence	80
5.3	Results and discussion	81
5.3.1	Global description of the flow	81
5.3.2	Velocity fields	85
5.3.3	Instantaneous structures	87
5.3.4	Velocity fluctuations	89
5.4	Flow sensitivity to viscous effect	91
5.4.1	Blood rheology	91

5.4.2	SGS modelling	95
5.5	Conclusion and outlook	97
Chapter 6 Turbulent assessment of a left heart flow		101
6.1	Problem formulation	102
6.1.1	Numerical domain	102
6.1.2	Governing equations	103
6.1.3	Computational mesh and simulation details	103
6.1.4	Data reduction	105
6.2	Data convergence	105
6.3	Results	107
6.3.1	Temporal evolutions	107
6.3.2	Kinetic energy	112
6.3.3	Production of turbulent kinetic energy	119
6.3.4	Turbulence characteristics	121
6.3.5	Spectral analysis	125
6.4	Final remarks	128
Chapter 7 A healthy subject: analysis and comparisons		131
7.1	Heart model	132
7.1.1	Heart model and extraction of the deformations	132
7.1.2	Computational mesh and simulation details	133
7.2	Results and discussion	136
7.2.1	Data convergence	136
7.2.2	Global description of the flow	140
7.2.3	Instantaneous structures	140
7.2.4	Velocity fields and signals	142
7.2.5	Atrial swirl motion	145
7.2.6	Kinetic energy	148
7.2.7	Time-frequency analysis	153
7.3	Final remarks	153
IV Lagrangian analysis		157
Chapter 8 Study of tracers transport in left hearts		159
8.1	Introduction	160
8.2	Method	160
8.3	Results for the <i>heart A</i>	163
8.3.1	Ventricle global behaviour	163
8.3.2	Left ventricle: residence time	164
8.3.3	Left ventricle: penetration	165
8.3.4	Left ventricle: path length travelled	168

8.3.5	Left ventricle: mean particle velocity	169
8.3.6	Left atrium: residence time	169
8.3.7	Left atrium: mean particle velocity	170
8.4	Results for the <i>heart B</i>	172
8.4.1	Global behaviour	172
8.4.2	Left ventricle: residence time	173
8.4.3	Left ventricle: penetration	174
8.4.4	Left ventricle: path length travelled	176
8.4.5	Left ventricle: mean particle velocity	176
8.4.6	Left atrium: residence time	177
8.4.7	Left atrium: mean particle velocity	178
8.5	Conclusion	179
Conclusion		181
Chapter 9 Main results, discussions & perspectives		183
9.1	Global conclusion	183
9.2	Discussions	185
9.2.1	Morphological modelling	185
9.2.2	Blood modelling	186
9.3	Perspectives	187
Nomenclature		189
List of Figures		190
List of Tables		199
Bibliography		201

Part I

Introduction

Thesis introduction

Chapter contents

1.1	Thesis general introduction	3
1.1.1	Motivations	3
1.1.2	In vivo blood flow visualization	4
1.1.3	CFD: a complementary and comprehensive method?	6
1.1.4	About turbulence	7
1.2	Thesis aims	9
1.3	Thesis outline	10
1.3.1	Part I - Introduction	10
1.3.2	Part II - Image-based CFD method	10
1.3.3	Part III - Eulerian analysis	11
1.3.4	Part IV - Lagrangian analysis	12
1.3.5	Conclusion	12

In this introductory chapter, the general context of the thesis is exposed, as well as the objectives and contributions of this work. The thesis outline is then presented while the main results of each chapter are exposed.

1.1 Thesis general introduction

1.1.1 Motivations

Today, heart diseases still represent the leading cause of death in the world [111] and causes each year over 2.0 million deaths in the European Union [6]. Intracardiac flow visualization can provide novel methods to assess cardiac health of a subject. Intracardiac hemodynamics is closely related to the morphology and function of the heart: changes of the heart shape or of its wall dynamics alter the blood flow patterns. Therefore,

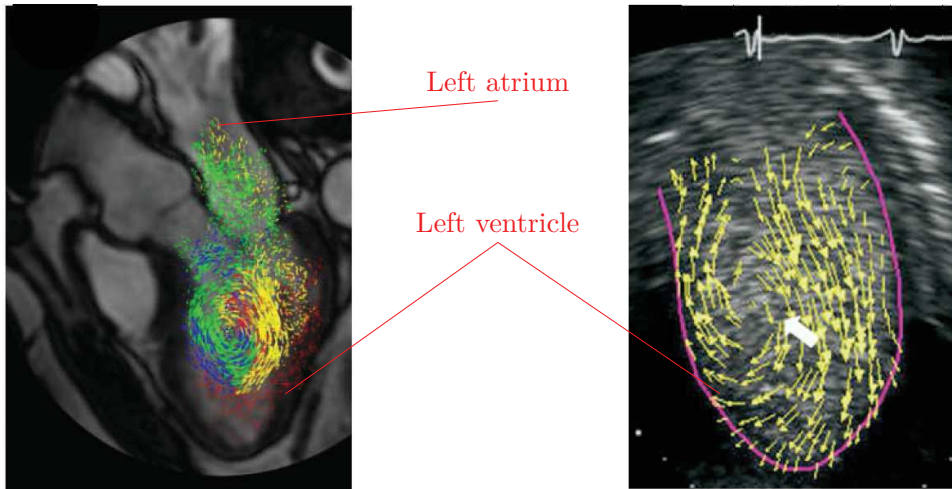


Figure 1.1: Visualization of blood flow in a left heart. (a) Phase-contrast magnetic resonance imaging (from [109]) and (b) Echo-PIV (from [84]).

analysing the blood flow spatial and temporal distribution in the heart may provide information on cardiac abnormalities.

Since the 1980s, recent technological innovations in medical imaging techniques have provided valuable opportunities for non-invasive assessment of hemodynamics [154]. Blood flow velocities can be measured *in vivo* using phase-contrast magnetic resonance imaging (PC-MRI) or by echocardiography techniques. However, these techniques still suffer from several drawbacks.

As a matter of fact, in the clinical routine hemodynamics is mostly observed indirectly through global variables such as the cardiac output in order to assess the cardiac performance. Indeed, a synthetic description of the available flow information and its relation with the heart function is still lacking. Yet, analyzing the spatial and temporal distribution of blood flow in the cardiovascular system may provide diagnostic and prognostic information.

1.1.2 In vivo blood flow visualization

MRI phase-contrast technique

Using the velocity encoded MRI phase-contrast technique [121], blood flow velocities can be measured in any direction, generating 3D flow velocity maps. PC-MRI studies have widely contributed to the understanding of hemodynamic features these last years [20, 24, 51, 62, 90, 93, 109]. Although very comprehensive (see Fig. 1.1a), the PC-MRI velocity mapping suffers from some drawbacks. In addition of the potentially disruptive signal-to-noise ratio, the MRI operator must specify the range of velocities *a priori*. If not appropriate, this choice leads to aliasing errors in the high-speed range.

Note also that the flow mapping is not real-time. In order to encode the flow in all the spatial directions, velocity components measurements are not done simultaneously. Finally, the flow map is obtained by combining the information from several heartbeats. Hence, beat-to-beat variations in the flow cannot be recorded (the k-space is filled over many cardiac cycles). Moreover, PC-MRI suffers from a relatively low spatio-temporal resolution. Today, cardiac blood flow can be measured with a spatial resolution of roughly 3 mm^3 with a temporal resolution of 50 ms, precluding observation of small-scale and fast time-varying flow features [83, 94, 186].

Echocardiography techniques

Echocardiography techniques, with higher spatio-temporal resolution, make an alternative to PC-MRI (see Fig. 1.1b). However, an important limitation though is that echocardiography only gives access to the velocity components directed towards or away from the ultrasonic beam, while one would want to measure the full 3D flow vectors. However, using color doppler one may reconstruct bi-directional velocity map under the assumption of planar flow, by using the continuity equation [63].

Echo-PIV technique seems to be a promising approach. By using particles in a contrast agent, the PIV principle [4, 88] is applied using the ultrasound beams as the imaging source instead of the classical light sheet generated by a pulsed laser. However, has several technical limitations inherent to the ultrasound technology such as its limited field of view, and its relative dependence on the skills of the operator.

Nevertheless, using echocardiography techniques, investigations have been conducted on normal and abnormal hearts, leading to potential hemodynamics-based biomarkers for cardiac health [38, 55, 69, 84, 91].

What about the Lagrangian data?

Although these advances appear promising, Eulerian blood flow maps as obtained from PC-MRI, color Doppler or echo-PIV are inadequate to observe particles trajectories in such complex flows. Complementary information can be obtained through Lagrangian-based descriptions. The motion of the blood itself or particles transported by the blood flow provides supplementary information. Simulating Lagrangian particles mimicking red blood cells can for example provide distribution of residence time data, which indicates area potentially favouring thrombosis.

Studies have been conducted using MRI [20, 23, 51]. However, they usually suffered from low spatio-temporal resolution, thus making the time integration difficult. An interesting study has been conducted by Hendabadi *et al.* [79] using novel processing of Doppler-echocardiography. The reconstructed velocity field is only two-dimensional but the temporal resolution is better than MRI. The obtained velocity fields data are used to perform trajectory-based computation of Lagrangian coherent structures in ventricles.

1.1.3 CFD: a complementary and comprehensive method?

Computational fluid dynamics (CFD) has been more and more used to predict blood flow in the heart over the last decade. In silico replications of heart chambers, mainly the left ventricle (LV), have been considered. Simulations in idealised ventricles [12, 43, 137, 176] or in more realistic geometry [187] have been performed. As in vitro experiments [27, 60], such fundamental CFD studies are particularly useful to isolate and elucidate the effect of well-controlled parameters on the blood flow. Likewise, numerical simulations focusing on Lagrangian-based descriptions in idealized left ventricle have been conducted by Zheng *et al.* [188] and Seo *et al.* [156] focusing on residence time and blood mixing. Still, Lagrangian data in the ventricle are fragmented and are lacking in the entire heart.

Inherent simplifications of the human ventricle raise the question of the relevance of the conclusions for individual clinical cases. CFD starts to be a mature technique for arterial flows [67, 96, 157, 169], but its application to study the full heart haemodynamics faces additional challenges:

- the geometry of the blood domain is complex and it undergoes large deformations,
- opening and closing valves make the topology of the domain change over the cardiac cycle,
- the flow is the result of a complex electrical-fluid-structure interaction problem,
- the flow regime is most probably transitional between laminar and turbulent and varies over the cardiac cycle.

Two main different strategies have been developed to obtain simulation of the blood flow in realistic heart geometries. The most natural one is to extract the heart geometry at one particular instant in the heart cycle and to solve an electrical-fluid-structure interaction (EFSI) problem [31, 49, 95, 132, 133, 166, 178]. In this approach, patient-specific data are needed [162, 171]. What is the exact rheology of the myocardial muscle? What is the load produced by the heart environment? How to reproduce the mechano-electric coupling in the heart muscle? All these questions are still mostly open, thus making this fully coupled approach extremely challenging. Another strategy consists in using realistic heart wall movements extracted from cine MRI or Computed Tomography (CT) scan data. The heart movement is not computed, but prescribed from the patient-specific medical images, which can be acquired using standard clinical imaging procedures. Such a computational approach, where the geometry and its deformation are extracted from images will be referred to as image-based computational fluid dynamic (IB-CFD). Different research teams have developed IB-CFD methods for heart flows, more specifically to study the left ventricle alone [101, 114, 146, 147, 151]. Recently, more advanced work has been published, using a full heart model obtained from CT images [116] or a heart model fed from MR images [42]. The feasibility of cardiac

IB-CFD has been shown, but the flow results notably suffered from limited spatial resolution or partial geometries (LV only in the majority of the cases). Furthermore, there has been remarkably little focus on the presence of turbulence in the heart, except in a few experimental works [54, 143].

1.1.4 About turbulence

A signature of abnormal flows

Under pathological conditions, it is commonly believed that topological changes, not only in the heart but also in the whole human cardiovascular system may result in *abnormally* disturbed flows. However, little *in vivo* studies focusing on turbulence have been reported on human beings, as the direct measurement of turbulence quantities requires access to the patient instantaneous blood flow. Still, measurements of high-frequency velocity fluctuations suggesting the presence of turbulence, or at least intense cycle-to-cycle variations, were published in a few studies performed on humans in the seventies. Ferguson [57] recorded sounds indicative of turbulence with a phonocatheter from the sacs of 10 out of 17 intracranial aneurysms exposed at surgery (with a peak Reynolds number of 400 approximately). Invasive conventional experimental fluid dynamics methods were used as well. Stein & Sabbah [165] used thermal anemometry to estimate the intensity of velocity fluctuations. They measured the standard deviation of repeated velocity measurements on a probe location within the ascending aorta. The results of this study indicate that turbulent flows occurs consistently in the ascending aorta of individuals with abnormal aortic valves.

In order to avoid the pitfall of *in vivo* studies, numerical simulations have been carried out over the last years with an increased focus on the use of proper numerical schemes, meshes and temporal resolution [174]. Highly unstable and turbulent flows have been observed in numerical simulations, in areas where the physiological Reynolds numbers are in the range of 100-2500, as in abdominal aorta aneurysms [96], carotid siphons [173] or in cerebral aneurysms [117, 172]. These observations are in accordance with idealized numerical simulations which showed that turbulence could occur for low Reynolds numbers in simple geometries, with pulsatile inflows (e.g.: studies conducted in idealized stenosis by [118] or [175]). In the heart, using numerical simulations in an idealized left ventricle, Domenichini *et al.* [43] suggested that turbulence could be observed in abnormal conditions. Particle image velocimetry experiments showed turbulence as well in phantoms hearts [54, 143].

Only in abnormal flow?

Interestingly, the experiment conducted on human aorta by Stein & Sabbah [165] showed that high-frequency disturbances can also occur in the ascending and in mid-ascending aorta of subjects with normal cardiac function. Figure 1.2a and Fig. 1.2b show the high frequency disturbances observed at these two sites. In the same period, thermal

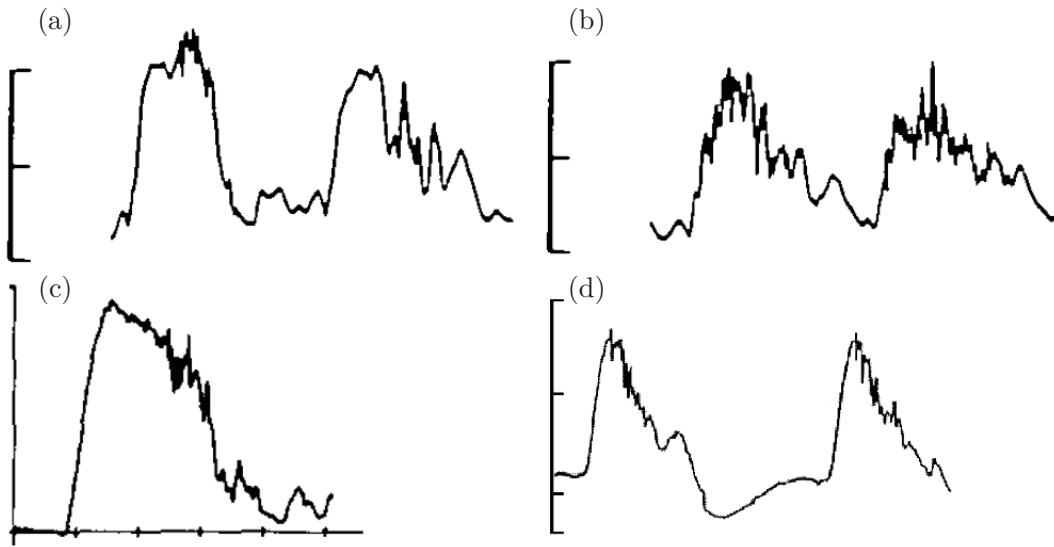


Figure 1.2: Velocity measurements on healthy human subject from [165]: high-frequency disturbances were observed above the aortic valve (a) and in mid-ascending aorta (b). (c) and (d) shows blood flow velocity records in a canine ascending aorta. (c) from [181] and (d) from [153].

anemometry was used to estimate the intensity of velocity fluctuations in canine aortas. The same type of signal has been observed in animal studies by Seed & Wood [153], Nerem *et al.* [127] and by Yamagushi *et al.* [181, 182] (see Fig. 1.2c and Fig. 1.2d).

Through phase-contrast Magnetic Resonance Imaging (MRI) methods, which allow non-invasive blood flow measurements, Stalder *et al.* [163] studied the aortic flow in a large cohort of 30 healthy subjects. They computed a critical peak Reynolds number for turbulent transition depending on the measured Womersley and Strouhal numbers according to an empirical correlation proposed by Peacock *et al.* [136]. Their conclusion was that flow instabilities were present in healthy subjects at rest in the ascending and descending aorta as supracritical Reynolds numbers are likely. More recently, Dyverfeldt *et al.* [47] developed a new MRI method based on the intravoxel velocity standard deviation to calculate the flow turbulent kinetic energy (TKE). This MRI method strengthens the idea that turbulence can occur in healthy human subjects, although it is weaker than in pathological cases. Indeed, non-negligible levels of TKE values in healthy aorta, in left atrium [48] and in left ventricles [185] were measured.

Under the light of the cited experiments and simulations, the idea of an always laminar flow seems now questionable in the cardiovascular system, particularly in the human heart. If transitional and turbulent flows are observed in a simple cerebral aneurysm, what can be expected for a complex domain like the heart? It is believed that only a pathological cardiovascular system topology may yield flow separation, recirculation

and reattachment, as well as strong shear layers. These features combined with flow pulsatility can result in periodic transition to turbulence. However, it appears that all these features could be found in the healthy cardiovascular system as well, notably in the left heart.

The left heart acts as a pump for the oxygenated blood coming from the lungs. The left heart is composed of two cavities, the atrium and the ventricle. These heart cavities have a complex shape and are deformed over the cardiac cycle. The ventricle is also connected to the aorta. The atrium has generally four entrances (the four pulmonary veins), connected to the lungs. The oxygenated blood pumping can be described in two main phases. First, an *admission* phase called diastole, and an *ejection* phase called systole. During diastole, blood rushes from the atrium, which is filled with oxygenated blood, to the ventricle. Then, during systole, the ventricle volume decreases up to 60 % of its maximum volume, to push out blood through the aorta. In the meantime, four oxygenated blood jets are formed in the atrium thanks to four inlets: the left and right superior pulmonary veins and the left and right inferior pulmonary veins.

Complex and highly moving cavities topology, Reynolds numbers up to 5000: in a few words, the heart seems to be a breeding ground for turbulence. This suggests that turbulence may exist in healthy subjects. Still, there has been little or no focus on the turbulence in the heart blood flow simulation, despite its potential medical importance. Turbulence in blood is not only interesting from a phenomenological point of view. It is also from a pathological point of view as turbulence may be a cause of pathophysiological changes [33] as initiation and progression of atherosclerosis [29], platelet activation [16], red blood cells aggregation [164] or hemolysis [87].

However, patient-specific simulations have only focused on the laminar flow regime [42, 101, 114, 116, 147, 151]. There is a real gap between the knowledge gained through the few *in vivo* studies, the numerical simulations in simple physiological system and the heart simulations done today. It is even more puzzling that this gap exists between experiments and simulations of the heart itself.

Whether or not *haemo-turbulence* analysis is clinically relevant remains an open question. If the intracardiac flow is turbulent, when and where during the heart cycle does turbulence occur? Because of which mechanisms? In addition, from a modelling point of view, if turbulence is present, what is the impact of the blood flow on haemolysis model based on integrated mean local stress? What about the residence time of red blood cells commonly computed on averaged blood flows? If turbulent, is direct numerical simulation of the flow possible? Could the turbulence be modelled and how?

1.2 Thesis aims

The first objective of this thesis is to generate and analyse CFD-based databases for the intracardiac flow in realistic geometries. To this aim, an IB-CFD strategy is applied to both a pathological and a healthy human left hearts. The second objective is to

illustrate how the numerical database can be analysed in order to gain insight about the intracardiac flow, mainly focusing on the unsteady and turbulent features.

The following tasks have been achieved during the course of this PhD work:

- Adapt an existing algorithm used for simple vessels (aorta and aneurysm) to extract the heart deformations from medical images.
- Develop a new numerical solver within an existing code and develop models for the heart valves.
- Use large eddy simulation (LES) for simulating blood flows within left hearts.
- Characterize the obtained flow in a full patient left heart and in an healthy subject.
- Investigate the obtained turbulent flows and compare them.
- Use this tool to investigate the Newtonian hypothesis by comparing two simulations using either a Newtonian fluid or a Carreau-Yassuda fluid.
- Use a Lagrangian-based description to investigate blood transport using tracers as red blood cells.

1.3 Thesis outline

1.3.1 Part I - Introduction

In addition to the current chapter, this introductory part contains a short chapter (chapter 2) providing to the reader the required knowledge about the physiology, the function and properties of the human left heart.

1.3.2 Part II - Image-based CFD method

The second part focuses on the numerical methods, either adapted from previous works or developed specifically. An image-based CFD method is presented. As in the aforementioned IB-CFD works [101, 114, 147, 151], medical images are used to generate a moving patient-specific domain, in which the blood flow equations are solved. The geometry movements are generated from a 4D sequence (MRI or CT scan images) treated by an appropriate image registration algorithm [122, 129]. This approach has been used before to compute blood flow in aortas [115]. It is further developed for application to the left heart flow, notably by introducing valve modelling.

This chapter is part of: C. Chnafa, S. mendez and F. Nicoud, "Using image-based CFD to investigate the intracardiac turbulence". Published as a chapter in the book "The Cardio-Circulatory System: from Modeling to Clinical Applications", 2014 [34].

1.3.3 Part III - Eulerian analysis

Chapter 5 - First insights in a left heart flow

In order to demonstrate the ability of the method to compute the flow in the heart, its application to a complete patient-specific left heart is exposed in the first chapter of the second part of this manuscript. Using 4D CT scan images, a realistic left heart flow is computed using large-eddy simulation. The dynamic Smagorinsky-Lilly model [68] is used in this chapter. This heart is referred to as "heart A" all along this manuscript. As cycle-to-cycle velocity fluctuations are observed, 20 cardiac cycles are simulated for phase averaging and results are presented in chapter 5. An extensive description of the flow obtained is provided and the main flow characteristics usually reported in the literature are emphasised. The flow sensitivity to LES models (the dynamic Smagorinsky-Lilly model and the σ -model [130]) and a quick comparison between simulation of blood as a Newtonian fluid and blood as a Carreau-Yasuda fluid are presented.

This chapter is part of: C. Chnafa, S. Mendez and F. Nicoud, "Image-based large-eddy simulation in a realistic left heart". Published in *Computers & Fluids*, 2014 [35].

Chapter 6 - Turbulent assessment of a left heart flow

Chapter 6 provides an extended analysis of the flow in *heart A*. Large-eddy simulation is used to compute flow and turbulence statistics over 50 cardiac cycles. In the light of the conclusions drawn from the last chapter, the σ -model is used for the sub-grid scale (SGS) model instead of the dynamic Smagorinsky-Lilly model. The resulting complex cyclic flow shows a transitional nature, a significant amount of turbulence being generated during some specific phases of the heart cycle.

The unsteady development of turbulence is analysed by studying flow statistics, the turbulent stresses, the turbulent kinetic energy, its production and through spectral analysis. It is revealed that two mechanisms create turbulence in the studied left heart: the impingement of a vortex structure on the lateral wall of the ventricle during diastole and the collision of inflowing jets in the atrium during both diastole and systole.

The transient turbulent field is also examined by the invariant map of the turbulent stress anisotropy. It is revealed that the turbulence, when present, is close to an axisymmetric state. The flow field relaminarizes when the systolic phase begins, thanks to the stabilizing effect of the acceleration. The entire process of vortex structure undergoing turbulent breakdown and subsequent relaminarization occurs at each cycle, although significant cycle-to-cycle differences are observed.

This chapter is part of: C. Chnafa, S. Mendez and F. Nicoud, "Turbulence characterisation in a patient-specific human left heart. A numerical study". To be submitted for

publication in *Journal of Fluid Mechanics*.

Chapter 7 - A healthy subject: analysis and comparisons

In chapter 7, large-eddy simulation is used to compute flow and turbulence statistics over 30 cardiac cycles in a healthy heart, referred to as "heart *B*" in the following. The numerical domain is extracted from a temporal series of 3D medical images from a MRI exam. Thus, the blood flow unsteadiness is investigated thanks to a properly executed subject-specific large-eddy simulation. As for *heart A*, the resulting complex cyclic flow shows a transitional nature and turbulence is generated during some specific phases of the heart cycle. A comparison of the two intracardiac flows *A* and *B* is provided.

1.3.4 Part IV - Lagrangian analysis

This last part contains one chapter: "Study of tracers transport in left hearts". Flows described in Part III are seeded with massless particles to mimic the trajectories of red blood cells in hearts (atrium and ventricle). Statistical data are gathered and analysed. Statistics on the residence times, mean particle velocity will be provided for both atrium and ventricle cavity. Particles penetration and travelled path length in the ventricle will be described as well. Results between the two presented hearts are compared.

1.3.5 Conclusion

In this last chapter the main findings and conclusions drawn from this thesis are given. Discussions about the presented results and the hypotheses made in this thesis are provided. Perspectives for future researches are then discussed.

Physiological overview

Chapter contents

2.1	The cardiovascular system	13
2.1.1	The circulatory loop	13
2.1.2	The cardiac cycle	15
2.1.3	The human heart	16

Before getting to the heart of the matter, an introduction to the cardiovascular system is proposed to the reader. This short chapter provides the necessary knowledge about the human heart and exposes the vocabulary employed in this manuscript. The complexity of the cardiovascular system is just sketched here. The interested reader can get a more exhaustive presentation by consulting a relevant bibliography as [17, 98, 158].

2.1 The cardiovascular system

2.1.1 The circulatory loop

The cardiovascular system transports approximately 5 litres of blood through a network of vessels in the human body. This cardiovascular system is powered by a natural pump about the size of a closed fist: the heart. Figure 2.1 provides a schematic view of the circulation of blood (figure from [17]). This system is composed of two primary circulatory loops: the pulmonary circulation loop and the systemic circulation loop.

The pulmonary circulation transports deoxygenated blood (parts in blue in Fig 2.1) from the right side of the heart to the lungs, where the blood picks up oxygen and returns to the left side of the heart. The pumping chambers of the heart that support the pulmonary circulation loop are the right atrium and the right ventricle.

The systemic circulation carries highly oxygenated blood (parts in red in Fig 2.1)

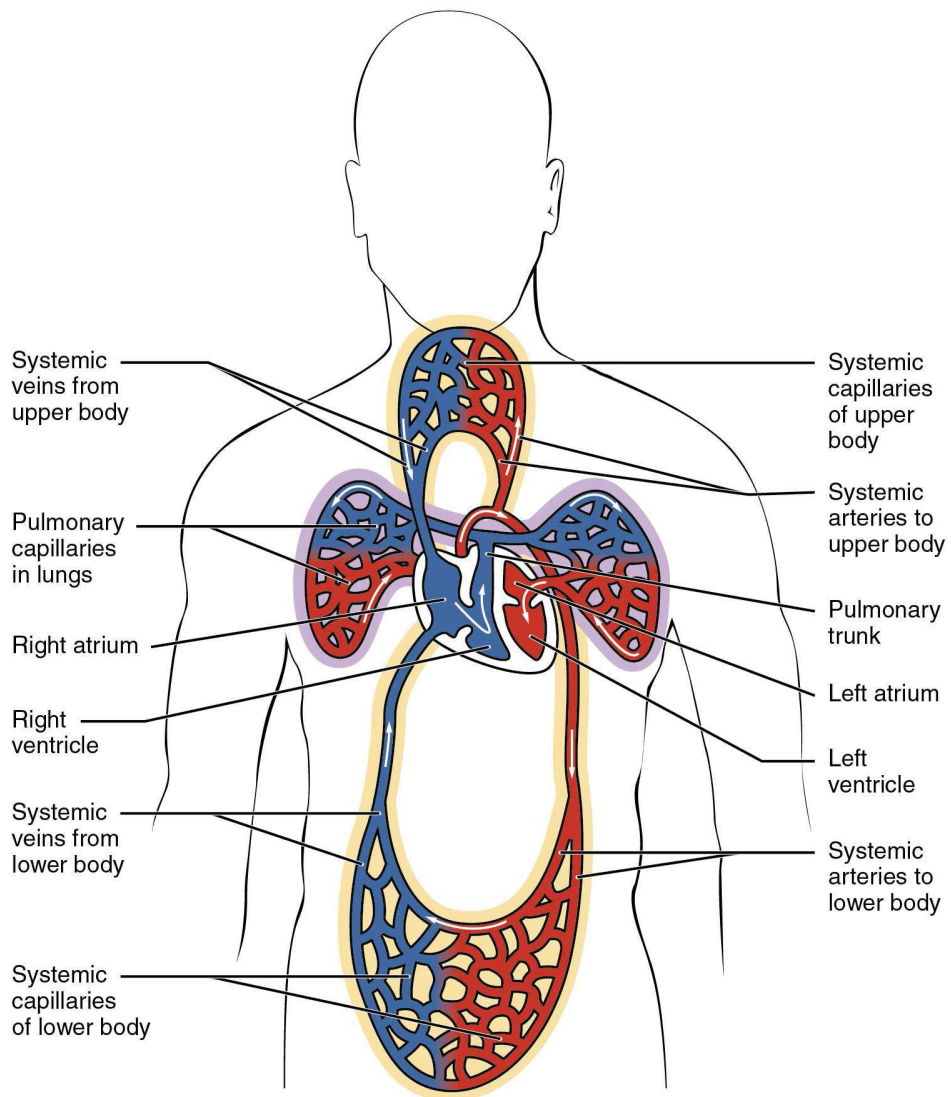


Figure 2.1: Sketch of the circulatory system (from [17]).

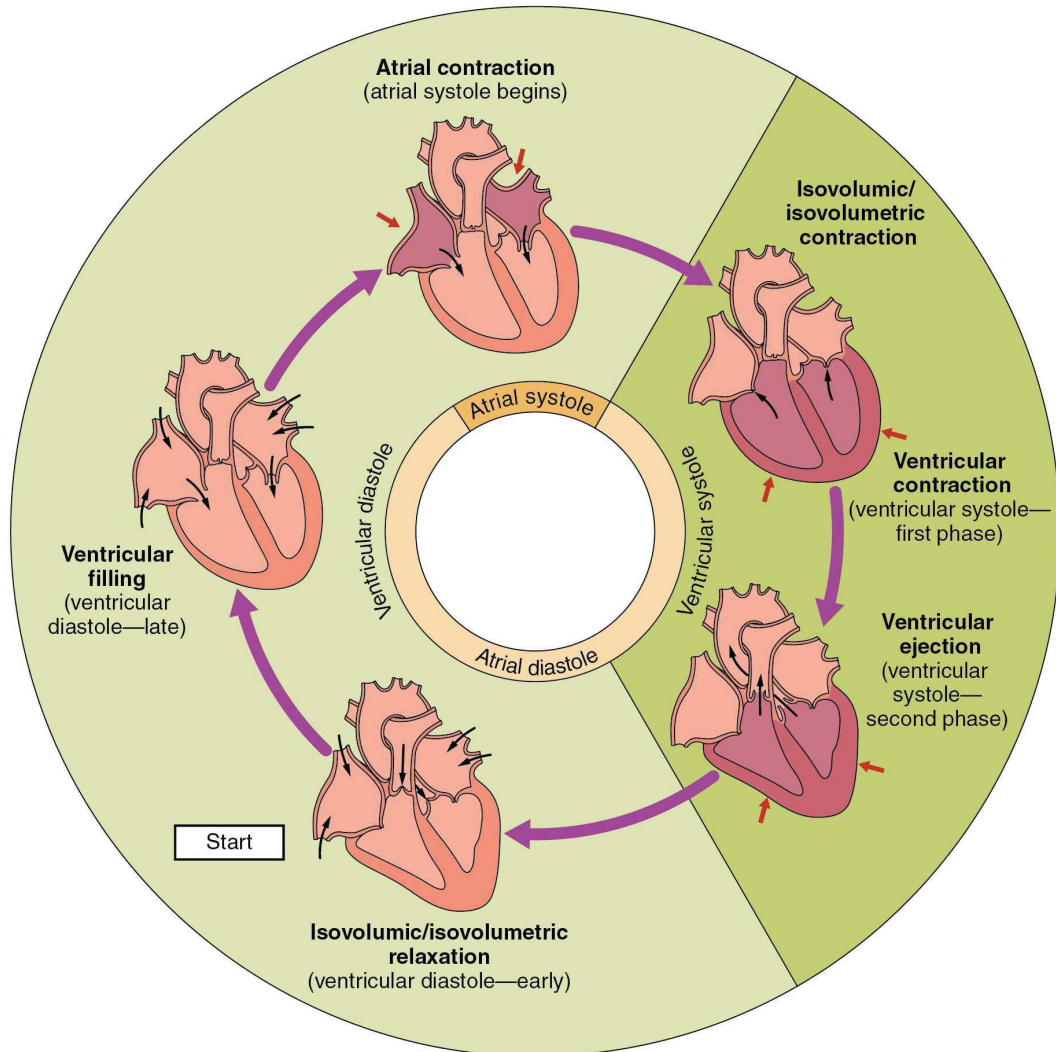


Figure 2.2: Cardiac events occurring in the cardiac cycle (from [17]).

from the left side of the heart to all of the tissues of the body (with the exception of the heart and lungs). Systemic circulation removes wastes from body tissues and returns deoxygenated blood to the right side of the heart.

2.1.2 The cardiac cycle

The blood pumping performed by the heart includes two main phases: diastole and systole. The term cardiac cycle refers to a complete heartbeat from the beginning of the diastole to the end of the systole. Its frequency is described by the heart rate, typically expressed in beats per minute (bpm). Each beat of the heart involves five

steps. Figure 2.2 describes these steps. The first three steps consist in a phase lasting roughly two thirds of the cardiac cycle and is referred to as the diastole.

During diastole, valves between atria and ventricles are open while valves between the ventricles and pulmonary artery (in the case of the right ventricle) and the aorta (in the case of the left ventricle) are closed. These valves prevent back-flow of the blood into the corresponding chamber. Hence, blood passes from the atria into the ventricles. In the left side of the heart, the ventricle filling is decomposed in two steps. At first, the ventricle volume increases rapidly, resulting in the admission of a high amount of blood coming from the atrium. This first blood wave is referred to as the "E wave". Second, the atrium contracts (it is referred to as the "atrial systole") and a second wave of oxygenated blood rushes in the ventricle. This second wave is referred to as the "A wave".

During systole, the ventricle volume decreases rapidly in order to eject blood from the ventricle to the pulmonary artery (in the case of the right ventricle) and the aorta (in the case of the left ventricle). During systole, valves between atria and ventricles are closed, while valves between the ventricles and the pulmonary artery (in the case of the right ventricle) and the aorta (in the case of the left ventricle) are open.

2.1.3 The human heart

As described in the last section, the heart is a four-chambered organ, where each side (left and right) operates as a separate pump during the cardiac cycle. Figure 2.3 displays schematically the human heart geometry. The left and right sides of the heart are separated by a muscular wall of tissue known as the septum of the heart. The right side of the heart receives deoxygenated blood from the inferior and superior vena cava and pumps it to the lungs through the pulmonary artery for oxygenation. The left side of the heart receives oxygenated blood from the lungs through the pulmonary veins and pumps it through the systemic arteries to the tissues of the body. Each heartbeat results in the simultaneous pumping of both sides of the heart. The left heart is composed of the left atrium (LA) and the left ventricle (LV). These cavities are the pumping chambers for the systemic circulation loop and are separated by the mitral valve. The aortic valve separates the aorta from the left ventricle.

Note that in cardiology, the performance of the ventricles are measured with several volumetric parameters as the end-diastolic volume (EDV), the end-systolic volume (ESV), the stroke volume ($SV = EDV - ESV$), the ejection fraction ($EF = SV / EDV$), the cardiac output ($CO = SV \times bpm$) and the E/A ratio ($E/A = \text{'blood velocity of the E wave'} / \text{'blood velocity of the A wave'}$).

Left ventricle

The left ventricle cavity is a long and narrow structure with a circular cross-section. It forms the apex of the heart and constitutes most of the posterior surface of the heart. Its walls are three times thicker than those of the right ventricle, being thickest near

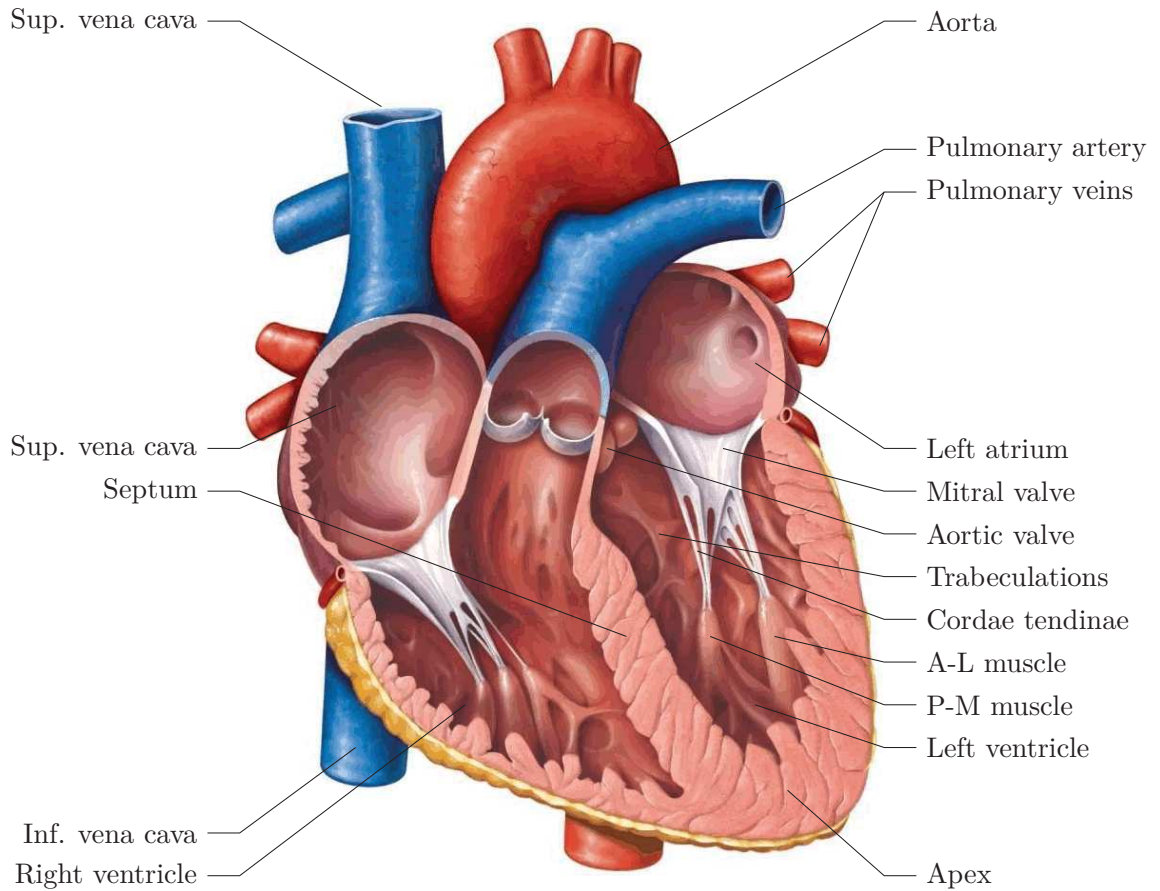


Figure 2.3: Sketch of the human heart. Blue components indicate de-oxygenated blood pathways and red components indicate oxygenated pathways. from [158]

the base and thinnest at the apex. This is because the left ventricle pumps oxygenated blood throughout the entire body while the right ventricle only pumps deoxygenated blood to the lungs.

There are two papillary muscles arising from the area between the apical and middle thirds of the left ventricular wall: the antero-lateral (A-L) papillary muscle is often composed of one body or head, and the postero-medial (P-M) papillary muscle usually composed by two bodies or heads. Each papillary muscle are attached to chordae tendinae, which are small fibrous strings connected to both mitral leaflets. These chordae tendinae attach the papillary muscles to the cusps of the mitral valve and contract to prevent inversion or prolapse of this valves during the cardiac cycle.

The endocardium surface of the left ventricle (the inner layer of the heart in contact with blood) is not smooth. It is covered by trabeculae carneae (also called trabeculations). The trabeculae carneae network is arranged like some sort of small wire mesh.

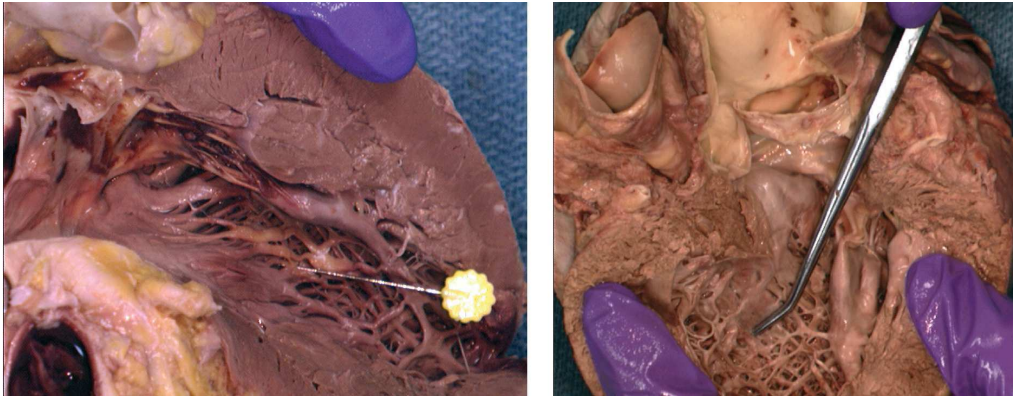


Figure 2.4: Trabeculae carneae on the inner surface of a left ventricle (from [1]).

Figure 2.4 shows trabeculae carneae in a human left ventricle.

Left atrium

The left atrium (LA) receives oxygenated blood from the pulmonary veins and pumps it into the left ventricle, via the mitral valve. The pulmonary veins (generally four) are distinct vessels named by their position: the right superior pulmonary vein (RSPV), the right inferior pulmonary vein (RIPV), the left superior pulmonary vein (LSPV) and finally the left inferior pulmonary vein (LIPV). The surface of the atrium is smooth. High in the upper part of the left atrium, between the LSPV and the LV, is a complex-shaped muscular pouch, the left atrial appendage (LAA) (not shown in the figures here).

The left heart valves

The mitral valve (MV) separates the LA and the LV. This valve is formed by two leaflets connected to the papillary muscles thanks to the cordae tendinae. It is the only valve composed of two leaflets in the human heart. The mitral valve function is to prevent back-flow of oxygenated blood in the LA when the LV volume decreases to eject blood through the aorta (AO).

The aortic valve (AV) normally has three leaflets and lies between the LV and the AO. During ventricular systole, pressure rises in the left ventricle. When the pressure in the left ventricle rises above the pressure in the aorta, the aortic valve opens, allowing blood to exit the left ventricle into the aorta. When ventricular systole ends, pressure in the left ventricle rapidly drops. When the pressure in the left ventricle decreases, the aortic pressure forces the aortic valve to close.

Part II

Image-based CFD method

Numerical methods for blood simulations

Chapter contents

3.1	Governing equations	22
3.2	Fluid equations in moving domains	23
3.2.1	Conceptual aspects	23
3.2.2	ALE formulation	23
3.3	Design of the time advancement scheme	26
3.3.1	Runge-Kutta scheme	26
3.3.2	Pressure treatment	28
3.4	Large Eddy Simulation	28
3.5	Immersed boundary method	30
3.6	Numerical test cases	32
3.6.1	ALE test cases	32
3.6.2	Immersed boundary test cases	41

This chapter describes the numerical methods developed and implemented in the YALES2BIO¹ solver [113]. The YALES2BIO solver is an adaptation of the YALES2² [123] research solver dedicated to the computation of energetic turbulent flows. As such it inherits from YALES2 its 4th-order central scheme in space on unstructured meshes and its capabilities of massively parallel computations of turbulent flows [124]. The blood governing equations in a general formulation are derived allowing the flow computation in a time varying computational domain. The developed method implemented during this work is described and tested. Subgrid-scale models for Large Eddy

¹www.math.univ-montp2.fr/~yales2bio

²www.coria-cfd.fr/index.php/YALES2

Simulation of transitional flows are used for accounting for the turbulence effects if present. Finally, the immersed boundary method implemented during this work is described and tested.

3.1 Governing equations

Blood can be modelled as an incompressible fluid, but red blood cells induce a complex rheological behaviour [59]. However, for high stress levels and in large vessels, non-Newtonian effects are usually neglected and blood is usually modelled as an incompressible Newtonian fluid in numerical simulations [169, 116]. Note that the numerical method presented in this chapter can be applied to non-Newtonian fluids and will be latter in this thesis. Taking the incompressible flow assumption into account and assuming blood as a Newtonian fluid, the fluid motion is described by the Navier-Stokes (NS) equations. These equations are solved on the moving blood domain $\Omega_f(t) \subset \mathbf{R}^3$ bounded by $\partial\Omega_f(t)$. The boundary $\partial\Omega_f(t)$ is such that $\partial\Omega_f(t) = \partial\Omega_f^i(t) \cup \partial\Omega_f^w(t) \cup \partial\Omega_f^o(t)$ and $\partial\Omega_f^i(t) \cap \partial\Omega_f^w(t) \cap \partial\Omega_f^o(t) = \emptyset$ where $\partial\Omega_f^i(t)$ represents a fluid inlet boundary where a Dirichlet condition is prescribed on the velocity field, $\partial\Omega_f^w(t)$ represents the vessels and heart wall boundary and $\partial\Omega_f^o(t)$ represents a fluid outlet boundary. The NS equations read:

$$\left. \begin{aligned} \frac{\partial \mathbf{u}_f}{\partial t} + (u \cdot \nabla)u &= -\frac{1}{\rho} \nabla p + \nu_n \nabla^2 u + \mathbf{f}, \\ \nabla \cdot u &= 0, \end{aligned} \right\} \quad \text{on } \Omega_f(t) \quad (3.1)$$

where u is the fluid velocity field, p is the pressure field, ν_n the kinematic viscosity, ρ the density and \mathbf{f} a volumetric force. The corresponding initial and boundary conditions are,

$$u(\mathbf{x}, 0) = u^0(\mathbf{x}) \quad \text{on } \Omega_f(0), \quad (3.2)$$

$$u(\mathbf{x}, t)|_{\mathbf{x} \in \partial\Omega_f^w(t)} = \mathbf{u}_s(\mathbf{x}, t) \quad \text{on } \partial\Omega_f^w(t), \quad (3.3)$$

$$u(\mathbf{x}, t)|_{\mathbf{x} \in \partial\Omega_f^i(t)} = -U^{in}(\mathbf{x}, t) \mathbf{n}_o(\mathbf{x}) \quad \text{on } \partial\Omega_f^i(t), \quad (3.4)$$

where $U^{in}(\mathbf{x}, t)$ is the inlet velocity profile imposed as a Dirichlet condition, \mathbf{n}_o the outward normal at the inlet faces, and \mathbf{u}_s is the endocardium surface velocity field imposed as a Dirichlet condition as well. A convective outlet boundary condition is imposed on $\partial\Omega_f^o(t)$ as,

$$\frac{\partial u(\mathbf{x}, t)}{\partial t} + U^{conv} \frac{\partial u(\mathbf{x}, t)}{\partial \mathbf{n}} = \mathbf{0}, \quad (3.5)$$

where \mathbf{n} is the outward normal at the outlet patch and U^{conv} the convective velocity. The uniform convective velocity U^{conv} is imposed in such a way to meet the global mass conservation over $\Omega_f(t)$. The surface velocity \mathbf{u}_s is not computed but extracted from the medical images and applied as boundary conditions for the fluid problem (see chapter 4).

3.2 Fluid equations in moving domains

3.2.1 Conceptual aspects

The aim is to solve the NS equations given in the former section to describe heart flows or more generally intra-vessels flows. Proper simulations require coping with potentially strong distortions of the studied domain. The classical Eulerian description thus cannot deal with this kind of simulation as the blood motion should be described relatively to a fixed mesh in space and time throughout the entire calculation.

Another description of motion is the Lagrangian one. Using this description, each blood subvolume corresponds to a mesh node which is thus charted over time. This description is generally used in case of "small" displacements (as in solid mechanics) and cannot describe the class of flows handled here without massive remeshing operations.

The idea of keeping a proper description of the flow domain without the requirement of frequent remeshing brought the idea of a framework combining the best features of both the Lagrangian and the Eulerian world: the *Arbitrary Lagrangian Eulerian* description [45, 58, 81, 82]. This description allows to move the mesh domain arbitrarily with the desired boundary deformations whilst computing properly the fluid. As the domain can be freely moved, domain deformation can be handled by a chosen continuous node rezoning. This mesh update procedure will be developed later in this chapter.

3.2.2 ALE formulation

Let us consider a domain $\hat{\Omega} \subset \mathbb{R}^{n_d}$ (with n_d is 2 or 3) an open bounded fluid domain. Each point of this continuum domain can be described by its coordinates \hat{x}_i . This reference domain follows a deformation all along the time $t \in \mathcal{T}$, with $\mathcal{T} = [t_0, t_f[$ (where t_0 and t_f are respectively the beginning and the end times of the observation) thanks to a one-to-one "material" mapping \mathcal{M} ,

$$\begin{aligned} \mathcal{M} : \hat{\Omega} \times \mathcal{T} &\rightarrow \Omega(t) \times \mathcal{T}, \\ (\hat{x}, t) &\mapsto \mathcal{M}(\hat{x}, t) = (x, t) \end{aligned}$$

where $\Omega(t)$ is the current state of the deformed domain $\hat{\Omega}$ thanks to a physical map as $\Omega(t) = \mathcal{M}(\hat{\Omega}, t)$. The Jacobian matrix of this deformation is defined as

$$\mathcal{J}_{\mathcal{M}} = \frac{\partial \hat{x}}{\partial x}. \quad (3.6)$$

The determinant $J_{\mathcal{M}}$ of the Jacobian $\mathcal{J}_{\mathcal{M}}$ is considered non null as the physical material mapping \mathcal{M} is considered invertible and positive as the transformation needs to be orientation preserving. The velocity of each point of the domain $\Omega(t)$ can be defined as the time derivative of the displacement between the points and their transformation, thus

$$\hat{u}(\hat{x}, t) = \frac{\partial}{\partial t}(\mathcal{M}(\hat{x}, t) - \hat{x}) \quad (3.7)$$

$$= \frac{\partial}{\partial t}(\mathcal{M}(\hat{x}, t)). \quad (3.8)$$

Let us now consider a third domain $\omega(t) \subset \Omega(t)$. This domain can be considered as an area where observation of the continuum is wanted. This domain is the future computational domain which will be latter discretized to compute the N.S. equations. This domain is deformed with another mapping which this time is not necessarily physical. This mapping will be named the ALE mapping \mathcal{A} and defined as,

$$\begin{aligned} \mathcal{A} : \tilde{\omega} \times \mathcal{T} &\rightarrow \omega(t) \times \mathcal{T}, \\ (\tilde{x}, t) &\mapsto \mathcal{A}(\tilde{x}, t) = (x, t) \end{aligned}$$

where $\tilde{\omega} = \omega(t = 0)$ is a domain of reference. As for the material mapping \mathcal{M} , the Jacobian is defined as

$$\mathcal{J}_{\mathcal{A}} = \frac{\partial \tilde{x}}{\partial x}. \quad (3.9)$$

Again, the determinant $J_{\mathcal{A}}$ of the Jacobian $\mathcal{J}_{\mathcal{A}}$ is considered non null and positive. The velocity of this domain $\omega(t)$ is defined as

$$w(\hat{x}, t) = \frac{\partial}{\partial t}(\mathcal{A}(\tilde{x}, t)). \quad (3.10)$$

Two observations:

- if the transformation $\mathcal{A} = \text{Id}_{\tilde{\omega}}$, i.e. the function \mathcal{A} maps every element to itself, the *observation domain* remains still during time. This is the Eulerian formulation.
- if the transformation $\mathcal{A} = \mathcal{M}$, i.e. the function \mathcal{A} allows the *observation domain* to move following the same physical law as the fluid continuum. In this case, the *observation domain* follows the same material fluid particles all along the observation time t .

Besides these two particular cases, the general case is the arbitrary Lagrangian Eulerian one, the "arbitrary" term coming from the "arbitrary" choice of the mapping \mathcal{A} . Figure 3.1 shows the different domains and mappings in this case.

To recast the NS equation in this general formulation, the time differential operators need to be properly defined as they depend on the chosen formulation. The ALE time derivative for a physical quantity q (which can be a tensor of any order) is define as

$$\left. \frac{\partial}{\partial t} \right|_{\mathcal{A}} q(x, t) = \frac{d}{dt}(q(\mathcal{A}(\tilde{x}, t))). \quad (3.11)$$

This ALE derivative of q at (x, t) is interpreted as the rate of total variation in time of q on a particular point \tilde{x} of the *observation domain*. This observation point moves thanks to the map \mathcal{A} and is located on the point x at the time t . The chain rule is then applied to this ALE derivative and yields,

$$\left. \frac{\partial q}{\partial t} \right|_{\mathcal{A}} = \frac{\partial q}{\partial t} + w \cdot \nabla q. \quad (3.12)$$

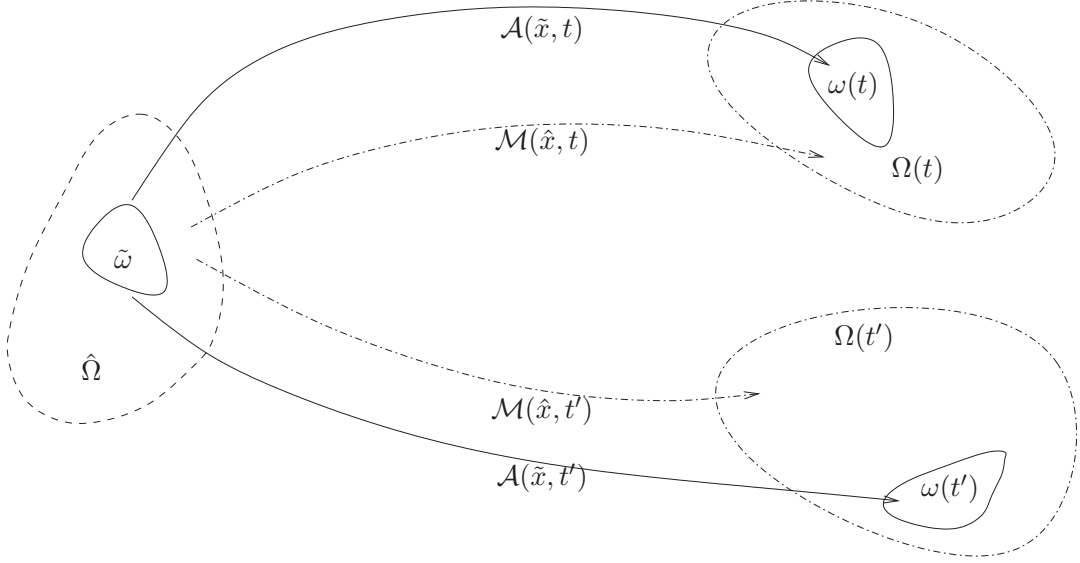


Figure 3.1: Representation of a transformed material domain Ω and *observation domain* ω at times t and t' thanks to a material and a ALE mappings for the general case.

This relation can be reversed to the classical Eulerian derivative $\frac{\partial}{\partial t}$ if mapping $\mathcal{A} = \text{Id}_{\tilde{\omega}}$ or in other words, when $w = 0$. In the Lagrangian case, w becomes the material velocity \hat{u} and the relation is reversed to the classical Lagrangian derivative.

Now, the framework to recast the Eulerian NS equations expressed at 3.1 is fixed. As only transient and convective terms change between the different formulations, equation 3.1 is rewritten as

$$\frac{\partial u}{\partial t} + (u \cdot \nabla)u = \mathbf{RHS}, \quad (3.13)$$

where the **RHS** contains the viscous fluxes, the pressure gradient and the body force. By replacing the Eulerian derivative by the ALE one thanks to relation 3.11, the equation 3.13 is rewritten as

$$\frac{\partial u}{\partial t} \Big|_{\mathcal{A}} + ((u - w) \cdot \nabla)u = \mathbf{RHS}. \quad (3.14)$$

Immediate observation is that introduction of the ALE formulation induces a correction in the convective term thanks to velocity of the *observation domain* $\omega(t)$.

The YALES2BIO solver uses a finite volume method which is based on the spatial integration of physical quantities on closed domains. Thus, equation 3.14 needs to be integrated on a domain, let us say on the *observation domain* $\omega(t)$. Equation 3.14 yields

$$\int_{\omega(t)} \frac{\partial u}{\partial t} \Big|_{\mathcal{A}} d\omega + \int_{\omega(t)} ((u - w) \cdot \nabla)u d\omega = \int_{\omega(t)} \mathbf{RHS} d\omega. \quad (3.15)$$

However, the future numerical time integration will be easier if the volume integration of the time derivative commute. Here, the domain $\omega(t)$ is potentially time dependant

which prevents this commutation. A way of bypassing this issue is the derivation of a volume integration of the first left hand side term over a volume fixed in time, as the reference one $\tilde{\omega}$. In order to do this, the Jacobian determinant $J_{\mathcal{A}}$ is introduced in relation 3.15. Using

$$\left. \frac{\partial u J_{\mathcal{A}}}{\partial t} \right|_{\mathcal{A}} = J_{\mathcal{A}} \left. \frac{\partial u}{\partial t} \right|_{\mathcal{A}} + u \left. \frac{\partial J_{\mathcal{A}}}{\partial t} \right|_{\mathcal{A}}, \quad (3.16)$$

$$= J_{\mathcal{A}} \left. \frac{\partial u}{\partial t} \right|_{\mathcal{A}} + u J_{\mathcal{A}} \nabla \cdot w, \quad (3.17)$$

the time derivative of equation 3.15 can be replaced and this expression is obtained:

$$\int_{\omega(t)} \frac{1}{J_{\mathcal{A}}} \left. \frac{\partial u J_{\mathcal{A}}}{\partial t} \right|_{\mathcal{A}} d\omega + \int_{\omega(t)} \nabla \cdot (u(u-w)) d\omega = \int_{\omega(t)} \mathbf{RHS} d\omega. \quad (3.18)$$

As \mathcal{A} is bijective, supposed a continuously differentiable function and u a continuous function, successive integrations by substitution can be applied to on the first left hand side term:

$$\int_{\omega(t)} \frac{1}{J_{\mathcal{A}}} \left. \frac{\partial u J_{\mathcal{A}}}{\partial t} \right|_{\mathcal{A}} d\omega = \int_{\tilde{\omega}} \left. \frac{\partial u J_{\mathcal{A}}}{\partial t} \right|_{\mathcal{A}} d\tilde{\omega}, \quad (3.19)$$

$$= \left. \frac{\partial}{\partial t} \right|_{\mathcal{A}} \int_{\tilde{\omega}} u J_{\mathcal{A}} d\tilde{\omega}, \quad (3.20)$$

$$= \left. \frac{\partial}{\partial t} \right|_{\mathcal{A}} \int_{\omega(t)} u d\omega. \quad (3.21)$$

Finally, equation 3.13 in ALE formulation and integrated on a domain becomes

$$\left. \frac{\partial}{\partial t} \right|_{\mathcal{A}} \int_{\omega(t)} u d\omega + \int_{\omega(t)} \nabla \cdot (u(u-w)) d\omega = \int_{\omega(t)_c} \mathbf{RHS} d\omega. \quad (3.22)$$

The *observation domain* called $\omega(t)$ can now be discretized and the equations can be solved.

3.3 Design of the time advancement scheme

3.3.1 Runge-Kutta scheme

In the following, the domain $\omega(t)$ is discretized thanks to a mesh. Defined as a finite collection of disjoint simplices and form a partition of $\omega(t)$. The mesh topology remains unchanged during the simulation time and each mesh node posses a velocity w as defined in the last section. Here, data are node-located and a control volume named $\omega_c(t) \subset \omega(t)$ is considered. Integrating equations 3.22 between $t^n=t^0 + n\Delta t$ (Δt being the time step size) and t^{n+1} yields,

$$u^{n+1} V^{n+1} - u^n V^n + \int_{t^n}^{t^{n+1}} \int_{\omega(t)_c} \nabla \cdot ((u-w)u) d\omega dt = \mathbf{RHS}, \quad (3.23)$$

with V^n the cell volume at time t^n . The time advancement scheme applied on the equations 3.23 is chosen as an explicit low-storage four-step Runge-Kutta scheme [180] recast in an ALE formalism. This scheme is coupled with the Chorin's projection correction method [36] for the pressure term (details will be given in subsection 3.3.2). Thus, velocity at time t^{n+1} is computed thanks to a time advancement scheme using four sub-steps. Leaving the **RHS** term apart, they are computed as:

$$\begin{aligned} u^0 &= u^n \\ u^i &= u^n \frac{V^n}{V^i} + \alpha_i \frac{\Delta t}{V^i} \int_{\omega} \nabla \cdot (u^{i-1} - w^{n+1}) u^{i-1} d\omega \quad \text{for } i = 1, \dots, 4 \\ u_{\star}^{n+1} &= u^4, \end{aligned} \quad (3.24)$$

where $\mathbf{u}_{\star}^{n+1} = \mathbf{u}_{\star}(t^{n+1})$ is the predicted (non-solenoidal) velocity field, α_i is a coefficient as $\alpha_i = [1/4, 1/3, 1/2, 1]$ and V^i the cell volume at time $t^i = t^n + \alpha_i \Delta t$. Note that if the mesh velocity is zero, the volumes V^n and V^i are equal and a classical low-storage four-step Runge-Kutta scheme is recovered. Grid nodal velocity w are considered constant during the computational time step. Each Grid node x is advanced at the beginning of each sub-step i as,

$$\begin{aligned} x^0 &= x^n \\ x^i &= x^{i-1} + w^{n+1} \beta_i \Delta t \quad \text{for } i = 1, \dots, 4 \\ x^{n+1} &= x^4 + \beta_f \Delta t, \end{aligned} \quad (3.25)$$

and grid metrics are recomputed at the end of each sub-step. Coefficients β_i are linked to α_i and are equal to $\beta_i = [1/8, 1/24, 1/12, 1/4]$. They allow the grid to move at the wanted midpoint configuration. At the end of the fourth step, the grid is at a configuration corresponding to time $t^{n+1/2}$ as confirmed by the summation of the β coefficients. A final step is thus imposed to the grid with a coefficient of $\beta_f = 0.5$ to reach its final position. The reader's attention is drawn to the integration volume ω in equation 3.24. It is crucial to establish at which time evolving domain the equation must be integrated. A way to answer this question is to require that the numerical method satisfies a discrete version of the so-called Geometric Conservation Law (GCL) [56, 19]. Referring to the classical interpretation of the GCL, the numerical method has to preserve the state of a constant flow U . A discrete GCL arises from the presented numerical scheme for each sub-step as:

$$V^i - V^n = -\alpha_i \Delta t \int_{\omega} \nabla \cdot w^{n+1} d\omega \quad \text{for } i = 1, \dots, 4. \quad (3.26)$$

For each control volume, this relation states that the change in volume where the equations are integrated between t^n and t^{n+1} must be equal to the volume swept by the

control volume boundary during $t^{n+1} - t^n$. Grid nodal velocity w is constant and the metrics evolve linearly during the computational time step. In order to satisfy exactly Eq. 3.26, the integration must then be computed at the midpoint configuration for each sub-step. Thus, the numerical scheme (3.24) satisfies the Discrete GCL for each sub-step. The **RHS** is computed with values taken at $i - 1$ at the midpoint mesh configuration as well.

A practical use of equation (3.26) is made in the YALES2BIO solver. During the numerical integration of the NS equation, as stated by the scheme (3.24), intermediate control volume is needed at time $t^i = t^n + \alpha_i \Delta t$ for the i -th step. Beside, metrics are needed at midpoint configuration of each of the sub step. In order to be efficient, the Discrete GCL is used to transport the volumes for each sub-step. Thus, the Discrete GCL is respected while an efficient volume computation is done.

3.3.2 Pressure treatment

At the end of this *prediction step*, the grid reaches its final position for the considered time step. Hence, the *projection step* to calculate pressure is performed over this fixed grid at the configuration corresponding to the time t^{n+1} . The pressure contribution is removed from the non-solenoidal predicted velocity equation,

$$u^{n+1} = u_{\star}^{n+1} + \frac{\Delta t}{V^{n+1}} \nabla p. \quad (3.27)$$

The wanted velocity field u must be a solenoidal field. Application to the divergence operator to equation 3.27 leads to the *projection step* and a Poisson equation for the pressure needs to be solved:

$$\Delta p = -\frac{V^{n+1}}{\Delta t} \nabla \cdot u_{\star}^{n+1}. \quad (3.28)$$

A Deflated Preconditioned Conjugate Gradient algorithm is used to solve this Poisson equation [107]. A homogeneous Neumann condition is applied for the pressure calculation and the pressure constant is fixed as the averaged pressure in the numerical domain so that the volume-averaged pressure over the domain $\omega(t)$ is zero. Next the *correction step* is applied,

$$u^{n+1} = u_{\star}^{n+1} - \frac{\Delta t}{V^{n+1}} \nabla p. \quad (3.29)$$

The obtained velocity field u^{n+1} is a non-solenoidal field as wanted.

3.4 Large Eddy Simulation

Direct numerical simulation (DNS) is suitable for low Reynolds number flows: all the large and small scales are resolved in this approach, requiring high grid densities. Reynolds Averaged Navier-Stokes (RANS) approaches for modelling turbulence are

hardly predictive, especially in the case of transitional flows at moderate Reynolds numbers (one assumption often made when developing RANS models is that the Reynolds number is very large if not infinite).

In the present work, the Large Eddy Simulation (LES) approach is used. While the large scales of the flow are resolved, the smaller subgrid scales (SGS) are modelled using two SGS models based on eddy-viscosity. The σ -model able to handle wall bounded flows in complex geometries is used [130] as well as a well established Dynamic Smagorinsky formulation [68] in order to assess the robustness of our results to the turbulence modelling.

Under the incompressible flow assumption and assuming blood as a Newtonian fluid, the fluid motion is described by the Navier-Stokes (NS) equations as previously stated. The NS equations on the moving blood domain $\Omega_f(t) \subset \mathbf{R}^3$ bounded by $\partial\Omega_f(t)$ can be written for the resolved velocity \overline{U}_i and pressure \overline{P} as

$$\left. \begin{aligned} \frac{\partial \overline{U}_i}{\partial t} + \frac{\partial \overline{U}_i \overline{U}_i}{\partial x_j} &= -\frac{1}{\rho} \frac{\partial \overline{P}}{\partial x_i} + \nu_n \frac{\partial^2 \overline{U}_i}{\partial x_j \partial x_j} - \frac{\partial \tau_{ij}}{\partial x_j} + f_i, \\ \frac{\partial \overline{U}_i}{\partial x_i} &= 0, \end{aligned} \right\} \text{ on } \Omega_f(t) \quad (3.30)$$

where ν_n is the kinematic viscosity, ρ the density and f_i a volumetric force. Note that the $\overline{\cdot}$ operator is used to denote filtered quantities fluctuating over scales which are large enough to be resolved by the computational mesh. The residual-stress tensor $\tau_{ij} = \overline{U_i U_j} - \overline{U}_i \overline{U}_j$ results from the unresolved subgrid-scale contributions and are modelled by a subgrid-scale (SGS) model in this study. Subscript i takes value of 1,2,3. The chosen SGS model for the residual-stress tensor τ_{ij} is:

$$\tau_{ij} = -2\nu_t \overline{S}_{ij}, \quad (3.31)$$

with $\overline{S}_{ij} = (\frac{\partial \overline{U}_i}{\partial x_j} + \frac{\partial \overline{U}_j}{\partial x_i})/2$ and ν_t the turbulent viscosity:

$$\nu_t = (C\Delta)^2 \mathcal{D}, \quad (3.32)$$

where Δ is the filter length (the cube root of the cell volume), \mathcal{D} the time-scale operator and C the model constant. When using the Dynamic Smagorinsky model, the time-scale operator is expressed as

$$\mathcal{D}_s = \sqrt{2\overline{S}_{ij}\overline{S}_{ij}}, \quad (3.33)$$

and the constant C_s is fixed dynamically [68]. Because of the ill-posedness of the dynamic procedure, the common practice inspired by [97] when dealing with complex geometries without homogeneous direction was adopted here: the classical least square formula was applied over a small volume surrounding the grid-point of interest and the remaining negative values of the dynamic constant were clipped to ensure $\nu_n + \nu_t \geq 0$. The Sigma model does not need extra filtering nor clipping since its timescale operator

\mathcal{D}_σ is positive by design:

$$\mathcal{D}_\sigma = \frac{\sigma_3(\sigma_1 - \sigma_2)(\sigma_2 - \sigma_3)}{\sigma_1^2}. \quad (3.34)$$

In this equation, $\sigma_1 \leq \sigma_2 \leq \sigma_3$ are the singular values of the velocity gradient tensor $\frac{\partial \bar{U}_i}{\partial x_j}$. This formulation has several interesting properties: it vanishes for a various number of canonical laminar flows, for which no SGS viscosity is expected: two-dimensional or two-component flows, axisymmetric and isotropic compression/dilatation. Furthermore, it also has the proper cubic behaviour in near wall regions and thus does not require any local dynamic procedure (the model constant C_σ was set to 1.35 as suggested by [130]). The model was validated against different academic cases (homogeneous isotropic turbulence, turbulent channel, periodic free jet), and with different numerical solvers [130, 145, 14].

3.5 Immersed boundary method

Highly deformable objects immersed in the fluid are encountered in biomechanical problems. These objects are hardly described by an Eulerian framework though. To overcome this issue, moving boundary can be taken into account by using immersed boundary (IB) methods. IB methods allows the consideration of temporally highly distorted interface between blood and vessel at the expense of potentially flaws on the geometrical description of interface. This solution consists of the introduction of a body-force field f_i in the NS equations such that a desired velocity distribution u_i can be assigned over a boundary. This idea is not new since Peskin [138] reported at the beginning of the seventies simulations of the blood flow through a model of mitral valve using this technique.

The required body-force f_i can be computed through two different methods. By "feedback forcing" [74, 149] or by "direct forcing". In the first case, arbitrary constants are needed and the scheme can results in spurious oscillation near the interfaces. The "direct forcing" approach consists of an imposition of the velocity boundary conditions on the immersed surface without introducing or computing any forcing term. If the boundary configuration is known (as in this thesis), the computation of the body-force f_i becomes simpler. In this case, only local information is needed instead of the complete force distribution over the immersed boundary. Mohd-Yusof [120] first proposed to consider the problem of forcing directly in the context of the partially discretized NS equations,

$$\frac{\mathbf{u}_f^{n+1} - \mathbf{u}_f^n}{\Delta t} = RHS^n + \mathbf{f}^n, \quad (3.35)$$

where Δt is the simulation time step, \mathbf{f}^n the force imposed at time t^n and RHS^n the right hand side containing the convective, viscous and pressure terms at t^n . To mimic

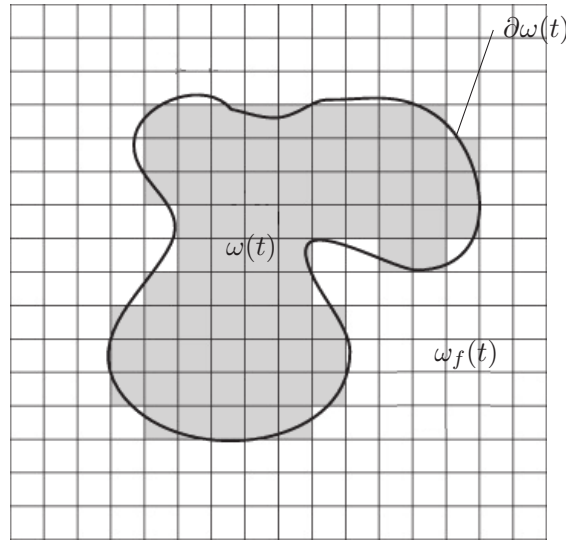


Figure 3.2: Scheme illustrating where the body-force is applied in the body Ω , immersed in the fluid domain Ω_f .

a still solid in the flow, the forcing can be explicitly defined so that a zero velocity is set in the immersed object as,

$$\mathbf{f}^n = -RHS^n - \frac{\mathbf{u}_f^n}{\Delta t}. \quad (3.36)$$

On top of the ease of implementation, the main advantage in this case is that no additional parameters is introduced in the equations as in the "feedback forcing". This expression for the forcing force must then be applied to the numerical nodes included in the immersed object and at the interface. As the grid generally does not coincide with the immersed boundary, an interpolation procedure is needed to reconstruct the immersed object boundary. Many different techniques are available to do so; they can be classified in two groups: a spreading of the forcing function in the vicinity of the immersed surface [138] or schemes that produce a local reconstruction of the solution based on the target boundary values [177].

In this work, the more simple approach has been implemented: the boundary is reconstructed by applying the force f_i to the neighbouring cell. In Fig. 3.2, Ω domain is the solid object immersed in the fluid domain Ω_f . The interface of the solid domain is roughly reconstructed by applying the force f_i at each node within Ω .

3.6 Numerical test cases

3.6.1 ALE test cases

In this subsection, the accuracy, convergence and verify of the discrete geometric conservation law (DGCL) of an arbitrary Lagrangian Eulerian (ALE) method will be investigated. A proper designed ALE numerical scheme must notably to respect the DGCL criterion in order to reproduce exactly a constant solution. This condition will be first tested and the impact of a well-respected DGCL criterion will then be highlighted. Finally, analytical solutions were developed in order to confront them to numerical simulations in both two-dimensional and three-dimensional cases.

Uniform flow

The aim of this test case is to evaluate the ability of different numerical schemes to meet their discrete geometric conservation laws (DGCLs). These tests are performed on a two-dimensional non-zero uniform flow $U(x, y, t) = U^*$ inside a regular hexagon of side length $l = 0.4$ m. The computational domain is initially discretized using twelve triangular faces and periodic boundaries conditions are specified at the boundaries. The boundaries of the domain are fixed but the inner mesh points move with a velocity following

$$\dot{x}_i(t^n) = A \omega \cos(\omega t^n + \phi_i^x),$$

$$\dot{y}_i(t^n) = A \omega \cos(\omega t^n + \phi_i^y),$$

where \dot{x}_i and \dot{y}_i are the velocity components of node i , A is the movement amplitude, ω the pulsation. For each node i , phases ϕ_i^x and ϕ_i^y are initially randomly set in the interval $[-\pi, \pi]$. Each inner mesh point (x_i, y_i) possesses its own unique velocity components. For our case, $\omega = 2\pi \text{ rad.s}^{-1}$ and $A = l/10$. The mesh deformations are illustrated by Fig. 3.6.1 for one period $\tau = 2\pi / \omega$.

The simulations are run over 100τ using a fixed time step $\Delta t = 5$ ms. Four simulations are presented, differing only by the numerical scheme used. The two schemes are a temporal explicit Euler method and the already presented RK4 method. The tests are done with both a 2nd- and a 4th-order finite-volume schemes. The relative error is then computed using

$$E_2(t^n) = \frac{\|U(t^n) - U^*\|_2}{\|U^*\|_2}$$

Figure 3.4 shows these errors for the two different schemes; all the schemes satisfy their DGCL criterion by preserving the flow uniformity.

In order to illustrate the necessity of respecting the DGCL, a non-respecting DGCL criterion scheme is studied to compare with the previous tests. The parameters of this

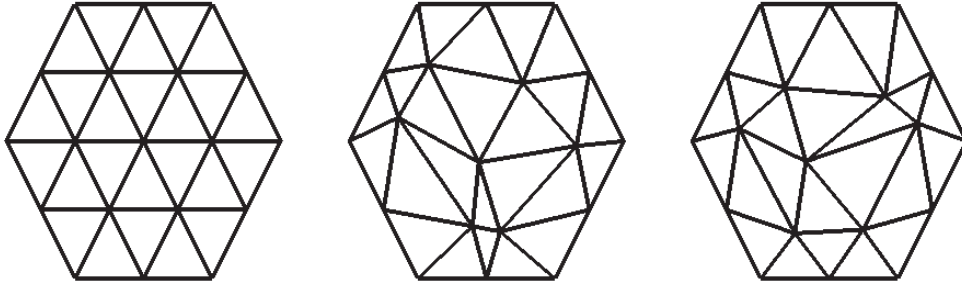


Figure 3.3: Visualization of the mesh deformation. From left to right, mesh at $t = 0$, $t = \tau/3$, $t = 2\tau/3$

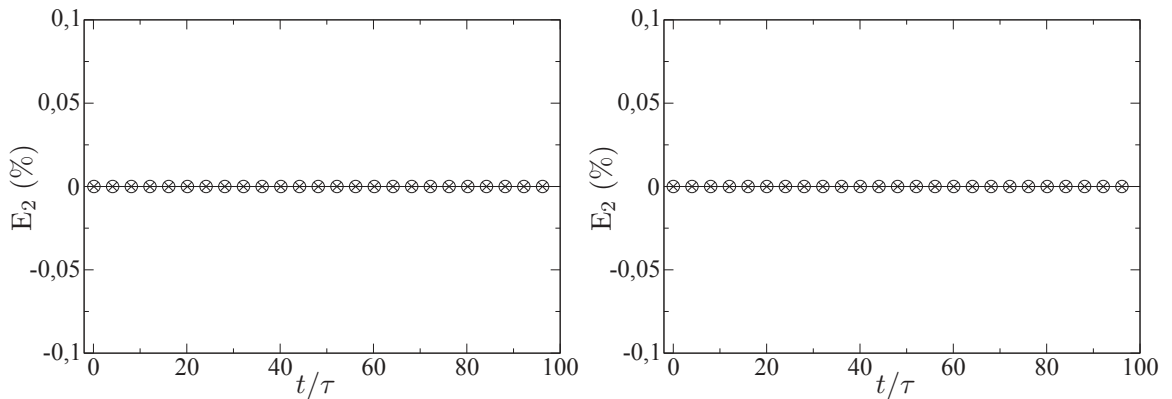


Figure 3.4: Uniform flow case. Explicit Euler (left) and RK4 method (right). \circ 2nd-order; \times 4th-order scheme in space.

simulation are the same except for the amplitude A which is divided by four ($A = 0.01$) to emphasize the importance of the DGCL criterion. The simulation is done with the RK4 time discretization scheme and the 4th-order scheme in space without taking any precautions for the DGCL. The volume used in the scheme being set at a wrong time, t^n instead of $t^{n+1/2}$. As a consequence, the scheme violates the DGCL criterion and Fig. 3.5 shows how this impacts the result for this simple test case.

2D Validation - Wall-induced channel flow

Problem definition

In this section, two main issues are investigated in a simple case:

- the accuracy of the ALE method for the RK4 time scheme by comparing analytical and numerical solutions,
- the convergence of the same method for both the 2nd- and 4th-order space schemes.

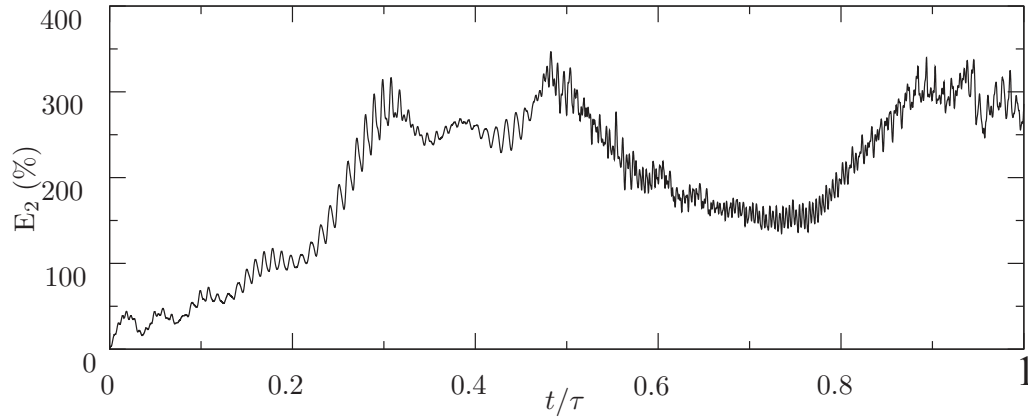


Figure 3.5: Uniform flow case. RK4, 4th-order scheme in space. Non-respecting DGCL scheme.

One of the simplest example of a flow in a time-dependent domain is provided by the flow of a Newtonian fluid in a long, straight, two-dimensional channel subjected to a time varying height (see Fig. 3.6). The flow is induced by a moving wall at $y = h(t)$ on the top of the channel which remains parallel to the x-axis and follows

$$h(t) = h_0 (1 + \epsilon e^{-j\sigma t}) \quad (3.37)$$

where σ is the pulsation of the movement, h_0 the mean distance between the symmetry axis ($y = 0$) and the moving wall and ϵ the amplitude of the oscillations.

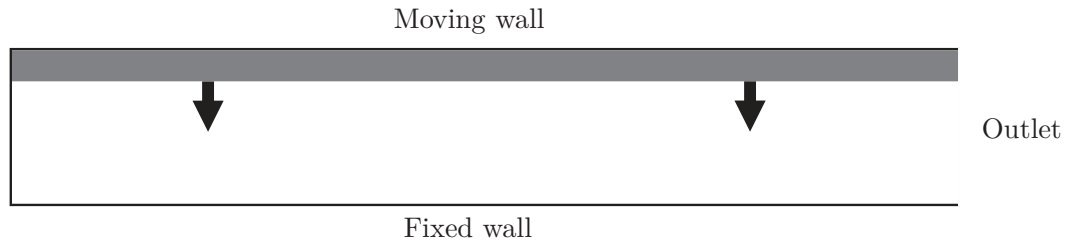


Figure 3.6: Principle of the test case. The fluid outlet is on the right.

Analytical solution

The analytical solution has been investigated by seeking a stream function of the form

$$\Psi = x F(\eta) e^{-j\sigma t}, \quad (3.38)$$

where η is the reduced coordinate $\eta = y/h(t)$. One may derive the following equation for the function $F(\eta)$

$$F'''' + \frac{h'h}{\nu_n}(\eta F'''' + 2F'') + \frac{j\sigma}{\nu_n}h^2 F'' = 0. \quad (3.39)$$

By expressing the function $F(\eta)$ as a power series of the small parameter ϵ , $F(\eta) = \epsilon F_0(\eta) + \epsilon^2 F_1(\eta) + o(\epsilon^3)$ and following the same method employed in Nicoud [128], one obtains the following first order solution

$$F_0 = j\omega h_0 \frac{\eta - \sinh(\alpha\eta)/\alpha \cosh(\alpha)}{1 - \tanh(\alpha)/\alpha}, \quad (3.40)$$

where $\alpha = j^{3/2}W_o$ is proportional to the Womersley parameter $W_o = h_0\sqrt{\frac{\omega}{\nu_n}}$.

Simulations

The flow must be considered at small Reynolds number in order to be in close agreement with the analytical solution. The Reynolds number is set between zero and 0.4 (based on the wall velocity $\dot{h}(t)$, the height $h(t)$ and the kinematic viscosity ν_n) using the parameters :

- $\epsilon = 0.05$,
- $\sigma = 2 \pi \text{ rad.s}^{-1}$,
- $h_0 = 0.001 \text{ m}$,
- $\nu_n = 8.10^{-7} \text{ m}^2.\text{s}^{-1}$.

The flow between the two walls is simulated on four grids using a domain (for the finest grid) of 190,000 triangular elements and of dimensions $[0, 25h_0]$ in the streamwise (x) direction and $[0, h(t)]$ in the vertical (y) direction. The grids are quasi-uniform for the four grids used with a characteristic edge length of $\Delta x = 0.2h_0$, $0.1h_0$, $0.05h_0$, and $0.025h_0$. The velocity is assigned vertically at the wall on the top of the domain using $\dot{h}(t)$ (see Eq. (3.37)), while at the plane at $y = 25h_0$ an outlet boundary condition is specified. Free-slip condition is applied at the bottom of the domain. Simulations are performed with both 2nd- and 4th-order space schemes and a respecting DGCL RK4 scheme in time.

Figure 3.7 shows the simulation at two different times. The results for the finest grid are considered accurate, and the L_2 and L_{inf} norms of the error obtained on the coarser grids are calculated and shown in Fig. 3.8. The results demonstrate the third-order, almost fourth-order accuracy of the method.

The simulation results are then compared with the analytical data from the Eq. (3.40). Figure 3.9 shows four phases: $t = 0$, $t = T/4$, $t = T/2$ and $t = 3T/4$. Numerical results are in very close agreement with the numerical simulation results. However, a slightly

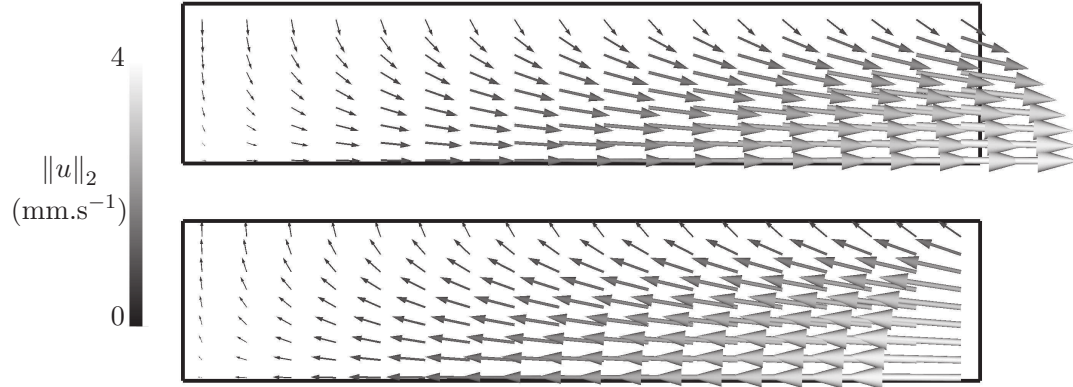


Figure 3.7: Simulation at $t = T/4$ (top figure) and $t = 3T/4$ (bottom plot). Outlet is on the left, moving piston on the top.

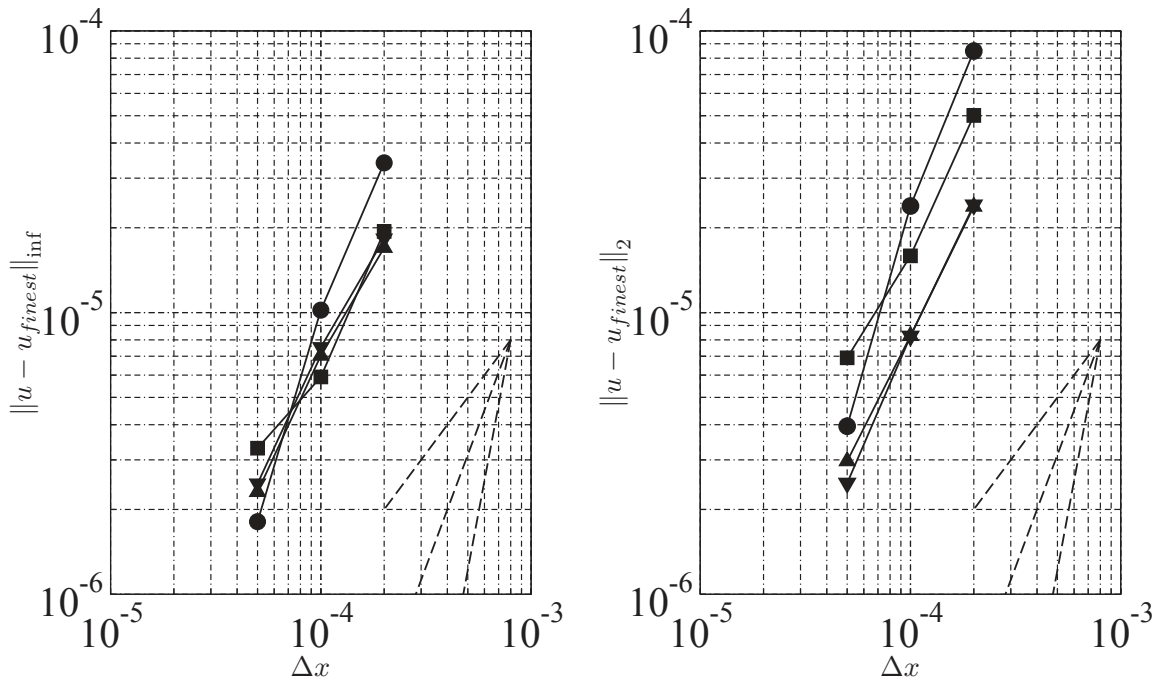


Figure 3.8: Grid convergence study. Left L_{inf} , right L_2 norms of the error.

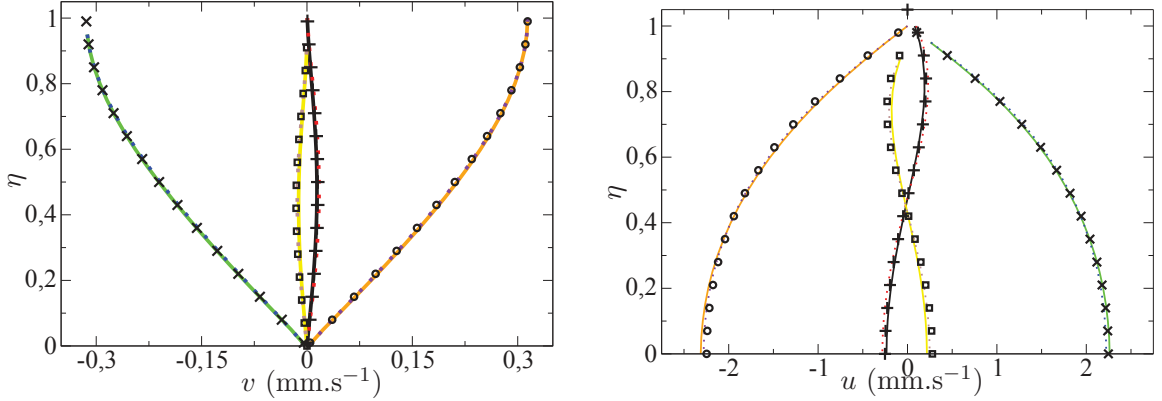


Figure 3.9: Analytical (symbols) and numerical (lines) streamwise (right) and normal wise (left) velocity profiles at $x = 5$ mm and at times $+ t = 0$; $\times t = T/4$; $\square t = T/2$; $\circ t = 3T/4$. Dotted lines, 4th order in space; solid lines, 2nd.

better behaviour of the 4th-order space scheme with regard to the analytical solution for low η values for each phase of the streamwise velocity. In addition, the maximum differences between the velocity calculated using the approximated analytical solutions and the simulation results for the four phases is less than 5% for the two space schemes and take mainly place for low η values.

3D Validation - Wall induced pipe flow

Problem definition

In order to verify the accuracy of the schemes in a three-dimensional configuration, the analytical solution used previously was first extended to the case of wall-induced pipe flow (Fig. 3.6). The inner surface of the tube is considered as a moving wall and its position is given by a function of time. A symmetry condition is imposed at one boundary while an outlet one is prescribed to the other boundary as in the two-dimensional case (see Fig. 3.6).

Analytical solution

Formulation of the mathematical problem

The analytical solution is calculated under the following hypothesis:

- the fluid is incompressible,
- the flow is axisymmetric,
- the amplitude of the oscillations are very small with regard to the radius $R(t)$.

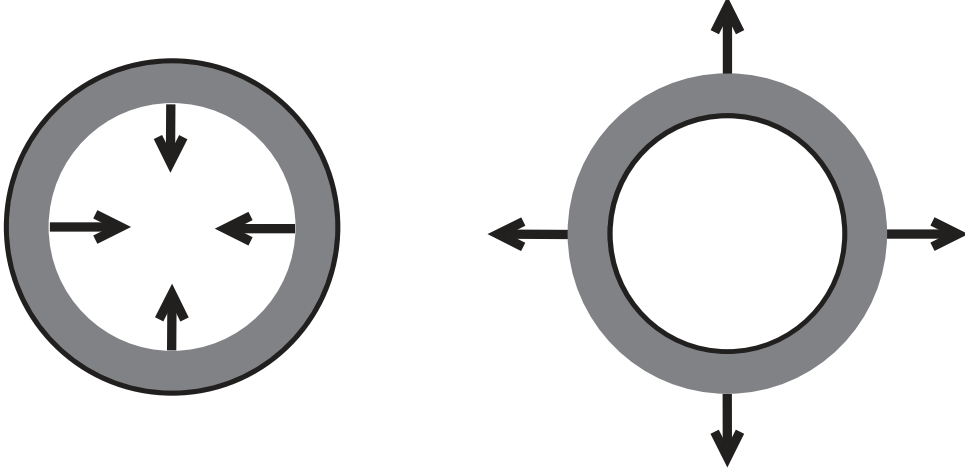


Figure 3.10: Principle of the 3D test case. Left, beginning of the cycle. Right, half-cycle.

Owing to the axisymmetric of the flow, cylindrical polar coordinates (z, r, θ) are chosen such that $r = 0$ is the symmetry axis of the tube. The equations of motion governing the flow are

$$\frac{\partial u_r}{\partial t} + u_r \frac{\partial u_r}{\partial r} + u_z \frac{\partial u_r}{\partial z} = -\frac{1}{\rho} \frac{\partial p}{\partial r} + \nu_n \left[\frac{1}{r} \frac{\partial}{\partial r} \left(r \frac{\partial u_r}{\partial r} \right) + \frac{\partial^2 u_r}{\partial z^2} - \frac{u_r}{r^2} \right] \quad (3.41)$$

$$\frac{\partial u_z}{\partial t} + u_r \frac{\partial u_z}{\partial r} + u_z \frac{\partial u_z}{\partial z} = -\frac{1}{\rho} \frac{\partial p}{\partial z} + \nu_n \left[\frac{1}{r} \frac{\partial}{\partial r} \left(r \frac{\partial u_z}{\partial r} \right) + \frac{\partial^2 u_z}{\partial z^2} \right] \quad (3.42)$$

$$\frac{1}{r} \frac{\partial}{\partial r} (r u_r) + \frac{\partial u_z}{\partial z} = 0 \quad (3.43)$$

where (u_z, u_r) are the velocity components in (z, r) directions respectively, p is the pressure, ν_n is the kinematic coefficient of viscosity and ρ is the density. The oscillations of the radius are set by the function,

$$R(t) = R_0 S(\epsilon, \sigma; t) \quad (3.44)$$

$$= R_0 (1 + \epsilon e^{-j\sigma t}) \quad (3.45)$$

where σ is the pulsation of the movement, ϵ the amplitude of the oscillations and R_0 the mean distance between the symmetry axis and the moving wall. According to the physical configuration, the boundary conditions are:

- The condition that the solution has to be regular on the axis of the tube

$$u_r(z, 0) = 0, \quad (3.46)$$

$$\frac{\partial u_z}{\partial r}(z, 0) = 0. \quad (3.47)$$

- The velocity at the wall is prescribed as

$$u_r(z, R(t)) = \dot{R}(t), \quad (3.48)$$

$$u_z(z, R(t)) = 0. \quad (3.49)$$

So as to simplify the resolution work and thanks to the symmetry, one can introduce the Stokes stream function ψ and the vorticity ω

$$u_r = -\frac{1}{r} \frac{\partial \Psi}{\partial z} \quad (3.50)$$

$$u_z = \frac{1}{r} \frac{\partial \Psi}{\partial r} \quad (3.51)$$

$$\omega = \frac{1}{r} \frac{\partial^2 \Psi}{\partial z^2} - \frac{1}{r^2} \frac{\partial \Psi}{\partial r} + \frac{1}{r} \frac{\partial^2 \Psi}{\partial r^2} \quad (3.52)$$

The curl of (3.41) and (3.42) can be taken and by seeking a stream function of the form

$$\Psi = z F(\eta) e^{-j \sigma t}, \quad (3.53)$$

where η is the reduced coordinate $\eta = r/R(t)$, one may obtain the following differential equation

$$\frac{\partial \omega}{\partial t} + \frac{1}{r} \left(\frac{\partial \Psi}{\partial r} \frac{\partial \omega}{\partial z} - \frac{\partial \Psi}{\partial z} \frac{\partial \omega}{\partial r} + \frac{1}{r} \frac{\partial \Psi}{\partial z} \omega \right) - \nu_n \left(\frac{\partial^2 \omega}{\partial z^2} + \frac{\partial^2 \omega}{\partial r^2} + \frac{1}{r} \frac{\partial \omega}{\partial r} - \frac{1}{r^2} \omega \right) = 0 \quad (3.54)$$

The boundary conditions (3.46) to (3.49) can now be written as

$$F'(1) = F'(0) = F(0) = 0, \quad (3.55)$$

$$F(1) = -\epsilon \sigma j R_0 R(t). \quad (3.56)$$

Equations solutions

The function $F(\eta)$ solution of the Eq. (3.54) is taken in the form

$$F(\eta) = \epsilon F_0(\eta) + \epsilon^2 F_1(\eta) + \dots \quad (3.57)$$

Substituting (3.57) in (3.54) and identifying the powers of ϵ , one may obtain the following differential equation for the order $o(\epsilon)$

$$\eta^3 F_0''''(\eta) - 2\eta^2 F_0''''(\eta) + F_0''(\eta) (\alpha^2 \eta^3 + 3\eta) - F_0'(\eta) (\alpha^2 \eta^2 + 3) = 0 \quad (3.58)$$

where α is equal to $\alpha = R_0 \sqrt{\frac{j\sigma}{\nu_n}}$. The resolution of this equation leads to the general solution:

$$F_0(\eta) = C1 + C2\eta^2 + C3\eta J(1, \alpha\eta) + C4\eta K(1, -\alpha\eta) \quad (3.59)$$

where $C1$ to $C4$ are four constants, $J(n, \cdot)$ and $K(n, \cdot)$ are the Bessel function of the first kind and the modified Bessel function of the second kind, respectively and n is the order of the Bessel functions. The boundary conditions (3.55) to (3.56) are used to determine the constants. One obtains

$$C1 = 0 \quad (3.60)$$

$$C2 = \frac{-i\sigma RSk\alpha J(0, \alpha)}{\alpha J(0, \alpha) - 2J(1, \alpha)} \quad (3.61)$$

$$C3 = \frac{2i\sigma RSk}{\alpha J(0, \alpha) - 2J(1, \alpha)} \quad (3.62)$$

$$C4 = 0 \quad (3.63)$$

Using these constants, the solution for the first ϵ order is finally given by

$$F_0(\eta) = \frac{-i\sigma RSk\eta(\alpha J(0, \alpha)\eta - 2J(1, \alpha\eta))}{\alpha J(0, \alpha) - 2J(1, \alpha)} \quad (3.64)$$

It is relevant for futur numerical application to consider the correction $\epsilon^2 F_1$ negligible. Hence, the convective acceleration is disregarded. From the above solution, one can determine the velocity components using the equations (3.50), (3.51) and (3.53). The solution for the velocity components is then up to the first order in ϵ :

$$u_r = \frac{-ie^{-i\sigma t}\sigma Sk(\alpha J(0, \alpha)\eta - 2J(1, \alpha\eta))}{\alpha J(0, \alpha) - 2J(1, \alpha)}, \quad (3.65)$$

$$u_z = \frac{2ize^{-i\sigma t}\sigma Sk\alpha(J(0, \alpha) - J(0, \alpha\eta))}{R(\alpha J(0, \alpha) - 2J(1, \alpha))}. \quad (3.66)$$

Simulations results

In this subsection, in order to illustrate the behaviour of the schemes in a three-dimensional case, the numerical solution of the physical problem presented in the section 3.6.1 is compared to the analytical solution obtained previously.

The flow is simulated using a domain of dimensions $[0, 25R_0]$ in the streamwise (z) direction and $[0, R(t)]$ in the radial (r) direction using 100,000 tetrahedral elements. The grid is quasi-uniform with a characteristic edge length of $\Delta x = 0.2R_0$. Non-zero radial velocity is assigned at the wall using $\dot{R}(t)$ (see Eq. (3.44)), while at the plane $z = 25R_0$ an outlet boundary condition is specified. Free-slip conditions are applied on the plane at $z = 0$.

The wall velocity used for the numerical simulation is set using the parameters :

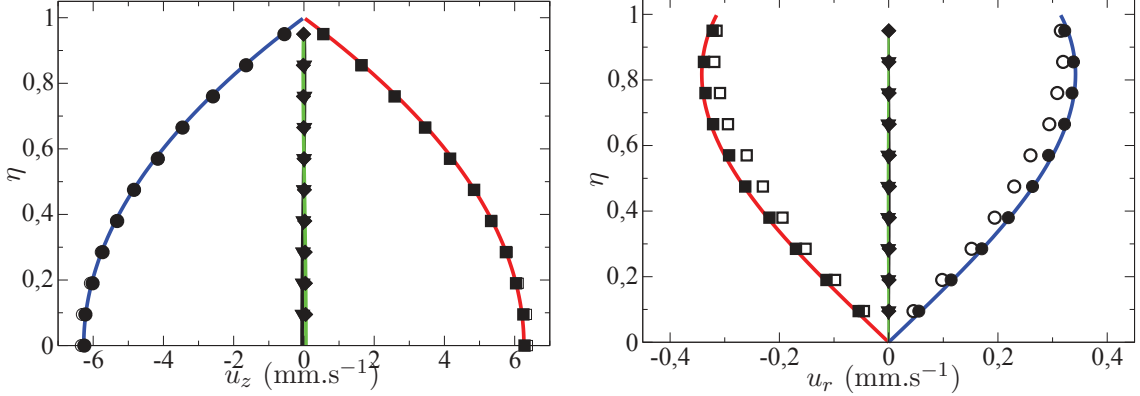


Figure 3.11: Analytical (lines) and numerical (symbols) streamwise (left) and normal wise (right) velocity profiles at $z = 0.05$ m and at times $\diamond t = 0$; $\square t = T/4$; $\nabla t = T/2$; $\circ t = 3T/4$. Filled symbols, 4th order in space; open symbols, 2nd.

- $\epsilon = 0.05$,
- $\sigma = 2\pi \text{ rad.s}^{-1}$,
- $R_0 = 0.001$ m.

The kinematic viscosity coefficient ν_n is set at $\nu_n = 1.517 \times 10^{-5} \text{ m}^2.\text{s}^{-1}$. On account of these parameters values, note that the Reynolds number is set to stay between zero and 0.02 which justifies the fact that there was no need to consider the superior order during the analytical development in this case. Figure (3.11) shows the comparison between the first order approximate solution (Eq. (3.65)) and the numerical profiles for $z = 0.05$ m using a fourth-order explicit time integration with a Runge-Kutta method and both a 2nd- and a 4th-order finite-volume schemes. The velocities from the analytical solution are in close agreement with the numerical simulation results for the four phases. Note that the 4th space order is closer to the analytical solution than the 2nd one for the most negative wall speed ($t = T/4$) and the maximum wall speed ($t = 3T/4$).

3.6.2 Immersed boundary test cases

A laminar flow around a circular cylinder is considered to test the implementation of the IBM. A rectangular domain is considered, with a cylinder of diameter $D=0.01\text{m}$ in its center. The flow around the cylinder is simulated using a domain of dimensions $[-8D,25D]$ in the streamwise direction and $[-5D,5D]$ in the vertical direction; the center of the cylinder is at $(0, 0)$. A steady uniform velocity is assigned at the inlet plane (U_{inf}), while at the outlet plane an outlet boundary condition are specified. Free-slip conditions are applied on the top and the bottom of the domain. The grid is uniform with $\delta x = \delta y = 0.05D$. $Re_D = 30$, based on the free-stream velocity U_{inf} , the cylinder diameter D and the kinematic viscosity $\nu_n = 10^{-5} \text{ m}^2.\text{s}^{-1}$. At such a low Re , the flow can be assumed to be steady after initial unsteady flow development. After 3400

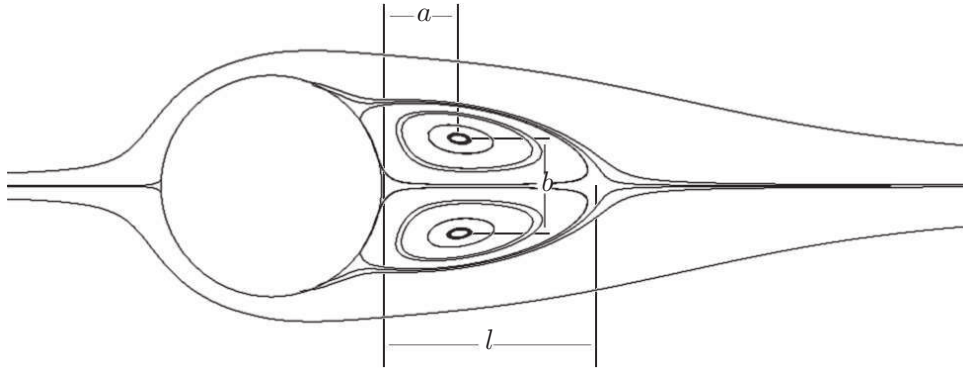


Figure 3.12: Measured data on the simulations.

	l/D	a/D	b/D
IBM	1.24	0.47	0.43
Conformal	1.57	0.54	0.52
Coutanceau and Bouard (exp.) [39]	1.55	0.54	0.54
Pinelli (num.) [140]	1.70	0.56	0.52

Table 3.1: Comparison of wake parameters for steady-state flow around a cylinder at $Re_D = 30$ with experimental and numerical data.

iterations, the probes put in the domain shows stable figures for the measured velocities. The absolute error between two successive iterations is under $10^{-9}m/s$. Two simulations were computed: one with a conformal mesh, one with all the rectangular domain meshed with the cylinder immersed in the flow using the IBM. Figure 3.12 shows the measured data on the simulations.

As the numerics used for IB is here very basic, weak results were expected on a coarse mesh.

Chapter key points:

- A RK4 scheme has been derived in a ALE framework and validated.
- SGS models used in this work have been introduced.
- The immersed boundary method used for representing the valves has been presented and tested.

From medical images to numerical simulations

Chapter contents

4.1	Methodology overview	46
4.1.1	First major step: measurements and images treatments	47
4.1.2	Second major step: image registration.	47
4.1.3	Third major step: CFD preparation	48
4.2	Mathematical setting	50
4.3	Model extraction from the <i>template</i> image	50
4.4	Image registration	54
4.4.1	Mathematical problem	54
4.4.2	Regularisation	54
4.4.3	Pyramidal strategy	56
4.4.4	Final formulation	57
4.4.5	Optimization	57
4.5	Numerical domain deformation	58
4.5.1	Application of the patient-specific deformation	58
4.5.2	Volumetric grid	59
4.6	Valves model	61
4.7	Inlet and outlet boundary conditions	65
4.8	Discussions	66

This chapter describes the framework developed for performing patient specific simulations based on 4D medical images. The method can be applied to any blood vessels. Here, the focus is on the human left heart. The key idea is to use *image registration* to deform the computational domain and to account for the valves by using immersed boundary method. Boundary

conditions are extracted from the domain movements. Patient specific 4D domain is thus obtained through this workflow.

*This chapter is part of: C. Chnafa, S. mendez and F. Nicoud, **Using image-based CFD to investigate the intracardiac turbulence**. Published as a chapter in the book "The Cardio-Circulatory System: from Modeling to Clinical Applications", 2014 [34].*

4.1 Methodology overview

Part of the framework described in this chapter is adapted from the work conducted during the OCFIA¹ (Optimised Computational Functional Imaging for Arteries) project, mainly focused on flow computations in aortas [115, 122, 129, 144]. The key idea of extracting deformations from medical images was kept and the method was adapted and extended to handle intra-cardiac blood computations. Image treatment tools and numerical methods for the fluid computation were not kept from the OCFIA project.

Determining the movement of the computational domain, where the NSE are solved is all but an easy task. Two main different strategies have been developed in the scientific community to obtain simulation of the blood flow in realistic heart geometries. The most natural one is to extract the heart geometry at one chosen moment in the heart cycle and to solve an electrical-fluid-structure interaction (EFSI) problem [31, 49, 95, 133, 166, 178]. In this approach, patient-specific data are needed [162, 171]. What is the patient-specific rheology of the myocardial muscle? What is the load produced by the heart environment? How to reproduce the mechano-electric coupling in the heart muscle? All these questions make such an approach extremely challenging.

Another strategy consists in using realistic heart wall movements extracted from cine MRI or Computed Tomography (CT) scan data. Heart movement is not computed, but prescribed from the patient-specific medical images, which can be acquired using standard clinical imaging procedures. Such a computational approach, where the geometry and the movements are extracted from images will be referred to as image-based computational fluid dynamic (IB-CFD). Different research teams have developed IB-CFD methods for heart flows, more specifically to study the left ventricle alone [101, 114, 147, 151]. Recently, more advanced work has been published, using a full heart model obtained from CT images [116] or a heart model fed from MR images [42].

In the following, an image-based CFD method is presented. As in the aforementioned IB-CFD works, medical images are used to generate a moving patient-specific domain, in which the blood flow equations are solved (see chapter 3 for the flow equations and the related numerical methods). This section provides an introduction to the method. It consists in three major steps and each of these steps are composed of diverse sub-problems. Details about the sub-problems are the objects of the following chapter sections.

¹www.ocfia.org

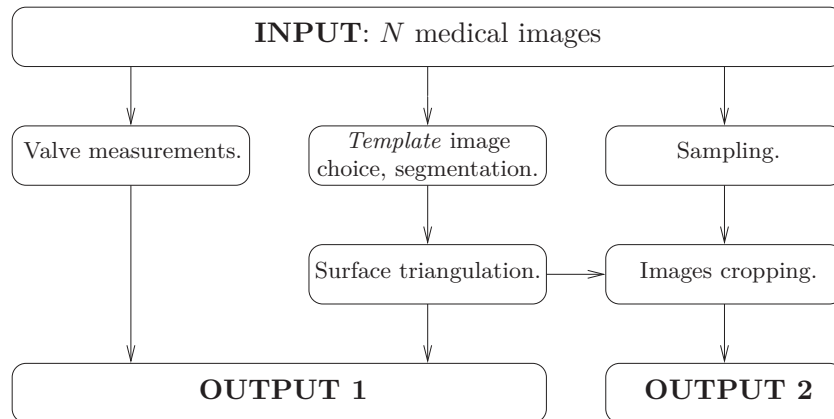


Figure 4.1: Flowchart representing the preparation to the intensity-based image registration process (see section 4.1.2) and the CFD preparation see section 4.1.3. 4D medical images (given as input data) are segmented, measured and treated providing the process outputs.

4.1.1 First major step: measurements and images treatments

Figure 4.1 shows the first major step of the workflow. Input data of the entire chain are only N medical images taken at different times during the heart cycle. Three actions have to be executed. Measurements of characteristics of the mitral valve and aortic valve have to be done. These measurements are used to feed the valves models describe in section 4.6. A *template* image has to be selected among the N medical images. A 3D model for the heart is extracted from this *template* image by a process called *segmentation*. Details about this procedure will be given in section 4.3. A surface triangulation of the 3D model is then performed to feed the third major step. Finally, the medical images are re-sampled in order to change their resolution if needed (note that all the images need to have the same resolution). They are then cropped in order to keep only the area of interest, according to a bounding box centred on the 3D model created before.

In a nutshell, at the end of this first major step, the outputs are a patient-specific triangulated surface of the studied heart, measurements of the heart valves and the set of N medical images treated.

4.1.2 Second major step: image registration.

The following question must then be addressed: given the N 3D images of a heart taken at different times in the heart cycle, how to extract the heart deformations from these images and how to deform the patient-specific numerical grid accordingly? The first part of the question is actually a classical *image registration* problem.

Nowadays, there is a growing interest in the development of cardiac image registra-

tion methods [105, 106]. Given two cardiac images, a *template* and a *reference* one, a transformation is determined to map the *template* image to the *reference* image. This computed transformation itself is of great importance because of its intrinsic information. The deformation field can notably provide clinical information on the myocardial contractile function. Here, the same process is used to compute the heart deformations, but instead of focusing on functional data of the heart muscle, the computed deformation is used to extract patient-specific boundary conditions for the blood flow computation.

Registration algorithms can be separated in two classes [119]: landmark-based registration [160, 150] and voxel similarity measures [80] method. The first method is based on the idea that the sought transformation is determined such as a finite number of features of the template image is mapped onto the corresponding features of the reference image. Note that however, compared to other human organs, the heart exhibits few accurate anatomical landmarks. In addition, in pathological conditions the functional alterations can also hide anatomical landmarks [72]. A voxel similarity measure technique was preferred in this study. This class of method operates directly on the image grey values, providing a flexible algorithm suitable for the complex heart movements, especially for intra-modality registration.

Figure 4.2 shows the second major step of the workflow: the image registration procedure. Input data are the previously chosen *template* image (as explained in section 4.1.1) and one of the medical image which is referred as the *reference* image. This step has to be executed for each of the medical image (except the *template* one) in order to obtain $N - 1$ fields of deformation between the *template* image and the others $N - 1$ ones. The algorithm treats first the two images by applying to them a gaussian filter. By applying this filter, high frequency of the images are removed. A measure of the similarity between the two images is then computed. If images are sufficiently close each other in regards of a parameter set by the user, higher frequencies are re-introduced and the distance is computed again. If the distance criterion is not met, an optimisation process is executed to find a transformation allowing the *reference* image to be closer to the *template* image. The optimisation process to find a suitable deformation field is referred as the *inner* iterations and the successive frequencies filtering the *outer* iterations. Finally, once the algorithm is converged, $N - 1$ deformation fields are obtained. Section 4.4 provides details about the entire registration procedure.

4.1.3 Third major step: CFD preparation

The $N - 1$ deformation fields computed from the medical images are then applied to the *template* surface. $N - 1$ surfaces are then generated. Each triangularized surface should correspond to one 3D image of the heart cycle. As the deformed heart model is needed at arbitrary instants, depending on the time step used in the future computation, a trigonometric interpolation for each surface nodes is computed. The knowledge of the trigonometric interpolation of each surface node provide the heart deformation at any

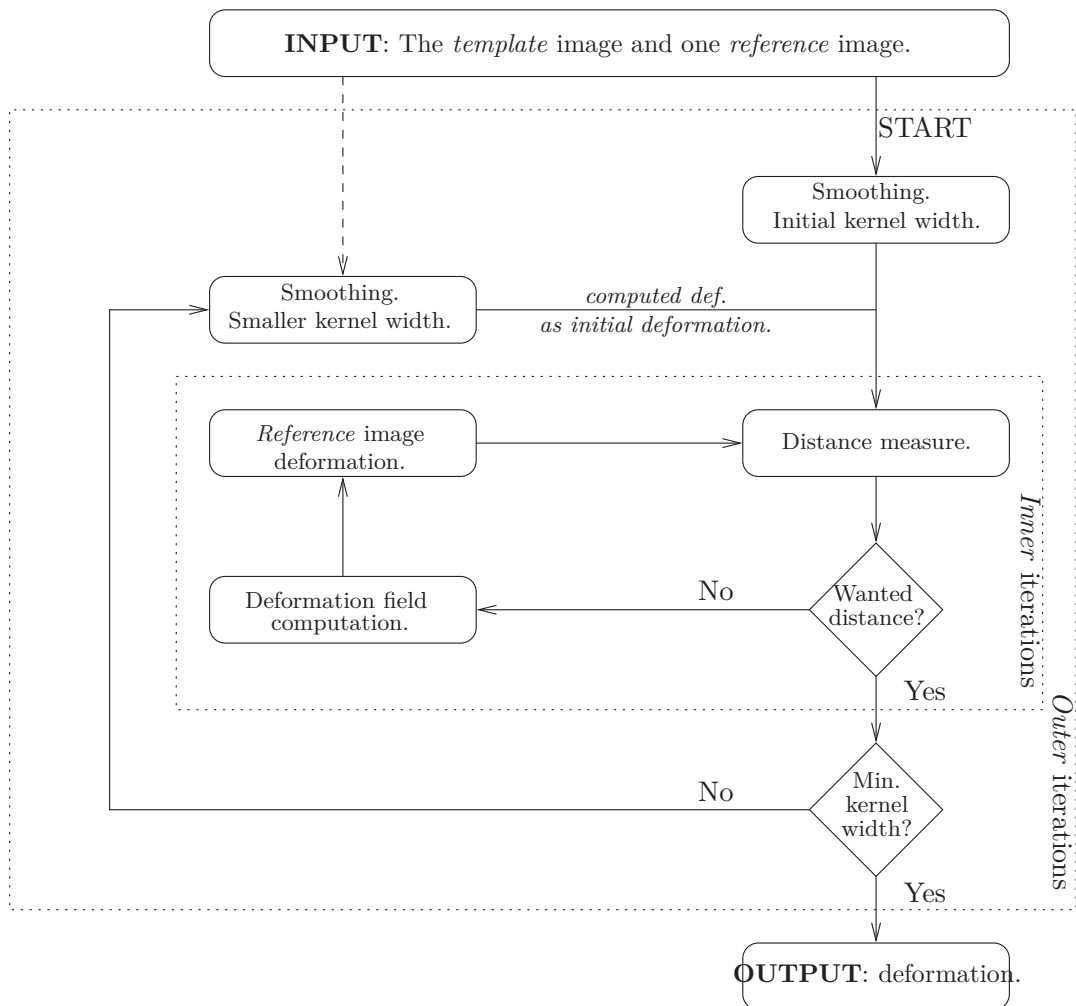


Figure 4.2: Flowchart representing the image registration process for each couple constituted of the *template* and one *reference* image. 3D deformation field between the two images (given as input data) is computed, providing the output of the process.

wanted time of the heart cycle.

Then, a 3D volumetric grid of the *template* is generated and valves models are included. Valves models are then fed by the measurements done during the first major step. The trigonometric interpolation can finally be applied to the surface of the *template* grid. The result is a 3D volumetric grid of the treated heart, deforming like the patient's heart during the heart cycle, with valve models included. Volumes of the different heart cavities are computed and fluid boundary conditions are computed from them (see section 4.7).

4.2 Mathematical setting

Before detailing the procedures described in the former section, a proper mathematical setting for the images is introduced. An image [119] can be seen as a mapping from spatial point x belonging to an *image volume* $\Omega \subset \mathbb{R}^3$ to a voxel gray value $b(x)$. Only 3D images are considered in this work and are defined as:

Definition 4.2.1. Any function $b : \mathbb{R}^3 \rightarrow \mathbb{B}$ is called a 3D image with $\mathbb{B} = \{0, \dots, 255\}$.

The following definition is also introduced:

Definition 4.2.2. The set of all 3D images is denoted by

$$\text{Img} := \{b : \mathbb{R}^3 \rightarrow \mathbb{B} \mid b \text{ is a 3D image}\}.$$

So, each spatial point x of the image has one light-intensity (a *grey value*) value between 0 and 255. 3D imaging modalities as CT or MRI generate this kind of light-intensity *grey values*. Thus, the scanned volume can be described by measured values at points placed on a structured image grid. This structured image grid is defined as a set $\mathbb{G} := \{x_k, k = 1, \dots, N\}$ with N an integer number defining the resolution of the image grid. The *grey value* is considered node located in the following. Thus, points x_k are in the centre of contiguous but non overlapping bricks partitioning the scanned image volume Ω . These bricks are called voxels, which are volumetric pixels (see Fig. 4.3d).

4.3 Model extraction from the *template* image

Before performing the model extraction, a suitable 3D image must be selected as the *template*. Ideally, the *template* image must be

- of "great" quality,
- far from the extremes times of the heart cycle (peak systole, end diastole).

The images quality can be heterogeneous for a set of images. Artefacts can be visible at some instants for example, especially for images from MRI. Peak ventricular or atrial systole should be avoided as well to minimize the distance between the template of the

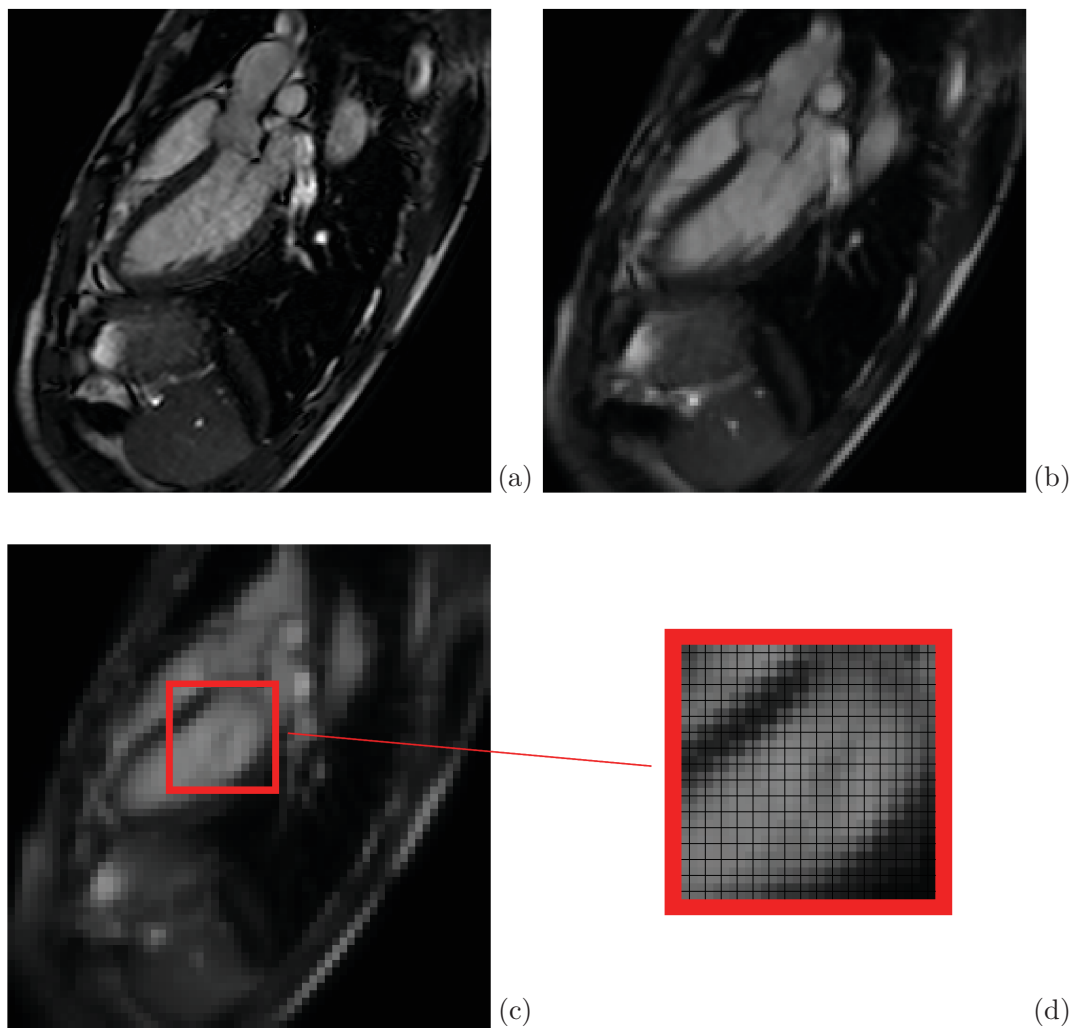


Figure 4.3: Heart image from a MRI scan. Down-sampling is applied to the image (a). Images (b) and (c) represent image (a) with a reduced resolution by scaling 0.25 and 0.5 respectively. The voxel-centred image grid is shown in image (d) for a sub-part of image (c).

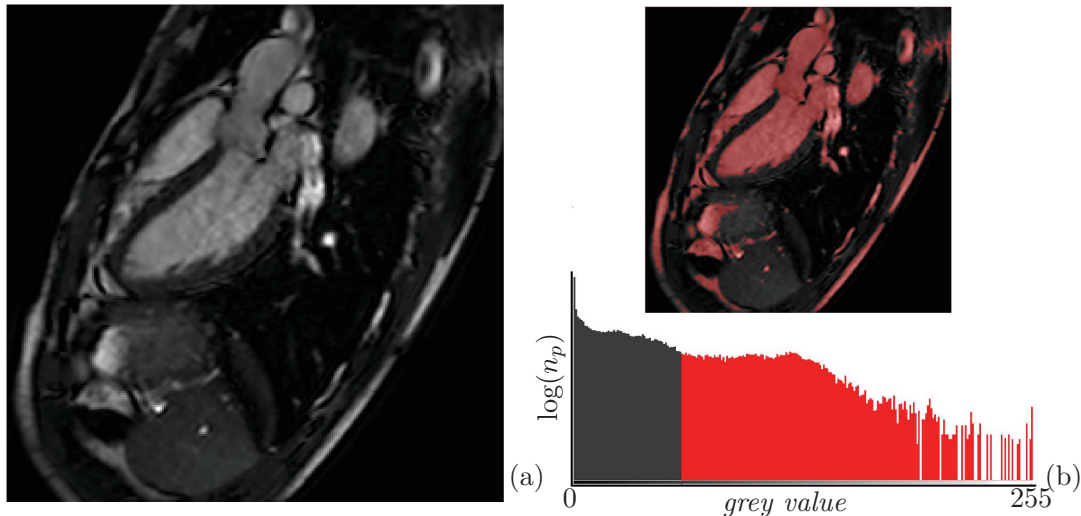


Figure 4.4: Chosen *template* image from a MRI scan (a). Images (b) represents the threshold applied to image (a) to the *grey values*. The threshold is represented by the histogram (*grey values* versus number of voxels n_p) and allow to keep the voxels with a *grey values* between 60 and 255 here. The corresponding *mask* is then created and depicted in red on the heart image.

$N - 1$ other images. Indeed, smaller the deformation between images is, better the computed deformation will be. By experience, a good choice of *template* image could be at the end of the E wave. Ventricle volume at this time is close to the cycle-averaged volume and almost the same remark can be made for the atrium. In any case, this choice has to be made with a good knowledge of the entire procedure and a trade-off has to be found between the image quality and the position of this image in the heart cycle (example, Fig 4.4a). From the selected *template* image, a 3D model of the blood domain must be extracted. Emphasis on the term "blood domain" is made here. Neither the heart muscle, nor the heart environment is considered, only the domain where blood flows. This model extraction is called segmentation [139]. Choices have to be done about the required level of modelization. Is the left atrium appendage wanted? The trabeculations? What about the papillary muscles²? Image resolution plays a role in the potential domain simplification at this step. Physiological features (see chapter 1, section 2.1) can either be kept or neglected depending on the image quality and spatial resolution available. Image can be smoothed to erase noise inherent to the medical imaging protocols but also to remove details as the trabeculations.

Once these choices are fixed, segmentation itself is executed. The *template* image is imported into ScanIP, a commercial image processing software environment (Simpleware Ltd., Exeter, UK). The simplest segmentation method is based on a threshold on the voxels *grey values*. Observation of the medical image histogram (*grey values* versus

²In this thesis, hearts models with and without papillary muscles are presented.

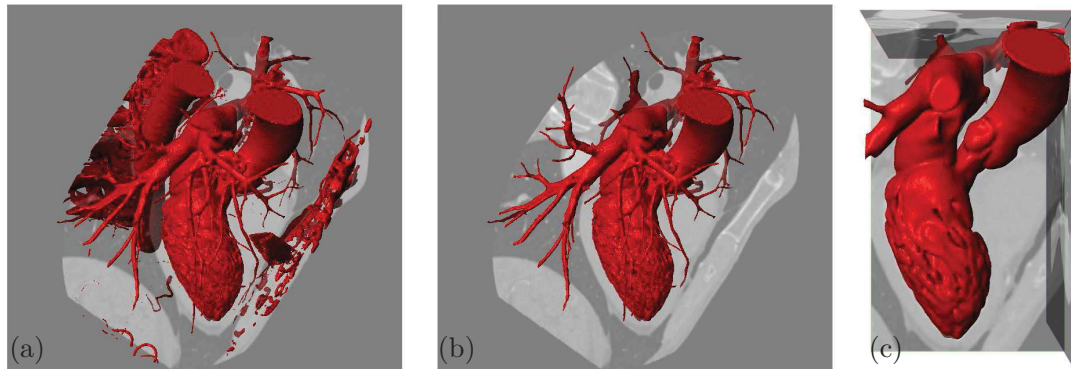


Figure 4.5: Segmentation from a CT scan. Slice of the volumetric image is depicted in transparency. Image (a) represents a segmentation only based on the *grey values* of the 3D image. Image (b) represents the same 3D model after manual treatments and image (c) the chosen area of interest for the blood computation.

number of voxels), as represented in Fig. 4.4b, helps the operator to chose a *grey values* range. By doing so, a sub set of the medical image is selected. This sub set is referred as the *mask* (in red in Fig. 4.4b). Choice of the threshold range is once again the choice of the operator. Very large range can "drown" the wanted blood domain by encompassing the heart muscles in the *mask* for example. Figure 4.5a shows a *mask* from a CT scan. Note that there is a lot of unwanted features as the spinal column (left of the figure) or the plexus (right of the picture). As only the blood domain is wanted, non connex features can be automatically deleted³ as represented in Fig. 4.5b. Nonetheless, a lot of the pulmonary trunk is still here, the LAA as well. Depending on the desired level of modelization wanted, the operator should treat the *mask* manually by deleting the unwanted features (see Fig. 4.5c).

This process is time consuming and in a clinical point of view, expensive. The operator must be an expert who knows the segmentation tools, has got a good morphological knowledge and has a lot of patience. In addition, inter- and intra- operator variability can be observed. Fully automated segmentation is of course fast, cheap, reproducible and hopefully robust. Automatic segmentation can be "easily" used for simple vessels but for the heart a tool which can be used for both CT scan and MRI modality is still lacking. Still, admirable work in this way was developed for CT scan images by Siemens [116].

Once the 3D model is extracted through the segmentation procedure, the surface of the geometric reconstruction of the heart is triangulated providing the *template* model surface.

³In the ideal case where these unwanted features are not connected to the left heart...

4.4 Image registration

4.4.1 Mathematical problem

Let N 3D images $I_i \in \mathbf{Img}$ of a patient heart which are taken at different times t_i , $0 \leq t_0, t_1, \dots, t_{N-1} < T$ during the heart cycle of period T . One of the N images is selected as a *template* image. Note that this choice is somewhat arbitrary and that, without loss of generality, one can always tune the time origin so that the *template* corresponds to the I_0 image at time t_0 . From this image, $N - 1$ transformations ψ_i are computed such that the transformed *template* image becomes similar to images I_i (i between 1 and $N - 1$) successively considered as the *reference* image: transformation ψ_i is search so that $I_0(\psi_i(\mathbf{x})) = I_i(\mathbf{x})$ for each voxel. Here, $I_i(\mathbf{x})$ stands for the voxel grey-level value at position \mathbf{x} in the i -th 3D discrete image.

Each mapping $\psi_i : \mathbb{R}^{n_d} \mapsto \mathbb{R}^{n_d}$ is calculated by minimizing a distance $\mathcal{D} : \mathbf{Img}^2 \mapsto \mathbb{R}$ between $I_0(\psi_i(\mathbf{x}))$ and $I_i(\mathbf{x})$, an appropriate distance measure being based on the so-called sum of squared differences. The transformation ψ_i is computed through an optimisation problem reading: given two images I_0 and I_i , find a mapping ψ_i such that the distance measure \mathcal{D} defined as the squared intensity differences between $I_0(\psi_i(\mathbf{x}))$ and $I_i(\mathbf{x})$ is minimized for each voxel.

4.4.2 Regularisation

At this point, the number of parameters describing the transformation is too high so that the solution ψ_i of this problem is not unique. Additional constraints are needed to reduce the search space where the mapping ψ_i is sought for.

In the present work, a constraint on ψ_i is applied thanks to prior knowledge of the deformation sought for [11]. The idea is to penalize unlikely deformations by imposing the heart deformations to be smooth. Bayesian statistics are used to obtain an *a posteriori* computation of the deformation field. The prior deformation probability is incorporated through the Bayes' theorem: $p(\mathbf{Y}|\mathbf{I}) \propto p(\mathbf{I}|\mathbf{Y})p(\mathbf{Y})$, where $p(\mathbf{I}|\mathbf{Y})$ is the likelihood of observing the images data \mathbf{I} (*template* I_0 and *reference* I_i images) given the deformation parameters \mathbf{Y} . $p(\mathbf{Y})$ is the prior knowledge of the deformation translated in the *a priori* probability of seeing the parameters \mathbf{Y} and $p(\mathbf{Y}|\mathbf{I})$ is the *a posteriori* probability of getting \mathbf{Y} knowing the two images data \mathbf{I} . Using this Bayesian framework, the goal is to maximise the probability $p(\mathbf{Y}|\mathbf{I})$. Knowing that a probability is related to its Gibbs form by $p(\mathbf{Y}) \propto e^{-H(\mathbf{Y})}$, the problem can be seen as a minimisation of the Gibbs potential:

$$H(\mathbf{Y}|\mathbf{I}) = H(\mathbf{I}|\mathbf{Y}) + H(\mathbf{Y}) + c, \quad (4.1)$$

where c is a constant. The likelihood potential $H(\mathbf{I}|\mathbf{Y})$ of observing the images data given the deformation parameters \mathbf{Y} is directly linked to the squared intensity difference between $I_0(\psi_i(\mathbf{x}))$ and $I_i(\mathbf{x})$ for each voxel:

$$H(\mathbf{I}|\mathbf{Y}) = \frac{1}{2} \int_{\Omega} (I_0(\psi_i(\mathbf{x})) - I_i(\mathbf{x}))^2 d\Omega, \quad (4.2)$$

where the integral is taken over the image volume Ω .

The second term $H(\mathbf{Y})$ in the right hand side of equation (4.1) is the wanted constraint, applied thanks to prior knowledge. The prior deformation knowledge put in this potential is expressed as a geometrical constraint on the mapping through the two studied images. Here, the discrete images are considered as being on a mesh of tetrahedra (see section 4.2 and Fig. 4.3d) and an uniform affine mapping between the voxels of each images is assumed. In 2D, if the images grids are divided into a triangular mesh where the nodes are centred on the pixels, the affine transformation can be defined as,

$$\begin{bmatrix} m_{11} & m_{12} & m_{13} \\ m_{21} & m_{22} & m_{23} \\ 1 & 1 & 1 \end{bmatrix} \begin{bmatrix} x_{11} & r_{12} & r_{13} \\ r_{21} & r_{22} & r_{23} \\ 1 & 1 & 1 \end{bmatrix} = \begin{bmatrix} t_{11} & t_{12} & t_{13} \\ t_{21} & t_{22} & t_{23} \\ 1 & 1 & 1 \end{bmatrix}, \quad (4.3)$$

where (t_{11}, t_{21}) , (t_{12}, t_{22}) and (t_{13}, t_{23}) are here the co-ordinates of the vertices of a triangle in the *template* image and (r_{11}, r_{21}) , (r_{12}, r_{22}) and (r_{13}, r_{23}) the vertices of the corresponding triangle in the *reference* image. Thus, the mapping and its matrix representation \mathbf{M} can be defined as:

$$M = \begin{bmatrix} r_{11} & r_{12} & r_{13} \\ r_{21} & r_{22} & r_{23} \\ 1 & 1 & 1 \end{bmatrix} \begin{bmatrix} t_{11} & t_{12} & t_{13} \\ t_{21} & t_{22} & t_{23} \\ 1 & 1 & 1 \end{bmatrix}^{-1}. \quad (4.4)$$

A suitable prior probability is linked to the deformation of each voxel of the *template* image and to the reverse deformation [10]. This potential acting as a regularization term allows a penalization based on the Jacobian of the locals deformations \mathbf{J} . As the Jacobian of an linear application is the application itself, the Jacobian \mathbf{J} is defined simply as,

$$\mathbf{J} = \begin{bmatrix} m_{11} & m_{12} \\ m_{21} & m_{22} \end{bmatrix}. \quad (4.5)$$

By using singular value decomposition, \mathbf{J} can be decomposed as $\mathbf{J} = \mathbf{U}\mathbf{S}\mathbf{V}^t$ where S is a diagonal matrix containing the singular values representing the relative stretching of the triangle and the matrices \mathbf{U} and \mathbf{V} represents rotations. Following Ashburner [10], a suitable form for the regularization term is,

$$h = (1 + \det(J))(\log(s_{11})^2 + \log(s_{22})^2)/2. \quad (4.6)$$

Hence, this function take into account the triangle volume change and the triangle stretching. This penalty function is minimized for a triangle when there is no deformation ($\det(J) = s_{11} = s_{22} = 1$). This regularization term is weighted by a parameter λ linked to the belief in the amount of deformation of the heart. A high value of the λ parameter results in a high penalty on the voxels deformation, hence only small and

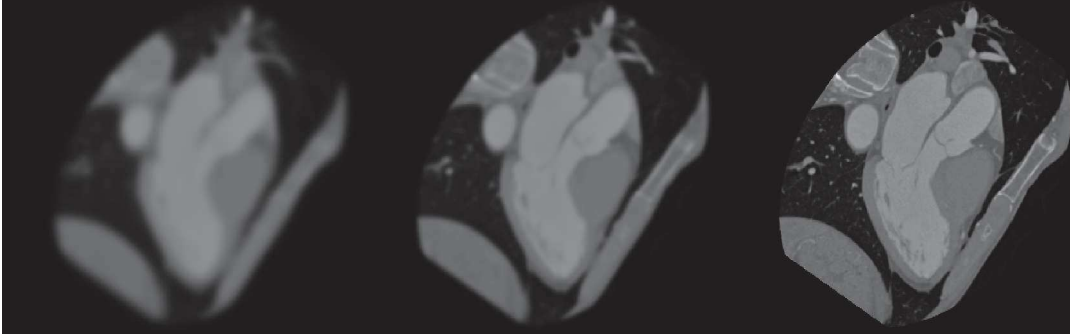


Figure 4.6: Heart image from a CT scan. Gaussian kernels applied from left to right: 3mm^3 , 1.5mm^3 and 0mm .

smooth deformations are allowed. Thus, the second term $H(\mathbf{Y})$ in the right hand side of equation (4.1) is defined for the whole image as,

$$H(\mathbf{Y}) = \lambda \sum_{i=1}^{n_t} h_i, \quad (4.7)$$

where n_t is the number of triangles in the image grid. A detailed description of this penalty term can be found in Ashburner [10] and the 3D application as well.

In our implementation, λ is set as a constant. Note that given the high deformation of the left heart, high λ values result in a high constraint thus, partial deformation and a high residual squared difference between the *template* image and the *reference* one. In the case of small values of λ , a lower residual squared difference will be reached, but the resulting deformation can be non physical due to excessive warping. Actually, the deformation of the flow domain is highly different from one region to the other. The aorta needs a priori high values of λ , whereas small values are needed for the atrium or the ventricle. Thus, search space is then bounded and one need to chose carefully the λ parameter for constrained as possible the search space while the sought solution is still in the search space.

4.4.3 Pyramidal strategy

One method of increasing the likelihood of achieving a good solution without introducing a spatial variability on λ (and consequently avoiding more operator-dependant work as well) is to apply successive filters to the images using a Gaussian smoothing convolution kernel \mathcal{G}^σ of width σ . This method is a classical Gaussian pyramid approach [3]. The high-frequency content of the image is first removed thanks to this filter then gradually re-introduced as the kernel width σ becomes smaller and smaller. This iterative process is defined as the *outer* iterations: for each kernel width, distance between the images is minimized. The process is illustrated in Fig 4.6 ; the registration algorithm works on more and more detailed images. This "coarse-to-fine" strategy has the effect of making

the registration algorithm estimate the most global deformation during the first *outer* iteration, leaving out fine-scale structures. The optimum transformation for this kernel width is used to initialize the computation of the next optimum computation, which deals with finer details. This method increases the likelihood of finding the globally optimal match while avoiding the classical problem of the intensity-based method: their susceptibility to poor starting estimates.

4.4.4 Final formulation

As the regularization term, the intensity difference (first term $H(\mathbf{I}|\mathbf{Y})$ in the right hand side of the equation (4.1)) is weighted. The weight for the j -th *inner* iteration is defined as the inverse of the residual sum of the squared differences computed at the previous *inner* iteration of a given *outer* iteration of the algorithm and is denoted by $\frac{1}{d^j-1}$. Because d has a high value for the first iterations, more weight is given to the regularization term, in order to get smooth deformations. As the algorithm gets closer to the final solution, d theoretically tends to zero, giving less weight to the priors and letting the algorithm computing more detailed deformations.

A way of seeing the resolved problem is: the sought transformation $\psi_i^{j,k}$ at the *inner* iteration j and the *outer* iteration k minimizes the function $f^{j,k}$ defined as:

$$f^{j,k}(\psi_i^{j,k}) = f_1^{j,k}(\psi_i^{j,k}) + \lambda f_2^{j,k}(\psi_i^{j,k}), \quad (4.8)$$

with,

$$f_1^{j,k}(\psi_i^{j,k}) = \frac{1}{2d^j-1} \int_{\Omega} ([\mathcal{G}^{\sigma^k} * I_0](\psi_i^{j,k}(\mathbf{x})) - [\mathcal{G}^{\sigma^k} * I_i](\mathbf{x}))^2 d\Omega, \quad (4.9)$$

$$f_2^{j,k}(\psi_i^{j,k}) = g(J(\psi_i^{j,k})), \quad (4.10)$$

where the function g is computed from the Jacobian singular values and determinant [11].

4.4.5 Optimization

Minimizing $f^{j,k}(\psi_i^{j,k})$ is equivalent to finding the set of parameters \mathbf{Y} minimizing the equation 4.1, which is also equivalent to find the most probable set of parameters (i.e. the maximum of $p(\mathbf{Y}|\mathbf{I})$). The optimization algorithm used here is a gradient descent one. It is a first-order optimization algorithm computing a local minimum; well chosen *outer* iterations help the computing of the global minimum. For the j -th inner iteration, the linear search reads,

$$y_i^{j+1} = y_i^j - \epsilon_i \frac{\partial H(\mathbf{Y}|\mathbf{I})}{\partial y_i}, \quad (4.11)$$

$$= y_i^j - \epsilon_i \left\{ \frac{\partial H(\mathbf{I}|\mathbf{Y})}{\partial y_i} + \frac{\partial H(\mathbf{Y})}{\partial y_i} \right\} \quad (4.12)$$

where ϵ_i is the distance "travelled" in the direction of the gradient for this parameter. This distance is set as a small value and can be modified during the optimisation process. When the image grid is deformed, if on Jacobian determinant becomes negative, the value of ϵ_i is halved and the image grid is deformed again. The same procedure is applied until the Jacobian determinant is positive. Finally, the $N-1$ deformations corresponding to the $N-1$ medical images are computed through this iterative optimisation process.

4.5 Numerical domain deformation

Once the $N-1$ mappings ψ_i are computed, a patient-specific computational grid must be extracted from the *template* image and warped thanks to the computed deformations. The *template* image corresponding to volumetric data I_0 is imported into the image processing software (ScanIP; Simpleware Ltd., Exeter, UK). A suitable image intensity range which encompasses the voxel intensities of the region occupied by blood in the heart is selected. The process is described in section 4.3. The 3D geometric reconstruction covers all the space occupied by blood in the left heart cavities. The surface of the geometric reconstruction of the heart is triangulated.

Once a *template* 3D patient-specific surface mesh is created, a procedure to deform this surface model thanks to the images must be provided. For each couple of images (I_0, I_i) a suitable spatial transformation ψ_i was found thanks to the method described in the previous section. These deformations ψ_i are 3D deformation fields. Trilinear interpolation from these deformation fields to the *template* surface mesh is done. Thus, a set of $N-1$ successive surface meshes matching the physiological cardiac images at different times t_i is produced as schematized in Fig. 4.7.

4.5.1 Application of the patient-specific deformation

Position and velocity of all surface points are needed at any discrete time of the simulation, not only at the times t_0, t_1, \dots, t_{N-1} . Since all the generated surface meshes share the same topology (number and connection between nodes, number of cells), temporal interpolation is used to compute the position and velocity of each node. As geometry variations are periodic, a trigonometric interpolation is used. The surface position and velocities read:

$$\left. \begin{aligned} \mathbf{x}_g(t) &= \sum_{i=0}^m [a_i \cos(2i\pi \frac{t}{T}) + b_i \sin(2i\pi \frac{t}{T})], \\ \mathbf{u}_g(t) &= \frac{2i\pi}{T} \sum_{i=1}^m [-a_i \sin(2i\pi \frac{t}{T}) + b_i \cos(2i\pi \frac{t}{T})], \end{aligned} \right\} \text{ on } \partial\Omega_f(t) \quad (4.13)$$

where T is the heart cycle period, m the number of Fourier modes ($m = \frac{N-1}{2}$ or $\frac{N}{2}$ depending on the parity of N) and a_i, b_i the Fourier coefficients. The surface velocity \mathbf{u}_s needed at the computation domain boundary $\partial\Omega_f(t)$ is hence not computed as a

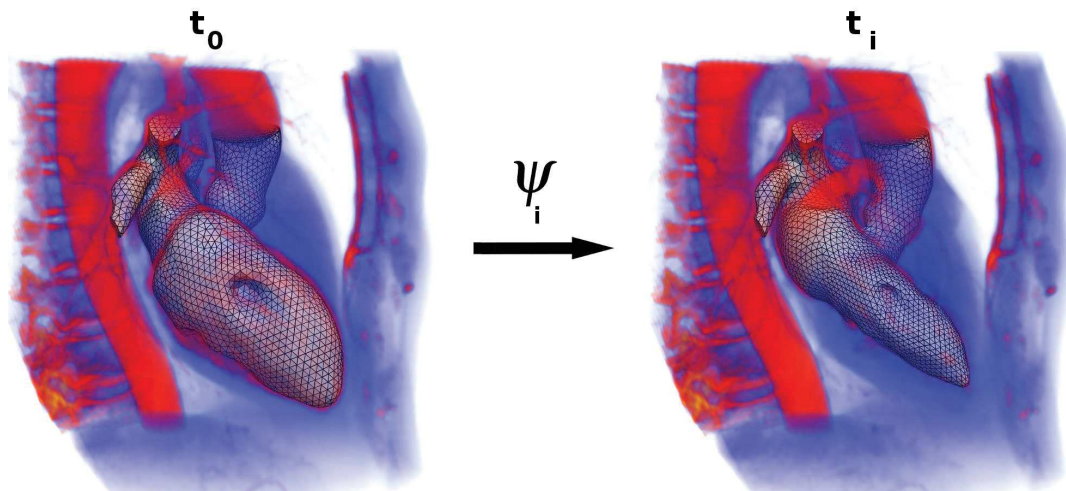


Figure 4.7: Mesh deformation procedure applied to a left human heart. The *template* mesh segmented from the image at time t_0 is deformed thanks to ψ_i to obtain the mesh at time t_i . This procedure is done for each image in the cardiac cycle in order to obtain the corresponding meshes.

FSI problem, but entirely extracted from the medical images. In the present study, it is used to handle the cardiac chambers and their connected vessels.

4.5.2 Volumetric grid

The *template* surface is imported in a commercial mesher (Gambit, ANSYS) to generate a *template* unstructured tetrahedral mesh. The computed boundary Fourier coefficients of Eq. (4.13) are interpolated on this *template* numerical domain surface. The computational mesh boundary now follows the shape of the patient endocardium and is updated in every step of the simulation. The motion of all internal points in the computational mesh is deduced from this prescribed boundary motion thanks to a harmonic extension of \mathbf{u}_g onto the numerical domain. At each iteration, nodal velocity \mathbf{u}_g is calculated as the solution of the following problem [110]:

$$\nabla \cdot (k(\mathbf{x})\nabla\mathbf{u}_g(\mathbf{x})) = \mathbf{0}, \quad \text{on} \quad \Omega_f(t) \quad (4.14)$$

and,

$$\mathbf{u}_g(\mathbf{x})|_{\mathbf{x} \in \partial\Omega_f(t)} = \mathbf{u}_s(\mathbf{x}) \quad \text{on} \quad \partial\Omega_f(t), \quad (4.15)$$

where $k(\mathbf{x})$ is the displacement diffusion coefficient. This coefficient is determined to preserve a good computational grid quality. The larger elements will distort at a faster rate than the smaller ones - a desirable feature for our application in order to preserve grid quality. When the boundary displacement becomes too large compared

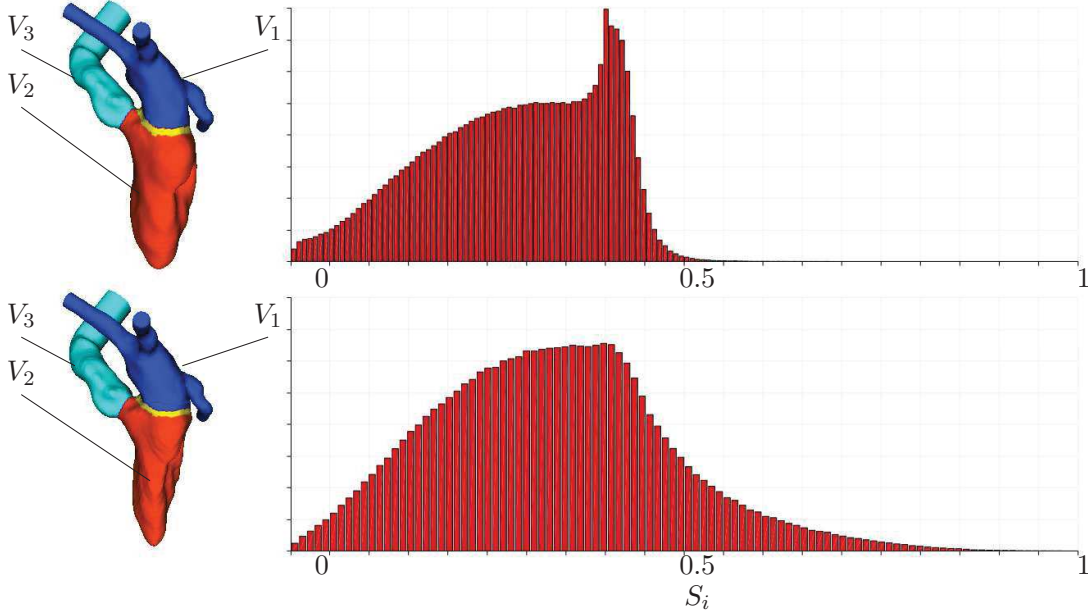


Figure 4.8: Skewness histograms for a left heart grid at end diastole (top figure) and mid-systole (bottom figure). Each left heart cavity is color tagged.

to the local cell sizes, the cell quality can be highly decreased and some cells can even become degenerated. This can lead numerical stability issues or negative cell volumes. The grid quality is this monitored all along the computation of each cell i in term of skewness S_i as,

$$S_i = \frac{V_{eq} - V_i}{V_{eq}}, \quad (4.16)$$

where V_i is the observed cell i volume and V_{eq} the volume of an equilateral cell with the same circumradius as the cell i . When a cell i is equilateral, S_i is null, which means that the quality is perfect. Cells quality is considered poor when S_i is higher than 0.8. Figure 4.8 shows an histogram of a test case. The upper figure shows a left heart at end diastole while mid-systole is shown in the bottom part. The grid is notably degraded as higher skewness values appears.

In this case, the numerical domain is re-meshed and the fluid solution is interpolated on a new discretised domain. Fourier coefficients of Eq. (4.13) are interpolated as well. The remeshing procedure is handled by MMG3D which is an isotropic/anisotropic tetrahedral fully automatic remesher [41] coupled with YALES2BIO.

In this case the Fourier coefficients are interpolated from one grid to another. A local orthogonal coordinate system associated to each node k of the new grid is introduced. It is composed of the approximate normal to the surface (sum of the neighbouring faces normals) and two unit orthogonal vectors: ξ and η . The origin of this coordinate system is centred on node k of the new grid. In this coordinates system, a neighbour of node

k has the following tangential coordinates:

$$x_\xi = (\mathbf{x} - \mathbf{x}_k) \cdot \xi; x_\eta = (\mathbf{x} - \mathbf{x}_k) \cdot \eta, \quad (4.17)$$

where \mathbf{x}_k is the coordinates of node k . The surface is then locally characterized as a function of the tangential coordinates \mathbf{x}_ξ and \mathbf{x}_η . The fitting procedure consists of finding a paraboloid surface approximating the old grid on the new one locally and for each node k . It is based on the procedure described in Garimella et al. [64]. A quadratic patch $f = f(x_\xi, x_\eta)$ where f is one of the a_i or b_i Fourier coefficient is defined as,

$$f(x_\xi, x_\eta) = \frac{1}{2}ax_\eta^2 + bx_\xi x_\eta + \frac{1}{2}cx_\xi^2 + dx_\eta + ex_\xi + f(x_k). \quad (4.18)$$

The values of the coefficients a, b, c, d and e are tuned in order to fit the paraboloid surface in the neighbourhood of the node k as much as possible. This is achieved by solving a system of form $Ms = F$:

$$\begin{bmatrix} \frac{1}{2}x_{\eta 1}'^2 & x_{\eta 1}'x_{\xi 1}' & \frac{1}{2}x_{\xi 1}'^2 & x_{\eta 1}' & x_{\xi 1}' \\ \vdots & \vdots & \vdots & \vdots & \vdots \\ \frac{1}{2}x_{\eta m}'^2 & x_{\eta m}'x_{\xi m}' & \frac{1}{2}x_{\xi m}'^2 & x_{\eta m}' & x_{\xi m}' \end{bmatrix} \begin{bmatrix} a \\ b \\ c \\ d \\ e \end{bmatrix} = \begin{bmatrix} f_1 - f(x_1) \\ \vdots \\ f_m - f(x_m) \end{bmatrix}. \quad (4.19)$$

This system is over-constrained. To find the values of the coefficients (gathered in the vector solution s) that provide the best fit, a least-square fitting approach is used. The least-square problem can be written as a linear system to solve, s is then obtained explicitly, provided that the inverse of $(M^t M)$ is calculated, $s = (M^t M)^{-1} M^t F$. For each node, this fitting procedure is applied for each Fourier coefficients.

4.6 Valves model

Models

Since the valves are thin highly-moving structures, their precise movements are hardly extractable from MRI or CT scan exams. Besides, on the numerical side, incorporation of moving valve leaflets in the grid topology would most probably imply a grid quality degradation, making numerous re-meshing mandatory. Hence, it was chosen to model the valves using an immersed boundary technique.

Valves annuli geometries are reconstructed by visual inspections of the medical images. The annulus geometry is represented as a cloud of points p_i , whose nodal coordinates are used to define the valves annulus within the numerical domain. These markers allow the reconstruction of the aortic and mitral annuli.

The shape of the aortic valve is simply approximated by the plane passing through the set of markers and obtained by a least squares method. As the focus of the study is on the flow in the atrium and the ventricle, it is not mandatory to develop a more

complex model for the aortic valve, since its morphology has very limited effects on the LA/LV haemodynamics. Note also that the physiological aortic valve open position offers virtually no resistance to the main flow passing through the aorta from the LV. The regression plane modelling the aortic valve is thus made alternatively fully permeable or impermeable depending on the phase in the cardiac cycle.

The mitral valve is represented by a more complex model, since its shape is expected to strongly impact the LV haemodynamics. A regression plane P_α is defined from the set of markers p_i with a least squares method and the mitral annulus geometric center C_α is computed. A plane P_β parallel to P_α is defined at a distance $l(t)$. When the MV is open, it is assumed that the cross section area seen by blood is elliptical. An ellipse ϵ of axes $a(t)$, $b(t)$ is defined on P_β and its angle in its plane set manually to fit the medical images. The ellipse center C_ϵ is not a direct projection of C_α on plane P_β , an eccentricity $e(t)$ is defined. The eccentricity $e(t)$ is the distance between the projection of C_α on plane P_β and the ellipse center C_ϵ . Leaflets are considered as the surface linking the mitral annulus to the elliptical opening ϵ . Position of the annulus markers are projected on the ellipse. Therefore, the leaflets surface is reconstructed by triangles pieces between the annulus markers and the projected annulus markers on the ellipse (see Fig. 4.9). To summarize, the quantities needed to feed this model are:

- the mitral annulus markers p_i ,
- the average leaflets length $l(t)$ which is the distance between C_α and the generated plane P_β ,
- the eccentricity $e(t)$ of the ellipse center C_ϵ compared to the projection of C_α on plane P_β ,
- the ellipse axis $a(t)$, $b(t)$ and its angle in the P_β plane.

The model and its numerical representation are shown in Fig. 4.9.

Time evolution of the ventricle volume is used to switch between the open or closed positions for each valve. LV volume decreases during systole, then increases during diastole: these two parts of the cardiac cycle are determined by computing the ventricle volume variations. The opening and closing valve time is less than 5% of the heart cycle duration [184]. Therefore, the opening of the mitral valve and closing of the aortic valve (vice versa) can be considered as instantaneous and simultaneous events as a first approximation. This means that the left heart has only two topological configurations during the cardiac cycle:

- MV closed, AV open: this corresponds to the systolic phase,
- MV open, AV closed: this corresponds to the diastolic phase.

Note that MV and AV happen to be closed at the same time in physiological conditions. This corresponds to the isovolumic phases which last for only a small fraction of the

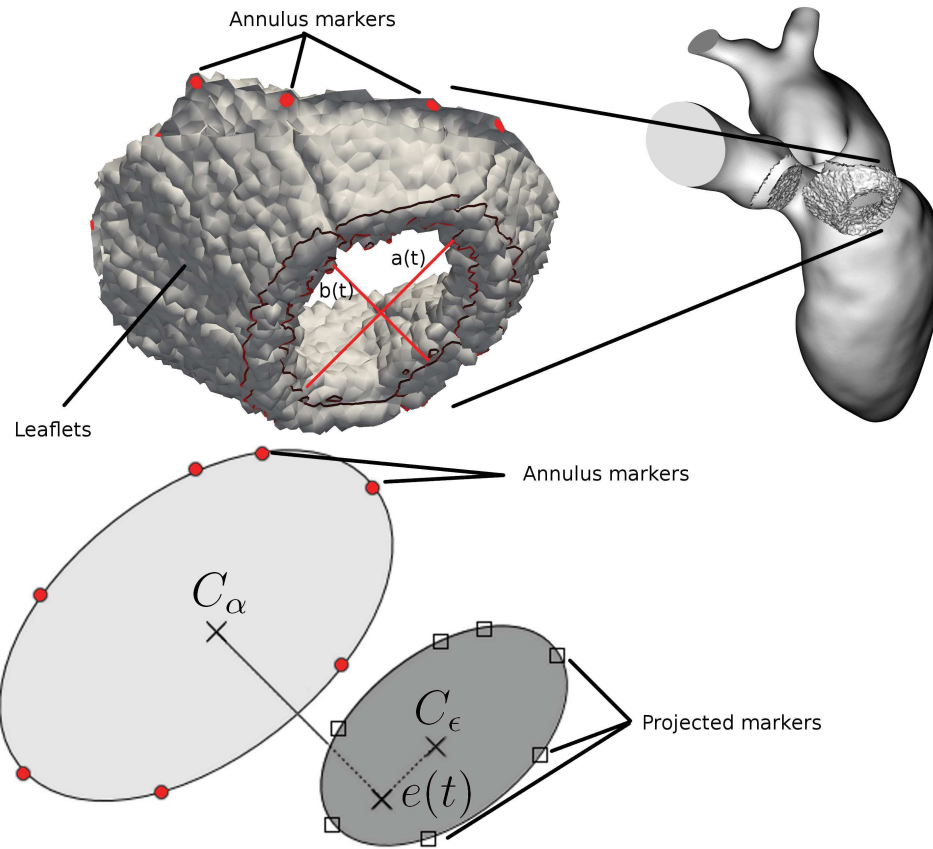


Figure 4.9: Top left: annulus markers and modelled MV leaflets. Parameters a, b of the ellipse ϵ are indicated. Top right: full MV model included in the numerical domain (the AV is represented as well). Bottom: MV scheme.

cardiac cycle. Given the poor time resolution reachable by 4D medical imaging systems (IRM and CT scan), the isovolumic phase cannot be described accurately anyway. Assuming that the MV and AV are never closed at the same time is thus an acceptable assumption given the accuracy of the medical data used to feed the CFD solver.

Knowing the MV leaflets position during the heart cycle, their effect on the blood flow is accounted for thanks to an immersed boundary method (IBM) [120] described in chapter 3. For this purpose, the leaflets representations (plane for AV and triangle by parts for the MV) are first given a thickness s so that a few mesh nodes are located within the valves.

Grid nodes are tested to decide whether they are in the leaflets volume or not. For the AV, the distance from the AV plane is computed. If the node distance is within the closed interval $[-\frac{s}{2}, \frac{s}{2}]$ the node is tagged as belonging to the AV valve. For the MV, each node being at a distance within $[-\frac{s}{2}, \frac{s}{2}]$ of one of the MV triangle are treated. The node is projected on the corresponding triangle and the triangle barycentric coordinates

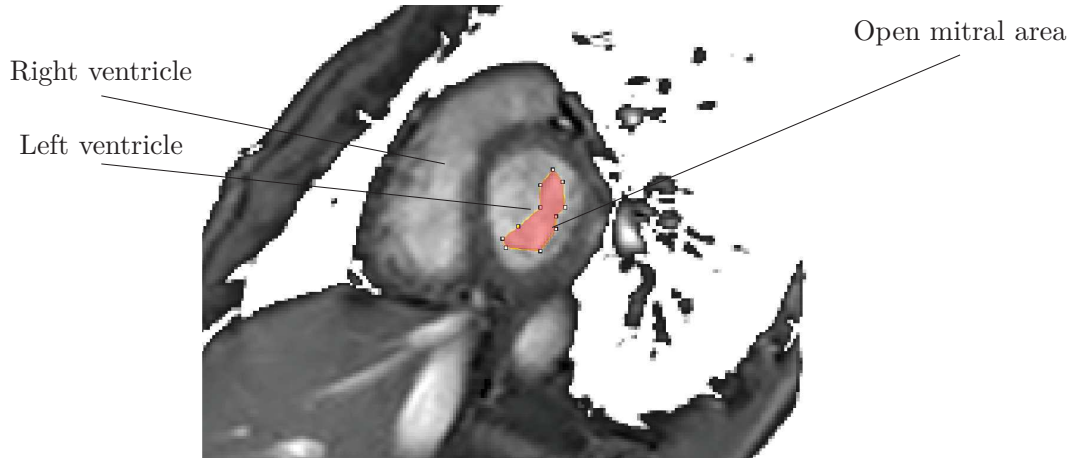


Figure 4.10: Manual measure of the open mitral area for a healthy subject (in red). The right and left ventricles are indicated for information.

are computed. The node is tagged as belonging to the MV valve if all of the barycentric coordinates are greater than zero. Then, a force \mathbf{f} in the NS equations (3.1) is set to impose the fluid velocity to zero within the leaflets as described in chapter 3 section 3.5. The force \mathbf{f} is used at each mesh node lying within one of the valve region. The finite-volume scheme used being node centred and since the force \mathbf{f}^n is imposed at nodes lying into valve leaflets, a null velocity is imposed in the entire dual cell where the governing equations are integrated. Thus, there is no interpolation of the forcing term and the valves geometry is described in a stepwise way. \mathbf{f}^n is set to zero anywhere else.

Note that, as the opening/closing of the valve is not resolved, valves switch instantaneously from closed position to open position and vice versa. When open, some small displacements may be seen because of the displacement of the valve annulus, but they are here neglected. As a consequence, the source term used mimics the presence of valves as fixed obstacles.

Models parameters

Mitral valve parameters are measured manually on the medical images and with help of 3D model segmented from it. The mitral annulus can be distinguished easily with proper imaging modalities. Markers coordinates are then measured on the *template* segmented model. Once these markers are set on the numerical grid, they are moved in the same way the grid nodes are moved or spatially interpolate in case of the computation needs an interpolation.

The length of the valves are measured from the images. The length between the tips of the valves and the mitral annulus is observed for the short and the long leaflet

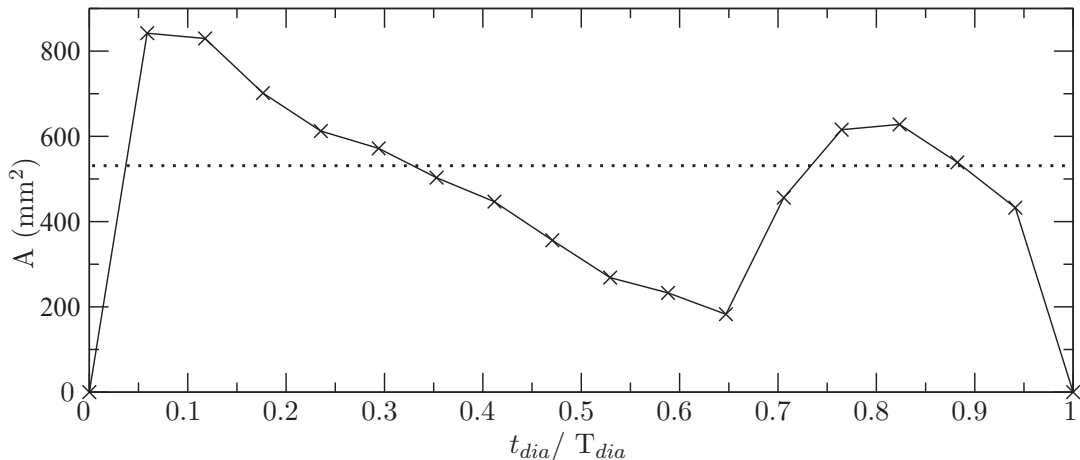


Figure 4.11: Measures (cross symbols) of the open mitral area during the diastole t_{dia} . The median of the measures is indicated by a dotted line at 520 mm^2 .

on each medical images during the heart cycle. The measures are averaged and used as the leaflet length in the model.

The open mitral area is manually measured for each images taken during the diastole. Figure 4.10 shows the mitral area measured at one instant and Fig. 4.11 shows the measurements along the diastole for an healthy subject. Median of this area is then set as the open area for the model. The form of the open area is approximatively an ellipse (this approximation is commonly used). The large axis of the ellipse is the distance of the extremal points on Fig. 4.10, the small axis is then deducted by the measured open area. The orientation of the large axe is set to be parallel to the papillary muscles.

Finally, the eccentricity of the ellipse center is set as the averaged measured vectors between the geometric center of the open area and the geometric center of the mitral annulus. The eccentricity between the mitral annulus geometrical center and the open mitral area can be observed on the example image Fig. 4.10.

4.7 Inlet and outlet boundary conditions

Inlet boundary conditions can be extracted from PC-MRI and interpolated on the computational domain inlet surfaces. However, if only CT scan images are available, a different strategy must be used. As blood is incompressible, a reasoning based on mass conservation can be made to overcome the lack of inflow and outflow information. As already stated in the last section, only two topological configurations are considered (MV closed, AV open or AV closed, MV open). This assumption allows a consistent definition of the inlet/outlet boundary conditions. Indeed, mass conservation imposes, for the first case (MV closed, AV open):

$$Q_i(t) = \frac{dV_1}{dt}, \quad (4.20)$$

where $Q_i(t)$ is the inlet flow rate to be imposed at the pulmonary veins V_1 the LA volume. In the second case MV open, AV closed, mass conservation imposes:

$$Q_i(t) = \frac{dV_1}{dt} + \frac{dV_2}{dt}, \quad (4.21)$$

Where V_2 is the LV volume. Therefore, the flow rates are only determined by the time evolution of the heart geometry, which is directly related to the medical images. Computation of each cavity volume must be done consistently with the valves definition. In order to properly define each cavity, the valves were considered both closed and a propagation 'tagging' was set. Each inlet and outlet nodes were given a specific color. Each node in a valve was given another specific number. As each node is linked to another nodes by the grid connectivity, a test is made to compare the actual node and the other nodes linked to this one. For one node i , the question for each related node is: is the linked node color the same as for node i ? If not, is it a valve node? In case it is not, the node is coloured as node i . If it is a valve node, no color propagation is made. Hence, each cavity is tagged with a specific color and the propagation stop when a valve is encountered. In order to speed up the color tagging, the wall boundary is color tagged first, then the volumetric propagation is made.

Once the volumes and their changes are computed, consistent velocity at the four inlets $U_j^{in}(\mathbf{x}, t)$ ($j=1, \dots, 4$) can be prescribed once the shape of the profile is known. For uniform inflows, the Dirichlet condition (see Eq. 3.4) simply reads:

$$U_j^{in}(t) = \frac{Q_i(t)}{A_j} \zeta_j, \quad (4.22)$$

where A_j is the cross-section area of the j -th pulmonary vein and ζ_j the flow distribution between the four pulmonary veins ($\zeta_j=0.25$ for all j corresponding to an equipartition of the inflow). Note that in practice, only the inflow conditions are imposed as the Dirichlet outflow condition automatically adjusts to ensure exact mass conservation in the complete domain through a convective outflow scheme.

4.8 Discussions

The spatio-temporal resolution of the medical images, is an important limitation which imposes temporal interpolation and geometrical simplifications of the heart model. It also makes it difficult to accurately account for short phases as the isovolumic contraction and relaxation. Still, ten images per cardiac cycle enable a convincing flow description as it will be shown in chapter 5. Indeed, most of the significant heart deformations last more than $T/10$. However, specific tests of this point should be performed to precisely assess the impact of the temporal resolution of the medical images on the flow field.

Another limitation is the unknown flow distribution between the pulmonary veins, which has to be prescribed in the simulations. In this work, an equipartition has been supposed due to the lack of information.

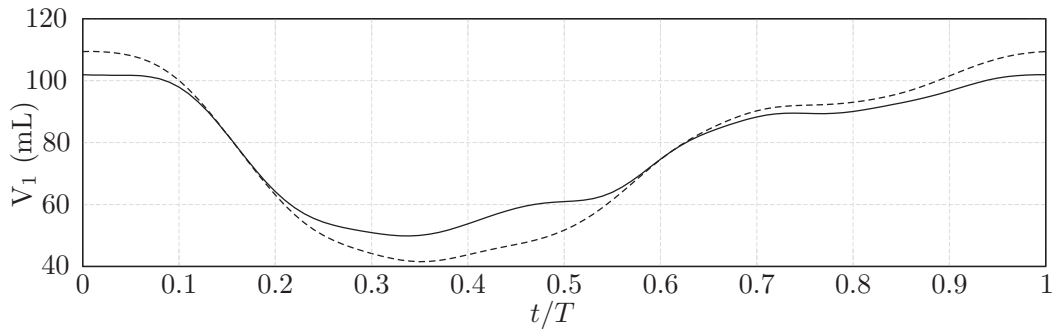


Figure 4.12: Volumes obtained for a ventricle from a set of 4D medical images. Solid line, deformation (*i*), dashed line, deformation (*ii*).

About the valves, the model used here highly depends on the anatomical information that can be extracted from the images. Consistently with their insufficient spatio-temporal resolution, a rough model of the valves was used. Better valve models should notably include valve opening and closing, change of aperture area along time. Aortic valve leaflets were notably completely omitted during systole, which most probably impacts the flow at the beginning of the aorta.

Two other sources of error are discussed more deeply in the following: the image registration parameters and the tangential deformation extracted from the computed deformations.

Image registration algorithm

Beside the segmentation itself and the choice of the *template* the parameters choice is of prime importance. The validity of the computed deformation depends partly upon the validity of the parameters.

Figure 4.12 shows the volume of deformed meshes with the same template, the set of medical images and parameters excepting the regularization term λ . Deformation (*i*) was computed using $\lambda = 2$, while deformation (*ii*) with $\lambda = 1$. In both cases the global algorithm converged. However, the deformations are different. As the parameter λ is linked to the belief in the amount of deformation of the heart, the deformations are more important at the extrema volumes ($0.34 T$ and T). The optimal parameters set giving the most realistic deformations is all but obvious. Several tests with different parameters set are mandatory. Once the deformations are obtained (in the case where the algorithm converged), visual inspection of the deformed meshes compared to medical images must be done implying an expertise on the field.

Ventricle twist

It is well known that the ventricle has a twist-untwist movement during the heart cycle [155]. Twist during ventricular ejection predominantly deforms the myocardial

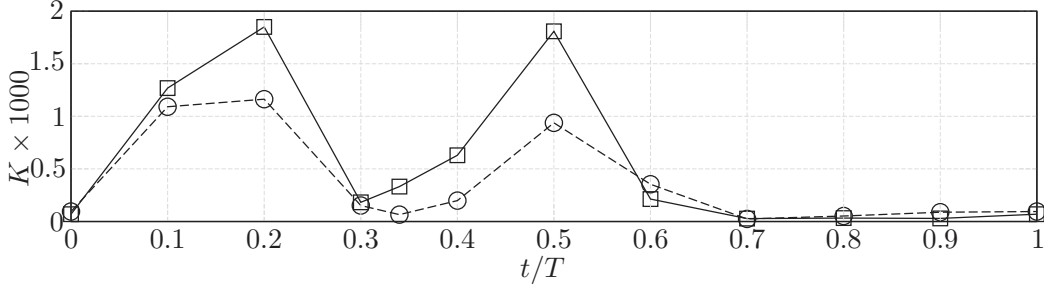


Figure 4.13: Average ventricle rotation obtained from a set of 4D medical images. Full line, tangential velocity kinetic energy K_t , dashed line, normal velocity kinetic energy K_n .

fibre matrix, resulting in a storage of potential energy. The release of these forces happens when the subsequent recoil of twist deformation occurs. This 'untwist' during diastole releases the mechanical energy and contributes to LV diastolic relaxation and early diastolic filling [126].

Therefore, this movement is important in cardiac mechanics but mainly in a mechanical point of view. The common methods for measuring myocardial motion are tagging or phase contrast velocity mapping using MRI [50] and tracking of unique speckle patterns created by the interference of ultrasound beams within tissue using echocardiography [92]. Conventional analysis of these images are computer-assisted.

Figure 4.13 shows the integrated kinetic energy of both the tangential myocardium velocity and the normal velocity computed for *heart A* after deformation computed through the presented image registration algorithm. The solid line represents the tangential velocity kinetic energy K_t and the dashed line represents normal velocity kinetic energy K_n . The energies are defined as,

$$K_n = \frac{1}{2S} \int_S (\mathbf{u}_g \cdot \mathbf{e}_n) \mathbf{e}_n dS, \quad (4.23)$$

$$K_t = \frac{1}{2S} \int_S \mathbf{u}_g - (\mathbf{u}_g \cdot \mathbf{e}_n) \mathbf{e}_n dS, \quad (4.24)$$

with S the endocardium surface, the grid nodal velocity \mathbf{u}_g , \mathbf{e}_n the normal vector.

Two peaks are visible at the same moment for both energies. The first one at $0.2T$ during the systole and the another one is at $0.5T$. Considering a characteristic radius for the heart of $R = 0.025$ m, and the diastolic peak rotational energy, $K_t = 1.75 \times 10^{-3} \text{ m}^2 \cdot \text{s}^{-2}$, the corresponding averaged velocity for the diastolic peak can be computed as $\sqrt{2K_t}/R \sim 2.3 \text{ rad} \cdot \text{s}^{-1}$ or $\sqrt{2K_t} \sim 0.06 \text{ m} \cdot \text{s}^{-1}$. Velocity obtained from LES in the ventricle is about $1 \text{ m} \cdot \text{s}^{-1}$ at this time of the heart cycle. Thus, it is believed that the tangential velocity can be considered negligible in the blood dynamic.

Using MRI [134] and echocardiography [135], the same range of tangential velocity is obtained. This is illustrated in Fig. 4.14. The averaged LV rotational and torsional velocity profiles in 20 subjects at different location (from Notomi *et al.* [135]) is displayed. Focus is on the violet line representing the total torsion during the heart cycle.

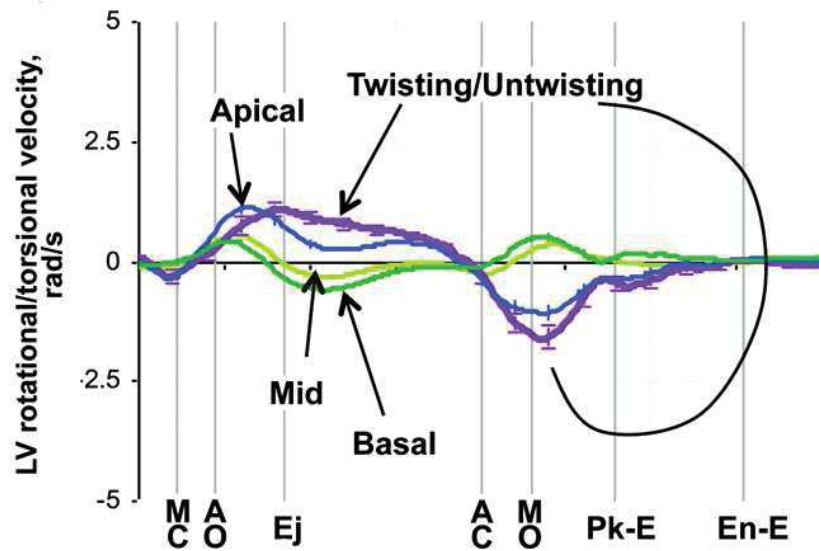


Figure 4.14: Averaged LV rotational and torsional velocity profiles in 20 subjects. Blue, light green, dark green, and violet lines indicate apical, middle, and basal rotations and LV torsion, respectively. MC indicates mitral valve closure; AO, aortic valve opening; Ej, peak ejection flow velocity in the outflow tract; AC, aortic valve closure (ie, end systole); MO, mitral valve opening; Pk-E, peak early filling velocity; and En-E, end of E wave. From [135].

Note that temporal evolution of the tangential velocity is qualitatively coherent with our data (see Fig. 4.13). In addition, velocity magnitude order are similar. As the image registration algorithm used in this thesis is based on a similar principle of tracking unique patterns through deformation, it is believed that the twist-untwist of the ventricle is roughly captured. The image registration performs well thanks to the multitude of specific structures within the heart as the papillary muscles or the captured trabeculations. Notwithstanding, observing a smooth object without special feature would not allow to capture these movements. Let us consider an academic case: a uniformly white cylinder surrounded by a black background. A rotation is then applied to this object. The possible deformations are actually infinite. Hence, the algorithm could not find the right deformation, but fortunately this is not the situation with the human ventricle. Thus, it is believed that we retrieve a rather good tangential velocity at the ventricle endocardium and even if one cannot be sure of the validity of these velocities, they can be considered negligible in the blood dynamic.

Chapter key points:

- A framework for hemodynamics simulations in patient-specific hearts was presented.
- Heart movements are extracted from morphological medical images using an image registration algorithm.
- Valves models are fed with data from medical images.
- Blood boundary conditions are extracted from medical images as well.

Part III

Eulerian analysis

First insights in a left heart flow

Chapter contents

5.1	Introduction	74
5.2	Numerical simulation setup	74
5.2.1	Heart model and extraction of the deformation	74
5.2.2	Computational mesh and simulation details	75
5.2.3	Phase-averaged and fluctuating velocity definitions	79
5.2.4	LES quality assessment	79
5.2.5	Data convergence	80
5.3	Results and discussion	81
5.3.1	Global description of the flow	81
5.3.2	Velocity fields	85
5.3.3	Instantaneous structures	87
5.3.4	Velocity fluctuations	89
5.4	Flow sensitivity to viscous effect	91
5.4.1	Blood rheology	91
5.4.2	SGS modelling	95
5.5	Conclusion and outlook	97

This chapter describes the application of the developed framework on a patient left heart referred to as *heart A*. Here, the attention is focused on the physiological patterns commonly reported in the literature and the flow is mainly analysed through phase-averaged data. A first look at the cycle-to-cycle velocity variations is presented, paving the way for the more advanced analysis provided in chapter 6. Finally, a rapid discussion on the use of Carreau-Yasuda model and its consequences on the presented results is provided.

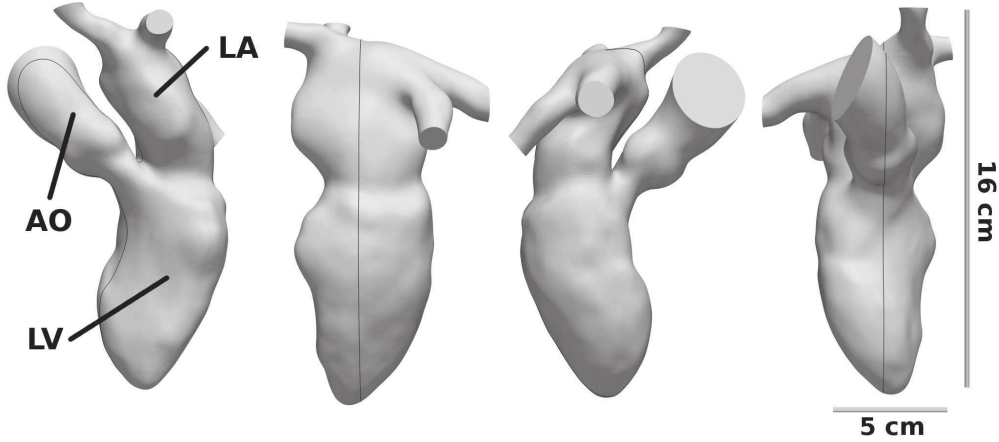


Figure 5.1: *Template* computational domain extracted from a 3D medical image. The same domain is represented for four different points of view and the left ventricle (LV), left atrium (LA) and Aorta (AO) are indicated. Black line passing through the left heart indicates the position of slices used to describe the flow in section 5.3.

*This chapter is part of: C. Chnafa, S. Mendez and F. Nicoud, **Image-based large-eddy simulation in a realistic left heart**. Published in *Computers & Fluids*, 2014 [35].*

5.1 Introduction

A first application of the framework detailed in the previous two chapters is presented here. The blood flow computation of a patient-specific left heart flow is presented. The flow is characterized by its transitional nature, resulting in a complex cyclic flow. Flow dynamics is analysed in order to reveal the main fluid phenomena and to obtain insights into the physiological patterns commonly detected. It is demonstrated that the flow is neither laminar nor fully turbulent, thus justifying a posteriori the use of Large Eddy Simulation. In this chapter, the dynamic Smagorinsky-Lilly model is used for the SGS model.

5.2 Numerical simulation setup

5.2.1 Heart model and extraction of the deformation

Using the framework described in the last chapter, deformations along a cardiac cycle are built from an actual CT exam of a patient treated at the University Hospital of Toulouse Rangueil (France). The exam consists in $N = 10$ medical images of spatial resolution $2 \times 2 \times 2$ mm (corresponding to $128 \times 148 \times 156$ voxels) which are available

	RSPV	RIPV	LSPV	LIPV
Small diameter (mm)	11.8	12.0	14.0	10.3
Large diameter (mm)	14.9	12.7	15.5	15.2
Area (mm ²)	138.1	119.7	170.43	123.0

Table 5.1: Geometric characteristics of the ostia. Ostia are oval in shape. The areas reported are obtained by assuming elliptic shapes.

along the cardiac cycle lasting $T = 1000$ ms. The *template* geometry is extracted at a given time t_0 taken during mid-diastole (it is shown with different angles in Fig. 5.1).

Due to limitations in spatial and temporal resolutions, the complex intracardiac geometry cannot be fully reconstructed from medical images. The acquisition frequency of the images forbids precise observation of potential fast heart movements. However, the analysis of the flow features in the next sections suggests that this frequency is sufficient for this application. As shown in Fig. 5.1, the *template* numerical domain extracted includes the LA, LV, the aortic root and four pulmonary veins. The left atrial appendum and the papillary muscles are omitted. The LV has a height of 8.8 cm from the MV to the apex (the lowest extremity of the LV in Fig. 5.1) and a maximum diameter of the order of 5 cm. The LA has a height of 5.5 cm from the MV to the upper pulmonary root and a maximum diameter of the order of 4 cm. Heart measures are within the classical figures found on humans [5].

A focus on the left atrium and its four pulmonary veins is shown in Fig. 5.2 (left). Sketch of inflow angles of the four pulmonary veins is also shown, to give an idea of the flow trajectory in the atrium. Table 5.1 shows measures of the ostia in the atrium.

A nearly isotropic surface mesh is generated from the geometry reconstructed from medical images. The characteristic length of each triangle is imposed to be close to 2 mm. The *template* surface grid is deformed based on the method described in chapter 4. The deformation procedure uses 12 *outer* iterations: the initial Gaussian kernel width being $\sigma_0 = 40$ voxels with a decrement between each of the *outer* iterations of 3 voxels. The *inner* iterations are either stopped after 20 iterations or when the total residual squared difference is under 0.01. The regularization weight λ is set to 1.0 (see chapter 4). The boundary Fourier coefficients are computed from the obtained meshes in order to deform the left heart during the flow numerical simulation.

5.2.2 Computational mesh and simulation details

A nearly isotropic grid is created from the heart model described in the above section, using the commercial software Ansys Gambit, which was selected for its ability to generate good-quality tetrahedral meshes, appropriate for finite-volume formulations. The spatial resolution is imposed to be close to 0.8 mm in all three spatial directions along the cycle, which yields grids of approximately three-million tetrahedral elements.

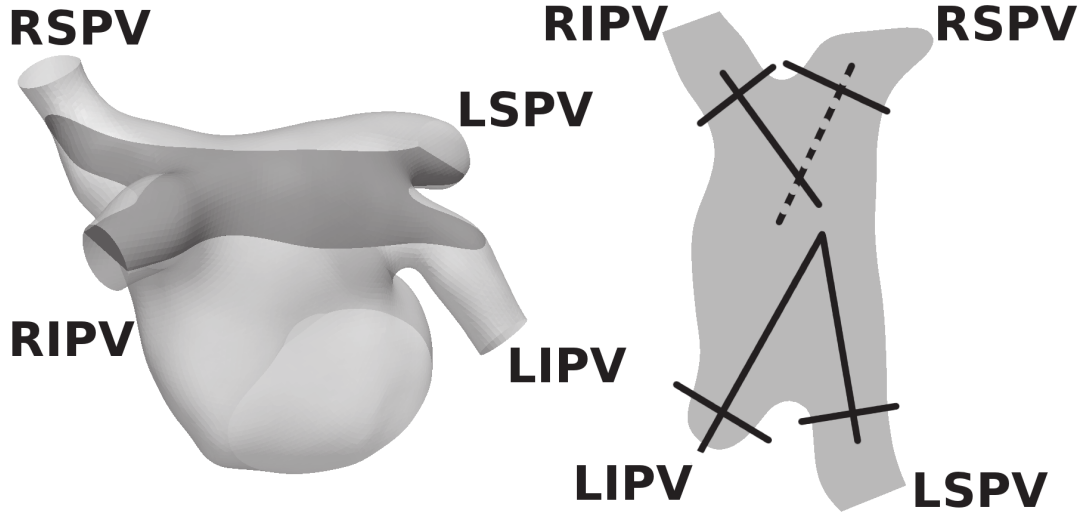


Figure 5.2: Left: left atrium with its four pulmonary veins labelled. Right: sketch of inflow angles and the four pulmonary veins projected on a plane (the plane is displayed in the left picture). The dashed line indicates that the flow coming from the RSPV is directed toward the MV compared to the others.

Computed Fourier coefficients are interpolated on this model surface. In this study, re-meshing was used at each acquisition instant t_i , $i = 0, \dots, 9$ in order to ensure good mesh quality and small numerical errors over the whole cardiac cycle.

Valves are modelled as explained in chapter 4 section (4.6). A close examination of the medical images from the CT scan allowed to set the leaflets length to $l = 12$ mm for the MV. The open area presented to the blood flow is represented by an ellipse of axe $a = 15$ mm and $b = 8$ mm. This area is supposed constant over time when the MV is open. Eccentricity is fixed to $e = (0.0, 5.0)$ mm from the same medical data.

The simulation time step is fixed by a CFL condition (CFL=0.9) consistent with the explicit time integration used in the CFD solver; this corresponds to a time step varying from 3.0×10^{-4} s to 8.0×10^{-4} s in the present computation.

The flow waveform imposed at the four inlet conditions of the computational domain (the four PV) is calculated based on the mass conservation principle, as explained in chapter (4). The resulting flow rate varies in time during the cycle and is periodic. The partition of the inflow is not known in this case and detailed information about averaged flow rates repartition between PVs have not been found in the literature. From data presented by Dahl [40], it has been chosen to set the flow rate at each of the pulmonary vein equally distributed ($\zeta_j = 0.25$). Note that the resulting blood flow, in particular in the atrium, may be sensitive to this repartition. Figure 5.3 represents flow rates at the aortic valve (top plot), mitral valve (middle plot) and the heart inflow which is the sum of the flow rates from the four PV (bottom plot). Two vertical dotted lines separate the systolic phase and the diastolic phase. For this heart, systole lasts $0.36T_a$ (from $t/T_a =$

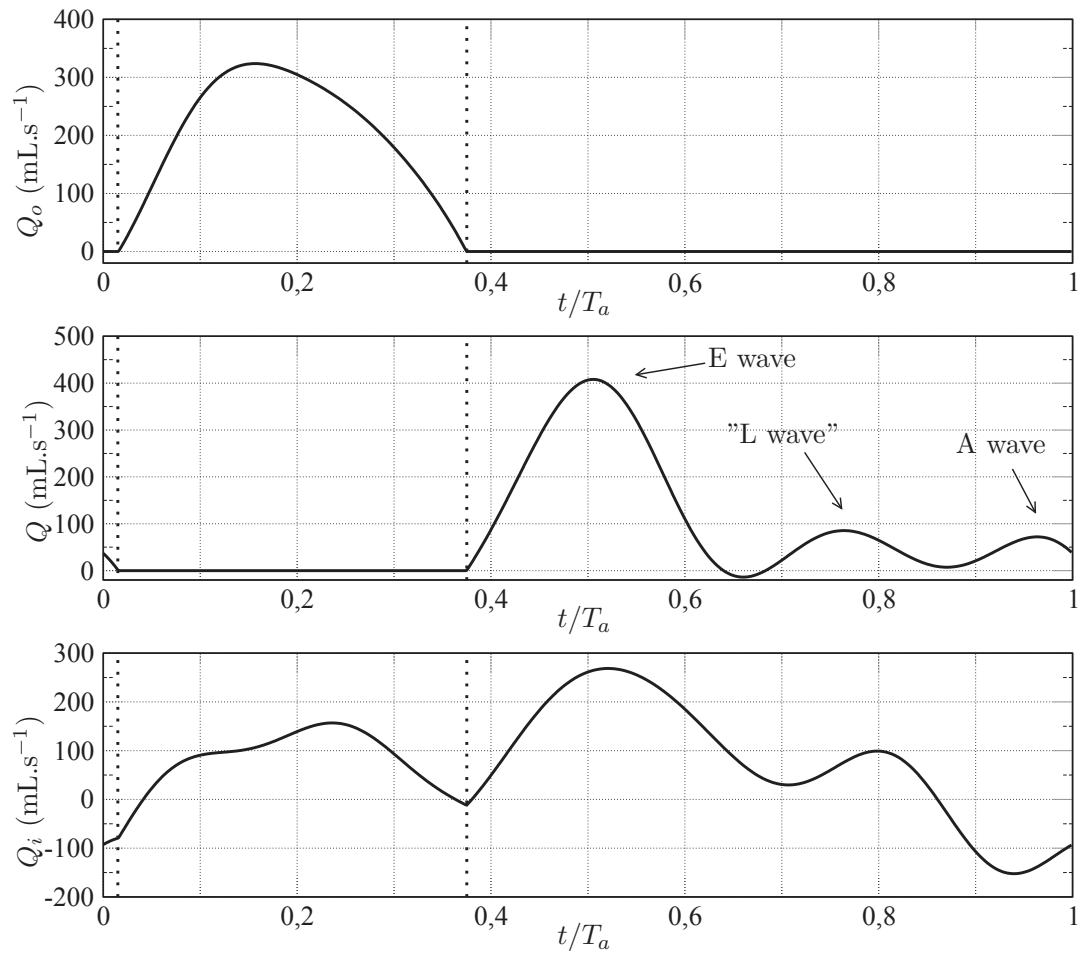


Figure 5.3: Flow rates at the aortic valve (top plot), mitral valve (middle plot) and the total heart inflow (bottom plot) imposed at the pulmonary veins during the heart cycle. Vertical dotted lines mark the limit between the systolic phase (t/T_a between 0.015 and 0.375) and the diastolic phase. The E wave, L wave and A wave are indicated on the mitral flow.

	<i>Heart A</i>	Normal range
Heart rate (bpm)	60	60 - 100
E/A ratio	5.5	1.0 - 2.0
EDV (mL)	130	65 - 240
ESV (mL)	55	16 - 143
SV (mL)	75	55 - 100
Cardiac output (L.min ⁻¹)	4.5	4.0 - 8.0
Ejection Fraction (%)	58	55 - 70
Open area MV (cm ²)	3.77	4.0 - 6.0
U_{max} at MV (in m.s ⁻¹)	1.08	0.6 - 1.0
Re_{max} at MV	5000	-
U_{max} at AV (in m.s ⁻¹)	0.96	≤ 2.5
Re_{max} at AV	5300	-
Acquisition	CT scan	-

Table 5.2: Main characteristics for *heart A*.

0.015 to 0.375) and diastole $0.64T_a$.

The pulmonary flow rate is coherent with classical medical data, the flow reversal associated with the atrial contraction being even visible from $t/T_a=0.86$ onward. The aortic valve flow rate behaves as expected: it increases during systole until its maximum ($Q=320$ mL.s⁻¹) and then decreases until its shutting at $t/T_a=0.375$. The aortic flow rate stays null until the next systolic event. The mitral flow rate is usually composed by two peaks: the E wave or rapid filling and a second one, the A wave corresponding to the late diastole separated by a phase with almost no heart motions, called the diastasis. Here, the flow rate shows three peaks in this case: the first one ($t/T_a=0.51$, $Q=410$ mL.s⁻¹) represents the E wave, the last one a weak A wave ($t/T_a=0.98$, $Q=75$ mL.s⁻¹). The fact that the A wave is so weak is symptomatic of pathologies [161]. The E/A ratio is thus high with a value of 5.5 which is higher than the normal physiological range which is between 1 and 2 [125]. A weak third peak is also present during diastasis ($t/T_a=0.78$, $Q=85$ mL.s⁻¹). Having no information on the velocity profile, it is assumed uniform for this simulation.

Due to the lack of medical information and to the small number of images in the CT scan ($N = 10$), it is actually impossible to guarantee that this patient indeed has a filling in three waves, with an additional L wave at $t/T_a=0.78$. However, this peak may correspond to this so called L wave [77] and in order to simplify the flow description, this peak will be referred to as the L wave. Note also that such type of filling flow rate does exist for some patient. A high E/A ratio is symptomatic of a severe forms of diastolic dysfunction and are referred to as "restrictive filling dynamics". Thus, it is considered in all the following work that *heart A* suffers from restrictive filling.

The fluid density ρ and the kinematic viscosity ν_n are supposed to be constant in the first part of this chapter: $\rho = 1040$ kg.m⁻³ and $\nu_n = 4 \times 10^{-6}$ m².s⁻¹.

The Inlet Reynolds number for each pulmonary vein varies from 0 to approximately 2000, based on the vein inlet diameter. The Reynolds number at the mitral tips varies from 0 to approximately 5000 (based on the effective mitral mean diameter $D = 2R_a = 2\sqrt{ab}$, the area of the open mitral valve, the kinematic viscosity and the maximum flow rate). The maximum transmitral velocity U_{max} falls into the usual measurements [78]. The maximum Reynolds number of the aortic valve is about 5300. These ranges of Reynolds numbers, the complex moving geometry of the heart and the pulsating nature of the inlet flow indicate that the nature of this complex cyclic flow may be transitional if not turbulent.

Table 5.2 reports the characteristics of *heart A* and the normal range [13, 22, 98, 125] for comparison.

5.2.3 Phase-averaged and fluctuating velocity definitions

Using the framework described before, twenty cardiac cycles were simulated and phase-averages were gathered over the last $n=15$ cycles. The phase average over n cardiac cycles is defined as,

$$\langle \mathbf{u}_f(\mathbf{x}, t) \rangle = \frac{1}{n} \sum_{k=0}^{n-1} \mathbf{u}_f(\mathbf{x}, t + kT), \quad (5.1)$$

where $\langle \mathbf{u}_f(\mathbf{x}, t) \rangle$ is the phase-averaged fluid velocity, \mathbf{x} denotes the spatial coordinates and t the time. The root mean square (r.m.s.) velocity \mathbf{u}_{rms} is defined as

$$\mathbf{u}_{rms}(\mathbf{x}, t) = \sqrt{\langle \mathbf{u}_f^2(\mathbf{x}, t) \rangle - \langle \mathbf{u}_f(\mathbf{x}, t) \rangle^2}. \quad (5.2)$$

5.2.4 LES quality assessment

The Kolmogorov length scale η was assessed using the fluctuating part of the velocity $\mathbf{u}' = \mathbf{u}_f - \langle \mathbf{u}_f \rangle$ ($\langle \mathbf{u}_f \rangle$ being defined in the section 5.2.3) over the last 15 heart cycles: $\eta = \nu_n^{3/4} / (2(\nu_n + \nu_t) S'_{ij} S'_{ij})^{1/4}$ (S'_{ij} is the symmetric part of the fluctuating strain rate tensor). By estimating the small scales dissipation and under the hypothesis of a homogeneous isotropic turbulence, the smallest length scales are of order of 2×10^{-5} m in the domain and the spatial averaged value is of order of 10^{-4} m. Such length scale makes the DNS of numerous heart cycles hardly reachable today: more than one billion cells would be needed to resolve all turbulence scales. Then, proper computation are still manageable thanks to LES.

In order to achieve a quality assessment of the presented simulation, the Pope criterion [142] is used. The evaluation of the LES quality is estimated through the fraction of the turbulent kinetic energy in the resolved scales. This fraction $M(x, t)$ is defined as

$$M(\mathbf{x}, t) = \frac{k_{tot}(\mathbf{x}, t) - k_{sgs}(\mathbf{x}, t)}{k_{tot}(\mathbf{x}, t)}, \quad (5.3)$$

$$= 1 - \frac{k_{sgs}(\mathbf{x}, t)}{k_{tot}(\mathbf{x}, t)}, \quad (5.4)$$

where k_{sgs} is the SGS kinetic energy, k_{res} the resolved kinetic energy of the velocity fluctuations and k_{tot} is the summation of k_{res} and k_{sgs} . Evaluation of this fraction $M(x, t)$ requires computing the resolved turbulent kinetic energy which is defined as

$$k_{res}(\mathbf{x}, t) = \frac{1}{2} \left(u_1'(\mathbf{x}, t)^2 + u_2'(\mathbf{x}, t)^2 + u_3'(\mathbf{x}, t)^2 \right), \quad (5.5)$$

The SGS kinetic energy k_{sgs} was estimated from the expression [148]:

$$k_{sgs}(\mathbf{x}, t) = \frac{\nu_t(\mathbf{x}, t)^2}{(\Delta(\mathbf{x}, t)C_s(\mathbf{x}, t))^2}, \quad (5.6)$$

where ν_t is the SGS turbulent viscosity given by the dynamic Smagorinsky-Lilly model, C_s the dimensionless dynamic constant of this model and Δ the filter width (equal to the characteristic grid size in this work). According to the Pope criterion, a good LES should be able to resolve at least 80% of the turbulent kinetic energy. Looking at the phase where the turbulent activity is the highest ($t/T_a=0.65$), it was found that computation captures more than 80% of the turbulent kinetic energy in 85% of the numerical domain. The last 15% are mainly located on the atrium surface and in the atrial cavity, where turbulence levels are actually low.

5.2.5 Data convergence

Several probes have been set in the numerical domain during simulations. The data of two representative probes are shown here. Figure 5.4, left figure, shows the numerical domain with the location of the two probes. The upper probe located in the atrium is referred to as p_1 . The probe located in the ventricle is referred to as p_2 . Figure 5.4, right figure, shows the corresponding probes data. Top plots display data from probe p_1 while the bottom plots display data from probe p_2 . For the four plots, solid lines represent the phase-averaged velocity magnitude computed using n_c cycles. n_c being set from 1 to the total number of simulated cycles, which is 15. The dots represent the instantaneous velocity magnitude for the n -ith cycle. All the velocities are nondimensionalised by a reference velocity. The reference velocity named u_a is computed as $u_a = \dot{q}l_s/V_s = 0.1 \text{ m.s}^{-1}$ where \dot{q} is the cardiac output ($\dot{q}=7.50 \times 10^{-5} \text{ m}^3.\text{s}^{-1}$), V_s the end systolic volume ($V_s = 5.55 \times 10^{-5} \text{ m}^3$) and l_s is the ventricle length at the end of the systole ($l_s=7.40 \times 10^{-2} \text{ m}$). The first column of plots represents the data at $t/T_a = 0.20$, the second column at $t/T_a = 0.65$. First represented time at $t/T_a = 0.20$ is within the systole while $t/T_a = 0.65$ occurs during the diastole.

For all four signals, the maximum velocity difference for the last three phase-averaged values (δ_a) is compared to the maximum max velocity difference for the instantaneous velocity (δ_i). These differences are defined for a velocity u as $\delta(u) = \max(u) - \min(u)$. Considering probe p_1 at $t/T_a = 0.20$, differences are $\delta_i = 0.99 u_a$ and $\delta_a = 0.03 u_a$. Same probe, at $t/T_a = 0.65$, differences are $\delta_i = 2.33 u_a$ and $\delta_a = 0.04 u_a$. In the ventricle at probe p_2 and at $t/T_a = 0.20$, differences are $\delta_i = 1.37 u_a$ and $\delta_a = 0.03 u_a$. At $t/T_a = 0.65$, differences are $\delta_i = 5.67 u_a$ and $\delta_a = 0.06 u_a$.

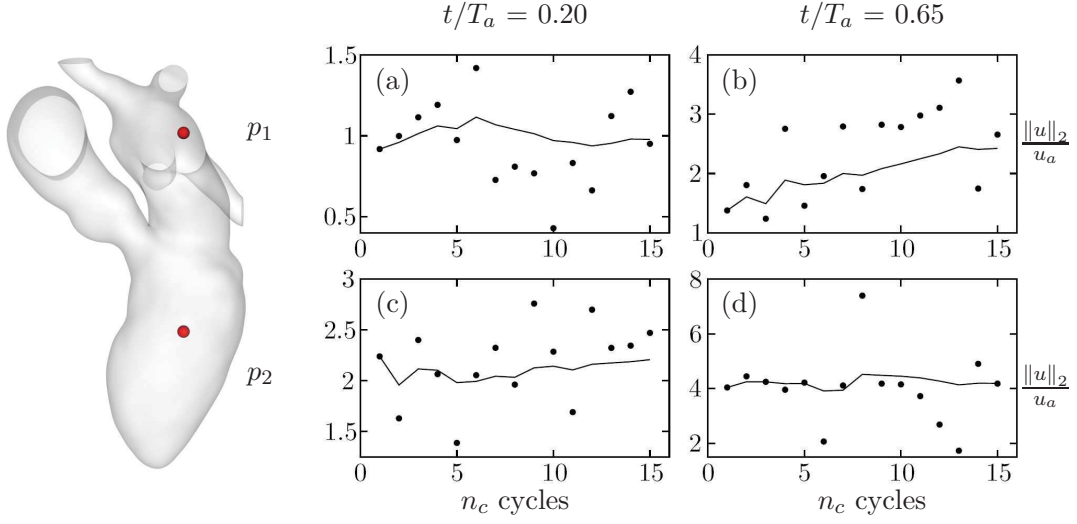


Figure 5.4: Left: left heart with probes p_1 and p_2 indicated. Right: solid lines represent the phase averaged velocity magnitude at probes locations using n_c cycles. The dots represent the instantaneous velocity magnitude for the n -ith cycle. The first column of plots represents the data at $t/T_a = 0.20$, the second column at $t/T_a = 0.65$. Top plots represent data from probe p_1 while the bottom plots represent data from probe p_2 .

For both probes and both considered times, high instantaneous fluctuations are observed. Still, the averaged velocity using 15 cycles shows δ differences of two order of magnitude than the instantaneous velocity differences. The same behaviour were observed on other probes in the numerical domain. Thus, this convergence study showed that the number of simulated cycles were sufficient to look at the phase-averaged velocity. Note that the averaged flow will be mainly described in this chapter and the characterisation of the high velocity fluctuations will be the main object of the next chapter.

5.3 Results and discussion

5.3.1 Global description of the flow

Figure 5.5 shows 3D vorticity magnitude maps of the phase-averaged velocity field, nondimensionalised by the period T_a . The following visualizations were made using the software named Paraview. Six salient instants of the heart cycle are shown: the ventricular mid-systole ($t/T_a=0.25$), the end of the ventricular systole ($t/T_a=0.35$), the beginning of the E wave ($t/T_a=0.45$), its peak ($t/T_a=0.55$), its end ($t/T_a=0.65$) and the end of the A wave, just before the beginning of the next ventricular systole ($t/T_a=0.99$).

In the first row of Fig. 5.5, the first two images correspond to systole. The mitral

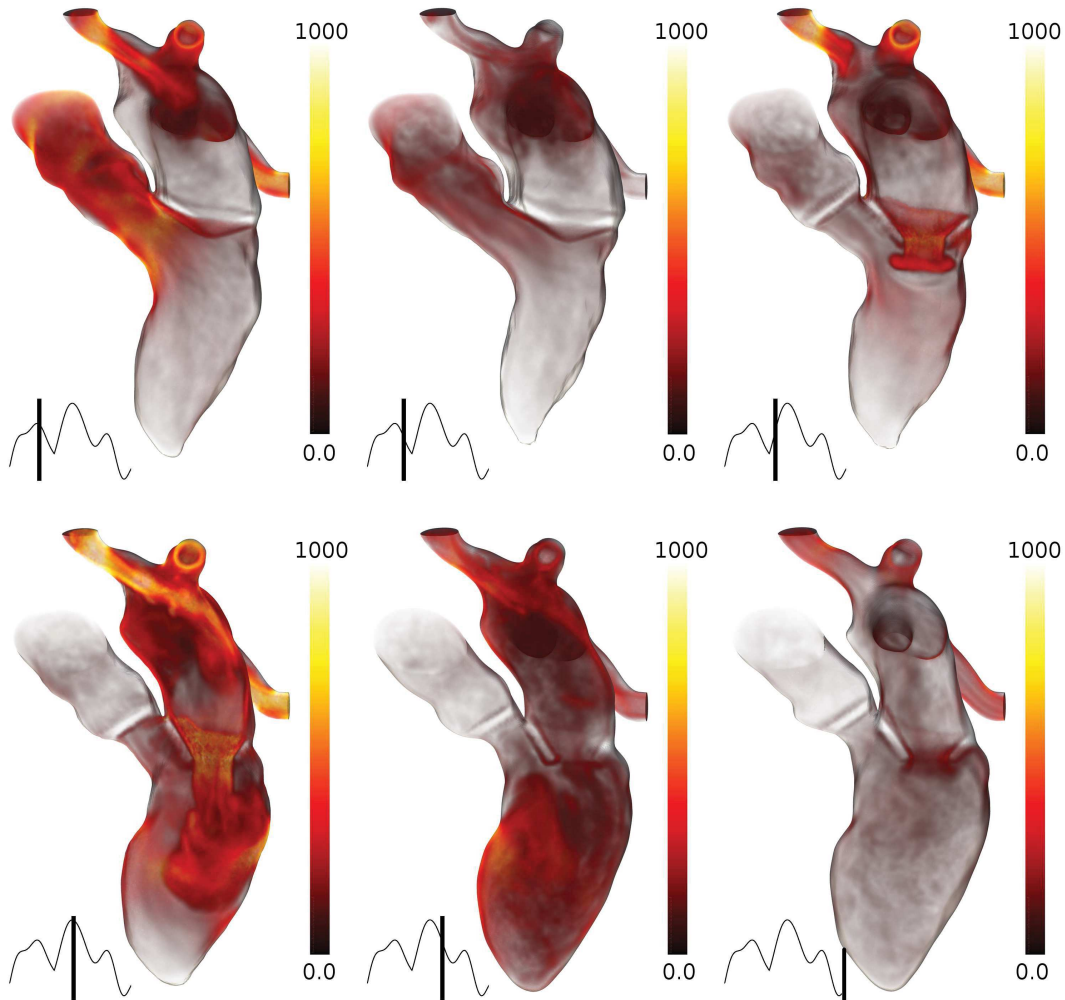


Figure 5.5: Volume rendering of non-dimensional vorticity magnitude of the phase-averaged velocity fields at different times of the simulation. First row, left plot: $t/T_a=0.25$. Center plot: $t/T_a=0.35$. Right plot: $t/T_a=0.45$. Second row, left plot: $t/T_a=0.55$. Center plot: $t/T_a=0.65$. Right plot: $t/T_a=0.99$. Sketch of the inflow flow rate presented in Fig. 5.3 is reported with a time indication. The mapping relating vorticity magnitude with opacity is linear. Heart wall is made partially transparent to allow observation of the flow behaviour.

valve is closed, while the aortic valve is open. The ventricle volume is conspicuously decreasing, causing ejection of the blood into the aorta. The narrowed geometry of the aorta root generates high vorticity in the shear layer clearly shown at $t/T_a=0.25$, while the ventricle remains free of vorticity. At the same time, the LA volume increases and is filled with blood. Four jets are present, three of them colliding head on, while the lower part of the LA remains vorticity-free. Blood coming from the RSPV (on the left side of the images) follows a trajectory tangential to the atrial wall, giving rise to a net swirling motion in the atrium as observed in vivo [62] and in experimental work [167]. High vorticity is visible at the pulmonary veins roots due to their narrowed geometry. At the end of systole, the vorticity begins to decrease in the entire heart, as shown at $t/T_a=0.35$ (top center plot in Fig. 5.5). At the end of the ventricle contraction, the aortic valve closes and the mitral valve opens: the ventricle filling starts.

The ventricle diastole starts at $t/T_a=0.375$ (not shown): the LV volume increases and blood passes from the LA to the LV, forming a strong jet through the MV. The shear layer between the jet generated and the surrounding quiescent fluid rolls-up and shapes the jet head as a vortex ring [95]. The top right plot in Fig. 5.5 depicts this vortex ring at $t/T_a=0.45$. This mechanism was reported and studied by several authors, notably by Domenichini [43]. A similar process is visible in the LA where formation of four vortex rings takes place at the four pulmonary veins (only two are visible in the top right image in Fig. 5.5).

At the E wave peak (bottom left image in Fig. 5.5, $t/T_a=0.55$), three of the LA jets collide head on, as described before, but in a more intense way, as the pulmonary veins flow rate is higher at the E wave peak than at $t/T_a=0.25$. Again, Fig. 5.5 shows that blood coming from the RSPV follows clearly a trajectory that is tangential to the atrial wall. As the E wave head jet is getting closer to the wall with an angle of approximately 50 degrees, a shear layer is generated at the lateral heart wall (the right hand sided wall on plots). The part of the vortex ring that is closer to the lateral wall interacts with it and dissipates. The other part of the vortex ring is marginally affected and thus remains almost intact, moving towards the apex of the ventricle, as described in the literature [116].

As expected for a flow at such a Reynolds number [30], small-scale vortices are also generated with the vortex-wall interaction at $t/T_a=0.65$ (Fig. 5.5, bottom center plot). At the end of the E wave, numerous small vortices are present in the whole LV.

As the inlet flow decreases, the vorticity magnitude decreases as well in the entire heart. The LV volume remains stable during this phase called diastasis. Vorticity magnitude progressively decreases in all the left heart due to dissipation of the vortices by viscosity.

This is confirmed by the vorticity levels observed in Fig. 5.5 at $t/T_a=0.99$ (bottom right image). Vorticity is now small everywhere, except near the mitral valve, due to the small A wave. Note that contrary to what is seen during the E wave, blood is not entering the LA during the A wave. The contraction of the LA to finish the LV filling

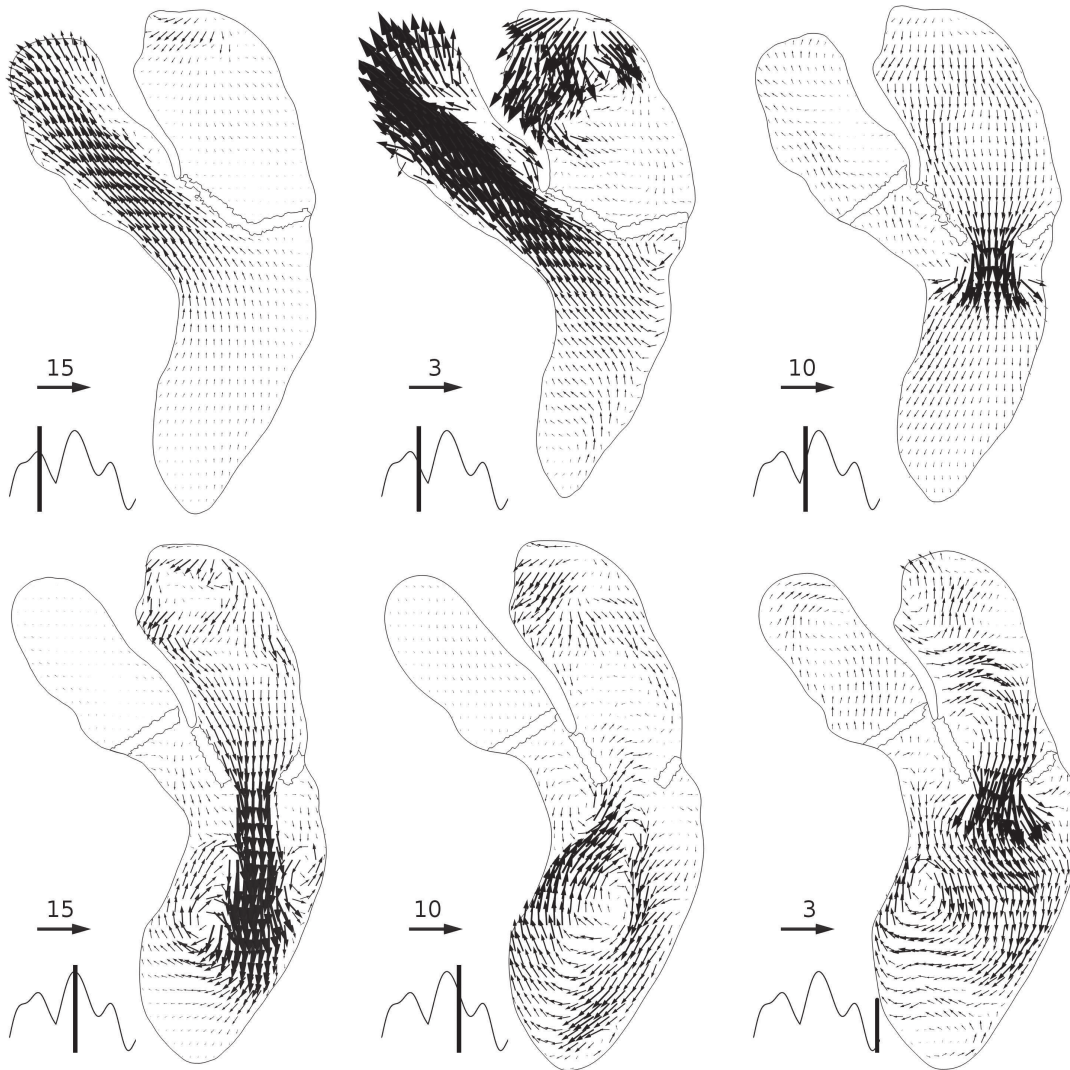


Figure 5.6: Phase-averaged non-dimensional velocity field (\mathbf{u}_f/u_a) projected on a slice of the heart. Velocity vector scale is not constant though the heart cycle and is indicated for each plot. First row, left plot: $t/T_a=0.25$. Center plot: $t/T_a=0.35$. Right plot: $t/T_a=0.45$. Second row, left plot: $t/T_a=0.55$. Center plot: $t/T_a=0.65$. Right plot: $t/T_a=0.99$. Sketch of the inflow flow rate presented in Fig. 5.3 is reported with a time indication.

results in a small outward flow through the pulmonary veins, visible on the vorticity field.

5.3.2 Velocity fields

The velocity vector fields of the phase-averaged flow are shown in Fig. 5.6, for the same instants shown in Fig. 5.5. The non-dimensional velocity vectors \mathbf{u}_f/u_a are shown over the slice through the left heart indicated in Fig. 5.1. The slice was selected and oriented to encompass the specific regions of interest in this heart. Note that due to the strong velocity variations along the cycle, the vector scale is adapted for the different instants. Again, the first two images of Fig. 5.6 correspond to systole. At the beginning of systole, high velocity is mainly observed in the ascending aorta as shown in Fig. 5.6 top left image. About the end of systole at $t/T_a=0.35$ (top center image in Fig. 5.6), just before the opening of the MV, blood entering the LA is already directed towards the LV. In the lower half part of the LA, coexistence of an axial movement toward the MV and a rotational movement is observed. This helical flow has been reported in-vivo [90, 109]. In order to see this flow feature hardly discernible in Fig. 5.6, Fig. 5.7 (left plot) shows the velocity field projected on a plane perpendicular to the cutting plane of Fig. 5.6. Above the MV at $t/T_a=0.35$, a net swirling motion is visible in this area. The axial movement towards the MV is actually much smaller than the intensity of this rotational structure.

In the ventricle, the contraction resulting in blood ejection through the aorta generates a small recirculation under the MV (on the right of the top center image). Another recirculation area is noticeable in the aorta: a normal anatomic feature of the ascending aorta is a dilatation of the vessel just above the AV. During the whole systole, blood recirculation occurs in it [89], which can clearly be observed in the velocity field shown at $t/T_a=0.35$. However, the aortic valve leaflets dynamics are not modelled here when the valve is open. Consequently, the flow dynamics observed in that region may change if a more realistic aortic valve model were used.

At the beginning of diastole (top right image in Fig. 5.6), blood enters the LA and the LA contracts, resulting in the E wave through the MV. In the LA, blood is clearly directed towards the MV [62]. The E wave vortex ring signature can also be seen in the top right plot in Fig. 5.6 at $t/T_a=0.45$ and its evolution can be followed with the bottom left plot, at $t/T_a=0.55$. There, the vortex ring is no more symmetric, as the lateral wall prevents its full development. On the other side, the vortex ring gains strength, as described in the previous section. At the same time, the atrial flow seems separated in two halves again. Blood in the lower half is directed to the MV while in the upper half, the flow is a more chaotic due to the collision of the pulmonary veins blood streams.

At $t/T_a=0.65$ (bottom, center plot in Fig. 5.6), a large recirculating cell is visible in the LV, as described classically in the literature [84, 109, 101]. It is characteristic of the flow in the ventricle after the E wave. Note that the intense upward motion along the septum wall is responsible for the high values of vorticity already described in Fig. 5.5 at $t/T_a=0.65$. Two small blood recirculation zones can be detected: one at the apex, which is visible during the whole diastole and an intermittent one between the aortic valve and one of the MV leaflets. These blood recirculations were previously reported

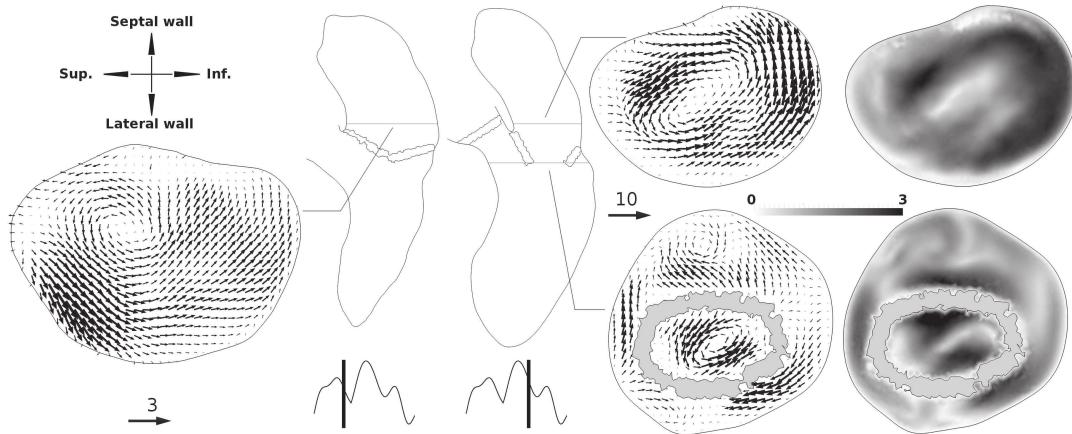


Figure 5.7: Phase-averaged non-dimensional velocity (\mathbf{u}_f/u_a) vectors field projected on planes and velocity magnitude. Planes are indicated on the heart sketches and are viewed from the top of the heart in the apex direction (plane's orientation is indicated). The MV leaflets are visible in the right bottom plots and are coloured in gray. Left: $t/T_a=0.35$. Right: $t/T_a=0.65$. Sketch of the inflow flow rate presented in Fig. 5.3 is reported with a time indication.

in-silico [42, 116, 151]. Figure 5.7 (right image) shows the averaged non-dimensional velocity field on another plane at $t/T_a=0.65$. As at $t/T_a=0.35$, in the lower part of the atrium, the downward axial movement towards the MV is rather low compared to the rotational movement: Fig. 5.7 shows a net swirling motion, visible not only above the MV (top right plot) but also at the tip of the leaflets (bottom right plot). The swirling motion at the MV is visible during all the remainder of diastole, supporting the fact that the velocity field at the MV is not only skewed [40, 78] but has also a non-negligible rotational component. This flow feature can actually be observed at each of the decelerations of the pulmonary veins inflow: a swirling motion in the lowest part of the atrium maintains blood motion in the LA even without net incoming flow through the pulmonary veins. Figure 5.7 (right image) shows the phase-averaged non-dimensional velocity magnitude on the same planes. Velocity fields show that for this heart simulation, a skewed velocity profile is obtained. Both the order of magnitude and the structure of the velocity fields show similarities with the ones presented by Dahl *and al* [40]. Note however that the velocity field in the left atrium at the MV may strongly depend on the chosen flow distribution at the pulmonary veins.

Between the E wave and the A wave, the recirculating cell core in the LV moves from the ventricle center to the septum wall. During the A wave (bottom, right plot in Fig. 5.6) occurring at $t/T_a=0.99$, the blood flux passing through the MV strengthens the recirculating cell in the LV, as classically reported. The atrial contraction expels blood from the LA, both through the MV, as seen in the lower half part of the LA, and through the pulmonary veins, as shown by the upward velocity vectors visible in the upper half part of the LA.

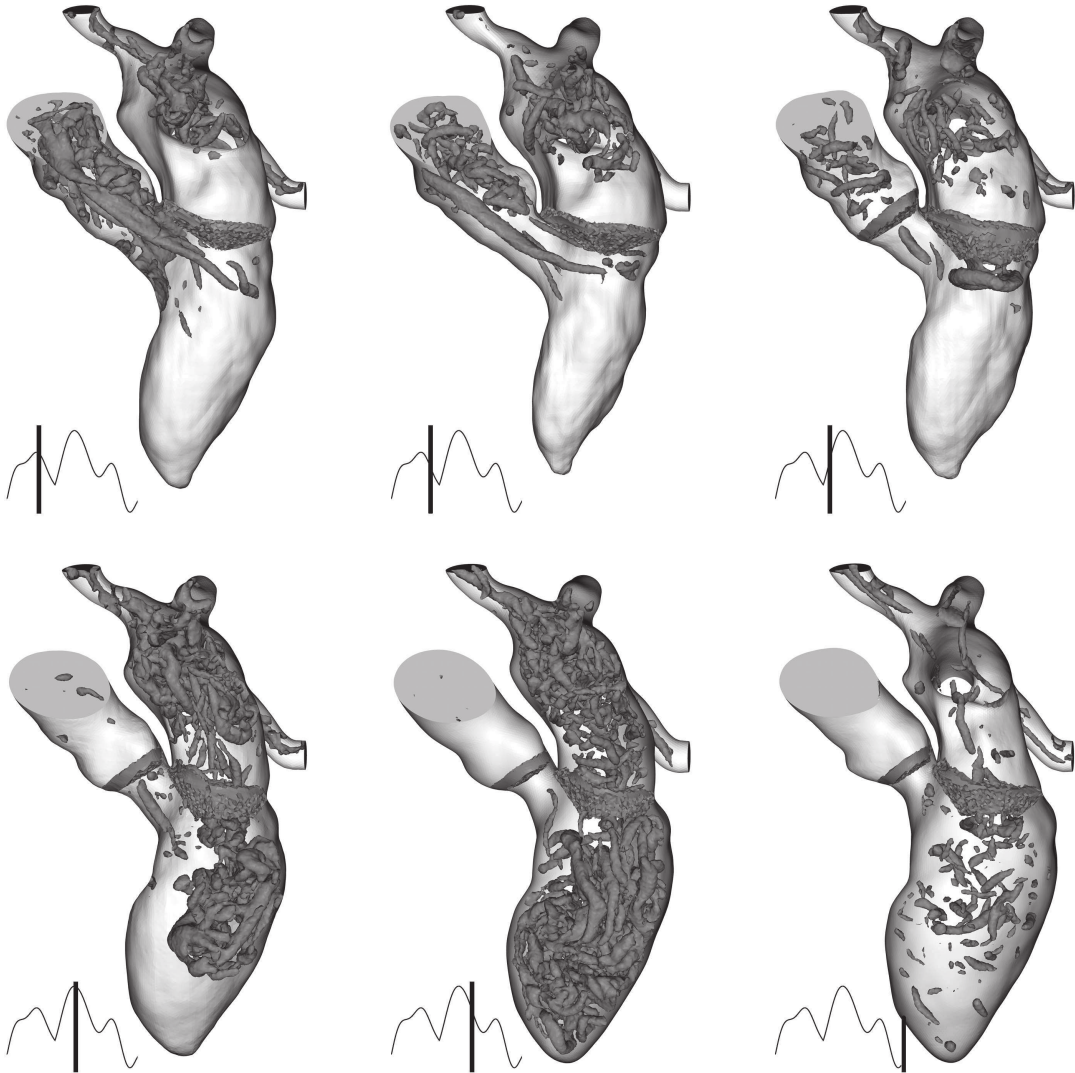


Figure 5.8: Evolution of Q criterion isosurface ($Q = 30u_a^2/R_a^2$) showing the structures present in the instantaneous field, through the heart cycle. First row, left plot: $t/T_a=0.25$. Center plot: $t/T_a=0.35$. Right plot: $t/T_a=0.45$. Second row, left plot: $t/T_a=0.55$. Center plot: $t/T_a=0.65$. Right plot: $t/T_a=0.99$. Sketch of the inflow flow rate presented in Fig. 5.3 is reported with a time indication.

5.3.3 Instantaneous structures

Instantaneous flow features have been ignored in the previous sections. In order to describe them, the Q criterion, first introduced by [85], is displayed. This criterion uses the second invariant of the velocity gradient tensor,

$$Q = \frac{1}{2}(\mathbf{\Omega}^2 - \mathbf{S}^2), \quad (5.7)$$

where $\mathbf{\Omega}$ and \mathbf{S} are respectively the antisymmetric and the symmetric components of the velocity gradient tensor. Thus, a positive Q criterion indicates a higher rotation rate compared to the strain rate, allowing to detect vortical structures. Images of Q criterion isosurfaces are presented in Fig. 5.8 at different instants of the heart cycle. The instants are the same as in the previous sections and the isosurface at $Q = 30u_a^2/R_a^2$ is shown. The Q criterion is calculated using the instantaneous velocity fields.

At the beginning of systole (Fig. 5.8 top left image), the flow vortical structures are the remnants of the late diastole flow field. The late diastole instantaneous flow structure can be observed in the bottom right image in Fig. 5.8).

In the course of the following systole, such structures are convected and smoothly elongated towards the aorta. During this process, a unique vortical structure of length up to $10 R_a$ is formed as shown in Fig. 5.8 top left and center plots. Pieces of this structure remain in the ventricle even after the aortic valve is closed. Figure 5.8 shows the remnant structure under the aortic valve even after the beginning of the E wave at $t/T_a=0.55$. The curvature of the aorta generates a helicoidal movement at the exit of the ventricle. The LV remains almost free from vortical structures during systole, as does the lower half part of the LA. However, the upper half of the LA shows many structures and swirling flow is noticeable thanks to the Q criterion at the pulmonary veins on the top left plot in Fig. 5.8.

At $t/T_a=0.45$ (top right plot in Fig. 5.8), vortex rings are created at the ostia of the pulmonary veins, due to the unsteady flow entering the LA. Two of the vortices are clearly visible in the figure. Figure 5.9, right plot, shows a better view of these structures at $t/T_a = 0.51$. Two red arrows indicates the vortex ring structures. The vortex ring at the MV described before is also visible. The MV vortex ring travels about two radius R_a in direction of the apex during a time interval of $T_a/10$ before it hits the lateral wall. The Q criterion isosurfaces in the left and bottom center images in Fig. 5.8 show the evolution of the vortical structures in the LV from the initial ring-like shape to the final complex 3D flow, when the ventricle cavity is almost completely filled by vortical structures, at $t/T_a=0.65$. At the same time, the LA also shows an intense vortical activity as well. The swirling motion at this time cannot be well represented by the instantaneous structure although hardly discernible structure following the e_3 axe is generated by the swirl. Figure 5.9, left plot shows the instantaneous streamlines in the atrium at $0.75T_a$, the swirling being well visible.

During the late ventricle filling, the atrium contracts and generates a small vortex ring (bottom right plot in Fig. 5.8). However, its intensity is much lower than the one generated during the E wave, and it is hardly visible. The vortex head only travels about one radius R_a within a time span of $T_a/12$, which corresponds to a velocity 60% smaller than the vortex ring created by the E wave. Finally, vortical structures dissipate almost everywhere in the heart. It has to be noticed that the swirling flows visible at the pulmonary veins at $t/T_a=0.25$ and $t/T_a=0.65$ through the Q criterion are also visible at $t/T_a=0.99$: the pulmonary veins geometry generates this helicoidal inflow.



Figure 5.9: Left: streamlines in the atrium at $0.75T_a$. Right, isosurface of Q-criterion ($5 \frac{u_a^2}{R_q^2}$) showing the structures present in the instantaneous field at $0.51T_a$. Vortex rings are indicated by the two red arrows.

5.3.4 Velocity fluctuations

This flow configuration is a breeding ground for weak turbulence. The transitional nature of this cyclic flow due to high Reynolds numbers and unsteady inflows results in cycle-to-cycle variations. These variations can be quantified through the non-dimensional kinetic energy of the velocity cycle-to-cycle fluctuations. Note that in the present case, the fluctuations energy do not only measures the turbulent activity, but more generally cycle-to-cycle variations. However, in this manuscript, this energy will be referred to turbulent kinetic energy (TKE).

This turbulent kinetic energy (TKE) is defined as,

$$E_k = \frac{1}{2}(u_{rms}^2 + v_{rms}^2 + w_{rms}^2), \quad (5.8)$$

where u_{rms} , v_{rms} and w_{rms} are the root mean square values of the velocity fluctuations in the three directions.

Figure 5.10 shows the spatial distribution of the TKE along the heart cycle, over the same cutting plane as in Fig. 5.6. The beginning of systole is associated with a relaminarization process in the LV. TKE intensity levels across the ventricle during systole (top left and center plots in Fig. 5.10) stay almost null. The highest TKE levels are present in the root of the aorta between $t/T_a=0.25$ and 0.35 . Note however that the TKE levels downstream of the AV may be mispredicted here, due to the absence of AV leaflets modelling when the AV is open. Meanwhile, fluctuations are increasing in the upper half of the LA (up to $10 \frac{u_a^2}{R_q^2}$) where the inflowing jets collide.

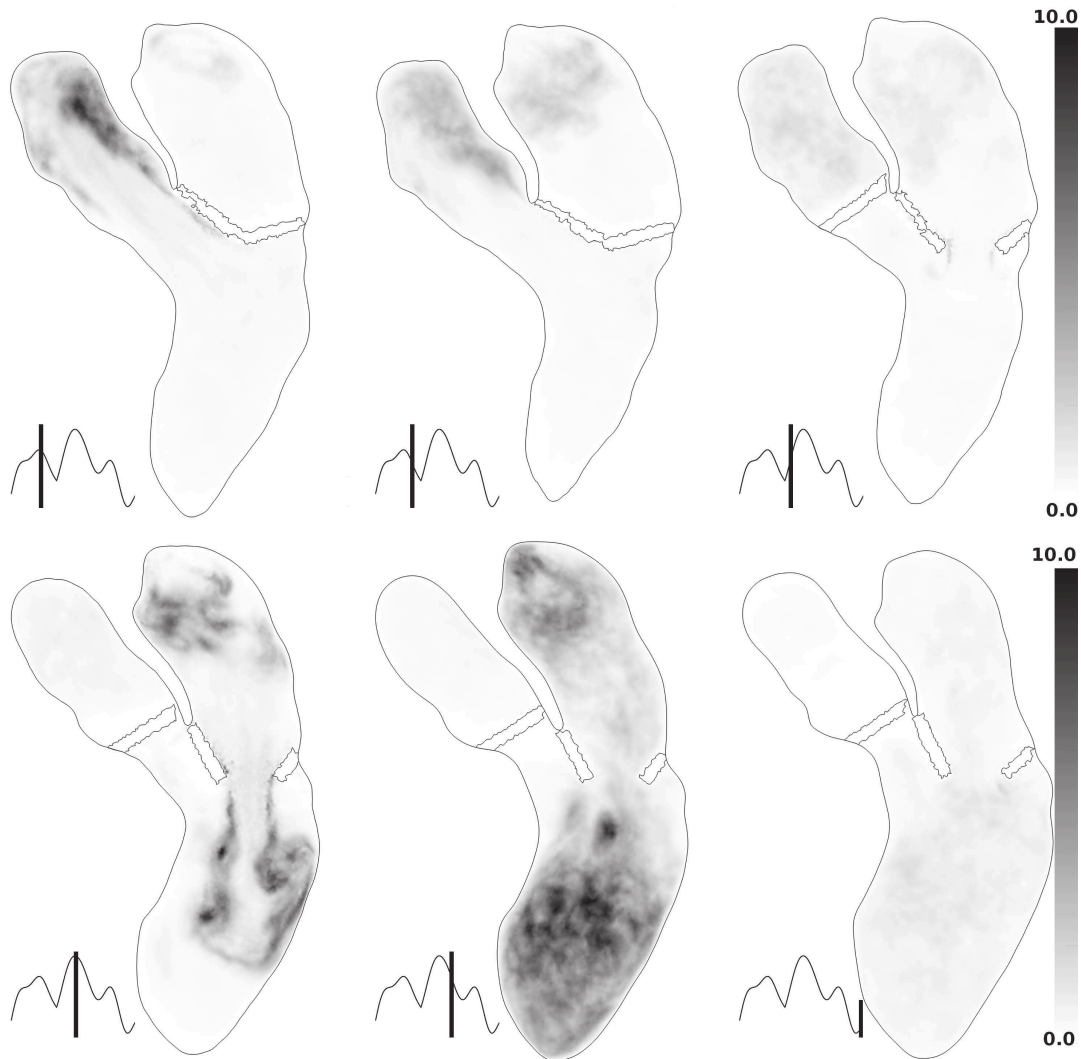


Figure 5.10: Nondimensional fluctuating kinetic energy E_k/u_a^2 . First row, left plot: $t/T_a=0.25$. Center plot: $t/T_a=0.35$. Right plot: $t/T_a=0.45$. Second row, left plot: $t/T_a=0.55$. Center plot: $t/T_a=0.65$. Right plot: $t/T_a=0.99$. Sketch of the inflow flow rate presented in Fig. 5.3 is reported with a time indication.

During the formation of the MV vortex ring at $t/T_a=0.45$ (top right plot in Fig. 5.10) until the jet hits the wall, the TKE is more intense in the vicinity of the jet. These fluctuations are mainly due to small differences in the location of the shear layer and of the vortex ring, where the velocity gradients are high. At the E wave peak ($t/T_a=0.55$, bottom left plot in Fig. 5.10), high TKE (about $5 u_a^2$) is observed in the jet edge which becomes increasingly unstable throughout the onset of the MV flow deceleration. Furthermore, high TKE levels are also visible along the lateral wall.

As shown by the TKE field at $t/T_a=0.55$, the impact of the vortex ring on the lateral wall is a zone of high velocity fluctuations. At the same time, the E wave starts to decrease. At $t/T_a=0.65$ (bottom center image in Fig. 5.10), the flow through the mitral valve is approximately null. However, the flow in the ventricle is far from quiescent. The mitral jet impact has made the initial vortex ring shatter into small vortices, that occupy the main part of the ventricle. In accordance with this transition to (weak) turbulence, the TKE field shows high values over almost the whole ventricle. Largest values of TKE (from 6 to $10 u_a^2$) are observed at the core of the recirculating cell. These high values of TKE are due to the differences in the position of recirculating cell center between cycles, as previously reported in similar geometrical configuration [46]. The TKE in the LA also indicates that the pulmonary jets impact in the upper part of the LA is associated with intense velocity fluctuations from one cycle to another. TKE is about three times lower in the bottom half of the LA. Such a ratio of TKE between the upper and bottom halves of the LA remains approximately the same during the entire heart cycle.

At the end of diastole ($t/T_a=0.99$, bottom right plot in Fig. 5.10), the TKE becomes more homogeneous in the heart, albeit with higher values at the center of the ventricle recirculating cell (see also Fig. 5.6) and at the MV tips due to the A wave vortex ring. As soon as systole begins, a relaminarization process is engaged in the ventricle: blood acceleration reorganizes the blood flow and destroys all the remaining vortices. Comparing the TKE fields at $t/T_a=0.99$ and at $t/T_a=0.25$ shows that late diastole velocity fluctuations do not persist in systole.

5.4 Flow sensitivity to viscous effect

5.4.1 Blood rheology

The calculation reported in this chapter has limitations related to the blood modelling. Blood has been modelled as a Newtonian fluid and we will keep this modelling assumption in the next chapters. Even if this approximation is commonly accepted for heart flow and more generally for cardiovascular flows in large vessels, a non-Newtonian model could be included in the present method in order to assess the impact of the rheological model on the flow. In order to take into account of the shear-thinning behaviour of blood, the Carreau-Yasuda model [18] was used. This model was chosen among others [183] because of the following advantages. First, the bounded nature of

the model is an advantage over other non-linear models. Then, the model is computationally effective, has a low implementation complexity and a negligible computational cost compared to the Newtonian model by directly relating the shear strain rate to the shear stress.

The popularity of the Carreau-Yasuda model is partly due to its success in reproducing experiments performed using a blood analogue fluid. Gijzen *et al.* [70, 71] conducted a series of experiments on two academical configurations in order to investigate the influence of the non-Newtonian properties of blood on the velocity field. In these works, the shear-thinning behaviour of the blood analogue fluid was accounted for in the numerical simulations thanks to the Carreau-Yasuda model, leaving aside the thixotropic and viscoelastic properties of the fluid (and of blood). Gijzen *et al.* obtained a good comparison between the experiment and the simulations with the Carreau-Yasuda model, while the simulations with the Newtonian model showed larger differences. One could conclude that the Carreau-Yasuda model is better than the Newtonian model. However, one should not overrate the capability of the Carreau-Yasuda model to represent blood: the Carreau-Yasuda model is actually a reasonable model of blood analogue fluids (which are imperfect blood models), not of blood itself.

This simple model is far from describing accurately the blood rheology. In particular, rheological models as the Carreau-Yasuda model assumes an instantaneous relation between the shear rate and the effective viscosity. However, it is well known that the increase of viscosity at low shear rates is strongly related to the formation of rouleaux of red blood cells, which is a time-dependent process [32]. This effect is neglected in the Carreau-Yasuda model. Nevertheless, simulations using a shear-thinning model can provide some information about the importance of shear-thinning effects on the configuration of interest. Configurations showing small differences between simulations using a Newtonian model or the Carreau-Yasuda model are probably less sensitive to rheological models.

A quick study has thus been conducted to compare simulations with a Newtonian fluid or a Carreau-Yasuda fluid, to estimate the impact of the rheological model. Results are briefly discussed in the next paragraphs. The reader will find further discussion on blood modelling and its implication on flow and turbulence in the concluding chapter of this thesis (chapter 9, section 9.2.2).

The Carreau-Yasuda model was then included in the YALES2BIO in order to make comparisons with the results already presented in the Newtonian case. The Carreau-Yasuda model reads

$$\frac{\nu_c - \nu_\infty}{\nu_0 - \nu_\infty} = (1 + (\lambda_c \dot{\gamma})^{a_c})^{(n_c - 1)/a_c}, \quad (5.9)$$

where $\dot{\gamma}$ is a scalar measure of the rate of the deformation tensor D . It is related to the second invariant of the rate of deformation tensor [104]:

$$D = \frac{1}{2}[\nabla \mathbf{u} + (\nabla \mathbf{u})^t], \quad (5.10)$$

$$\dot{\gamma} = \sqrt{2tr(D^2)}. \quad (5.11)$$

ν_0 (m ² .s ⁻¹)	22×10^{-6}
ν_∞ (m ² .s ⁻¹)	2.2×10^{-6}
ν_n (m ² .s ⁻¹)	4.0×10^{-6}
a_c	0.644
n_c	0.392
λ_c (s)	0.110

Table 5.3: Set of parameters used in the Carreau-Yasuda model. Data fitted from work by Thurston [170].

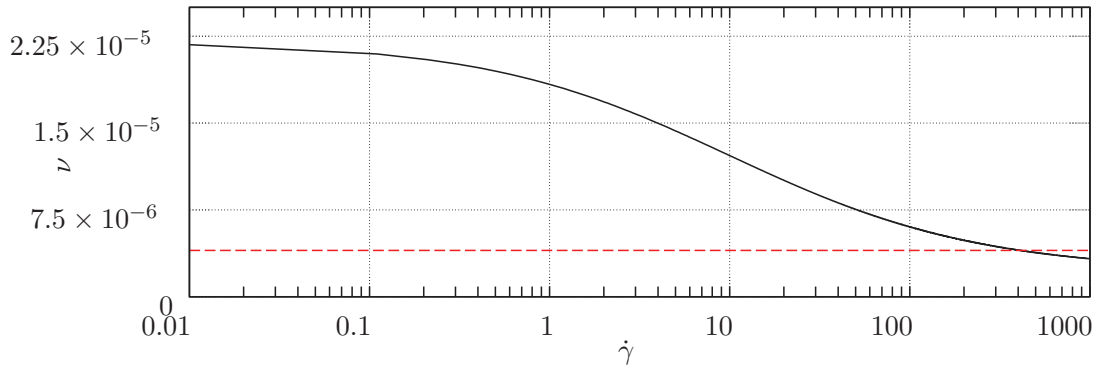


Figure 5.11: Comparison of viscosity ν_c and shear rate $\dot{\gamma}$ relationship as predicted by the Carreau-Yasuda model (solid line). The constant viscosity ν_n used in the Newtonian hypothesis is indicated using the red dashed line.

The other parameters are ν_0 the viscosity at zero shear rate, ν_{inf} the viscosity at infinite shear rate, λ_c a relaxation time, n_c the power index coefficient and a_c a dimensionless parameter describing the transition between the first Newtonian plateau and the power-law range. The numerical values of the parameters used here were also used in Gijzen *et al.* [70] and in Chen *et al.* [28]. These parameters were obtained by fitting experimental data from Thurston [170]. The parameters are reported in Tab. 5.3. The constant viscosity used in the simulations under the Newtonian assumption, referred to as ν_n here, is also recalled.

Figure 5.11 shows the viscosity behaviour under a large range of shear rate $\dot{\gamma}$. Note that at a scalar shear rate of 400 s^{-1} , the Newtonian and Carreau-Yasuda fluids have the same viscosity. At high shear rate ($\dot{\gamma} \gg 1$), the viscosity value is below the constant viscosity used in the simulations under the Newtonian hypothesis.

A 30-heart-cycle LES was conducted with the Carreau-Yasuda blood model. Figure 5.12 shows the spatial distribution of the ratio ν_c/ν_n , ν_c being the viscosity computed by the Carreau-Yasuda model and ν_n the constant viscosity used all along this manuscript. This ratio is mapped along the heart cycle, over the same cutting plane as in Fig. 5.6.

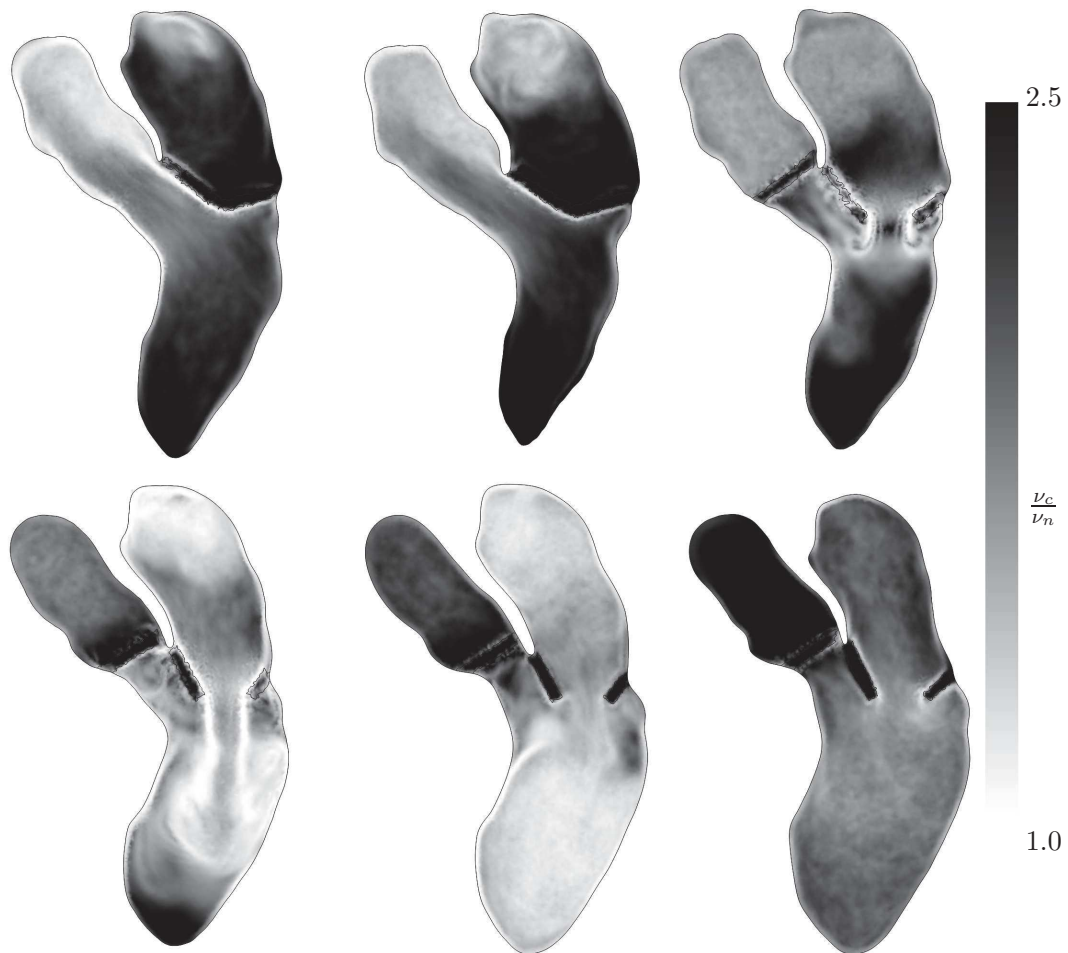


Figure 5.12: Ratio between viscosity ν_c computed with Carreau-Yasuda model and constant viscosity ν_n . First row, left plot: $t/T_a=0.25$. Center plot: $t/T_a=0.35$. Right plot: $t/T_a=0.45$. Second row, left plot: $t/T_a=0.55$. Center plot: $t/T_a=0.65$. Right plot: $t/T_a=0.99$.

Under the light of the previous section, it has to be noted that the location where high fluctuations are observable correspond to high shear area and thus, low fluid viscosity. Hence, the viscosity drops in the upper part of the atrium during disturbed flow. Likely, the E wave jet in the ventricle and the following diastasis are associated with low viscosity regions. Viscosity rises in regions of quiet flow, in the lower part of the atrium or in the ventricle during diastole. During all the heart cycle, maximum viscosity was approximately of $4 \nu_n$. The velocity distributions are not shown here, as the differences against the Newtonian case are barely observable. Regarding the fluctuating kinetic energy, the higher viscosity implies lower energy levels because of the higher dissipation. However, the energy levels behaviour are almost identical and the maximum decrease in fluctuating kinetic energy when using the shear-thinning model is about $\sim 10\%$ compared to the Newtonian case.

5.4.2 SGS modelling

As shown in section 5.3.4, turbulence is generated in the heart. It is hence anticipated that the numerical results could be sensitive to both the numerical scheme and the SGS model. We discuss in particular the impact of the SGS model on the flow as we have performed computation with the dynamic Smagorinsky model in this chapter. This section focuses on the comparison between the dynamic Smagorinsky model [68] and the σ model [130].

Comparisons of the Sigma and Smagorinsky LES models against direct numerical simulation has been conducted by Rieth *et al* [145] for grid-generated turbulence and in a channel flow. The study showed that the σ -model and the dynamic Smagorinsky model lead to comparable results for most of the settings examined. However in simulation with the σ -model, in addition to its significantly lower computational costs (as no dynamic procedure is used), the near wall region has been captured more accurately. Baya Toda *et al.* [15] have conducted comparison of the σ -model and the dynamic Smagorinsky model against experimental measurements on a pulsatile jet in turbulent cross-flow impinging on a plate. Such a configuration is close to what happens in the heart during diastole, when the E wave mitral jet impacts the lateral wall. Both subgrid-scale models give similar results during the first phase of the experiment. However, it was found that the dynamic Smagorinsky model could not accurately predict the vortex-ring propagation, while the σ -model provides a better agreement with the experimental measurements.

Here, the influence of the SGS viscosity model is investigated by comparing results from the σ -model and the dynamic Smagorinsky model used in this chapter. In both cases, the heart presented in this chapter is used and results are phase-averaged over 50 cycles.

Figure 5.13 shows the ratio of the SGS viscosity ν_t to molecular viscosity ν_n for both models at $t/T_a = 0.55$ and $t/T_a = 0.65$. The model viscosity obtained with the σ -model is much noisier than with the Smagorinsky model. High values (and thus non physical)

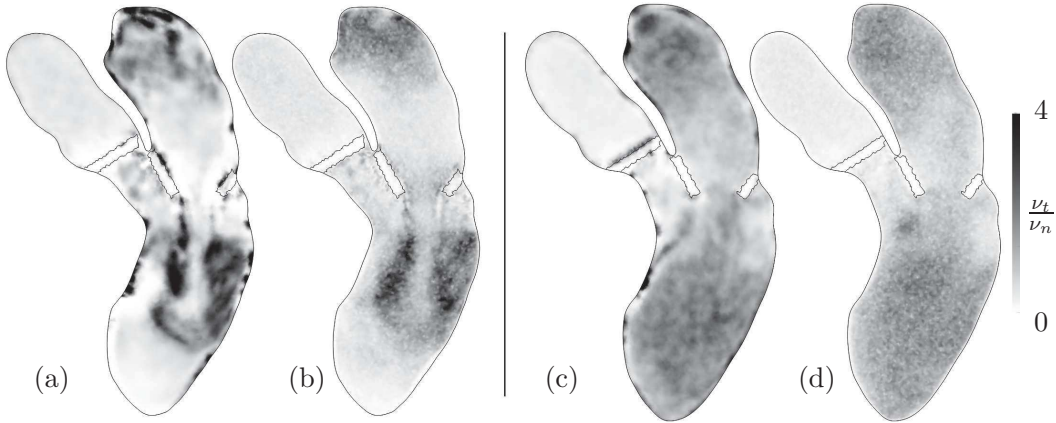


Figure 5.13: Maps of ratio of the SGS viscosity ν_t to molecular viscosity ν_n . Plot (a) and (c) display the ratio for the dynamic Smagorinsky model. Plot (b) and (d) are maps of the σ -model SGS viscosity ratio. Left plots (a and b) are maps of the ratio at $t/T_a = 0.55$ while the right plots (c and d) are maps at $t/T_a = 0.65$.

of SGS viscosity at wall nodes at $t/T_a = 0.55$ and $t/T_a = 0.65$ are observable for the Smagorinsky model. During diastasis at $t/T_a = 0.65$, the SGS viscosity drops for both models. The velocity magnitude is low and more likely resolved by the mesh, so that the damping of the viscosity is successful.

Concerning the σ -model, the fully local definition of the time scale (no explicit filtering or averaging needed) allows the subgrid-scale viscosity to automatically vanish near solid boundaries as long as there are some nodes in the boundary layer. As a result the viscosity level remains very low during the entire cardiac cycle, even when the velocity gradient at the wall is high, as at $t/T_a = 0.55$. In addition, the results shows that the σ -model adds less SGS viscosity than the dynamic Smagorinsky model, so that simulation is closer to a DNS.

Figure 5.14 shows the phase-averaged velocity and TKE maps at the same instant ($t/T_a = 0.65$). This instant was chosen for its high TKE magnitude levels. Velocity maps show that the overall flow structure is the same for the two SGS viscosity models. This statement stands for the rest of the heart flow apart for the recirculating cell in the ventricle at the diastole end (results not shown here). The center position of this cell is slightly different. However, turbulence characteristics changed, especially in turbulent levels. This results were expected as the dynamic Smagorinsky model is slightly more dissipative than the σ -model. The TKE results for the dynamic Smagorinsky model and the σ -model share an overall similar behaviour for the turbulent kinetic energy but differences in magnitudes are observed. TKE magnitude levels are roughly 10 % higher with the σ -model, and at $t/T_a = 0.65$, fluctuations are more concentrated in the ventricle center for the σ -model.

In the end, the changes in flow topology in *heart A* are not as drastic than the change

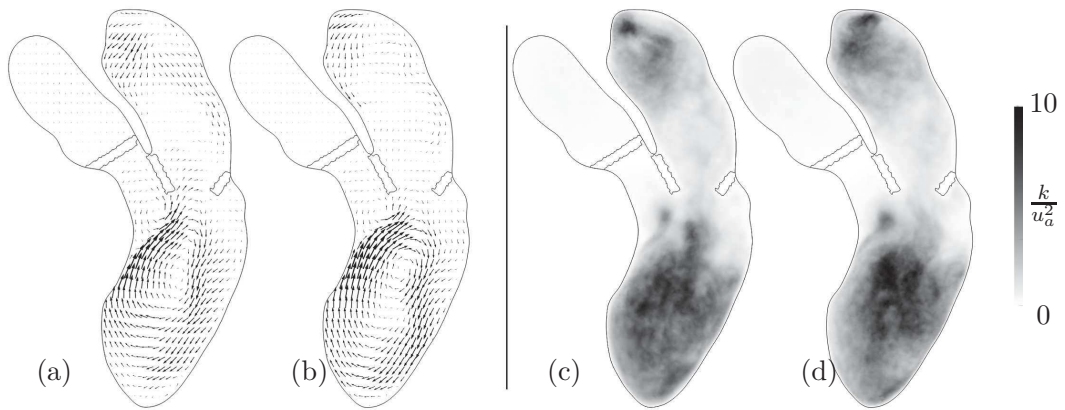


Figure 5.14: Velocity (left plots) and TKE maps (right plots) obtained with the dynamic Smagorinsky and with the σ -model . For each plots couple, the left is the results of simulation with dynamic Smagorinsky model, the right with σ -model. The displayed maps correspond to $t/T_a = 0.65$.

in Baya Toda *et al.* [15] case. However, the σ -model adds less viscosity to the flow, has a better behaviour at the walls and is less CPU-consuming. The σ -model will be thus used during the rest of this manuscript.

5.5 Conclusion and outlook

In this chapter, the application of the presented numerical framework to a patient left heart has been exposed. This numerical framework only requires gated 4D images of a patient heart and global morphological parameters of the mitral valve as input data for the computation. A numerical domain is extracted from one 3D medical image and the heart wall movements are automatically calculated to follow the heart wall displacements recorded in the 4D medical images, thanks to an image registration algorithm. Then, temporal interpolation of the geometry is used to generate a finite-volume mesh of the left heart at any time over the cardiac cycle.

A computation of the blood flow in a full left heart including the left ventricle, atrium and the aorta root has been conducted. The present numerical method provides results consistent with the current knowledge in terms of left heart flow. The E wave and the A wave are recovered showing high E/A ratio (5.5) characteristic of ventricle with restrictive filling. At the pulmonary veins, the flow reversal associated with the late atrial contraction is recovered as well.

In the left atrium, the flow reported shows a clear swirling motion, that maintains blood in motion even without net blood flow coming from the pulmonary veins. Furthermore, the well-known mitral jet, preceded by an energetic vortex ring, is also observed. The classical large recirculating cell, characteristic of the flow during diastasis, can also

be seen in the phased-averaged velocity fields. All these features have been reported several times in the literature, both in numerical and experimental studies and by medical imaging.

Furthermore, the use of a numerical method well adapted to turbulent flows enables the observation of cycle-to-cycle variations in the flow field. Such variations are expected in the present flow, because of the Reynolds numbers encountered and the unsteadiness of the flow coming from the pulmonary veins. The present results show that in spite of the rigorously identical contraction and boundary conditions, fluid inertia makes the flow differing from one cycle to the other. More precisely, cycle-to-cycle variations in the left atrium can be observed in its upper part, where the collision of the jets issuing from the pulmonary veins makes the flow particularly chaotic. Cycle-to-cycle variations are high after each peak in the pulmonary vein flow rate, during flow deceleration. In the left ventricle, velocity fluctuations are reported mainly in late diastole. Between the impact of the E wave jet on the lateral wall and the end of diastole, the left ventricle displays high levels of cycle-to-cycle fluctuations. Indeed, both the vortex ring impact and the E wave deceleration occur approximately at the same time, and both are features tending to promote turbulence. During late diastole, the large recirculation cell classically reported in the literature is recovered in the phase-averaged field.

The spatio-temporal resolution of the medical images used to feed the whole numerical procedure is an important limitation, which imposes temporal interpolation and geometrical simplifications of the heart model. It also makes it difficult to accurately account for short phases as the isovolumic contraction and relaxation. Although ten images per cardiac cycle enables a convincing flow prediction, specific tests should be performed to precisely assess the impact of the temporal resolution of the medical images on the flow field. Another limitation is the unknown flow distribution between the pulmonary veins, which has to be prescribed in the simulations.

In the present work, the main element to improve is certainly the valve modelling. The model used for valves highly depends on the anatomical information that can be extracted from the images. Consistently with their insufficient spatio-temporal resolution, a rough model of the valves was used. Better valve models should notably include valve opening and closing and the change of aperture area along time. Aortic valve leaflets were also completely omitted during systole, which most probably impacts the flow at the beginning of the aorta. In addition, the immersed forcing used in this work could be improved [52], notably by accounting for the exact valve velocity.

Still, the presented method does include important aspects of the physiological heart: the entire ventricle and atrium, the aorta root, the pulmonary veins and the valves. Such a geometrical complexity has rarely been accounted for. As a consequence, rarely or never reported features such as secondary vortex recirculation, vortical structure at the aorta, swirling motion at the MV, vortex rings, swirling motion at the pulmonary veins and velocity fluctuations have been discussed for the first time in details. Furthermore, the presented results underline the fact that over-simplified geometries cannot fully

reproduce certain physical events as for example the mitral in-plane swirling motion.

Chapter key points:

- The framework presented in the last chapters was successfully applied to compute a patient-specific heart blood flow.
- Heart model and movements are extracted from morphological medical images.
- Flow dynamics was analysed and commonly detected physiological patterns are reported.
- Large cycle-to-cycles fluctuations were observed.
- Negligible changes are observed when using the Carreau-Yassuda model instead of the Newtonian approximation.

Turbulent assessment of a left heart flow

Chapter contents

6.1	Problem formulation	102
6.1.1	Numerical domain	102
6.1.2	Governing equations	103
6.1.3	Computational mesh and simulation details	103
6.1.4	Data reduction	105
6.2	Data convergence	105
6.3	Results	107
6.3.1	Temporal evolutions	107
6.3.2	Kinetic energy	112
6.3.3	Production of turbulent kinetic energy	119
6.3.4	Turbulence characteristics	121
6.3.5	Spectral analysis	125
6.4	Final remarks	128

As seen in the previous chapter, in addition to retrieving the main fluid flow phenomena commonly observed in the left heart, the developed methodology allows the observation of high levels of cycle-to-cycle fluctuations. The present chapter focuses on these fluctuations and aims at characterizing them in *heart A*. The unsteady development of turbulence is analysed using mean flow, the flow statistics, the turbulent stresses, the turbulent kinetic energy, its production and through spectral analysis.

This chapter is part of: C. Chnafa, S. Mendez and F. Nicoud. "Turbulence characterisation in a patient-specific human left heart. A numerical study". To be submitted for publication in Journal of Fluid Mechanics.

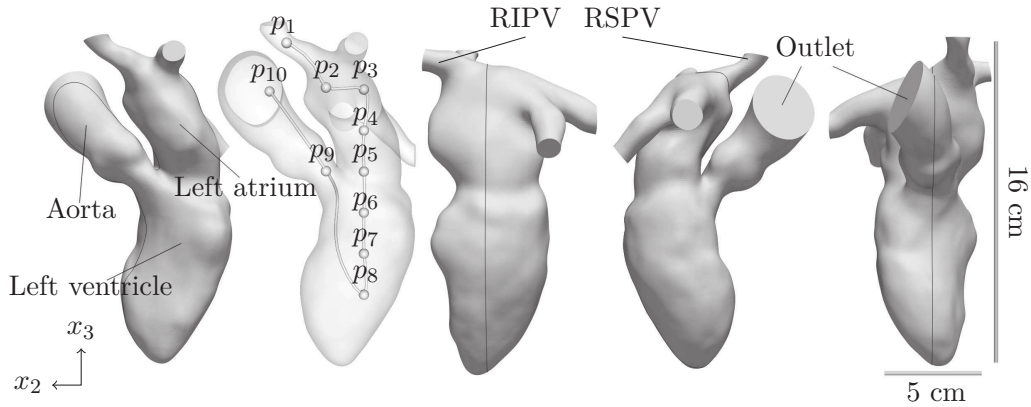


Figure 6.1: *Template* computational domain extracted from a 3D medical image. The same domain is represented from four different points of view and the left ventricle (LV), left atrium (LA), Aorta (AO) and two pulmonary veins are indicated. Black line passing through the left heart indicates the position of slices used to describe the flow in section 6.3. Probes locations and outflow patch are also indicated.

6.1 Problem formulation

The procedure which allows producing a proper numerical representation of the intra-cardiac flow from medical images was fully described in the last chapters. Only the main ingredients are given in the following sections.

6.1.1 Numerical domain

The same CT exam used in the last chapter is used here. As a reminder, the exam consists in $N = 10$ medical images which are available along the cardiac cycle lasting $T = 1000$ ms. The numerical domain is extracted from one particular medical image referred to as *template* image.

Fields of deformations between the *template* image and the other images taken at different times in the cardiac cycle are computed by an image registration algorithm. These deformations are then applied to the *template* mesh, producing a set of successive meshes matching the physiological cardiac images at different times.

In this study, both the aortic (AV) and mitral (MV) valves are handled by an immersed boundary method (IBM). The AV, which has a moderate impact on the ventricular flow, is modelled as a planar region being alternatively permeable and impermeable depending on the phase in the cardiac cycle. The MV is modelled by a more realistic geometry based on measurements (open surface, leaflets lengths) on the medical images.

6.1.2 Governing equations

Blood is modelled as an incompressible Newtonian fluid. so that the haemodynamics is described by the Navier-Stokes (NS) equations. These equations are solved on the moving blood domain $\Omega_f(t) \subset \mathbf{R}^3$ bounded by $\partial\Omega_f(t)$. The boundary $\partial\Omega_f(t)$ is such that $\partial\Omega_f(t) = \partial\Omega_f^i(t) \cup \partial\Omega_f^w(t) \cup \partial\Omega_f^o(t)$ and $\partial\Omega_f^i(t) \cap \partial\Omega_f^w(t) \cap \partial\Omega_f^o(t) = \emptyset$ where $\partial\Omega_f^i(t)$ represents a fluid inlet boundary where a Dirichlet condition is prescribed on the velocity field, $\partial\Omega_f^w(t)$ represents the vessels and heart wall boundary where a classical no-slip condition is applied and $\partial\Omega_f^o(t)$ represents a fluid outlet boundary. The NS equations for the resolved velocity \overline{U}_i and pressure \overline{P} are

$$\left. \begin{aligned} \frac{\partial \overline{U}_i}{\partial t} + \frac{\partial \overline{U}_i \overline{U}_i}{\partial x_j} &= -\frac{1}{\rho} \frac{\partial \overline{P}}{\partial x_i} + \nu_n \frac{\partial^2 \overline{U}_i}{\partial x_j \partial x_j} - \frac{\partial \tau_{ij}}{\partial x_j} + f_i, \\ \frac{\partial \overline{U}_i}{\partial x_i} &= 0, \end{aligned} \right\} \text{ on } \Omega_f(t) \quad (6.1)$$

where ν_n is the kinematic viscosity, ρ the density and f_i a volumetric force. The residual-stress tensor $\tau_{ij} = \overline{U}_i \overline{U}_j - \overline{U}_i \overline{U}_j$ results from the unresolved subgrid-scale contribution and is modelled by a subgrid-scale (SGS) model in this study. σ -model described in chapter 3 is used here instead of the Smagorinsky model. On the domain presented in Fig. 6.1 (left plot), x_1 , x_2 and x_3 corresponds to the forward to backward direction, the right to left direction and the bottom to top direction respectively.

As the assumption that either the aortic valve or the mitral valve is closed is made, the total mass flow rate entering the domain is entirely determined by the mass conservation constraint (see chapter 4). This total mass flow rate is equally distributed between the four PV. Flow rate at the MV and the total flow rate are redisplayed in Fig. 6.2 for the sake of completeness. Two vertical dotted lines separate the systolic phase and the diastolic one. For this heart, systole lasts $t/T_a=0.36$ (from t/T_a 0.015 to 0.375) and diastole $t/T_a=0.64$.

6.1.3 Computational mesh and simulation details

A nearly isotropic grid is used during the whole cardiac cycle. The spatial resolution is imposed to be close to 0.8 mm in all three spatial directions which yields grids of approximately three-million tetrahedral elements.

The simulation time step is fixed by a CFL condition (CFL=0.9) and a Fourier condition of $F_o = 0.2$ consistent with the explicit time integration used in the CFD solver. This corresponds to a time step varying from 3.0×10^{-4} s to 8.0×10^{-4} s in the present computation. The period of the whole cardiac cycle is $T = 1$ s.

The fluid density ρ and the fluid kinematic viscosity ν_n are supposed to be constant in this chapter: $\rho = 1040 \text{ kg.m}^{-3}$ and $\nu_n = 4 \times 10^{-6} \text{ m}^2.\text{s}^{-1}$. The reference velocity named u_a is computed as $u_a = \dot{q} l_s / V_s = 0.1 \text{ m.s}^{-1}$ where \dot{q} is the cardiac output ($\dot{q}=7.50 \times 10^{-5} \text{ m}^3.\text{s}^{-1}$), V_s the end systolic volume ($V_s = 5.55 \times 10^{-5} \text{ m}^3$) and l_s is the ventricle length at the end of the systole ($l_s=7.40 \times 10^{-2} \text{ m}$).

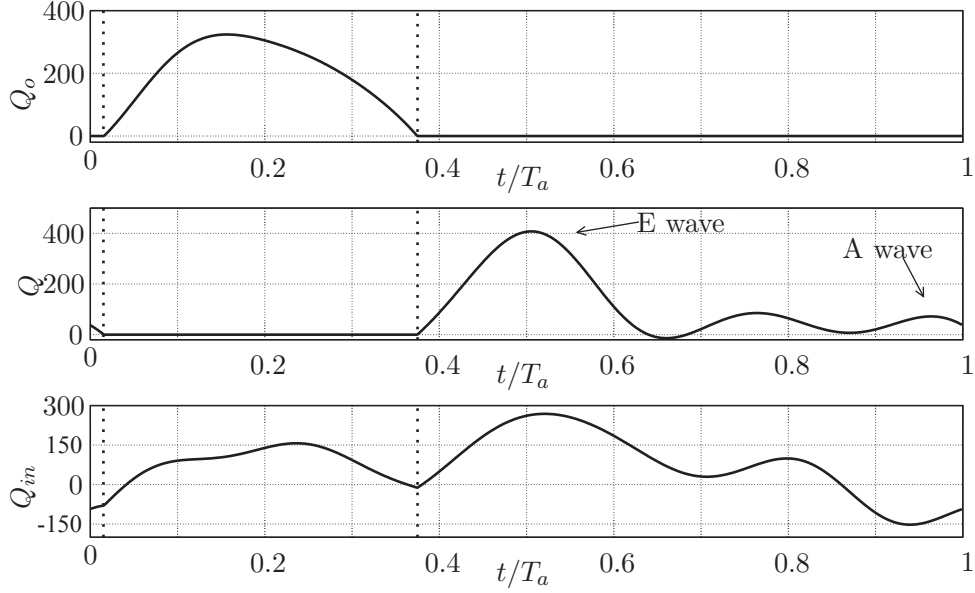


Figure 6.2: Flow rates (in $\text{mL}\cdot\text{s}^{-1}$) at the aortic valve (top plot), mitral valve (middle plot) and the total heart inflow (bottom plot) imposed at the pulmonary veins during the heart cycle. Vertical dotted lines mark the limit between the systolic phase (t/T_a between 0.015 and 0.375) and the diastolic phase. The E wave and the A wave are indicated on the mitral flow.

Element	U_{max}	$D = 2\sqrt{\frac{A}{\pi}}$	Re_{max}	t_m/T_a
AV	$0.96 \text{ m}\cdot\text{s}^{-1}$	2.20 cm	5300	0.16
MV	$1.08 \text{ m}\cdot\text{s}^{-1}$	1.87 cm	5000	0.52
Pulm. vein	$0.79 \text{ m}\cdot\text{s}^{-1}$	1.00 cm	2000	0.52

Table 6.1: Main flow characteristics describing the simulation. The section-averaged maximum velocity over the cardiac cycle is indicated as U_{max} . The maximum Reynolds number Re_{max} is based on the mean diameter D ($D = 2R_a = 2\sqrt{ab}$) and maximum velocity U_{max} . Time when the Re_{max} is reached is reported as t_m/T_a .

Table 6.1 recalls the maximum velocity magnitude and the maximum Reynolds number for different locations in the heart model: pulmonary veins, mitral valve and aortic valve.

6.1.4 Data reduction

Using the framework described before, 70 cardiac cycles were simulated and phase-average were gathered over the last $n=50$ cycles. The phase average over n cardiac cycles of a generic variable G is defined as,

$$\langle \mathbf{G} \rangle(\mathbf{x}, t) = \frac{1}{n} \sum_{k=0}^{n-1} \mathbf{G}(\mathbf{x}, t + kT), \quad (6.2)$$

where \mathbf{x} denotes the spatial coordinates and t is time. Deviation from this averaged is computed as,

$$g = G - \langle G \rangle. \quad (6.3)$$

The phase average $\langle G \rangle$ represents the time-varying deterministic part of the flow while a (turbulent) fluctuations are represented by the deviation g . Finally, the root mean square (r.m.s.) value \mathbf{g}_{rms} is defined as,

$$\mathbf{g}_{rms}(\mathbf{x}, t) = \sqrt{\langle \mathbf{G}^2 \rangle(\mathbf{x}, t) - \langle \mathbf{G} \rangle^2(\mathbf{x}, t)}. \quad (6.4)$$

Note that the $\bar{\cdot}$ denoting the filtered velocity and pressure fields is removed in the remainder of the chapter for sake of simplicity.

6.2 Data convergence

In order to get precise local information on the velocity signal, the numerical domain was seeded by Eulerian probes. Ten probes p_i , $i = 1, \dots, 10$ were selected over a virtual path that a red blood cell can follow, from one pulmonary vein (one of the four inflows) to the outlet, at the aorta. The second plot of Fig 6.1 shows the location of these probes. The ten selected probes provide one velocity signal near the RSPV ostium (p_1 position), four signals in the left atrium (p_2 to p_5), four signals in the left ventricle (p_6 to p_8 with one probe just beneath the aortic valve: p_9) and one in the ascending aorta (p_{10}). These probes will be used to analyse the flow. They are used here to observe the data convergence.

Figure 6.3 shows velocity data for three probes: p_3 , p_5 and p_7 . The top plot displays data on probe p_3 at $t/T_a = 0.65$. The middle plot and the bottom plot display data from probe p_5 at $t/T_a = 0.9$ and p_7 at $t/T_a = 0.65$, respectively. For the three plots, solid lines represent the phase-averaged velocity magnitude computed using n_c cycles, n_c being set from 1 to the total number of cycles used for data averaging, which is 50. The dots represent the instantaneous velocity magnitude for the n^{th} cycle. All the velocities are nondimensionalised by the reference velocity u_a (as a remainder: $u_a = 0.1 \text{ m.s}^{-1}$).

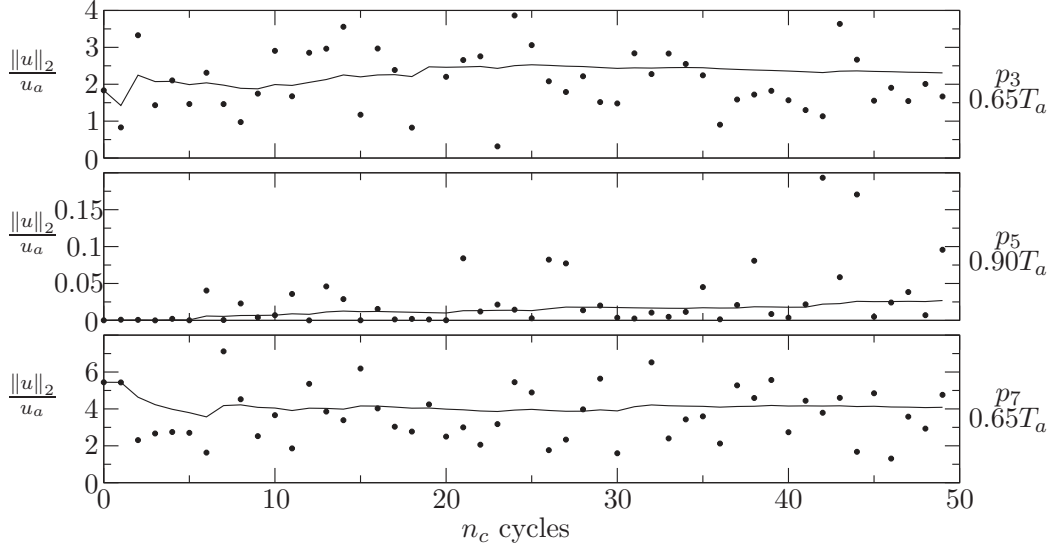


Figure 6.3: Solid lines represent the phase averaged velocity magnitude at probes locations using n_c cycles. The dots represent the instantaneous velocity magnitude for the n^{th} cycle. Top, middle, bottom plots represent data from probe p_3 at $0.65T_a$, p_5 at $0.90T_a$ and p_7 at $0.65T_a$ respectively.

For all the three signals, the maximum velocity difference for the last five phase-averaged values (δ_a) is compared to the maximum max velocity difference for the instantaneous velocity (δ_i). These differences are defined for a velocity u as $\delta(u) = \max(u) - \min(u)$. Considering probe p_3 at $t/T_a = 0.65$, differences are $\delta_i = 5.12 u_a$ and $\delta_a = 0.05 u_a$. For probe p_5 , at $t/T_a = 0.90$, differences are $\delta_i = 0.19 u_a$ and $\delta_a = 0.002 u_a$. In the ventricle, at probe p_7 and at $t/T_a = 0.65$, differences are $\delta_i = 7.3 u_a$ and $\delta_a = 0.04 u_a$.

For all the probes and all the times considered, high instantaneous fluctuations are observed. Still, the averaged velocity using 50 cycles shows δ differences of two orders of magnitude smaller than the instantaneous velocity amplitudes. The same behaviour were observed on other probes in the numerical domain. Thus, this convergence study shows that the number of simulated cycles is sufficient to analyse at the phase-averaged velocity.

Figure 6.4 shows probes data for the fluctuating energy of the third velocity component. The top plot displays data from probe p_3 at $t/T_a = 0.65$, bottom plot displays data from probe p_7 at $t/T_a = 0.65$. For the three plots, solid lines represent the turbulence kinetic energy computed using n_c cycles. n_c being set from 1 to the total number of simulated cycles, which is 50. The local turbulence kinetic energy along the x_3 direction is defined as:

$$k_3(\mathbf{x}, t) = \frac{1}{2} \langle u_3 u_3 \rangle. \quad (6.5)$$

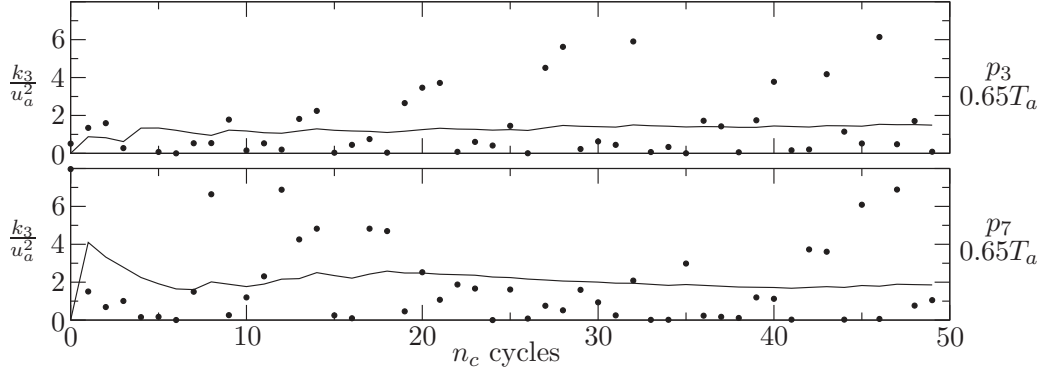


Figure 6.4: Solid lines represent the turbulent kinetic energy at probes locations using n_c cycles. The dots represent the instantaneous fluctuating energy for the n^{th} cycle. Top and bottom plots represent data from probe p_5 and p_7 at $0.65T_a$ respectively.

In the figure, dots represent the instantaneous kinetic energy k_3^i of the fluctuations for the third velocity component computed at the n^{th} cycle. This energy, for cycle n_c is defined as

$$k_3^i(\mathbf{x}, t) = \frac{1}{2}(u_3^{n_c} - \langle U \rangle), \quad (6.6)$$

$\langle U \rangle$ being the average third velocity component computed with the 50 cycles and $u_3^{n_c}$ the third velocity component for cycle n_c . All energies are nondimensionalised by the squared reference velocity u_a^2 .

For both signals, the maximum energy difference for the last five phase-averaged values (δ_a) is compared to the maximum energy difference for the instantaneous velocity (δ_i). Considering probe p_3 at $t/T_a = 0.65$, the differences are $\delta_i = 8.0 u_a^2$ and $\delta_a = 0.1 u_a^2$ while they are $\delta_i = 7.9 u_a^2$ and $\delta_a = 0.17 u_a^2$ for probe p_7 .

For both probes, the energy computed using 50 cycles shows δ differences of almost two orders of magnitude than the instantaneous energy differences. The same behaviour is observed on other probes in the numerical domain. This convergence study thus indicates that the number of simulated cycles is sufficient to provide quantitative data regarding velocity fluctuations.

6.3 Results

6.3.1 Temporal evolutions

Fifty cardiac cycles were simulated and phase-averaged, in order to provide a clear view of the flow organization over the cardiac cycle. A detailed flow description can be found in the last chapter; only the main flow characteristics are recalled here. The phase-averaged flow field is displayed over a cutting-plane through the left heart (see Fig. 6.1

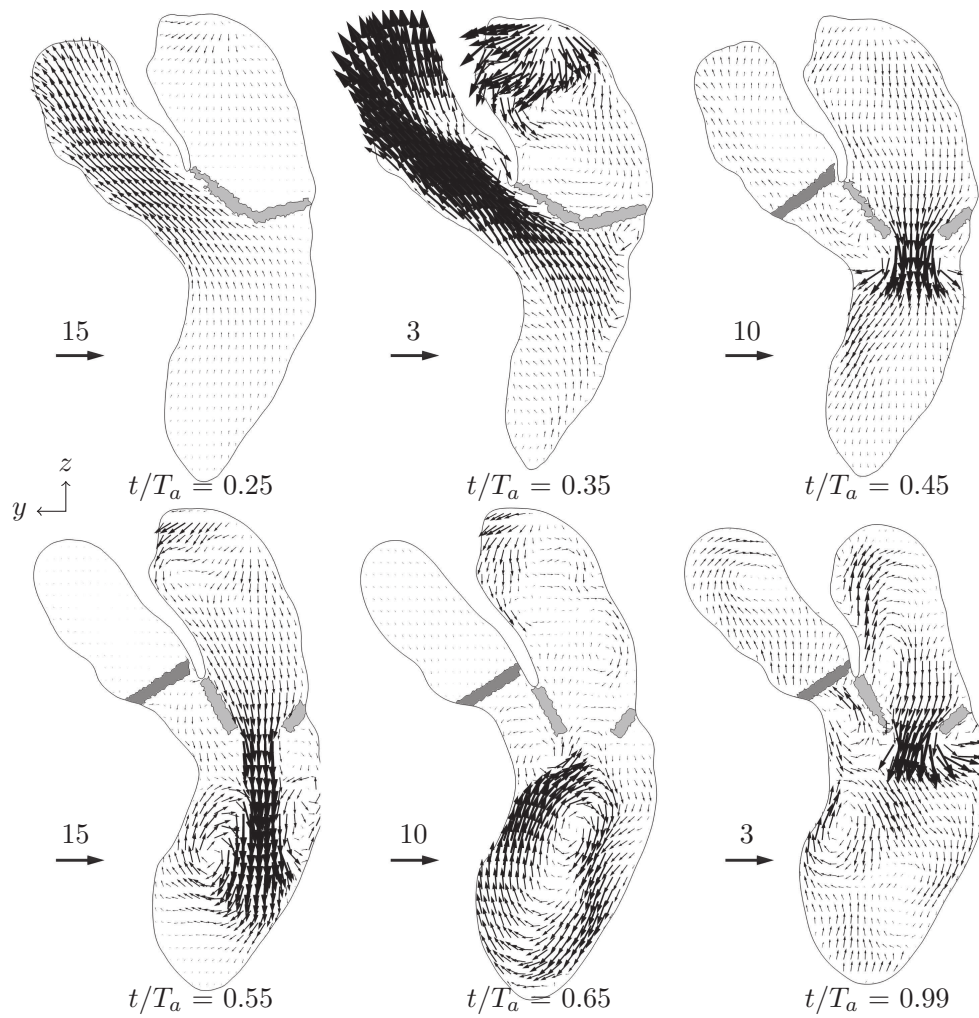


Figure 6.5: Phase-averaged non-dimensional velocity field ($\langle U_i \rangle / u_a$) over a cutting-plane through the left heart (see Fig. 6.1 for the position of the plane). The velocity vector scale is not constant through the heart cycle and is indicated for each plot. The mitral valve is depicted in light grey and the aortic valve in dark grey.

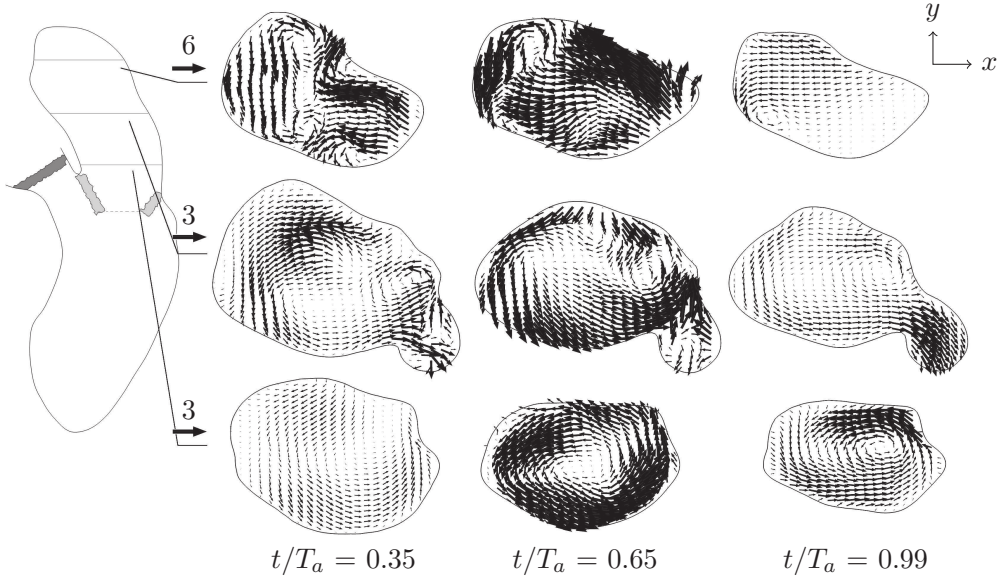


Figure 6.6: Phase-averaged non-dimensional velocity field ($\langle U_i \rangle / u_a$) over cutting-planes through the left atrium. The velocity fields are projected through the plane indicated in the left figure. The scale is fixed row by row.

for the position of the plane) at six salient instants in Fig. 6.5. The six instants are the ventricular mid and end-systole ($t/T_a=0.25$ and $t/T_a=0.35$), the beginning, peak and end of the E wave (respectively $t/T_a=0.45$, 0.55 , 0.65) and the end of the A wave, just before the beginning of the next ventricular systole ($t/T_a=0.99$). In addition, Fig. 6.6 illustrates the atrial flow through three planes, positioned perpendicularly to the plane of Fig. 6.5. The velocity field is scaled for both figures by $u_a = \dot{q}l_s/V_s = 0.1 \text{ m}\cdot\text{s}^{-1}$ where $\dot{q}=7.50 \times 10^{-5} \text{ m}^3\cdot\text{s}^{-1}$ is the cardiac output, $V_s = 5.55 \times 10^{-5} \text{ m}^3$ is the end systolic volume and $l_s=7.40 \times 10^{-2} \text{ m}$ is the ventricle length at the end of systole. Note that due to the strong velocity variations along the cycle, the vector scale was adapted for each instant displayed. Note also that, as stated in the last chapter, the global flow behaviour does not suffer major changes compared to the LES using the dynamic Smagorinsky model. Only the recirculating cell at $0.99T_a$ changed of position sufficiently to necessitating a slight change of the slice position to capture the velocity structure.

During systole, the mitral valve is closed (in light gray in Fig. 6.5), preventing backflow towards the atrium, while the aortic valve is open (in dark gray in Fig. 6.5). During this phase, the decrease of the ventricle volume causes ejection of blood into the aorta while inflowing jets are entering and colliding in the upper atrium part. As the atrium volume increases, high velocity magnitude is observed in upper part of the cavity during the entire systole. The computed flow at mid-systole ($t/T_a=0.25$) in the atrium is highly swirled, as reported *in vivo* [90, 109]. This movement is captured by the computation but is hardly discernible in Fig. 6.5, because the vortical movement is

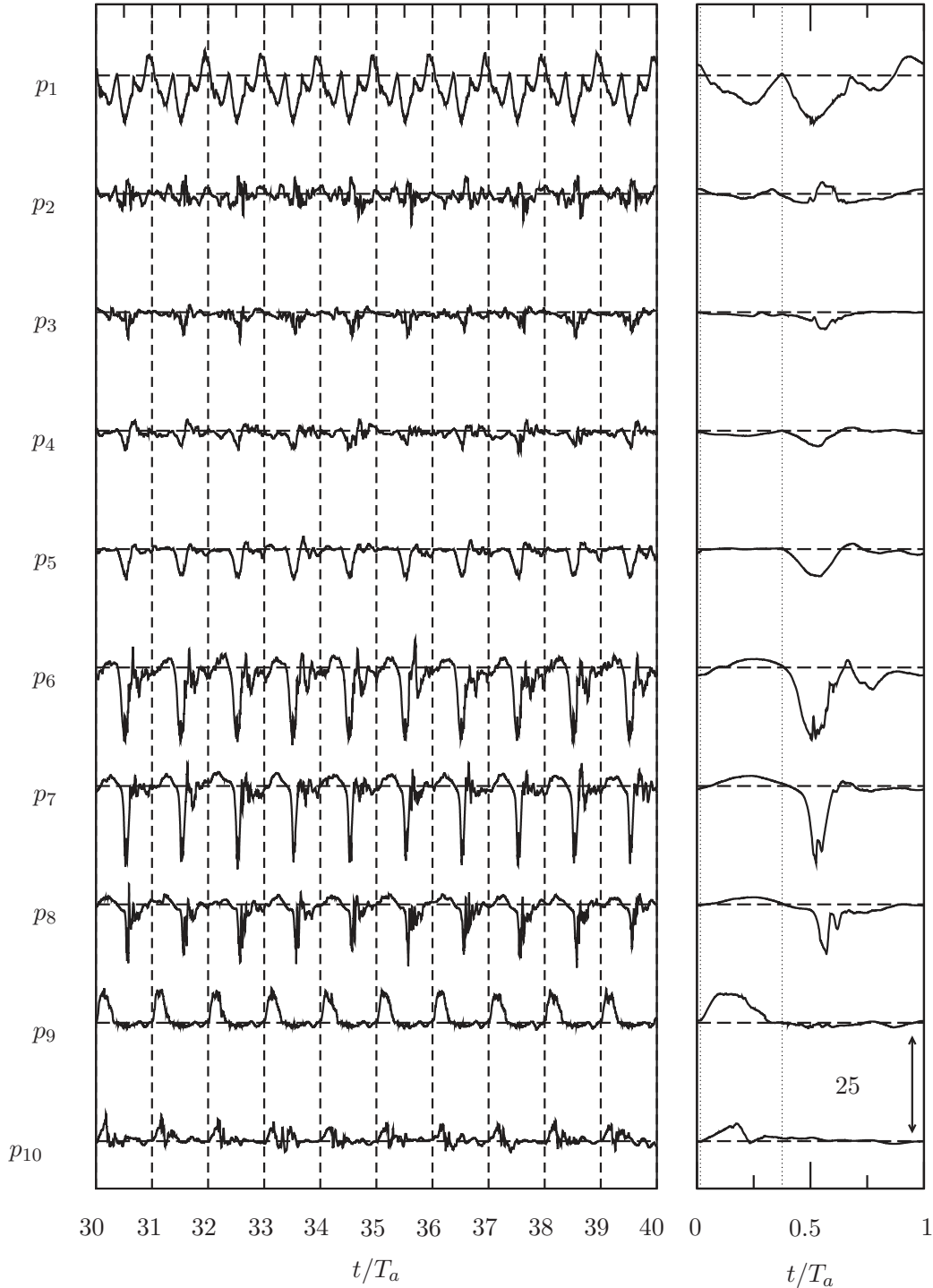


Figure 6.7: Left: time history of normalized vertical velocity U_3/u_a over 10 of the 50 cycles used for phase-averaging for the 10 probes studied. Right: phase-averaged of normalized vertical velocity $\langle U_3 \rangle / u_a$ at the same 10 points. The vertical dotted line delimits the systolic phase from the diastolic phase at $t/T_a = 0.375$.

perpendicular to the cutting plane. A better view of this feature is found in Fig. 6.6. The vortical movement is clearly visible in the lower cutting-plane, above the MV at $t/T_a=0.35$. A more disturbed flow, resulting from the complex interactions between the four pulmonary vein jets entering the atrium, is visible on the two upper cutting-planes in Fig. 6.6.

The systolic phase just described can be observed from another point of view thanks to the probes placed in the domain. Figure 6.7 shows the normalized vertical velocity signal U_3 over 10 cardiac cycles and the vertical velocity phase-averaged $\langle U_3 \rangle$ over 50 cardiac cycles at the ten probes positions described in section 6.1.1 (Fig. 6.1). The signal at probe p_1 located in the RSPV and shown in Fig. 6.7, is very similar (with opposite sign) to the inlet flow rate signal, as expected. This signal repeats itself with minor disturbances during the 10 presented cycles, as shown by the left plot in Fig. 6.7, suggesting laminar flow at this position. At positions p_2 to p_5 , the phase-averaged vertical velocity $\langle U_3 \rangle$, right plot in Fig. 6.7, remains small, expressing the average planar flow motion, perpendicularly to the vertical heart axis. Instantaneous velocities tend to be less and less prone to rapid fluctuations when observing the signals from top to bottom locations in the atrium. The large fluctuations are visible in the inflow jets collision region, while a more quiescent flow is present in the lower part of the LA. In the ventricle region, probes p_6 to p_8 show repeatable instantaneous signals, although with high-frequency fluctuations sometimes superimposed (see for position p_6 : cycles number 32, 34, 38 or 39, for example), suggesting a transition to turbulence. The phase-averaged velocities at these positions (located under the aorta) are positive during systole, because of the upward motion through the aorta. Probe p_9 measures an instantaneous signal with high-frequency fluctuations at peak-systole while the phase-averaged velocity has a similar shape as the outlet flow rate profile; positive velocity is observed during the major part of systole. Finally, probe p_{10} has a velocity peak during the peak systole. The averaged velocity then decreases to almost zero and the signal shows some fluctuations after this.

At $t/T_a=0.375$ (not shown in Fig. 6.5), the aortic valve closes and the mitral valve opens: the ventricle diastole starts. The LV volume increases and blood passes from the LA to the LV, forming a strong jet through the MV. The shear layer between the jet generated during the E wave and the surrounding quiescent fluid in the LV rolls up (see Fig. 6.5 at $t/T_a=0.45$) and shapes the jet head as a vortex ring, as classically reported [43, 95, 116]. The E wave vortex ring signature and its evolution are visible in Fig. 6.5 at $t/T_a=0.55$. Then, the mean flow rearranges itself as a large recirculating cell, clearly visible in the LV at $t/T_a=0.65$ (Fig. 6.5, bottom center). During the same time, a recirculating cell perpendicular to the observed plane of Fig. 6.5 is visible in the lower part of the atrium (see Fig. 6.6). This structure lasts until the end of diastole. The upper part of the atrium has a less organised flow structure, but a recirculation is visible on the right of the plane. During the A wave, occurring at $t/T_a=0.99$ (Fig. 6.5, bottom right), the blood flux passing through the MV strengthens the recirculating cell

in the LV as classically reported as well [137].

The diastolic phase just described is now observed through the local velocity at the different signals probes (see Fig. 6.7). Right from the beginning of the ventricular diastole ($t/T = 0.375$), an immediate amplification of the disturbances is visible in the atrium on the instantaneous signals, for p_2 and p_3 . Fluctuations are more and more visible, reaching their maximum between $t/T_a = 0.55$ and 0.75 . Then, the p_2 signal always shows strong disturbances while p_3 stays flat. The signal of probe p_4 shows little fluctuations and p_5 measures intermittent low fluctuations, as in cycle 35 or 39 suggesting a flow configuration on the onset of turbulent transition. In the atrium, blood is directed towards the MV at this time and the phase-averaged velocity signal of probes p_3 , p_4 and p_5 show its spatial acceleration: velocity magnitude is more and more important in direction of the LV during the first half of the diastole ($t/T_a \sim 0.5$), promoting a more laminar flow than in the upper part of the LA.

In the ventricle during diastole, high fluctuations are reported. The passage of the E wave jet vortex ring is clearly visible in the phase-averaged velocity signals, shown by high negative velocity at probes p_6 , p_7 and p_8 . Interestingly, the A wave velocity is only visible at location p_6 , through negative velocity around $t/T_a = 0.75$, while the signal at p_7 is almost flat. Thus, the A wave vortex ring travels less than $2 R_a$ in the ventricle, consistently with the weak A wave showed in section 6.1.3. As described before, the E wave vortex ring hits the lateral wall at $t/T = 0.55$. The subsequent generation of small eddies corresponds to an intense growth of the fluctuations. The instantaneous signal at probes p_6 , p_7 and p_8 show high-frequency fluctuations repeated from cycle to cycle suggesting a turbulent phase accompanying the jet breakdown. In the aorta at probes p_{10} , fluctuations can be observed in the instantaneous signal as the flow velocity decreases. These fluctuations are observed at each cycle while the phase-averaged velocity is near zero.

The fluctuations observed on the probes are sufficiently intense to sometimes alter the flow field in a visible way. Figure 6.8 shows instantaneous velocity flows of the last two successive cycles (Fig. 6.8a and Fig. 6.8b) at $t/T = 0.65$ as well as the phase-averaged velocity field at the same instant (Fig. 6.8c). Large-scale fluctuations are observable both in the atrium and the ventricle while a clean ventricle recirculating cell is only retrieved after phase-averaging.

6.3.2 Kinetic energy

Volumetric kinetic energy

The volumetric turbulent kinetic energy k^V and the volumetric mean flow kinetic energy K^V are defined as:

$$k^V(t) = \frac{1}{2V(t)} \int_{V(t)} \langle u_i u_i \rangle dV, \quad (6.7)$$

$$K^V(t) = \frac{1}{2V(t)} \int_{V(t)} \langle U_i \rangle \langle U_i \rangle dV, \quad (6.8)$$

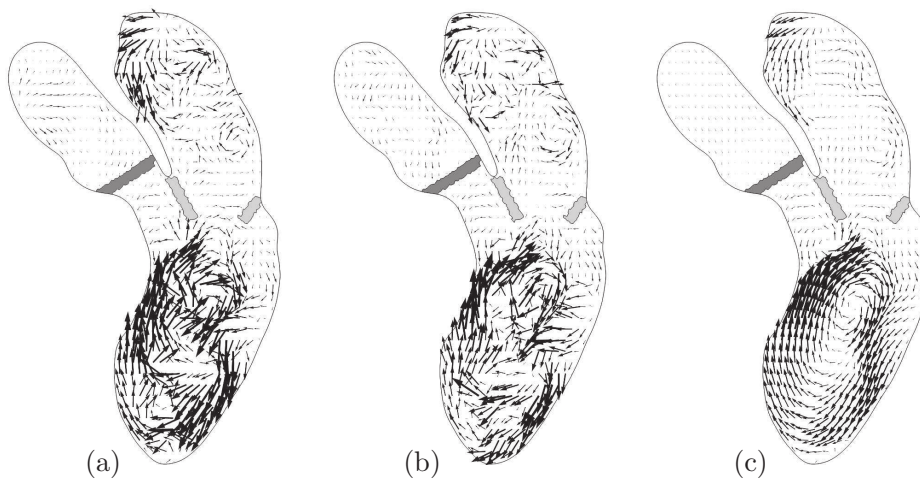


Figure 6.8: Left and middle plot: instantaneous non-dimensional velocity fields at $t/T = 0.65$. Right plot: phase-averaged non-dimensional velocity field at $t/T = 0.65$. Mitral

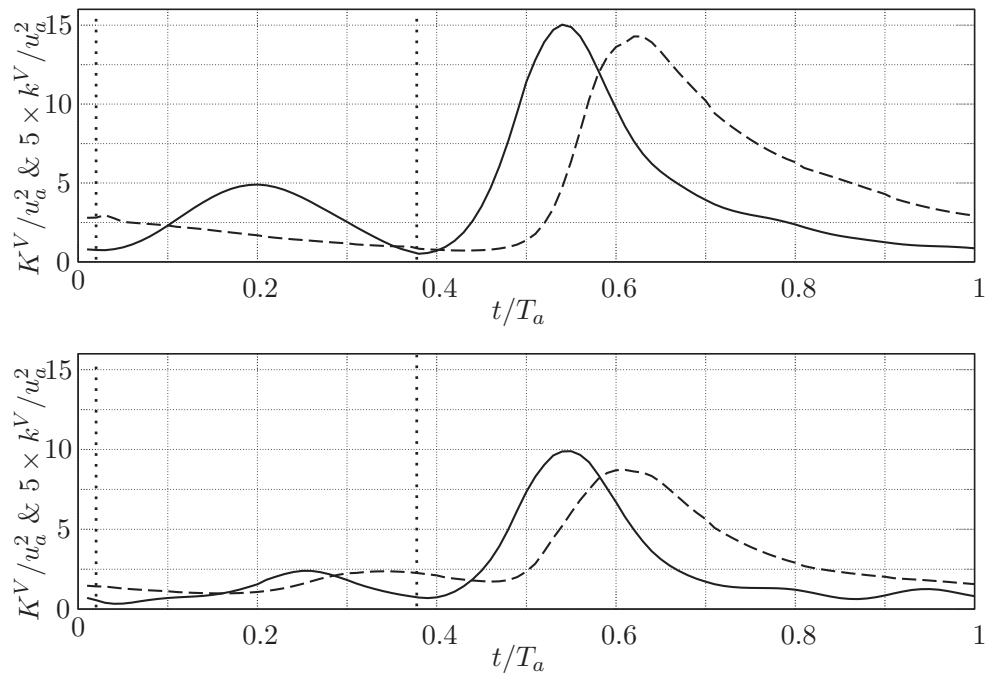


Figure 6.9: Volumetric mean flow kinetic energy K^V (full line) and five times the turbulent kinetic energy k^V (dashed line) in the left ventricle (top plot), and in the left atrium (bottom plot). The energies are nondimensionalised by u_a^2 . The vertical dotted lines delimit the systolic phase and the diastolic phase.

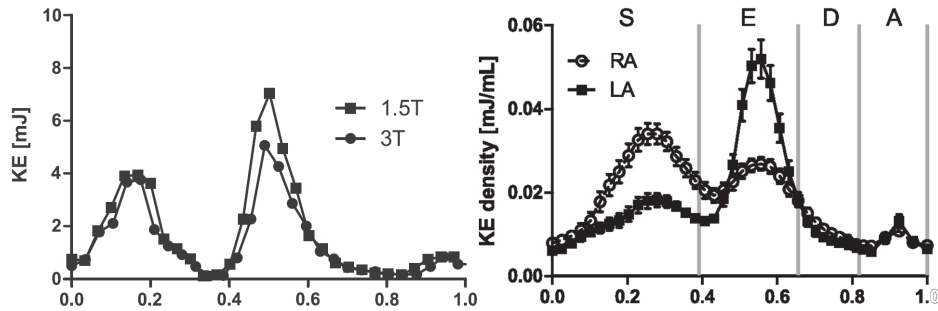


Figure 6.10: Left, kinetic energy measurements in healthy left ventricles using MRI (from [25]). Right, kinetic energy measurements in healthy left atria using MRI (from [9]).

with $V(t)$ being either the volume of the ventricle or of the atrium at time t . Figure 6.9 shows how these energies evolve over the heart cycle, both in the ventricle (top plot) and the atrium (bottom plot). The volumetric turbulent kinetic energy includes all the cycle-to-cycle fluctuations. Note that $5k^V$ is plotted, so that the same scale is used to represent both energies.

The mean flow kinetic energy evolves similarly in both cavities. During the systolic phase (t/T_a between 0.015 and 0.375), it increases and reaches a peak at $t/T_a=0.20$ in the ventricle, 0.255 in the atrium. After a decrease just before the beginning of diastole, the mean flow kinetic energy increases again and reaches a peak at $t/T_a=0.54$, viz. $0.04T_a$ after the peak of the E wave for both cavities. The maximum value of K^V corresponds to the presence of high velocities when blood flows from the atrium to the ventricle. It is three times (resp. four times) higher than the systolic peak in the ventricle (resp. atrium).

Carlsson *et al.* [25] have reported similar behaviour during the heart cycle, thanks to MRI. The same can be said for the atrial kinetic energy, the present results comparing well with the results from Arvidsson *et al.* [9]. Figure 6.10) displays the results from Carlsson *et al.* and Arvidsson *et al.*. Leaving aside our nondimensionalization for an instant, the ventricle mean flow kinetic energy peak for the presented case is 5.2 mJ for systole (Arvidsson *et al.* measured 4 mJ), and 16.7 mJ for diastole (Arvidsson *et al.* measured values from 5 to 7 mJ). The systolic peak value is remarkably close and it is not surprising that the peak diastole is two to three times higher as *heart A* suffers restrictive filling.

The ventricular turbulent kinetic energy k^V remains small, then decreases during the systolic phase, due to the stabilizing effect of the flow acceleration. In diastole it increases substantially, reflecting the amplification of the disturbances after the jet impingement on the lateral ventricle wall. The turbulent energetic peak is reached $T_a/10$ after the peak of mean flow kinetic energy, corresponding to the convection time of the vortex ring. This instant corresponds to the decelerating phase of the flow. The

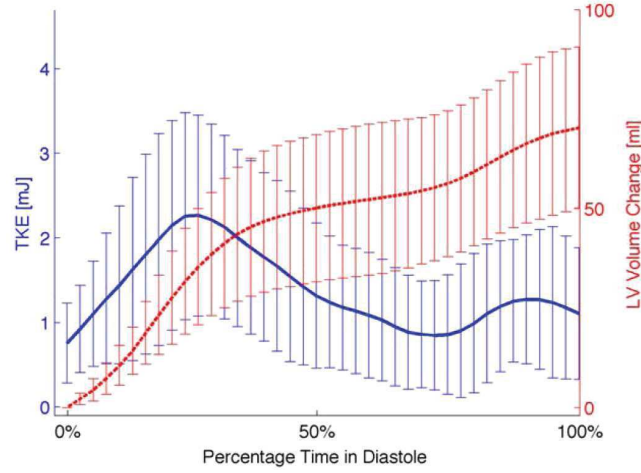


Figure 6.11: TKE (blue solid line) and LV volume change (red dashed line) over diastole (mean \pm SD) for 11 healthy subjects using MRI (from [185]).

turbulence intensity k^V/K^V in the ventricle is as high as 37 % during the k^V peak. The peak of turbulent energy is found during the deceleration of the E wave as found by Domenichini *et al.* [44] in an idealized ventricle. The same observation was made by Zajac *et al.* [185] and the same order of magnitude is found for the turbulent energy levels. Figure 6.11 displays measurements from Zajac *et al.* [185] for healthy ventricle. Leaving aside our nondimensionalization for an instant, the ventricle mean turbulent kinetic energy peak in *heart A* reaches value of 3.6mJ. This value is higher but of the same order of magnitude from the values measured by Zajac *et al.*. Considering the strong E wave of *heart A*, this was expected.

The atrial turbulent kinetic energy behaves somewhat differently. It increases during the last half of the systolic phase, because of the interaction/collision of the four inflowing jets issuing from the pulmonary veins. A first peak is thus reached just before the beginning of diastole. Turbulence intensity then decreases during the flow acceleration through the atrium, as expected, so that k^V and K^V have an opposite evolution during early diastole. The atrial turbulent kinetic energy rises again at $t/T_a=0.47$ and reaches its peak at $t/T = 0.61$, during the flow deceleration. Compared to the diastolic k^V , the atrium peak occurs earlier and is twice less intense. Still, it corresponds to a large turbulence intensity of approximatively 30 %. As in the ventricle, the turbulent kinetic energy then decreases until the end of the heart cycle.

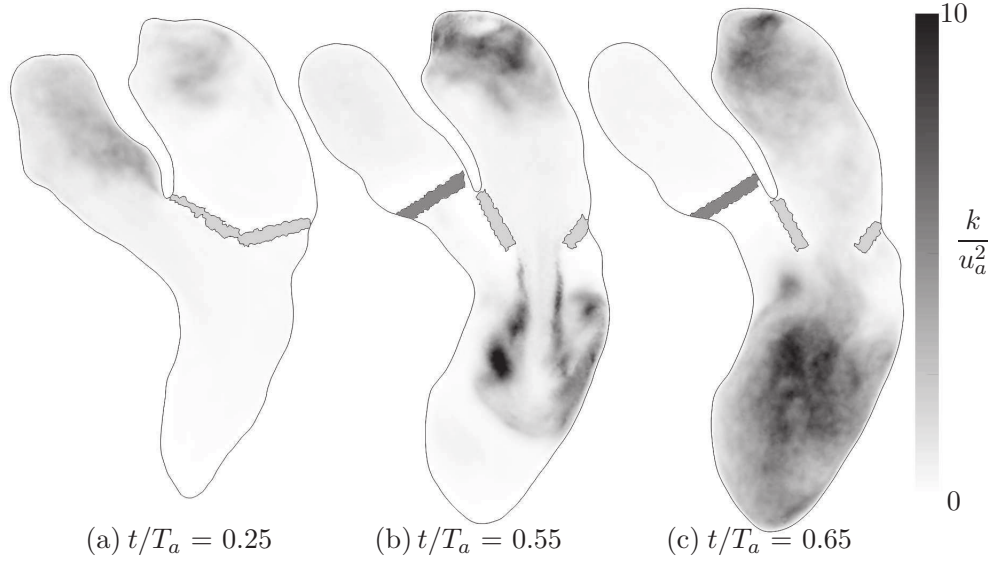


Figure 6.12: Nondimensional turbulent kinetic energy k/u_a^2 at three different times: $t/T_a = 0.25$ (a), $t/T_a = 0.55$ (b) and $t/T_a = 0.65$ (c).

Turbulent kinetic energy map

In order to provide a more detailed description of the turbulent nature of the intracardiac flow, maps of the local turbulence kinetic energy are shown. This energy is defined as:

$$k(\mathbf{x}, t) = \frac{1}{2} \langle u_i u_i \rangle. \quad (6.9)$$

Figure 6.12 displays the turbulent kinetic energy map at three salient instants $t/T_a = 0.25$, at the atrium systolic k^V peak, $t/T_a = 0.55$ at the E wave peak and at $t/T_a = 0.65$ when k^V is maximum in the ventricle.

The beginning of systole is associated with a relaminarization of the LV. The TKE intensity within the ventricle stays almost null during systole, as shown in Fig. 6.12 (a) at $t/T_a = 0.25$. The highest TKE levels are present in the root of the aorta between $t/T_a=0.25$ and 0.35 . Note however that the levels downstream of the AV may be mispredicted here, due to the absence of AV leaflets modelling when the AV is open. Meanwhile, fluctuations are increasing in the upper half of the LA (up to $6 u_a^2$) where the inflowing jets collide.

At the E wave peak at $t/T_a=0.55$, (Fig. 6.12, b), high TKE levels (about $8 u_a^2$) are observed in the jet edge, which becomes increasingly unstable throughout the MV flow deceleration (until $t/T_a=0.65$). Furthermore, TKE levels of the same order are visible at the lateral wall. As shown by the TKE field at $t/T_a=0.55$, the impact of the vortex ring on the lateral wall is a zone of high velocity fluctuations. High energy values are observable in the centre of the LV, up to $10 u_a^2$. At the same time, the E wave starts to decrease.

At $t/T_a=0.65$ (right plot in Fig. 6.12), the flow rate through the mitral valve is close to zero. However, the flow in the ventricle is far from quiescent; the volumetric TKE in the ventricle is maximum, as shown in Fig. 6.9. The mitral jet impact has made the initial vortex ring shatter into small vortices that occupy the main part of the ventricle. In accordance with this transition to turbulence, the TKE field shows high values over almost the whole ventricle. The largest values of TKE (from 7 to $10 u_a^2$) are observed at the core of the recirculating cell. These high values of energy are due to the differences in the position of the recirculating cell center between cycles, as reported before in the similar configuration of a in-cylinder engine flow [46]. The TKE in the LA also indicates that the pulmonary jets impact in the upper part of the LA is associated with intense velocity fluctuations from one cycle to another. The energy levels are about three times lower in the lower half of the LA. This ratio of TKE between the upper and bottom halves of the LA remains approximately constant during the entire heart cycle.

Local turbulent kinetic energy

Figure 6.13 shows the phase-averaged time evolution of the three components of r.m.s. velocity and the turbulent kinetic energy k at the ten probes $p_1 - p_{10}$ (see Fig. 6.1 for the probes location).

Probe p_1 is the one with the smallest velocity fluctuations and TKE levels, with velocity r.m.s. values less than $0.7 u_a$ and negligible the TKE levels during the whole cardiac cycle. Probe p_2 displays low r.m.s. velocity values, of the order u_a during systole and maximum levels of about $3 u_a$ for the x and z directions during diastole. The y direction has r.m.s. velocity twice lower. This is because of the flow direction at this location, the probe location being in the RSPV inflowing jet which lies in the xz plane. The TKE at this location is as high as $8 u_a^2$, at around $t/T_a = 0.6$ which corresponds to the beginning of diastole. This high value is caused by the high flow rate coming in the atrium at this time. Probes p_3 , p_4 and p_5 show similar r.m.s. velocity magnitudes for the three spatial directions. The TKE values decreases from p_3 to p_5 , the probes being further and further from the most turbulent region in the atrium (the upper half).

In the ventricle, probes p_6 , p_7 and p_8 present high r.m.s. values (about $3 u_a$) in the three directions and high TKE values (about $10 u_a^2$) during diastole. Interestingly, at $t/T_a = 0.55$, there is a sharp amplification of the turbulent energy levels at p_7 and p_8 , caused by the vortex ring hitting the lateral wall. At these locations, the levels decrease after $t/T_a = 0.65$. On the contrary, at probe location p_6 , a sharp increase of the turbulent energy level is measured and reaches its peak at $t/T_a = 0.7$. This is explained by the necessary time for the turbulence to be transported from its zone of production (the bottom of the LV) to the p_6 probe location.

Probe p_9 shows maximum r.m.s. velocity values of $0.7 u_a$ and quasi null values during systole where flow acceleration creates a very laminar unidirectional flow (see Fig. 6.8). At probe location p_{10} , velocity fluctuations resulting from the instability of the shear layer created at the aortic valve annulus are visible (see Fig. 6.12). Energy

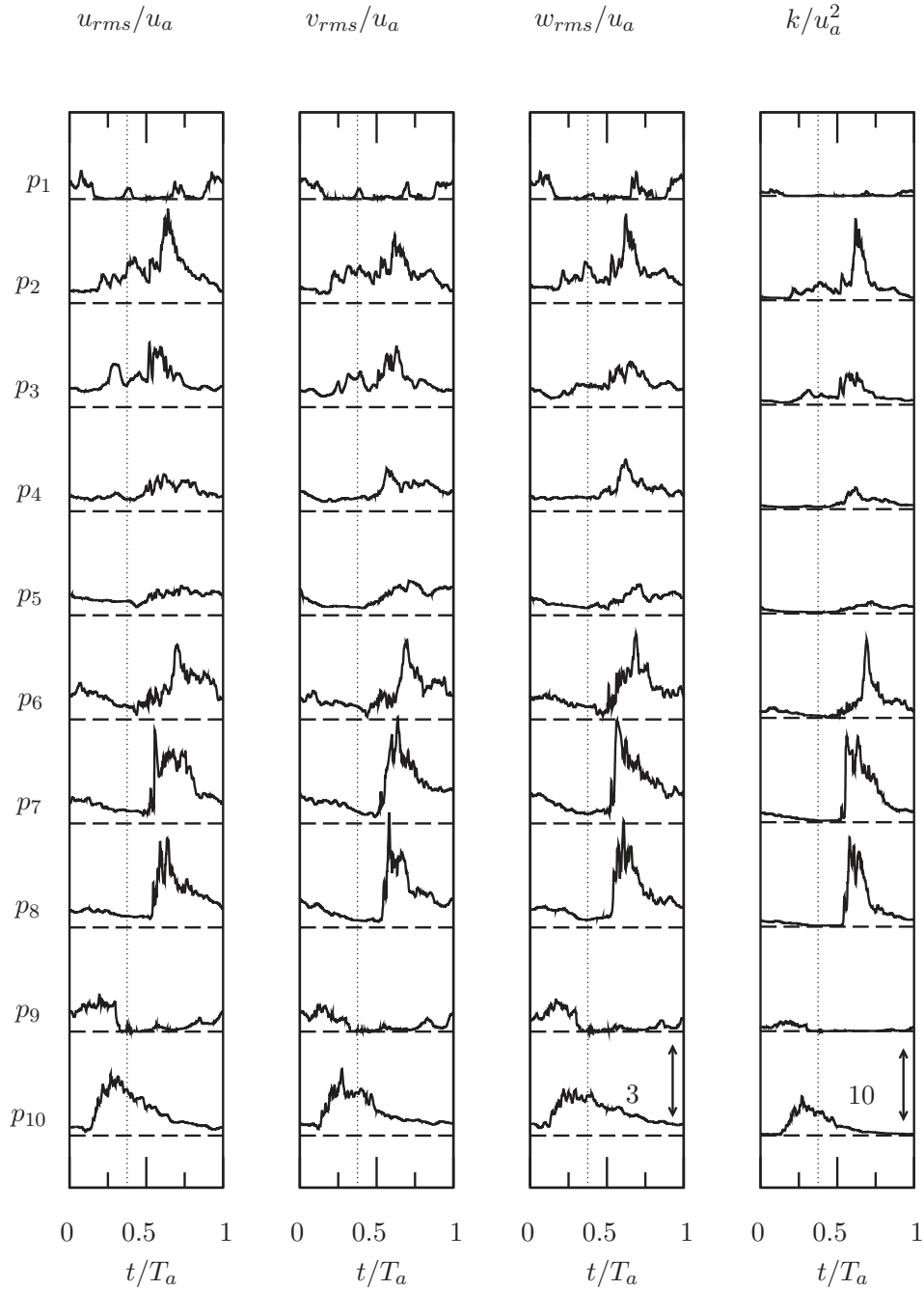


Figure 6.13: Left plots: time evolution of the r.m.s. of the 3 velocities components, nondimensionalised by u_a . Right plot: turbulent kinetic energy nondimensionalised by u_a^2 over the cardiac cycle at the ten probes p_1 to p_{10} . The vertical dotted line marks the limit between the systolic phase and the diastolic phase at $t/T_a = 0.375$.

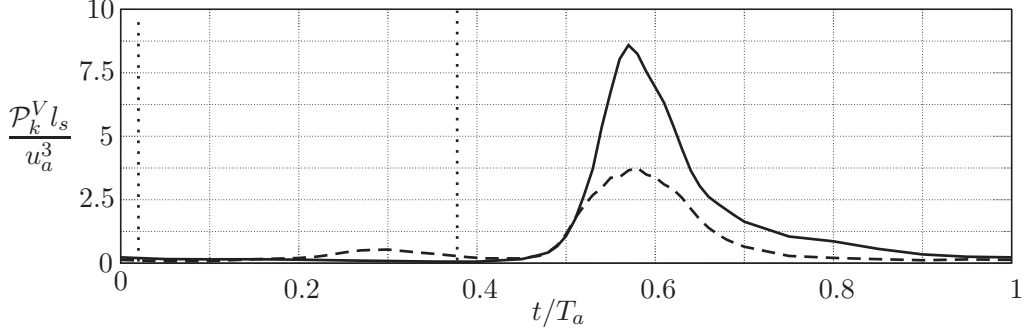


Figure 6.14: Volume-averaged production of turbulent kinetic energy \mathcal{P}_k^V in the ventricle (solid line) and in the left atrium (dashed line). Productions are both nondimensionalised by u_a^3/l_s . Vertical dotted lines mark the limit between the systolic phase (t/T_a between 0.015 and 0.375) and the diastolic phase.

level remains moderate, reaching a maximum of $4 u_a^2$ at $t/T_a = 0.25$.

6.3.3 Production of turbulent kinetic energy

In what follows, production fields of the turbulent kinetic energy are presented and discussed. The turbulent production \mathcal{P}_k gives the rate at which energy is extracted from the mean motion to feed the fluctuations and is defined as

$$\mathcal{P}_k(t) = -\langle u_i u_j \rangle S_{ij}. \quad (6.10)$$

This term is integrated over the ventricle and over the atrium to obtain a volume-averaged production of turbulent kinetic energy defined as

$$\mathcal{P}_k^V(t) = -\frac{1}{V(t)} \int_{V(t)} \langle u_i u_j \rangle S_{ij} dV, \quad (6.11)$$

with $V(t)$ the volume of the ventricle or the atrium at time t . Figure 6.14 shows the volumetric production of turbulent kinetic energy \mathcal{P}_k^V in the two cavities nondimensionalised by u_a^3/l_s . Remarkably, the TKE production in the ventricle is essentially concentrated in the first half of the diastole. From the time when the E wave jet enters in the ventricle cavity to some instants after the impingement of the jet, the production \mathcal{P}_k^V rises until its peak at $t/T_a = 0.57$. Thus, in the ventricle the turbulence described in the former section comes from the E wave jet and its loss of coherency. The production decreases during all the remaining time of diastole. The production is virtually null during the whole systole.

The atrium cavity sees non-zero production at two instants. During diastole, the production level rises to reach its peak around $t/T_a = 0.58$ with a magnitude roughly twice smaller than the ventricle production peak, then decreases at a similar rate than the ventricle production. During systole, between $t/T_a = 0.2$ and 0.3 , low values of TKE

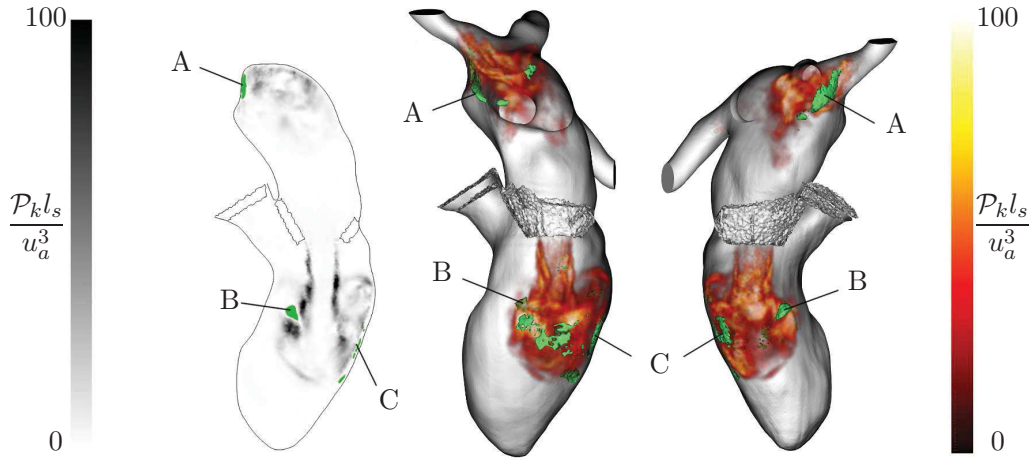


Figure 6.15: Production of turbulent kinetic energy \mathcal{P}_k nondimensionalised by u_a^3/l_s at $t/T_a = 0.55$. Left plot: production \mathcal{P}_k in the same plane in Fig. 6.1. Center and right plots: volume rendering of the non-dimensional TKE production \mathcal{P}_k on two different views. The mapping relating production magnitude with opacity is linear. Heart wall is made partially transparent to allow observation and the aorta was deleted as focus is on the LA and LV. On all plots, the three areas where $\mathcal{P}_k < 0$ are indicated by the letters A, B and C.

production in the atrium are observable, around ten times lower than the diastole peak. The mechanisms behind these productions during systole and diastole in the atrium for this heart are the collision and breaking of the inflowing jets coming from the pulmonary veins; the same mechanism occurs twice, as described in section 6.3.1, with different intensities. It is interesting to note that both atrial and ventricular production peaks occur at roughly the same time.

Figure 6.15 shows the production of turbulent kinetic energy \mathcal{P}_k in the heart at $t/T_a = 0.55$, which is close to the time when diastolic production peaks are reached in the atrium and in the ventricle. The left plot shows the production on the slice used in the previous sections. The center and right plots are three dimensional volumetric views of the turbulent kinetic energy production \mathcal{P}_k , from different points of view. The aorta was deleted on the three plots to ease the visualisation of other cavities as the focus is on the atrium and the ventricle cavities.

Production in the atrium comes from the collision of the inflowing jets. The area where the jets collide is visible in the three plots, in the upper half of the atrium. As seen for other turbulence quantities, large production values are also obtained in the shear layer of the trailing jet of the E wave vortex ring. Shear causes instabilities and high turbulence production, resulting in strong velocity fluctuations as described in section 6.3.2. Severe distortions of the jet seem to occur near the jet head where it hits the lateral wall accompanying large TKE production.

It is worth pointing out that it is often supposed that the TKE production is a pos-

itive quantity. However, regions with $\mathcal{P}_k < 0$ may exist. In other words, kinetic energy is transferred from the turbulent velocity fluctuations to the mean flow. This phenomenon has been observed in several investigations through numerical simulations [76] or experimental measurements [112]. In the present case, three locations show negative production. These regions are indicated by the capital letters A, B and C in Fig. 6.15 and their contours correspond to production iso-value of $-10 u_a^3/l_s$.

The regions A and C are close to the heart wall and correspond to jets impingement areas. This is a class of flows for which negative production has already been reported [65, 131]. Region A is the zone where the inflowing jet coming from the RIPV impacts the atrium wall. In the region C, mitral jet from the E wave impinges on the lateral wall. For this region, the negative production is visible in the area where the jet head touches the heart wall. In region B, negative energy production is observed, but there is no direct interaction with any solid boundary.

This phenomenon can be seen during short time windows; area A is visible for 8 % of the heart cycle between $t/T_a = 0.53$ and 0.61 ; area B is visible for only 3 % of the heart cycle between $t/T_a = 0.54$ and 0.58 ; area C is visible for 7 % of the heart cycle between $t/T_a = 0.53$ and 0.61 . Note that in terms of turbulence modeling, negative production would cause Reynolds-averaged Navier-Stokes (RANS) models to fail [26].

In the three regions, examination of the Reynolds stress tensor components in its eigenbasis shows high anisotropy. The turbulence is highly one dimensional; one eigenvalue value is at least one order of magnitude larger than the two others. In addition, large positive spatial gradients of the mean velocity are present, which contributes to the observed negative production.

6.3.4 Turbulence characteristics

The structure of turbulence is an interesting feature to study, as shown by the link between negative turbulence production and the turbulence anisotropy described in the last section. To study the structure of turbulence, the local Reynolds-stress anisotropy tensor

$$b_{ij} = \frac{\langle u_i u_j \rangle}{\langle u_k u_k \rangle} - \frac{1}{3} \delta_{ij}, \quad (6.12)$$

may be characterized by two invariants, considering that the trace b_{ii} vanishes by construction [102, 103]. They can be calculated from the anisotropy tensor terms by

$$\eta = \left(\frac{1}{6} b_{ij} b_{ji} \right)^{1/2}, \quad (6.13)$$

$$\xi = \left(\frac{1}{6} b_{ij} b_{jk} b_{ki} \right)^{1/3}. \quad (6.14)$$

For every locations in the numerical domain, at each instant during the heart cycle, the invariants ξ and η can be computed from the Reynolds tensor [141]. Any physically realizable state of the flow produces invariants ξ and η which lie in a triangular

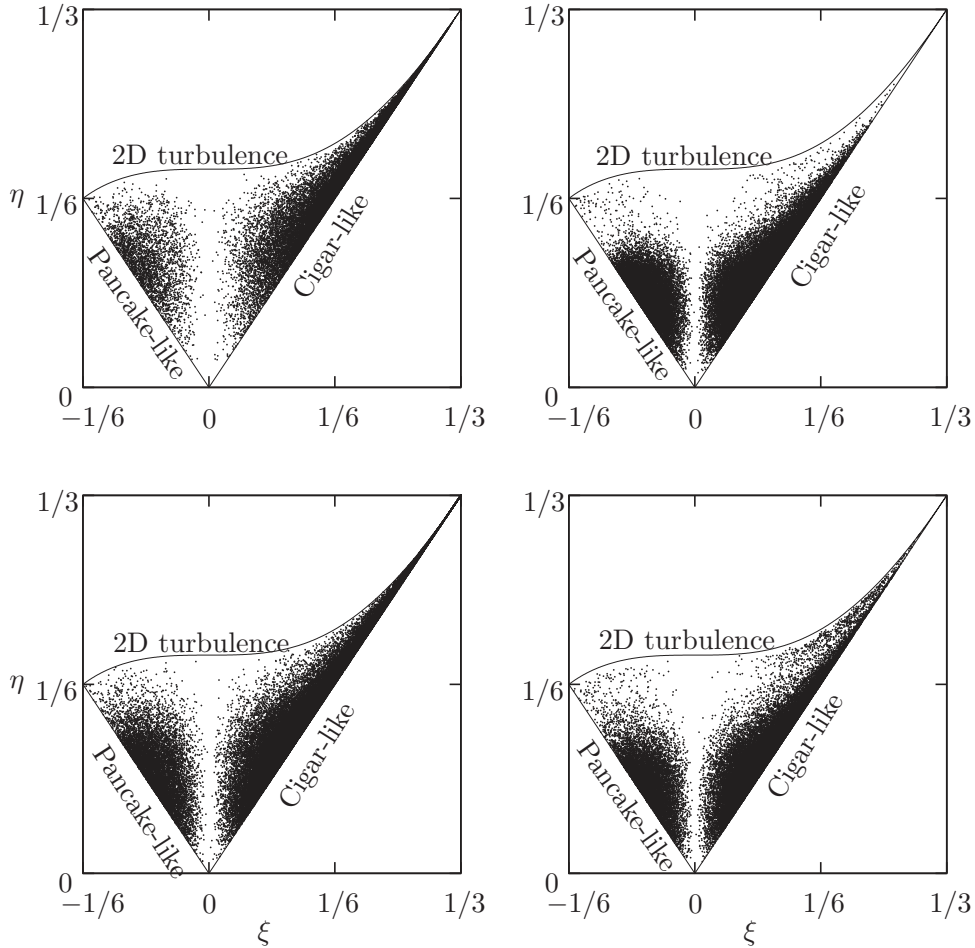


Figure 6.16: Lumley triangles at times $t/T_a = 0.5$ (left plots) and 0.7 (right plots) for the ventricle (top plots) and for the atrium (bottom plots).

domain in the $(\xi - \eta)$ -plane (see Fig. 6.16). This domain, commonly called the Lumley triangle, provides information about the Reynolds-stress character in a compact and graphical way [103]. Each border of this domain describes a specific character of the Reynolds-stress tensor. The upper line of the triangle corresponds to a two-dimensional turbulence. The right-hand corner of the triangle corresponds to a one-dimensional turbulence. The right-hand line to a "cigar-shaped" axisymmetric turbulence. The origin of the triangle ($\xi = \eta = 0$) corresponds to an isotropic turbulence and the left-hand line to a "pancake-shaped" axisymmetric turbulence. A detailed interpretation can be found in Simonsen *et al.* [159]. As a reminder, the different turbulent states are recalled in Fig. 6.16.

As proposed by Lumley, the invariants ξ and η can also be combined to produce an isotropy parameter,

$$I = 1 - 27(\eta^2 - 2\xi^3). \quad (6.15)$$

As the two invariants are null in isotropic turbulence, the parameter I is equal to 1.0 in this case. When the turbulence is two-dimensional or one-dimensional, the parameter I is zero, expressing the most anisotropic cases.

In the following, the turbulence within the heart is described using both the Lumley triangle and the isotropy parameter I . Figure 6.16 shows triangles for the ventricle domain (top plots) and the atrium domain (bottom plots) during diastole at $t/T_a = 0.5$ (left plots) and $t/T_a = 0.7$ (right plots). Only the data points with a TKE lying in the upper quartile of the data points are shown (the 25% most energetic data points). Figure 6.17 shows the evolution of the averaged isotropy parameter I over time; using the same data set, I is calculated every $T_a/10$ for the atrium and the ventricle cavities.

A first observation about Fig. 6.16 is that the majority of the points correspond as either axisymmetric or one dimensional turbulence. A preference for the cigar-shaped turbulent state is observed in the ventricle. Note also that here turbulence is almost never two-dimensional, as data points on the upper line of the Lumley triangle are rare, apart from the right-hand corner of the triangle (expressing one-dimensional turbulence). This statement is actually valid for the whole heart cycle (corresponding Lumley triangles are not shown here).

At $t/T_a = 0.5$ (left plots), several points corresponding to one-dimensional turbulence are observed (right-hand corner of the Lumley triangle). This kind of turbulence is seen in the jet trail of the E wave in the ventricle and for the inflowing jets in the atrium. The two sorts of axisymmetric turbulence (pancake-shaped and cigar-shaped) have no preferred physical location in the heart. At this time, the turbulence is highly anisotropic in the entire heart, as shown by the mean value of the parameter I in the ventricle ($I \simeq 0.4$) and in the atrium ($I \simeq 0.55$). Following the isotropy parameter values, the heart most anisotropic turbulence occurs at the same time as the peak of the E wave occurs, certainly because of the tendency to one-dimensional turbulence, which increases the mean I value.

At $t/T_a = 0.7$ (right plots), one-dimensional turbulence is not observed any more for the ventricle, while it is still visible for the atrium: some points near the atrium surface have this turbulent state. In both cavities, turbulence becomes more isotropic during the diastolic phase, as shown by Fig. 6.16. The data points move toward the origin of the triangle, giving evidence of a trend to isotropy in the diastolic phase. The isotropy parameter evolution confirms this tendency to isotropy: the parameter has a similar behaviour in the atrium and the ventricle, reaching maximum values of about 0.75.

The turbulence stays far from isotropy all along the heart cycle with a maximum mean value of I around 0.75 during diastole. During this phase, the isotropy decreases in the ventricle each time fluid passes from the atrium to the ventricle (around $t/T_a =$

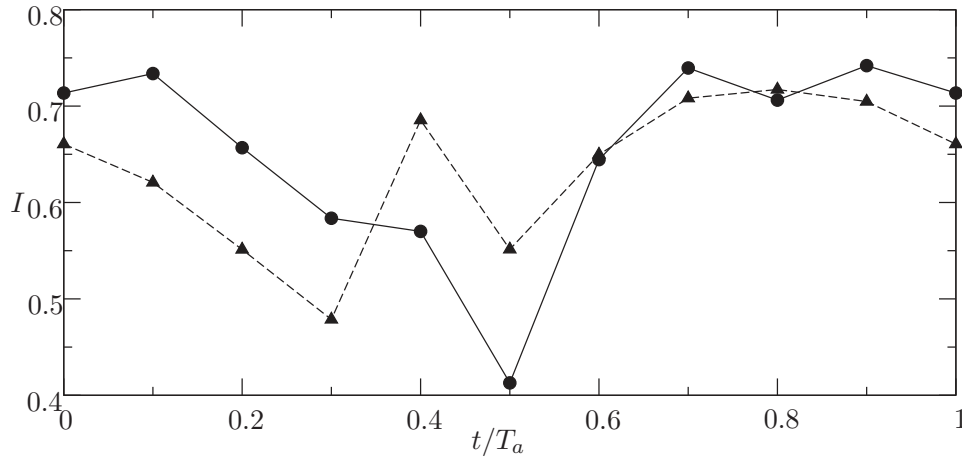


Figure 6.17: Evolution of the mean isotropy parameter I during the heart cycle for the atrium cavity (dashed line) and the ventricle cavity (solid line). The data are calculated every $T_a/10$ for the atrium and the ventricle cavities and are displayed respectively as triangles and circles.

0.5, at $t/T_a = 0.8$ and at $t/T_a = 1$). In the atrium, the isotropy drops when inflowing jets come in the atrium and during the flow reversal at the pulmonary veins. During the systolic phase, turbulence becomes more and more anisotropic in both cavities. The minimum isotropy state in the atrium is reached at $t/T_a = 0.3$ and turbulence regains isotropy before passing to diastolic phase. In the ventricle, the systolic flow, where the wall contracts to eject blood towards the aorta reorganizes the turbulent eddies in the direction of the flow (see the Q criterion views in the previous chapter).

The return to isotropy never fully occurs in this flow. The flow turbulent state seems to stabilize around value of I of 0.7 to 0.75, explained by the mean velocity gradient and the wall-bounded nature of the studied flow. In addition, using experimental evidence, Jacquin *et al.* [86] argued that solid flow rotation (in the case of a homogeneous turbulent flow) reinforces anisotropy and decreases the energetic decaying. The recirculating cell visible on the phase-averaged velocity field (see section 6.3.1) behaves like a solid-rotation with an angular velocity ω_r which can be roughly be estimated as $\omega_r = (5u_a)/(0.5l_s) \sim 13$ rad/s. This is in the range where the rotation effect on turbulence is non negligible. Also, homogeneous turbulence with positive ξ invariant (here the majority of observed point in the ventricle) seems to returns to isotropy at much lower rate than that with negative ξ invariant [66].

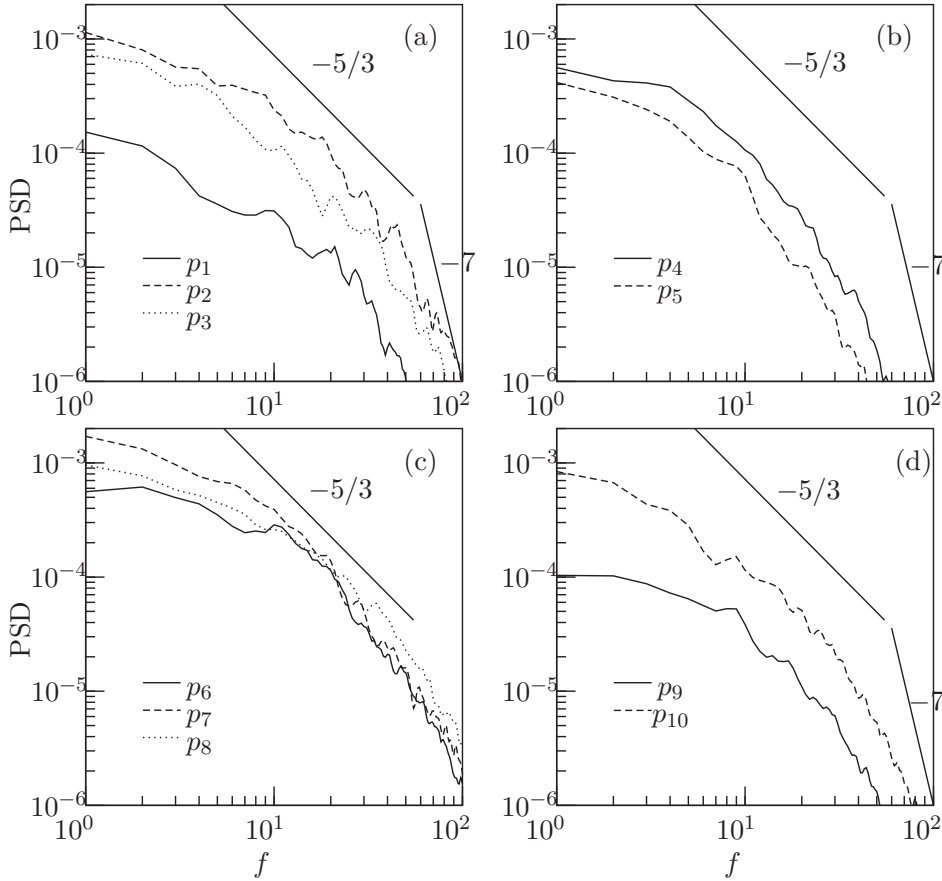


Figure 6.18: Power spectral density (PSD) of vertical velocity fluctuations u_3 at the 10 studied points.

6.3.5 Spectral analysis

General assessment

Additional information about the nature of turbulent fluctuations is usually provided by observing the energy spectra of the velocity fluctuations. This has notably been used in previous studies of pulsatile flows [118, 175]. The frequency spectra of the vertical fluctuating velocity u_3 at the ten probes spread over the domain are provided in Fig. 6.18. They were computed by using the Welch's overlapping averaged modified periodogram method [179]. The data were divided into 50 segments with 50% overlap, each section windowed with a Hann window; 50 modified periodograms were computed and averaged. As the simulation time step was piloted by a CFL condition and hence not constant, the velocity data were first resampled at a sampling rate of 2048 Hz, which corresponds to a Nyquist frequency of 1024 Hz. Lines corresponding to the

$-5/3$ and -7 slopes are included in Fig. 6.18, the former characterizing the inertial sub range, where energy cascades from the large eddies to smaller ones with minimal energy dissipation, and the latter corresponding to the viscous dissipation range [141]. Note that frequencies lower than 1 Hz are not considered here, as the heart cycle lasts one second. Also, frequencies higher than 100 Hz are not analysed because of the grid resolution. Considering a desired resolution of $l_c \sim \Delta x$, the cutoff frequency is estimated at $f_c = u_a/l_c \sim 100$ Hz (recall that $\Delta x \sim 0.8$ mm). Note that eddies with a larger frequency can be present in this flow: the maximum frequency is estimated with $f_{max} \sim \sqrt{\epsilon/(\nu_n + \nu_{sgs})} \sim 2.5$ kHz at maximum in the domain.

In Fig. 6.18(a), the power spectrum density (PSD) of u_3 at probes p_1 , p_2 and p_3 (located in the upper atrium) are shown. Probe p_1 shows low PSD levels (about one decade less than the two following probes), as expected from the results discussed in section 6.3.2. Locations p_2 and p_3 show a wider distribution of energy through the frequency spectrum. A decay of slope close to $-5/3$ is observed over half a decade followed by a smooth transition to a faster decay past $f \sim 70$ Hz.

PSD levels decrease in the lower part of the atrium, at p_4 and p_5 . Spectra shown in Fig. 6.18(b) rapidly fall down and eventually attain a slope close to -7 as viscous effects dominate this region.

Figure 6.18(c) shows spectra at probes p_6 , p_7 and p_8 , located in the bulk of the ventricular flow. The spectra show a more broadband nature, the ventricular flow being turbulent over a significant part of the heart cycle. Spectra at probes p_6 to p_8 are similar to the ones at p_2 and p_3 , with higher levels and a broader distribution. In Fig. 6.18(c), a decay of slope close to $-5/3$ is observed along one decade in frequency.

Figure 6.18(d) shows spectra at locations p_9 and p_{10} . At low frequency, p_{10} shows energy levels one decade higher than p_9 . This difference decreases at higher frequencies where low high-frequency PSD are obtained for both probes.

Time-frequency analysis

The spectra described in the last section essentially tell us which frequencies are contained in the signal as well as their corresponding power, but do not give information at which times these frequencies are present in the flow. Time-frequency representations are thus considered in this section. The signal of the vertical fluctuating velocity u_3 at each probes location is decomposed in 800 windows for which a Hann window with 50 % overlapping is applied and a short-time Fourier transform is used. The obtained spectrogram is then phase-averaged over the 50 cycles. Spectrograms computed with different overlappings and window functions display only small differences, showing that the following results are robust to the details of the signal processing.

Figure 6.19 displays the computed spectrograms. Each horizontal slice of a spectrogram exhibits the frequency spectra of the flow at a specific time. Note that in majority the spectra decrease by about three decades before exceeding 50 Hz during the heart cycle. At some probe locations as p_2 , p_3 in the atrium, p_6 , p_7 , p_8 in the ventricle and

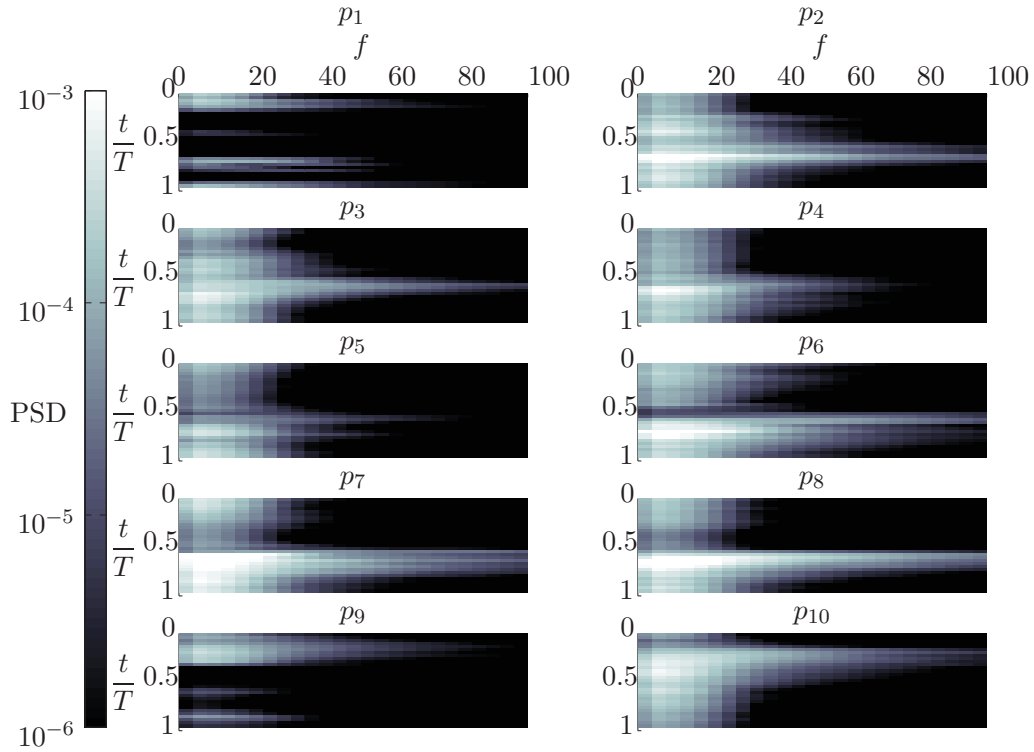


Figure 6.19: Time-frequency representation of the Power Spectral Density (PSD) of the vertical fluctuating velocity u_3 at the 10 probes locations. PSD is color coded (scale on the left) with the same range as Fig. 6.18.

p_{10} in the aorta, the spectra increases up to 100 Hz at certain instants.

Broadband spectra are visible in the atrium locations at $t/T_a \sim 0.65$ corresponding to the large TKE values described before (see section 6.3.2). Note that larger spectra at p_2 happens at $t/T_a = 0.7$ and earlier for p_3 at $t/T_a = 0.6$. This can be explained by the location of p_2 , more in the RSPV jet than p_3 , which is more exposed to the turbulence production due to the jets collision (see the production map in section 6.3.3). These developed spectra are only present in a tight time window; decays of three decades in less than 40 Hz are observed in the atrium at the other instants of the cardiac cycle.

Broadband spectra are present in the ventricle more often over the cardiac cycle. At probes locations p_6 , p_7 and p_8 , broadband spectra are clearly visible during the diastole. The widest spectrum is visible at probe p_8 at $t/T_a = 0.6$, but only for a narrow time window. Once the spectrum fills the frequency range from 1 to 100 Hz, the frequencies present in the flow decrease during the whole diastole. Note that the A wave is not visible on the spectra which indicates that it is too slow to strengthen the turbulent activity in the ventricle. The broad band spectra are observed during diastasis, after the

vortex ring structure of the E wave jet has scattered into small eddies. During systole, the spectra lose three decades of energy within the frequency range from 1 to around 50 Hz. Larger spectrum during systole are visible just behind the mitral valve at probe location p_6 .

The spectrum at probe location p_9 (aortic valve location) shows a widening in the frequency range during systole. Further, at probe location p_{10} (in the aorta root), broadband spectra are visible at $t/T_a = 0.65$. Spectra fall down in time during the diastole as the turbulence decays.

6.4 Final remarks

Although the intracardiac flow has been explored for many decades, there is still no consensus on whether or not there is significant turbulence within the heart. In the past, numerical simulations mainly used solvers based on low-order stabilizations terms, artificial viscosity or dissipative schemes and in most of the cases, the numerical grids were insufficiently refined, annihilating the possibility of capturing hypothetical instabilities. Proper computational modelling of such flow is challenging because of the heart geometry and the variety of the spatial and temporal scales present in the flow. In addition, the pulsatile nature of the heart flow prevents the conventional use of RANS turbulence models which are designed for fully developed turbulent flows [152]. The LES approach used here can handle transition and thus provides a satisfactory predictive tool. Using the LES combined with the described method for extracting patient-specific boundary conditions, this study describes the behaviour of a heart flow. A disturbed and transitional flow nature is revealed, accompanied by identified mechanisms of turbulence production for *heart A*. Note that high frequencies have been observed in the flow. These frequencies are intermittent and visible only in small period of time.

As these results have been obtained from a pathological heart, a legitimate question would be: is the same turbulence observed in a healthy heart? This is the aim of the next chapter.

Chapter key points:

- The unsteady development of turbulence is analysed from the mean flow, flow statistics, the turbulent stresses, the turbulent kinetic energy, its production and through spectral analysis.
- Turbulence is intermittent and fluctuations reaches high frequencies on short periods.
- It is revealed that two mechanisms create turbulence in the *heart A*: the dissipation of a vortex structure impinging the lateral wall of the ventricle during diastole and the colliding of inflowing jets in the atrium during both diastole and systole.
- Unusually, negative production of turbulent kinetic energy is measured in three locations in this heart
- It is revealed that the turbulence, when present, is close to an axisymmetric state most of the time but never reaches an isotropic state.

A healthy subject: analysis and comparisons

Chapter contents

7.1	Heart model	132
7.1.1	Heart model and extraction of the deformations	132
7.1.2	Computational mesh and simulation details	133
7.2	Results and discussion	136
7.2.1	Data convergence	136
7.2.2	Global description of the flow	140
7.2.3	Instantaneous structures	140
7.2.4	Velocity fields and signals	142
7.2.5	Atrial swirl motion	145
7.2.6	Kinetic energy	148
7.2.7	Time-frequency analysis	153
7.3	Final remarks	153

This chapter describes the left heart flow in a young, healthy subject. This heart is referred to as *heart B*. The heart model is extracted from MRI instead of CT-SCAN images for *heart A*. The σ -model is used and the Newtonian hypothesis for the flow is conserved for the presented LES. The computed flow is described focusing in particular on the turbulence characteristics. In the lights of the results described in chapters 5 and 6, comparisons are made between *hearts A* and *B*.

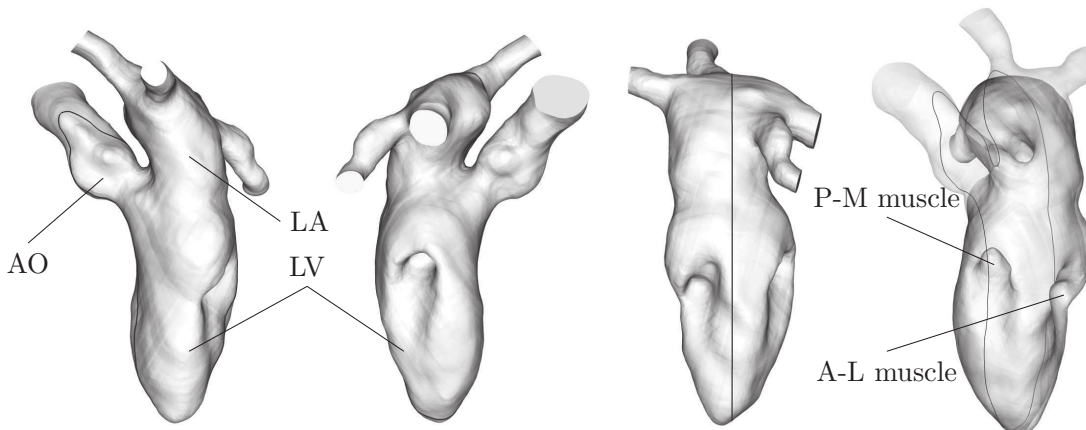


Figure 7.1: Full human left heart extracted from MRI images. The same domain is shown from four different points of view. The left ventricle (LV), left atrium (LA), Aorta (AO), Anterio Lateral (A-L) and Postero Medial (P-M) papillary muscles are indicated. A black line passing through the left heart indicates the position of the slice which will be used to describe the flow in the remainder of the chapter.

7.1 Heart model

7.1.1 Heart model and extraction of the deformations

Using the framework described in chapter 3 and 4, deformations along a cardiac cycle are extracted from a MRI exam of a healthy subject. The exam was conducted at the University Hospital of Toulouse Rangueil (France). The 4D image set consists in $N = 20$ three-dimensional images of spatial resolution $5.0 \times 1.1 \times 1.1 \text{ mm}^3$, which correspond to $21 \times 256 \times 256$ voxels. The patient was 26 years old and his cardiac cycles lasted $T_b = 750$ ms. The *template* geometry is extracted at a time when the ventricle volume is at its median value. As shown in Fig. 7.1, the numerical domain contains the LA, LV a part of the aorta and four pulmonary veins. As for *heart A*, this *template* domain does not include the trabeculations and the left atrial appendage. However, it does include the papillary muscles. The LV has a height of 7.8 cm from the tips of the MV to the apex and a maximum diameter of the order of ~ 4.0 cm. In comparison with *heart A*, this heart is more narrow due to the full segmentation of the papillary muscles.

A nearly isotropic surface mesh is generated from this geometry. The characteristic length of each triangle edges is close to 2 mm. This *template* surface grid is deformed based on the method previously described in chapter 4. The deformation procedure uses 10 *outer* iterations. The initial Gaussian Kernel width is set to $\sigma_0 = 32$ voxels with a decrement of 3 voxels between each of the *outer* iterations. The *inner* iterations are either stopped after 10 iterations or when the total residual squared difference is under 0.01. The regularization weight λ is set to 1.0, which corresponds to an equal weight between the likelihood potential and the regularization term (see chapter 4).

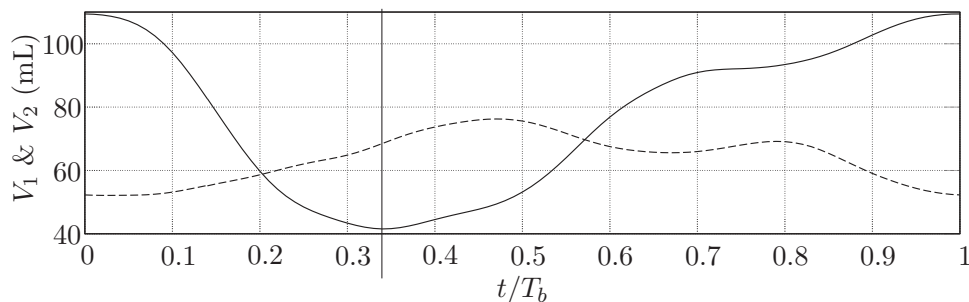


Figure 7.2: Volume of the ventricle (V_1 solid line) and of the left atrium (V_2 dashed line). The vertical black line marks the limit between the systolic phase and the diastolic phase at $t/T_b = 0.34$.

The Fourier coefficients for the deformation are computed (see chapter 3). The time evolution of the ventricular and atrial volumes are reported in Fig. 7.2. For the ventricle, the end diastolic volume is here of 109 mL while the end systolic volume is of 41 mL. The stroke volume is then of 68 mL and the ejection fraction is 62%. All these values are in normal range.

7.1.2 Computational mesh and simulation details

A nearly isotropic grid is generated from the heart model described in the above section using the commercial software Gambit. The grid has approximately ten millions of tetrahedral elements. The template grid spatial resolution is imposed to be close to 0.56 mm in all three spatial directions¹. As before, the surface is deformed thanks to trigonometric interpolation. For this heart, one re-meshing was necessary at half-systole ($t/T_b = 0.22$) as skewness became close to unity for some cells. Valves are modelled as before. The MV leaflets length was set to $l = 13$ mm after examination of the MRI images. The ellipse area is set in order to correspond to the median value of the open MV area. This value is from extracted measurements on the medical images during diastole. Hence, the open area presented to the blood flow is represented by an ellipse of axis $a = 15$ mm and $b = 11$ mm. The angle on the P_β plane is set to 20 degrees and the eccentricity parameter to $e = (2.0, -4.38)$ mm.

As shown in chapter 5, section 5.4.1, the impact of a non-Newtonian model reproducing the shear-thinning behaviour of blood is small. Blood is thus modelled as an Newtonian fluid in this chapter.

The simulation time step is fixed by a CFL condition, $CFL = 0.9$ and a Fourier condition of $F_o = 0.2$. These conditions are set to be consistent with the explicit time integration used in the CFD solver. The time step is thus varying from 7.0×10^{-5} s to

¹Considering only regular tetrahedra, the spatial resolution is computed as $\Delta x \sim \sqrt[3]{\frac{12V}{10^7 \sqrt{2}}}$, where $V = 211 \text{ mL}$ is the *template* grid volume.

4.0×10^{-4} s during the computation. In the light of the previous discussion on the SGS model (see chapter 5, section 5.4.2), the LES presented in this chapter is performed using the σ -model.

The flow waveform imposed at the four inlet conditions of the computational domain is calculated based on the mass conservation principle. Despite the fact that an MRI exam was used to obtain the medical images, no information on the velocity field was measured. Hence, the pulmonary veins are lengthened, so that the inflow conditions are five vessel diameters away from the ostium. There, a uniform velocity profile is applied. In addition, the inflowing flow rate has been chosen to be equally distributed between the PVs. Figure 7.3 displays the flow rates at the aortic valve (top plot) and the mitral valve (middle plot) and the total inflow imposed at the pulmonary veins (bottom plot). A vertical black line separates the systolic phase and the diastolic phase. For this heart, systole starts at $t/T_b = 0$ and lasts $0.34 T_b$. Diastole lasts $0.66 T_b$. The hand rule for the normal ratio of one third (systole) to two thirds (diastole) is respected.

The aortic outflow behaves as expected, with a peak flow rate of $560 \text{ mL}\cdot\text{s}^{-1}$ at $0.15T_b$. The flow rate then decreases and reaches zero at $0.34 T_b$. The aortic flow rate is null during diastole. Note that the maximum flow rate at the aorta is 75% higher than the peak systole flow rate of *heart A*, essentially because of the higher heart rate. The mitral flow rate is here composed by two main peaks corresponding to the E wave and the A wave. The E wave peak ($0.57 T_b$) corresponds to an entering flow rate of $365 \text{ mL}\cdot\text{s}^{-1}$ in the ventricle. The A wave peak being at $0.9 T_b$ and corresponds to an entering flow rate of $180 \text{ mL}\cdot\text{s}^{-1}$. The E/A ratio is very close to 2, which is a normal physiological value compared to the value of 5.5 of *heart A* [161]. Note that the E/A ratio is still high for *heart B*. However, this high value is normal for a young and healthy subject (subject was 26 years old) [125]. A weak peak is present at the very beginning of diastole. It should have little influence on the blood flow and is probably not physiological. It could be due to small errors in the deformation algorithm.

The fluid density ρ and the fluid kinematic viscosity ν_n are supposed to be constant: $\rho = 1040 \text{ kg}\cdot\text{m}^{-3}$ and $\nu_n = 4 \times 10^{-6} \text{ m}^2\cdot\text{s}^{-1}$. The Reynolds number at the mitral valve tips varies from 0 to approximately 4520 (the maximum was 5000 for *heart A*). This value is based on the effective mitral mean diameter $D = 2R_a = 2\sqrt{ab}$, the area of the open mitral, the kinematic viscosity and the maximum flow rate. The transmitral velocity for the E wave is $U_{max} = 0.7 \text{ m}\cdot\text{s}^{-1}$, which falls into the usual measurements [78]. The Reynolds number of the aortic valve is computed in the same way and is about 10,400 with a maximum velocity of $U_{max} = 2.5 \text{ m}\cdot\text{s}^{-1}$. These two values seem high but actually fall in the normal range [165]. Table 7.1 reports the characteristics of *heart B* accompanied with the characteristics of *heart A* and the normal ranges [13, 22, 98, 125] for comparison.

A reference velocity named u_b is computed as $u_b = \dot{q}_b l_s / V_s = 0.16 \text{ m}\cdot\text{s}^{-1}$ where \dot{q}_b is the cardiac output ($\dot{q}_b = 9.7 \times 10^{-5} \text{ m}^3\cdot\text{s}^{-1}$), V_s the end systolic volume ($V_s = 4.1 \times 10^{-5} \text{ m}^3$) and l_s is the ventricle length at the end of the systole ($l_s = 6.8 \times 10^{-2} \text{ m}$).

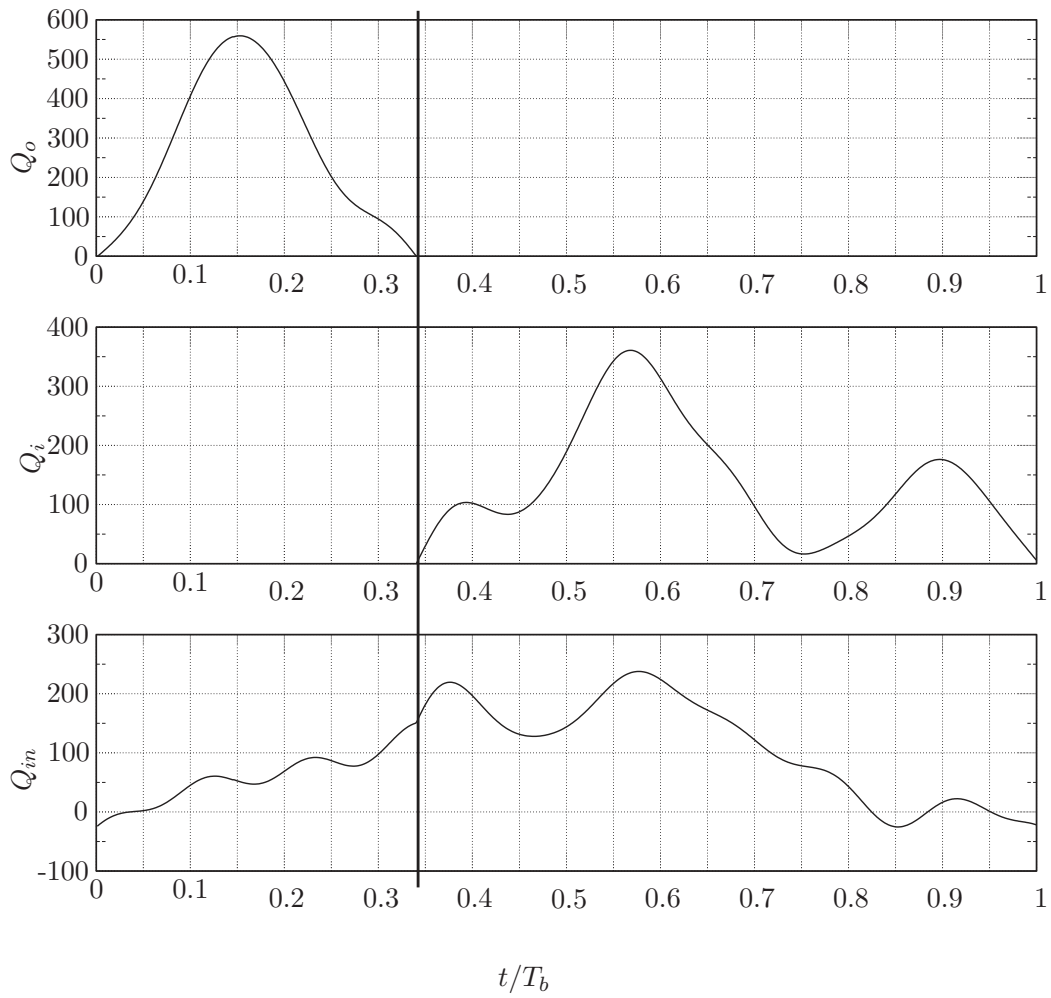


Figure 7.3: Flow rates in $\text{mL}\cdot\text{s}^{-1}$ at the aortic valve (top plot), mitral valve (middle plot) and the total heart inflow imposed at the pulmonary veins during the heart cycle (bottom plot). The vertical line delimits the systolic phase from the diastolic phase at $t/T_b = 0.34$.

	<i>Heart A</i>	<i>Heart B</i>	Normal range
Heart rate (bpm)	60	85	60 - 100
E/A ratio	5.5	2.0	1.0 - 2.0
EDV (mL)	130	109	65 - 240
ESV (mL)	55	41	16 - 143
SV (mL)	75	68	55 - 100
Cardiac output (L.min ⁻¹)	4.5	5.8	4.0 - 8.0
Ejection Fraction (%)	58	62	55 - 70
Open area MV (cm ²)	3.77	5.18	4.0 - 6.0
U_{max} at MV (in m.s ⁻¹)	1.08	0.70	0.6 - 1.0
Re_{max} at MV	5000	4520	-
U_{max} at AV (in m.s ⁻¹)	0.96	2.5	≤ 2.5
Re_{max} at AV	5300	10,400	-
Acquisition	CT scan	MRI	-

Table 7.1: Main characteristics for *heart A* and *heart B*.

7.2 Results and discussion

7.2.1 Data convergence

Due to the discretization applied on the numerical domain (roughly 10 millions of cells) and the subsequent amount of data, a smaller number of cycles were simulated. 35 cycles were computed, using the same heart deformation for each cycle. Phase-averages were gathered over the last $n=30$ cycles. The phase average over n cardiac cycles of a generic variable G is defined as

$$\langle G \rangle(\mathbf{x}, t) = \frac{1}{n} \sum_{k=0}^{n-1} G(\mathbf{x}, t + kT), \quad (7.1)$$

where \mathbf{x} denotes the spatial coordinates and t the time. Deviation from this averaged is computed as,

$$g = G - \langle G \rangle. \quad (7.2)$$

The phase average $\langle G \rangle$ represents the time-varying deterministic part of the flow while the (turbulent) fluctuations are represented by the deviation g . Finally, the root mean square (r.m.s.) value g_{rms} is defined as,

$$g_{rms}(\mathbf{x}, t) = \sqrt{\langle G^2 \rangle(\mathbf{x}, t) - \langle G \rangle^2(\mathbf{x}, t)}. \quad (7.3)$$

100 full data solutions with data for each grid node are written for each cycle, every $0.01T_b$. In addition, in order to get precise local information, the velocity signal was extracted at some specific locations at each simulation iteration. To do so, the numerical domain was seeded by Eulerian probes. Seven probes p_i , $i = 1, \dots, 7$ were selected over a virtual path that a red blood cell could follow, from the top of the atrium to the

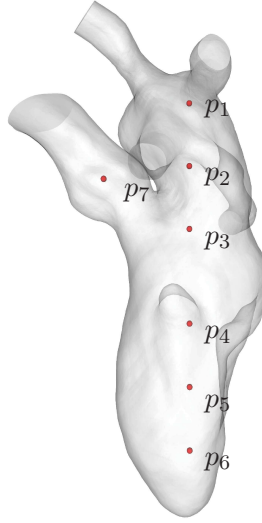
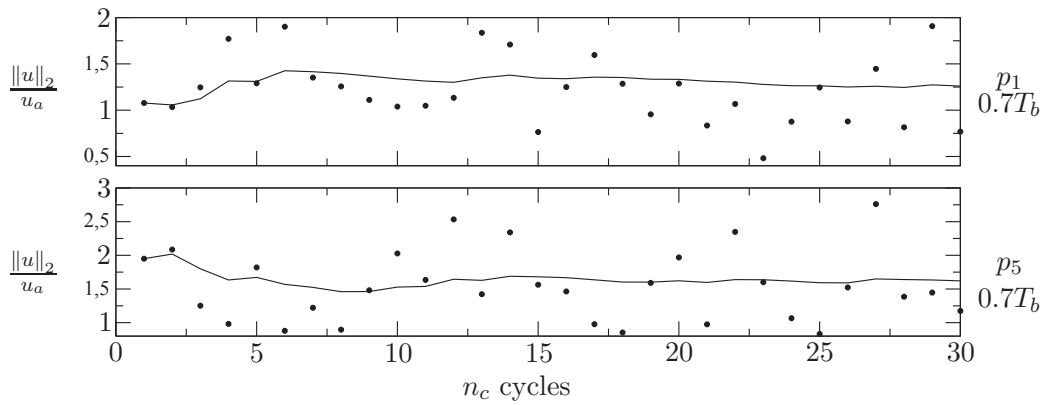
Figure 7.4: Positions of the seven probes in *heart B*.

Figure 7.5: Solid lines represent the phase-averaged velocity magnitude at 2 probes locations using n_c cycles. The dots represent the instantaneous velocity magnitude for the n_c -ith cycle. Top and bottom plots display data from probe p_1 at $0.7T_b$ and p_5 at $0.7T_b$, respectively.

outlet at the aorta. Figure 7.4 shows the position of the probes. The seven selected probes provide velocity signals near the top of the atrium to the mitral valve (p_1 to p_3 positions), signals in the left ventricle (p_4 to p_6), and above the aortic valve (p_7). These probes will be used to analyse the flow. They are used here to observe the data convergence.

Figure 7.5 shows velocity data for two probes: p_1 and p_5 . Both plots display data at $t/T_b = 0.7$. Solid lines represent the phase-averaged velocity magnitude computed

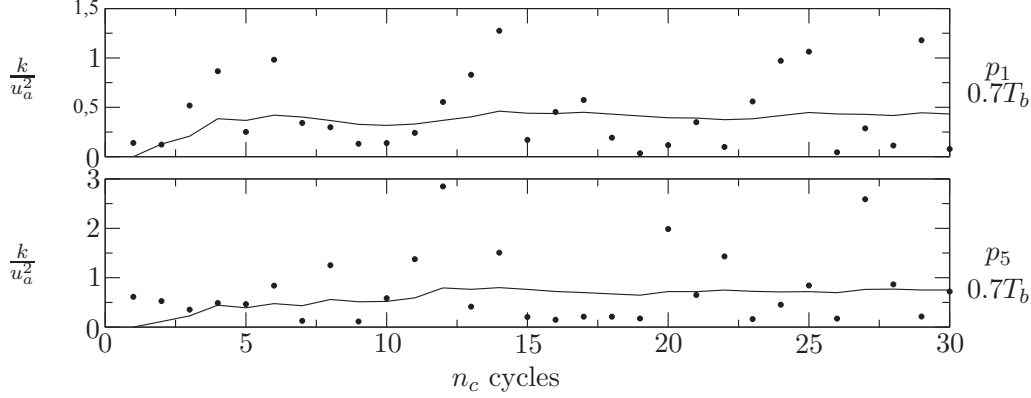


Figure 7.6: Solid lines represent the phase averaged TKE magnitude at 2 probes locations using n_c cycles. The dots represent the instantaneous TKE magnitude for the n_c -ith cycle. Top and bottom plots display data from probe p_1 at $0.7T_b$ and p_5 at $0.7T_b$, respectively.

using n_c cycles. n_c varies from 1 to the total number of cycles used for data averaging, which is 30. The dots represent the instantaneous velocity magnitude for the n -ith cycle. All the velocities are nondimensionalised by the reference velocity u_b (as a reminder: $u_b = 0.16 \text{ m.s}^{-1}$).

For all the probes and all the considered times, high instantaneous fluctuations are observed. Despite these high fluctuations, roughly 25 cycles are needed to reach data convergence.

Figure 7.6 shows probes data for the fluctuating energy of the velocity. The top plot displays data from probe p_1 , the bottom plot displays data from probe p_5 . Both plots display data at $t/T_b=0.7$. Solid lines represent the turbulence kinetic energy (TKE) computed using n_c cycles. n_c being set from 1 to the total number of simulated cycles, which is 30. The local turbulence kinetic energy is defined as:

$$k(\mathbf{x}, t) = \frac{1}{2} \langle u_i u_i \rangle. \quad (7.4)$$

In the figure, dots represent the instantaneous kinetic energy of the velocity fluctuations computed at the n -ith cycle. This energy, for cycle n_c is defined as

$$k^i(\mathbf{x}, t) = \frac{1}{2} (u^{n_c} - \langle U \rangle)^2, \quad (7.5)$$

$\langle U \rangle$ being the phase-averaged velocity computed with the 30 cycles and u^{n_c} the instantaneous velocity for cycle n_c . All energies are nondimensionalised by u_b^2 . High fluctuations are observed. About 25 cycles were necessary to obtain converged data.

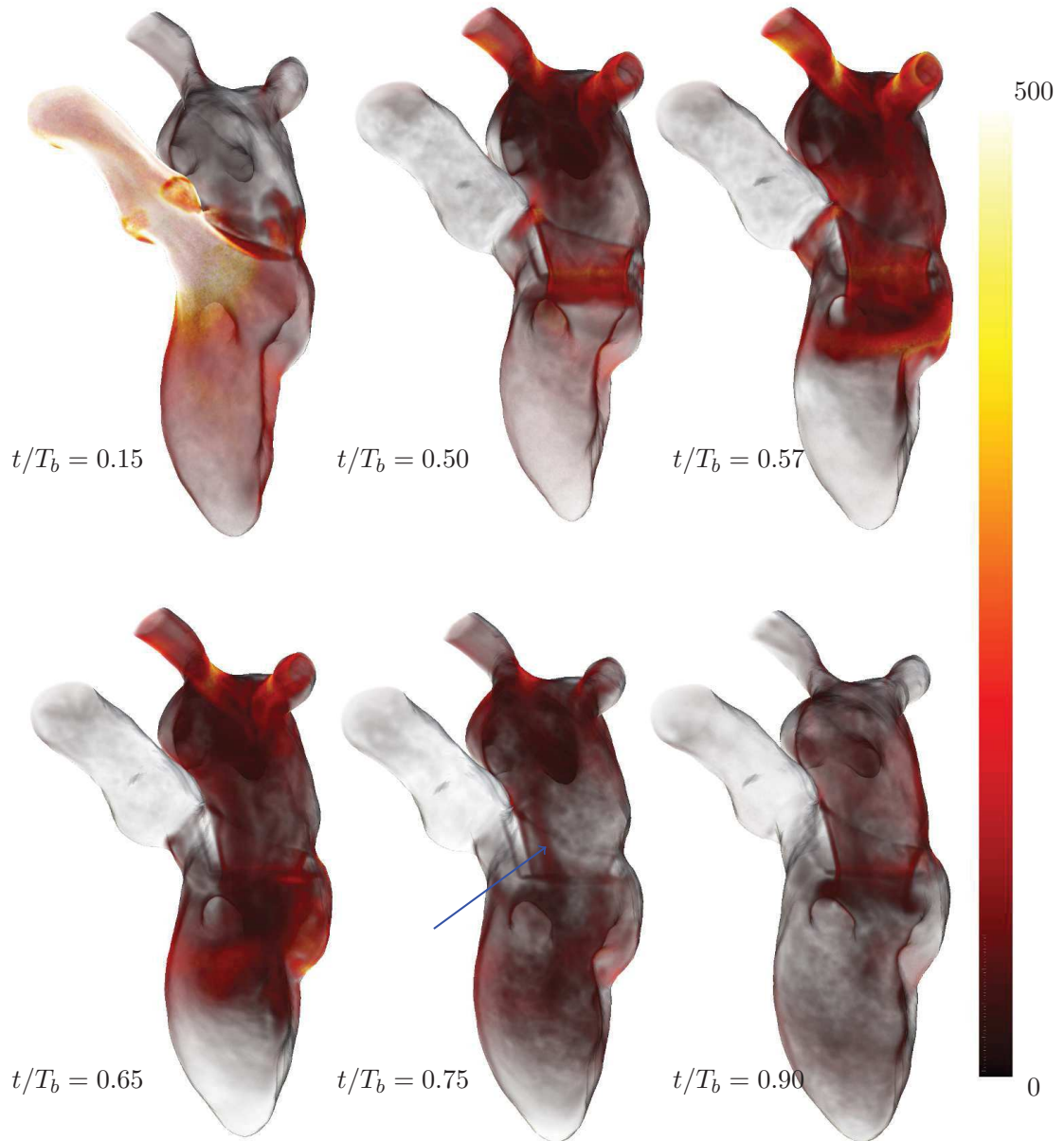


Figure 7.7: Volume rendering of non-dimensional vorticity magnitude of the phase-averaged velocity fields at different times of the simulation. First row, left plot: $t/T_b=0.15$. Center plot: $t/T_b=0.50$. Right plot: $t/T_b=0.57$. Second row, left plot: $t/T_b=0.65$. Center plot: $t/T_b=0.75$. Right plot: $t/T_b=0.90$. The mapping relating vorticity magnitude with opacity is linear. The heart wall is made partially transparent to allow a better observation of the flow behaviour.

7.2.2 Global description of the flow

Figure 7.7 displays the 3D vorticity magnitude map of the phase-averaged velocity field non-dimensionalised by the period T_b . Six salient instants of the heart cycle are shown: the ventricular peak systole ($0.15T_b$), the first half of the E wave, its peak and the last half of it at respectively 0.5 , 0.57 and $0.65T_b$, the diastasis ($0.75T_b$) and the peak A wave ($0.9T_b$).

In the atrium, the blood flow coming from the PV increases almost constantly during systole as shown by Fig. 7.3. No mechanism of violent collision is present for this heart during systole, contrary to *heart A*. As exposed in the last chapter, turbulence came with deceleration of the inflowing jets. The global swirling movement in the atrium is not visible on the vorticity maps but is also present in *heart B*. High vorticity is visible in the aorta root, the narrowed geometry of the aorta root plus the high flow rate generating a strong shear layer. The flow rate here is 70% larger than for *heart A*, also explaining the higher vorticity values here.

The ventricle diastole starts at $0.34T_b$. As described for *heart A*, a vortex ring is formed (at $0.5T_b$ here) and progresses through the ventricle (visible at the peak diastole at $0.57T_b$). The vortex ring has a larger radius than the one from *heart A* because of the larger open MV area. The papillary muscles are hit by this vortex ring, the shear layer against the anterio-lateral muscle being visible at $0.57T_b$. The vortex ring changes its orientation and breaks up by interacting with the lateral wall. The jet does not penetrate the ventricle as deep as in the case of *heart A*. The velocity at the E wave peak represents roughly 65% of the E wave peak velocity for *heart A* and the vortex ring interacts earlier with the lateral wall, explaining the smaller penetration. During diastasis, at $0.75T_b$, the ventricle volume remains almost constant and the vorticity magnitude decreases. From this moment, the atrial volume decreases and the A wave begins. The formation of a new vortex ring is visible at $0.9T_b$. This vortex stays between the tips of the papillary muscles and the tip of the mitral valve. It does not have time to hit the lateral wall before systole begins.

In the atrium, the RSPV and RIPV (pulmonary veins visible on Fig. 7.7) jets interact with each other during the whole cycle. These two jets form a flow with a trajectory tangential to the atrial wall. Jets do not seem to collide or disturb each other as in *heart A*. Contrary to what occurs in *heart A*, the jets path seems smoother. However, the general mechanism is the same that in *heart A*. The jets from the pulmonary veins create a swirled motion of the blood in the atrium. As a side note, a vortical structure is visible in the atrium, indicated by an arrow in Fig. 7.7 at $0.75T_b$. The length of this structure is of half the atrium height and is due to the swirling motion in the atrium. This structure was present, though less visible, in *heart A*.

7.2.3 Instantaneous structures

The instantaneous flow features are studied in this section. The 35th cycle which is the last simulated has been selected to display the instantaneous structures. The Q criterion

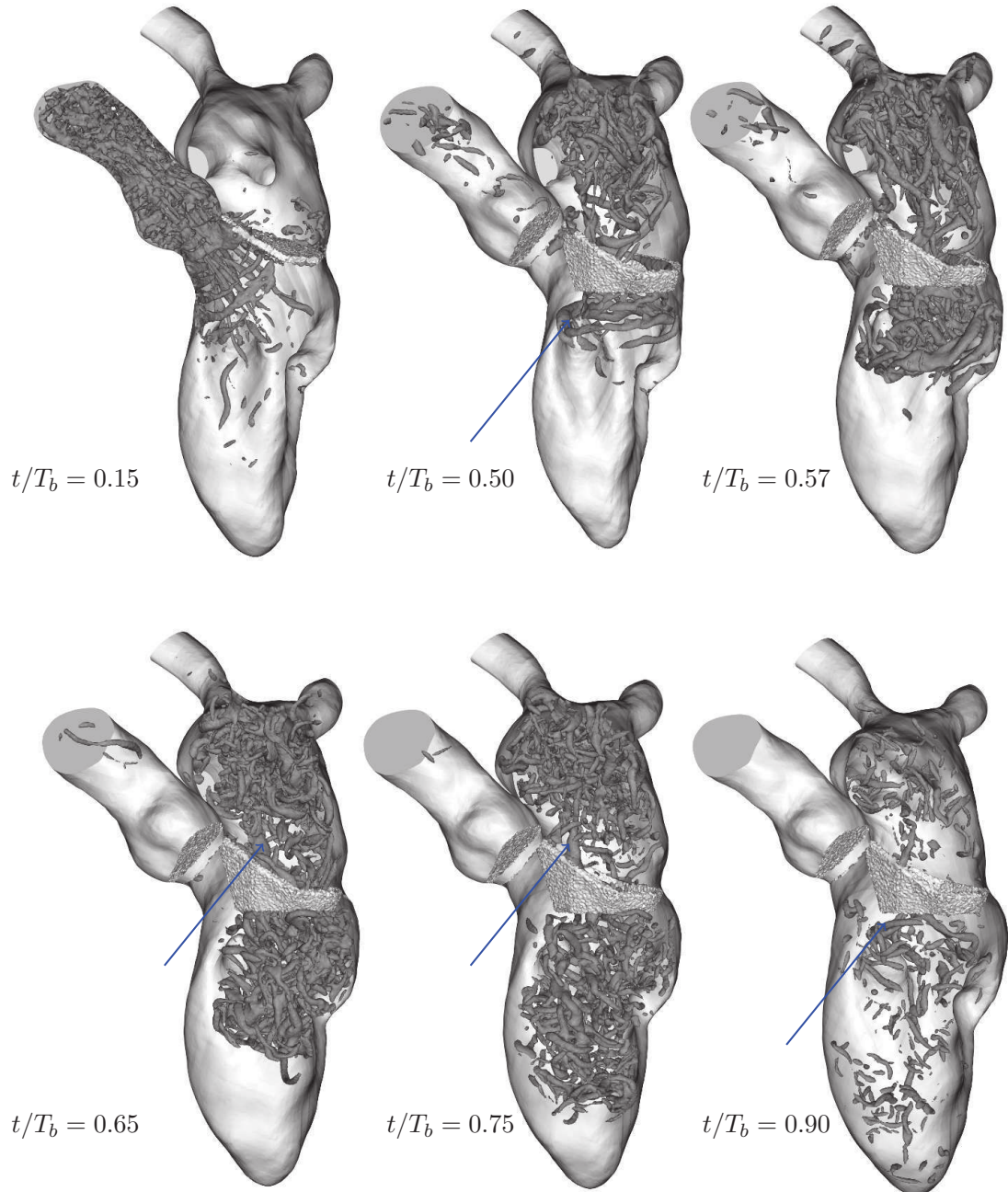


Figure 7.8: Evolution of Q criterion isosurface ($Q = 70u_b^2/R_a^2$) showing the vortical structures present in a typical instantaneous velocity field.

is displayed. Q criterion isosurfaces are presented in Fig. 7.8 at different instants of the heart cycle. The instants are the same as in the previous section and the isosurface at $Q = 70u_b^2/R_a^2$ is shown.

During systole, really few structures are visible in the atrium. As said before, the smooth and progressive increase in the pulmonary veins flowrate in this case does not yield intense vortical structures during systole. This was not the case for *heart A*, where many structures could be seen in the upper part of the atrium. At peak systole ($0.15T_b$ shown in Fig. 7.8), multiple elongated vortical structures roughly aligned with the main flow direction can be observed from the upper part of the ventricle to the ascending part of the aorta. This kind of structures has been reported in chapter 5. They seem characteristic of the systolic phase.

At $0.5T_b$, the structures which were visible in the aorta dissipate. However, a lot of small eddies are formed in the atrium at this time. Meanwhile, traces of the E wave vortex ring are visible at the MV tips (an arrow indicates it in Fig. 7.8 at $0.5T_b$). The vortex ring travels through the ventricle. It is then disturbed by the lateral wall and the papillary muscles. Its progression to the apex is stopped earlier compared to *heart A*. The non-dimensionally time interval where this vortex ring travels toward the lateral wall is of the order of $T_b/10$, as for *heart A*, but its velocity of propagation is smaller. The vortex ring evolves as a complex 3D flow after the impact. The small eddies do not fill up the entire ventricle as for *heart A* but seem to fill the first three quarters. Remarkably, the structure associated with the swirling motion in the atrium already mentioned in the last section, is visible here at 0.65 and $0.75 T_b$ (two arrows indicate it in Fig. 7.8). At $0.9 T_b$, the A wave vortex ring is visible in the upper part of the ventricle (an arrow indicates it).

7.2.4 Velocity fields and signals

The velocity vector fields of the phase-averaged flow solutions are shown in Fig. 7.9 for the same instants shown previously. The non-dimensional velocity vector fields are shown over a slice in the left heart, as indicated in Fig. 7.1. The reference velocity used to make the values non-dimensional is computed as $u_b = 0.16 \text{ m.s}^{-1}$. Note that the scale changes along the cycle and is indicated in the figure.

The global features reported in *heart A* are observable in *heart B* as well. During systole, the flow is less chaotic in the atrium compared to *heart A*. At the end of diastole, the recirculating cell in the ventricle does not move toward the septum wall as in *heart A*. The center of this structure seems to remain at the same place during all the diastole.

Figure 7.10 shows the normalized vertical velocity signal U_3 over 6 cardiac cycles and $\langle U_3 \rangle$, the vertical velocity phase-averaged over 30 cardiac cycles at the 7 probes positions described in section 7.2.1 (Fig. 7.4). In *heart A*, in the atrium, the velocity in the z direction was null during systole. Here, the probes in the atrium display non null velocity during systole, especially for p_3 just above the mitral valve. This is explained by the fact that the flow motion in *heart A* during the systole was perpendicular to

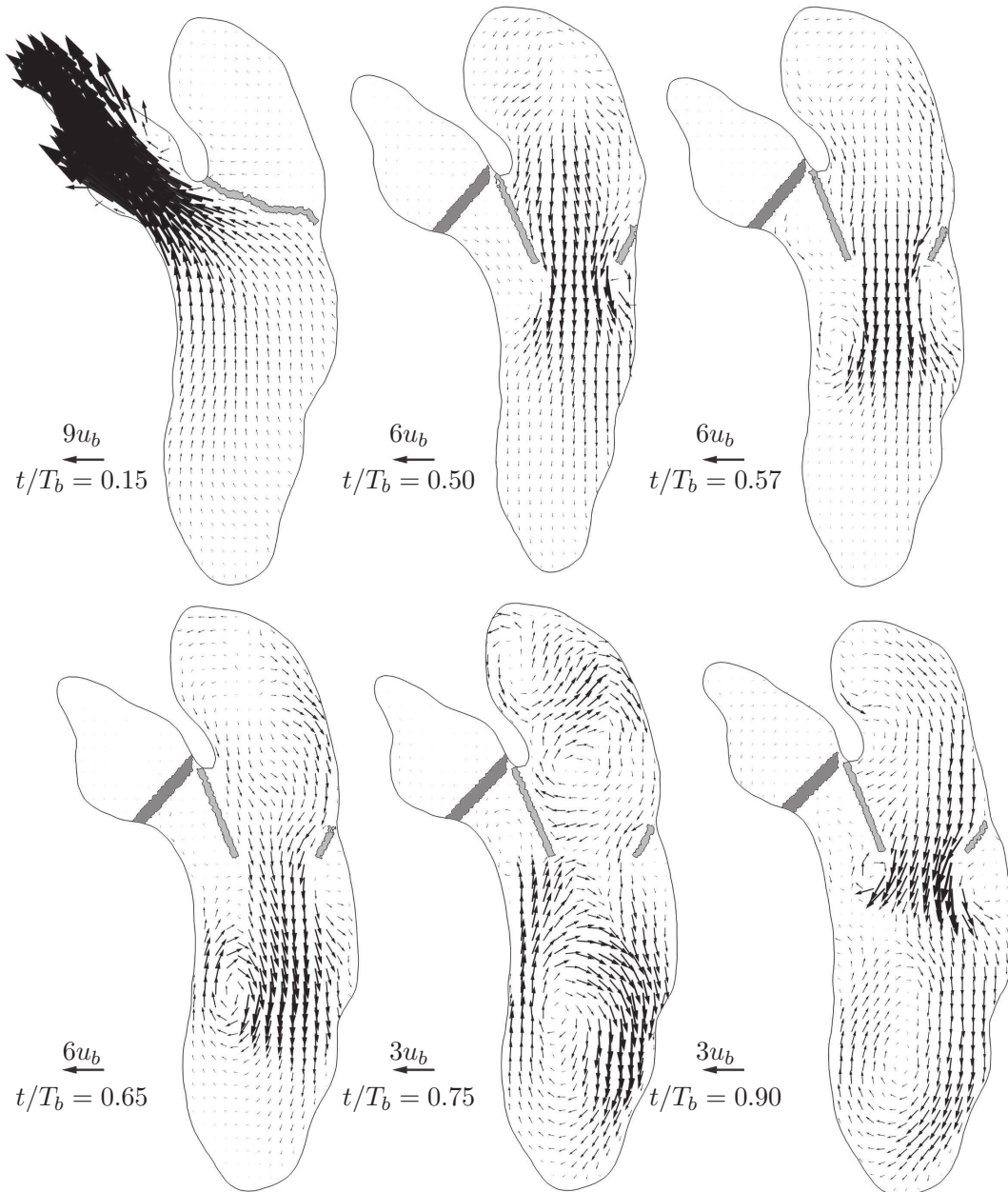


Figure 7.9: Phase-averaged non-dimensional velocity field over a cutting plane through the left heart (see Fig. 7.1 for the position of the plane). The velocity vector scale is not constant and is indicated for each plot. The mitral valve is depicted in light grey and the aortic valve in dark grey.

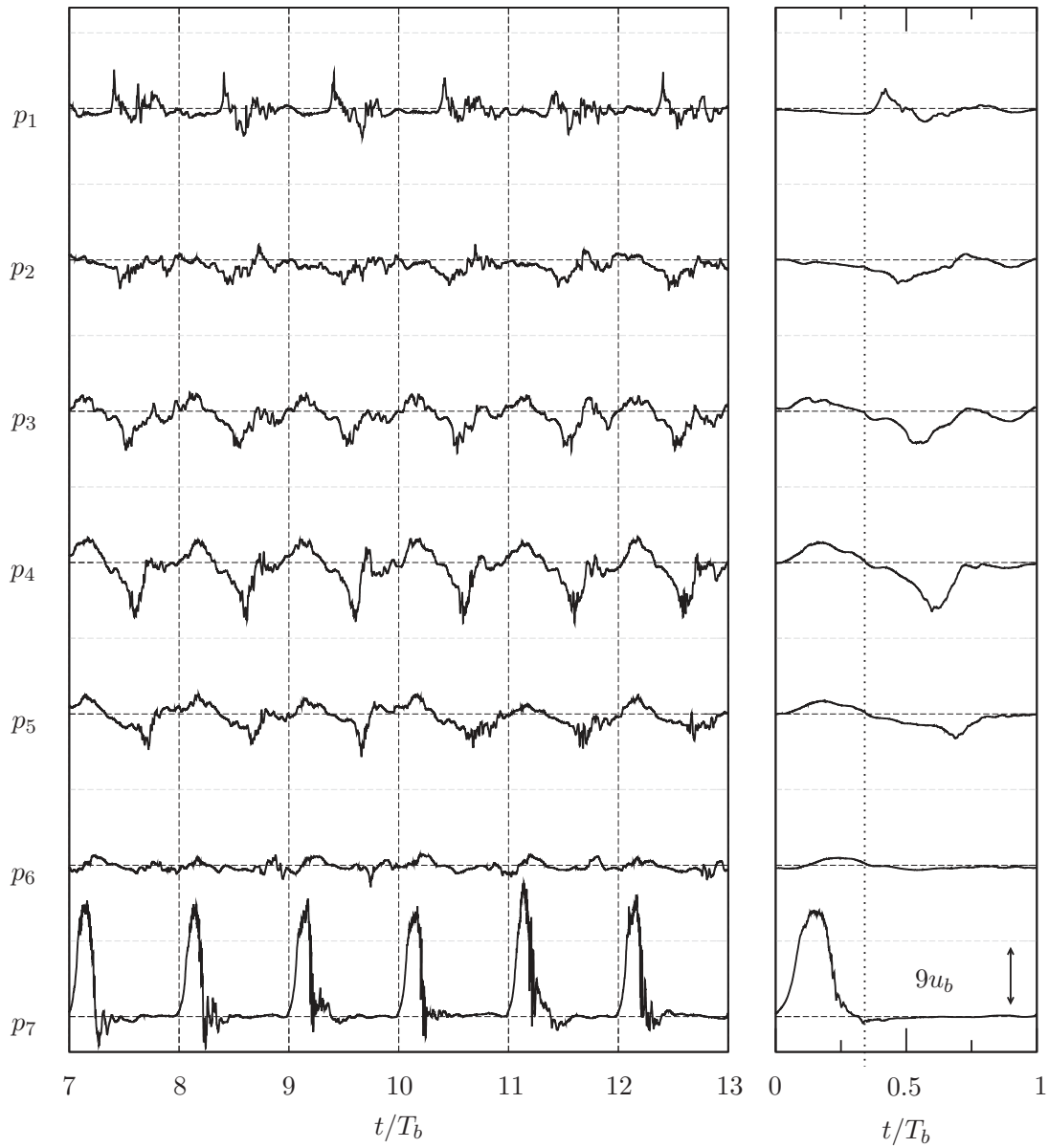


Figure 7.10: Left: time history of normalized vertical velocity U_3/u_b over 6 cardiac cycles of the 30 cycles used for phase-averaging at the 7 studied points. Right: phase-averaged of normalized vertical velocity $\langle U_3 \rangle / u_b$ at the same 7 points. The vertical dotted line delimits the systolic phase from the diastolic phase at $t/T_b = 0.34$.

the z direction which is not the case here. The atrial vortical structure is described in details in the next subsection.

The general behaviour of the velocity signal in the ventricle is really similar to the signals in *heart A*. Notable differences during the diastole are due to the lower penetration of the E wave vortex ring.

7.2.5 Atrial swirl motion

The swirling motion of the blood in the atrium has been mentioned not only in this chapter but also in the two last ones about *heart A*. This chiral motion present in the atrium was reported notably by Fyrenius [62] and Kilner [90] and its signature has been shown on the field of vorticity and Q criterion. Here, we investigate its origin and its evolution over the heart cycle. Figure 7.11 shows the 3D velocity vectors in the atrium, at two different moments during diastole. In Fig. 7.11 the two top figures display the atrium at $0.6T_b$ with two different views, while the bottom figure shows the atrium at $0.7T_b$.

At $0.6T_b$, the inflowing fluxes form a well organized flow (top figure), clearly less chaotic than in *heart A*. The RIPV and RSPV jets merge and then follow a trajectory tangential to the atrial wall. This trajectory is directed toward the MV, which is easily visible on the center plot. The LIPV jet is directed toward the upper part of the atrium, without interacting with the merged RIPV-RSPV flow. Part of the LSPV jet flows directly to the MV while the other part is entrained by the LIPV flow, passing under the RIPV-RSPV flow. The geometry of the pulmonary veins yields a general swirled flow. In the upper part of the atrium, the axis of the swirled structure is perpendicular to a plane in the atrium passing through all four pulmonary veins. The bottom figure depicts the atrial flow at $0.7T_b$. At this time, the flow rate passing through the mitral valve is minimal: note the lower inclination of the velocity vectors at the cut plane above the MV on the figure, indicating that the tangential flow component does not weaken compared to the normal flow component.

This swirling motion is also visible during systole, although with a smaller intensity. Figure 7.12 shows the swirling motion at $0.3T_b$. A plane passing by the four pulmonary veins is included in the figure. The axis of the swirled structure is perpendicular to this plane.

The described swirling motion can be further quantified by computing the averaged kinetic energy of the different velocity components. The tangential kinetic energy is computed by $K_{1,2} = (U_1^2 + U_2^2)/2$ and the kinetic energy of the axial flow velocity (along z) is computed by $K_3 = U_3^2/2$. These energies are computed using the phase-averaged flow field. Figure 7.13 shows these energies computed on the plane above the mitral valve which is visible in Fig. 7.11 (an arrow points at the plane).

During diastole, the axial flow energy K_3 has two main peaks, corresponding to the E wave and the A wave. This atrial swirling motion is very robust. It is generated at the same time as the E wave, then is slowly dissipated, and does not seem to be affected

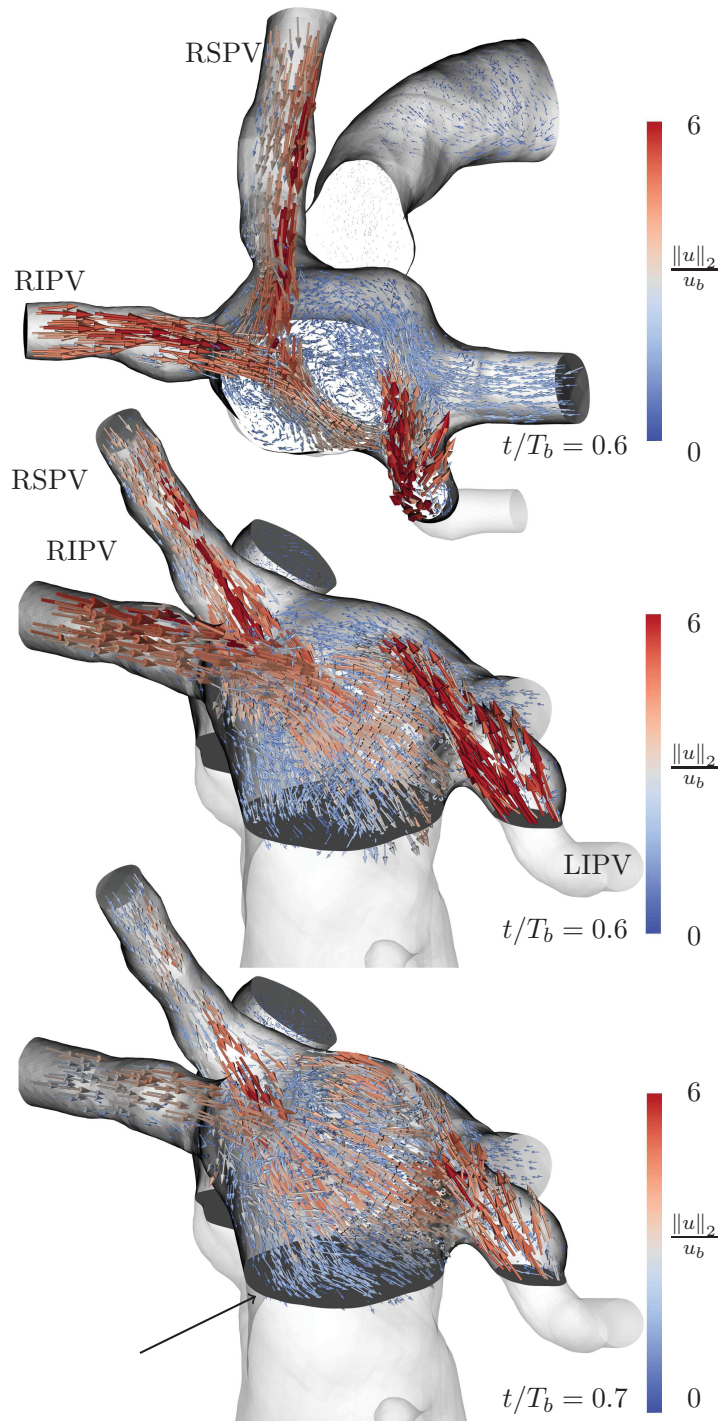


Figure 7.11: 3D velocity vectors in the atrium at $0.6T_b$ and $0.7T_b$. The velocity field is only shown in the atrium. Pulmonary veins are indicated. The black arrow in the bottom figure is pointing the plane where kinetic energy is computed in Fig. 7.13.

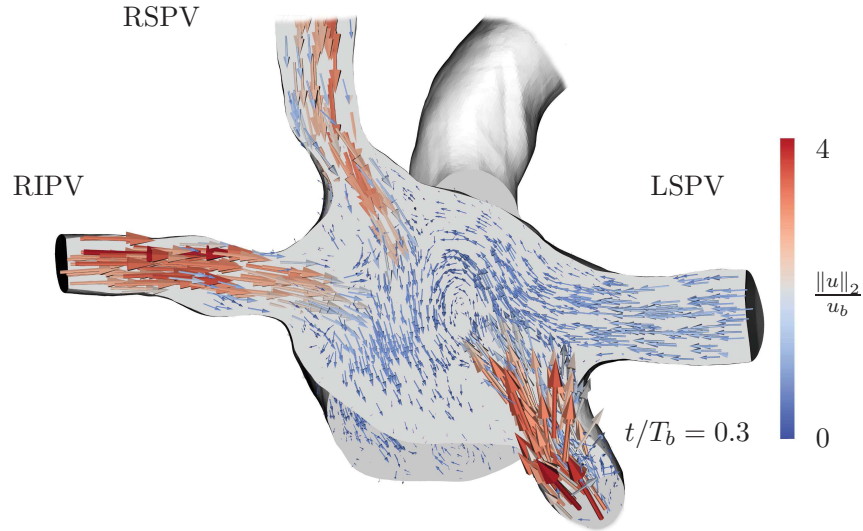


Figure 7.12: 3D velocity vectors in the atrium during systole at $0.3T_b$. The velocity field is only shown in the atrium. A plane passing through the four veins is included. Pulmonary veins are indicated.

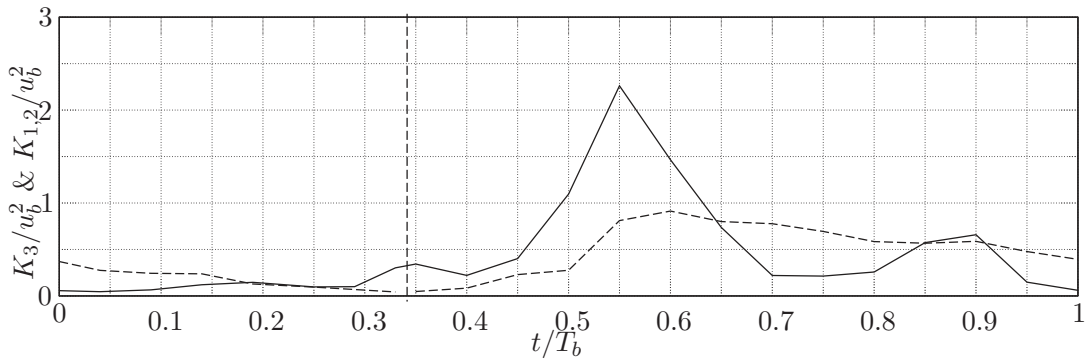


Figure 7.13: Kinetic energy of the axial flow velocity K_3 (solid line) and of tangential velocity component (dashed line) above the mitral valve. Figure 7.11 shows the location of the plane where K_3 and $K_{1,2}$ are calculated. Energies are nondimensionalised by u_b^2 . The vertical dotted line delimits the systolic phase from the diastolic phase at $t/T_b = 0.34$.

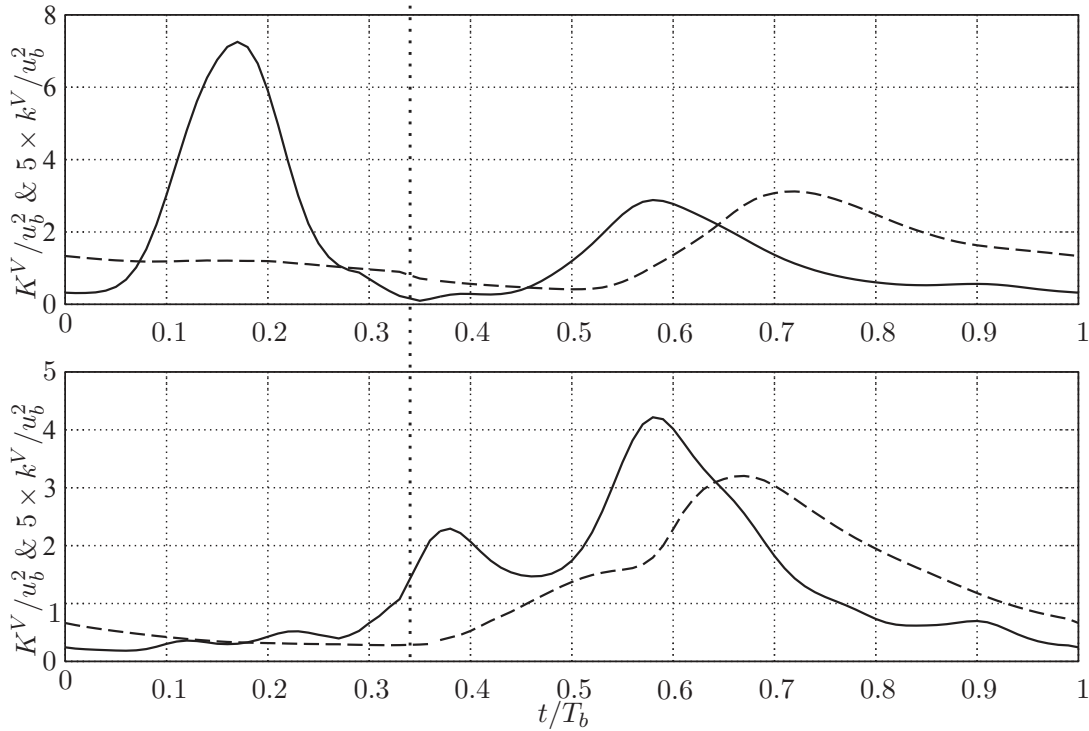


Figure 7.14: Volumetric mean flow kinetic energy K^V (full line) and five times the turbulent kinetic energy k^V (dashed line) in the left ventricle (top plot), and in the left atrium (bottom plot). The energies are nondimensionalised by u_b^2 . The vertical dotted line delimits the systolic phase from the diastolic phase at $t/T_b = 0.34$.

by what occurs in the axial direction (in particular by the A wave). This shows that even in the lower part of the atrium, blood motion is maintained thanks to this general swirling motion, whatever the details of the flow rate through the mitral valve.

7.2.6 Kinetic energy

Volumetric kinetic energy

The volumetric turbulent kinetic energy k^V and the volumetric mean flow kinetic energy K^V are defined as:

$$k^V(t) = \frac{1}{2V(t)} \int_{V(t)} \langle u_i u_i \rangle dV, \quad (7.6)$$

$$K^V(t) = \frac{1}{2V(t)} \int_{V(t)} \langle U_i \rangle \langle U_i \rangle dV, \quad (7.7)$$

with $V(t)$ being either the volume of the ventricle or the atrium volume at time t . Figure 7.14 shows how these energies evolve over the heart cycle, both in the ventricle (top plot) and the atrium (bottom plot). Note that $5k^V$ is plotted, so that the same scale is used to represent both energies.

In the ventricle, the volumetric turbulent kinetic energy k^V and the volumetric mean flow kinetic energy K^V behave like in *heart A*. However, during systole, the K^V level is more than 3 times higher than in *heart A* because of the higher velocities present at $0.17T_b$ in the ventricle for *heart B*. During diastole, the peak of K^V (at $0.58T_b$) is two times lower than in *heart A*. The k^V peak occurs at roughly $0.2T_b$ (it was $0.1T_b$ for *heart A*) after the K^V peak. The turbulent level during this peak in *heart A* is 1.7 times higher than in *heart B*. As described for *heart A*, the turbulent level measured in the ventricle is mainly due to the E wave jet and its wall interaction. Here, the weaker E wave jet explains the lower k^V observed.

In the atrium, the general behaviour observed in *heart B* follows what was described for *heart A*. Both energy levels stay small before the diastole. A first peak of mean flow kinetic energy (at $0.38T_b$), which was not present for *heart A*, is visible for *heart B* in the atrium. At $0.58T_b$, a peak of K^V is present with roughly the same energy level observed for *heart A*. The same remark stands for the turbulent kinetic energy.

Turbulent kinetic energy map

Figure 7.15 displays maps of the local turbulence kinetic energy. This energy is defined as:

$$k(\mathbf{x}, t) = \frac{1}{2} \langle u_i u_i \rangle. \quad (7.8)$$

Figure 7.15 displays the turbulent kinetic energy map at the same six instants displayed before. As expected, the beginning of systole is associated with a relaminarization of the LV. However, high level of k is visible in the aorta root ($0.15 T_b$). In the ventricle, the E wave vortex ring signature is visible from $0.5T_b$ to $0.65T_b$. Meanwhile, turbulent kinetic energy levels of the order of $2.3u_b^2$ are observed in the atrium. No clear separation is visible between the upper and the lower halves of the atrium, contrary to what was seen in *heart A*. However, slightly higher k values are visible in the upper right part of the atrium compared to the entire cavity. It is due to the interaction between the RSPV, RIPV and LIPV flows as explained in section 7.2.5. During diastasis ($0.75T$), the k level is well distributed in the atrium. The vortical structure provoked by the swirling motion in the atrium (described before in sections 7.2.2 and 7.2.3) is visible on the k map. The cycle-to-cycle variations of the vortical structure core is indicated by an arrow in Fig. 7.15. The ventricle is clearly not evenly filled by high values of k as in *heart A*. Here, the lower part of the ventricle looks free from turbulence. This result is due to the weaker E wave jet.

Production of turbulent kinetic energy

The turbulent production \mathcal{P}_k gives the rate at which energy is extracted from the mean motion to the fluctuations. It is defined as

$$\mathcal{P}_k(t) = -\langle u_i u_j \rangle S_{ij}. \quad (7.9)$$

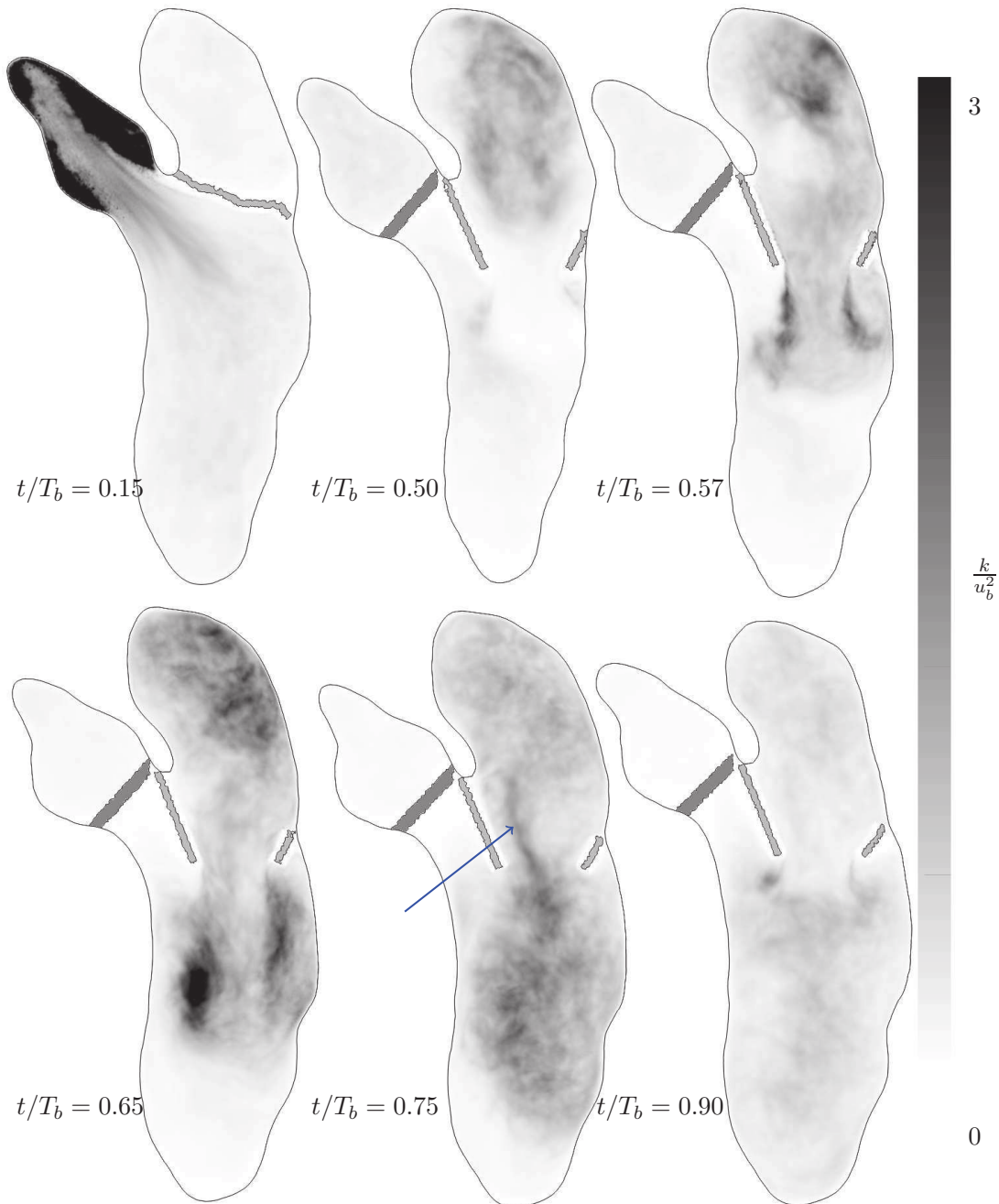


Figure 7.15: Nondimensional turbulent kinetic energy k/u_b^2 during the heart cycle.

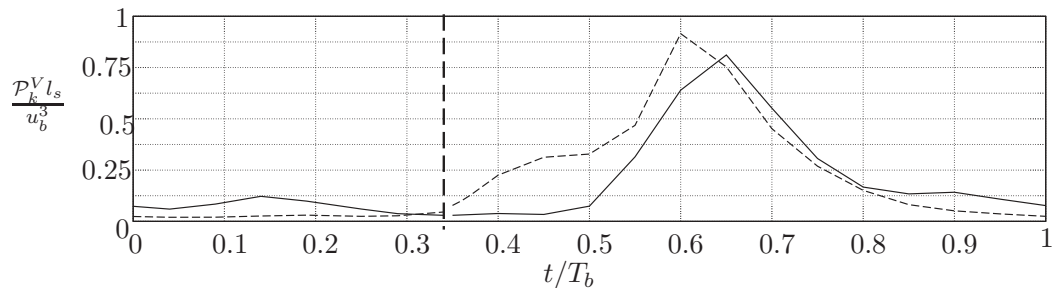


Figure 7.16: Volumetric production of turbulent kinetic energy \mathcal{P}_k^V in the ventricle (solid line) and in the left atrium (dashed line). Productions are both nondimensionalised by u_b^3/l_s . The vertical dashed line marks the limit between the systolic phase and the diastolic phase at $t/T_b = 0.34$.

This term is integrated over the ventricle and over the atrium, to obtain a volumetric production of turbulent kinetic energy defined as

$$\mathcal{P}_k^V(t) = -\frac{1}{V(t)} \int_{V(t)} \langle u_i u_j \rangle S_{ij} dV, \quad (7.10)$$

with $V(t)$ the volume of the ventricle or the atrium at time t . Figure 7.16 shows the volumetric production of turbulent kinetic energy \mathcal{P}_k^V in the two cavities, nondimensionalised by u_b^3/l_s . The general behaviour remains the same compared to *heart A*. Production peaks still occur roughly at the same time in both cavities. Production level in the atrium are roughly the same as in *heart A*. However, in the ventricle of *heart B*, the production level is half of the value measured in *heart A*.

Contrary to *heart A*, the TKE production in the ventricle is not essentially concentrated in the first half of diastole but for the first three quarters of T_b . From the time when the E wave jet enters the ventricle to some instants after the impingement of the jet, the production \mathcal{P}_k^V rises until its peak at $t/T_b = 0.65$. As for *heart A*, turbulence in the ventricle comes from the E wave jet and its loss of coherency. The production decreases during all the remaining time of diastole with a slight increase when the A wave enters the ventricle. As this vortex ring does not hit the lateral wall, the \mathcal{P}_k^V raises because of the cycle-to-cycle fluctuations of the jet trail. Still in the ventricle, non null \mathcal{P}_k^V levels exist during the systole. It was observed that part of the turbulence production was located at the postero-medial papillary muscles (which is indicated in Fig. 7.1). Physiologically, the papillary muscles are contracted during systole, leaving little room for generating shear and thus turbulence. It is possible that the papillary muscles deformations were not well modelled. On a side note, the chordae tendineae (see chapter 2) which are not modelled here should offer resistance to the flow and thus possibly creating turbulence in vivo.

In the atrium cavity of *heart A*, non-zero production was observed during systole. Here in *heart B*, the \mathcal{P}_k^V level is virtually null during systole. During diastole, raise of

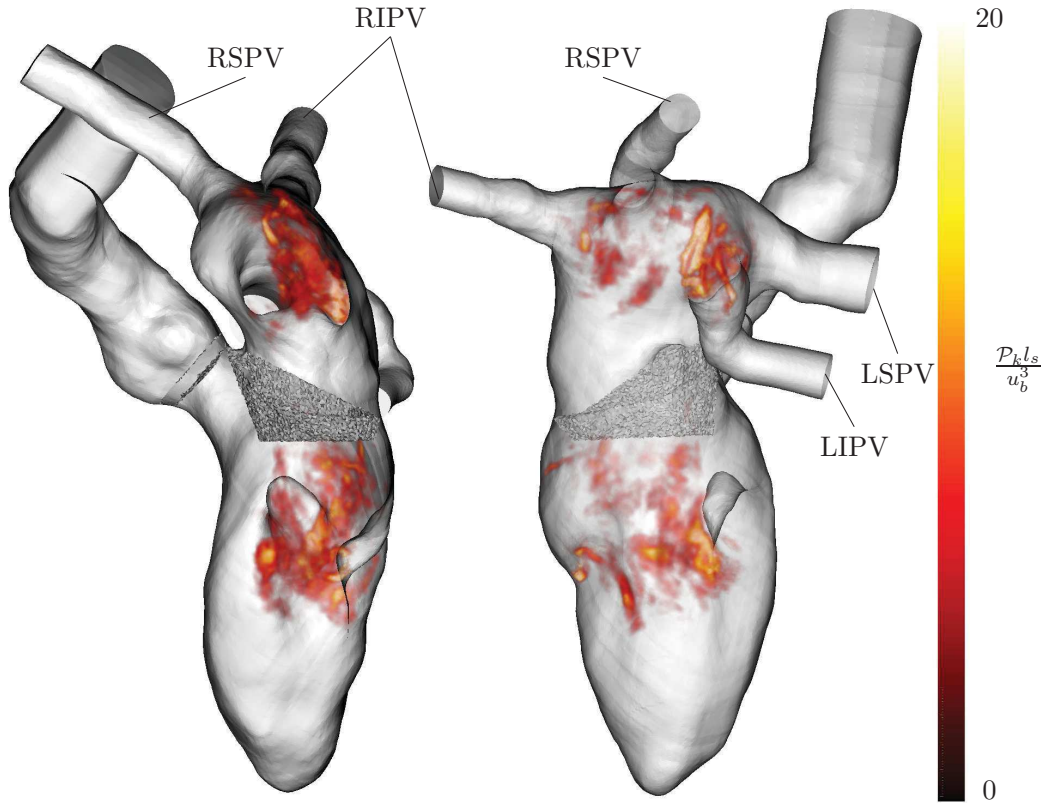


Figure 7.17: Volume rendering of the production of turbulent kinetic energy \mathcal{P}_k nondimensionalised by u_b^3/l_s at $t/T_b = 0.65$. The mapping relating production magnitude with opacity is linear. Heart wall is made partially transparent to allow observation.

\mathcal{P}_k^V in the atrium of *heart B* is not as sharp as in the atrium of *heart A*. The production is spread over one third of T_b .

Figure 7.17 displays the volume rendering of the production of turbulent kinetic energy at $0.65T_b$ for two different points of view. A part of the turbulent production in the atrium comes from the interaction of the inflowing jets from the RSPV and RIPV. The area where the jets are merging is visible in both plots in the upper right half of the atrium. In addition, the merged jets and their interaction with the atrial wall just before the LIPV ostium (merged jets can be seen in Fig. 7.11 top plot) generates shear, instabilities and thus turbulence production. In a similar fashion, the interaction between the merged jets and the inflowing jet from the LIPV is a source of turbulence production. Although the turbulence level is the same as in *heart A*, turbulence production does not come from direct jet collisions as in *heart A*.

In the ventricle, large production values are obtained in the shear layer of the trailing jet of the E wave vortex ring. Severe distortions of the jet seem to occur near the jet head, where it hits the lateral wall, accompanying large TKE production. The

turbulence production in the ventricle is the same as in *heart A*. However, it is worth pointing out that the production occurs in the upper half of the ventricle. As the E wave jet penetrates less in the ventricle, the turbulence produced in this area is less transported toward the ventricle apex.

7.2.7 Time-frequency analysis

Time-frequency representations are considered in this section. The signal of the vertical fluctuating velocity u_3 at each probe location is decomposed in 800 windows for which a Hann window with 50 % overlapping is applied and a short-time Fourier transform is used. The obtained spectrogram is then phase-averaged over the 30 cycles. Spectrograms computed with different overlappings and window functions display only small differences, showing that the following results are robust to the details of the signal processing. Frequencies higher than 200 Hz are not analysed because of the grid resolution. Considering a resolution of $l_c \sim \Delta x$, the cutoff frequency is estimated at $f_c = u_b/l_c \sim 280$ Hz.

Figure 7.18 displays the computed spectrograms. Each horizontal slice of a spectrogram exhibits the frequency spectrum of the flow at a specific time. Note that globally, the spectra decrease by about three decades before exceeding 50 Hz. In the ventricle at p_3, p_4, p_5 , for certain times during diastole, significant fluctuations may be observed even for frequencies higher than 100 Hz. p_6 is indeed close to the apex, where turbulence levels remain low in this heart. As in *heart A*, the high frequency fluctuations are only visible for a small time window. This time interval corresponds to the entering of the E wave jet in the ventricle and its scattering into small eddies. Then, the frequencies in the flow decrease during the whole diastole. Note that at location p_6 , the observed frequencies are under 75 Hz during the whole cycle. As expected regarding the high TKE levels in the aorta root (see Fig. 7.15), probe p_7 shows spectra exceeding 100 Hz during the whole systole.

The time-frequency behaviour in *heart B* is similar to *heart A*, the main differences being the A wave having influence in this heart and the fact that high frequencies are not visible in the apex area.

7.3 Final remarks

Looking at the hearts characteristics, differences between *heart A* and *heart B* principally lie in the E/A ratio, the mitral open area and the cycle duration. The general flow looks similar between both hearts. The main differences revealed in this chapter between these hearts are twofold. First, the flow seems more organized in the atrium and the general swirling motion is stronger in *heart B*. Second, the E wave jet is weaker.

However, the mechanism of turbulence creation remains the same here. Turbulence is created when jet impinges the heart wall or when velocity decreases. The TKE behaviour through the cycle is quite similar, even through levels in *heart A* are higher

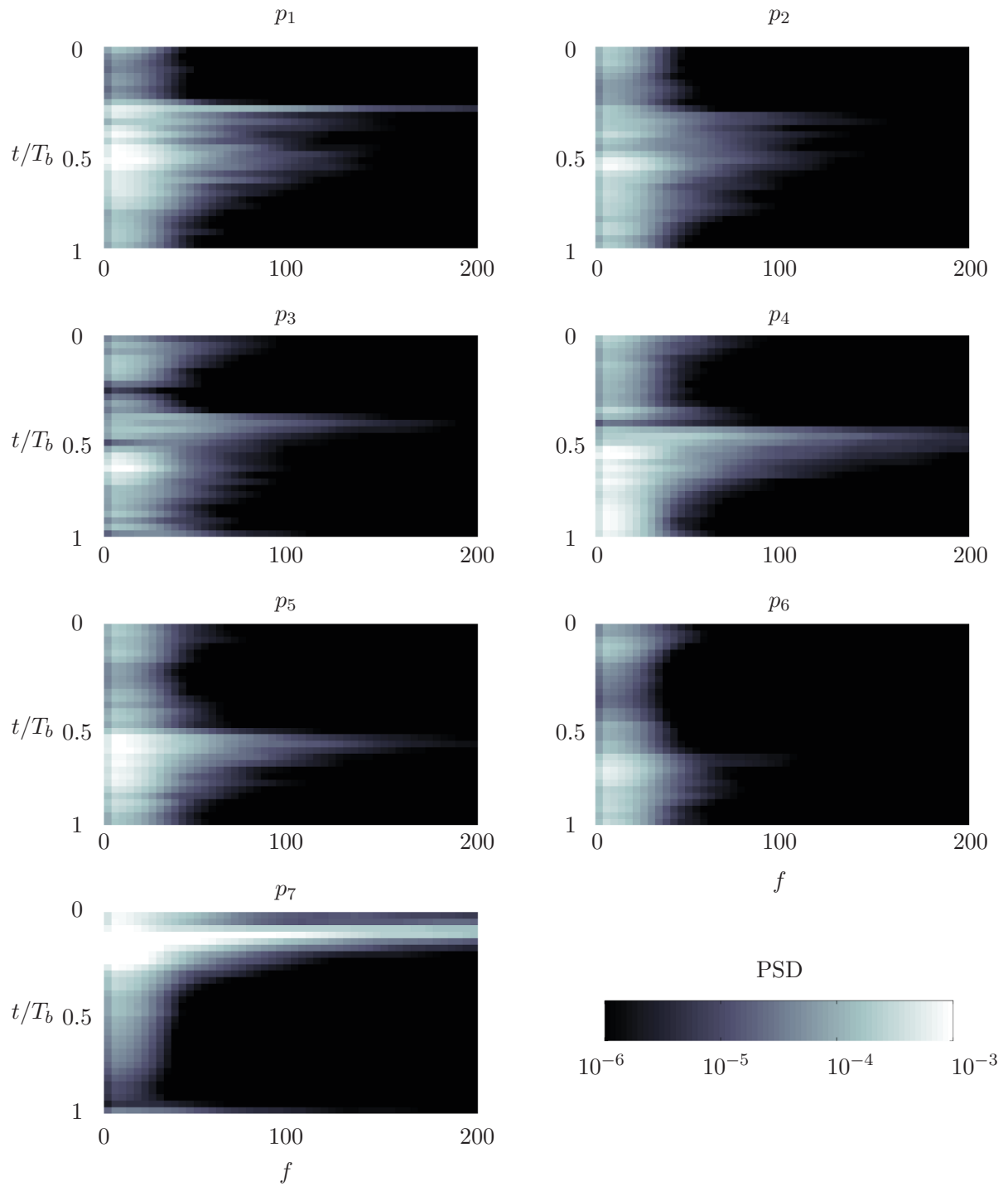


Figure 7.18: Time-frequency representation of the Power Spectral Density (PSD) of the vertical fluctuating velocity u_3 at the 7 probes locations. PSD is color coded (scale on the bottom right).

	<i>Heart A</i>	<i>Heart B</i>
Cardiac cycle (s)	$T_a = 1.0$	$T_b = 0.75$
E/A ratio	5.5	2.0
Ref. velocity (m.s ⁻¹)	$u_a = 0.10$	$u_b = 0.16$
Re_{max} at MV	5000	4520
Ventricle \mathcal{P}_k^V peak time	$0.57T_a$	$0.65T_b$
Ventricle \mathcal{P}_k^V peak value	$8.75u_a^3/l_s$	$0.79u_b^3/l_s$
Ventricle K^V peak time (diastole)	$0.54T_a$	$0.58T_b$
Ventricle K^V peak value (diastole)	$15.0u_a^2$	$2.9u_b^2$
Ventricle k^V peak time	$0.62T_a$	$0.71T_b$
Ventricle k^V peak value	$2.9u_a^2$	$0.59u_b^2$
Atrium \mathcal{P}_k^V peak time	$0.58T_a$	$0.6T_b$
Atrium \mathcal{P}_k^V peak value	$3.75u_a^3/l_s$	$0.91u_b^3/l_s$
Atrium K^V peak time (diastole)	$0.54T_a$	$0.57T_b$
Atrium K^V peak value (diastole)	$10.0u_a^2$	$2.9u_b^2$
Atrium k^V peak time	$0.6T_a$	$0.67T_b$
Atrium k^V peak value	$1.75u_a^2$	$0.62u_b^2$

Table 7.2: Main results for *heart A* and *heart B*.

than in *heart B* in the ventricle. However, same turbulence levels are measured in the atrium.

As suggested by the last chapter, the turbulence energy levels in the ventricle are determined by the energy of the E wave vortex ring. The E wave here is weaker: mitral velocity represents 65 % of the mitral velocity of *heart A*. As a consequence, the lower turbulence magnitude levels are not surprising. The peak value in the ventricle represents roughly 65 % of the *heart A* turbulence magnitude level. Table 7.2 summarizes some results of *heart B* accompanied with the counterpart results of *heart A* for comparison.

High frequency perturbations in the flow followed by a frequency decrease are observed as in *heart A*. Frequencies above 100Hz are only present during short time windows, of the order of $T_b/10$.

Chapter key points:

- The E wave jet does not reach the apex in *heart B*.
- As in *heart A*, the E wave jet is responsible of turbulence production in the ventricle.
- The E wave jet being weaker than in *heart A*, turbulence magnitude levels in the ventricle are lower than in *heart B*.
- In the atrium, unlike in *heart A*, the flow seems more organized. However, turbulence levels are similar between both atria.
- The TKE behaviour during the cycle is quite similar even if levels in *heart A* are higher than in *heart B*. Turbulence is created when jet impinges wall surface or when velocity decreases.
- High frequency fluctuations followed by more quiescent flow are observed as in *heart A*.

Part IV

Lagrangian analysis

Study of tracers transport in left hearts

Chapter contents

8.1	Introduction	160
8.2	Method	160
8.3	Results for the <i>heart A</i>	163
8.3.1	Ventricle global behaviour	163
8.3.2	Left ventricle: residence time	164
8.3.3	Left ventricle: penetration	165
8.3.4	Left ventricle: path length travelled	168
8.3.5	Left ventricle: mean particle velocity	169
8.3.6	Left atrium: residence time	169
8.3.7	Left atrium: mean particle velocity	170
8.4	Results for the <i>heart B</i>	172
8.4.1	Global behaviour	172
8.4.2	Left ventricle: residence time	173
8.4.3	Left ventricle: penetration	174
8.4.4	Left ventricle: path length travelled	176
8.4.5	Left ventricle: mean particle velocity	176
8.4.6	Left atrium: residence time	177
8.4.7	Left atrium: mean particle velocity	178
8.5	Conclusion	179

This chapter describes the transit of blood through the two left hearts described in the previous chapters. The flow is here described from a Lagrangian point of view. Flows are seeded with massless particles to mimic the trajectories of red blood cell in the heart. Statistical data are gathered and analysed.

8.1 Introduction

As already shown, the complex geometry of the left heart and its movement lead to complex flow patterns. In addition, cardiac cavities are not emptied at each cardiac cycle. This raises questions about the transit of red blood cells in the heart. For example, red blood cells can stay in the atrium or in the ventricle for several cycles. What is the repartition of the residence time? What are the cells trajectory in the heart? Transit of red blood cells was rarely accounted for in previous studies, due to its complexity. An Eulerian point of view has been adopted to describe the blood flow in this work so far. However, complementary information could be extracted from a Lagrangian approach.

Studies have been conducted using MRI [20, 23, 51], but they suffer from low spatio-temporal resolution thus making the results prone to large interpolation errors. A promising study has been conducted by Hendabadi *et al.* [79], using novel processing of Doppler-echocardiography. They were focusing on residence time and blood transport patterns. Likewise, numerical simulations of an idealized left ventricle have recently been conducted by Zheng *et al.* [188] and Seo *et al.* [156]. The focus was placed on residence time and blood mixing for different E/A ratios.

Still, the effects of filling process considering an entire heart has not been fully investigated in details. To this end, both models developed during this thesis is here used. The first heart described in this chapter corresponds to the large E/A ratio heart (ratio of 5.5) and described in chapter 5 and in chapter 6. It will be refereed as *Heart A* as in the previous chapters. The second one is the healthy heart with a E/A ratio of 2.0 presented in chapter 7. It will be refereed as *Heart B*.

The method applied in this chapter is briefly described in section 8.2. Results will be first presented qualitatively, providing a global view of the flow. Statistics on the residence times and mean particle velocity will be provided for both the atrium and the ventricle. Particles penetration and mean path length in the ventricle will be described as well. The results for *heart A* and *heart B* are respectively detailed in section 8.3 and section 8.4. Section 8.4, which focuses on the *heart B*, does not cover details about the features shared by both hearts. Instead, the section details comparisons between them. Finally, section 8.5 presents a discussion of the results and final remarks.

8.2 Method

The simulations presented in this chapter have been conducted simultaneously with the ones presented before. In the light of the previous comparison and discussion on the SGS model (chapter 5 section 5.4.2), the LES presented in this chapter are performed using the sigma model. Blood is still modelled as an incompressible fluid. As shown in chapter 5, the shear-thinning behaviour of blood does not have a major impact on the flow results. Blood is thus modelled as an incompressible Newtonian fluid in this chapter. The fluid motion is thus described, in the same way as the last chapters, by

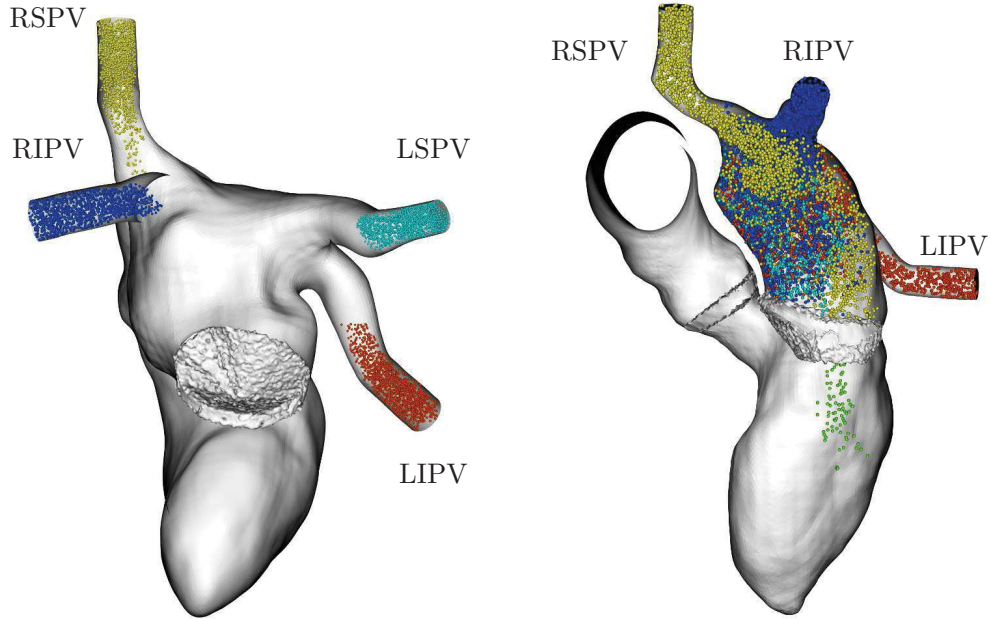


Figure 8.1: Scheme of *heart A*. The names of the four pulmonary veins are indicated. Statistics are saved first when the particles pass through the mitral valve (coloured in green in the right figure to indicate that they are accounted for in statistics) and then when the particles pass through the aortic valve.

the NS equations. Other parameters such as the boundary conditions and deformations were already described in chapter 6 for *heart A* and in chapter 7 for *heart B*.

The Stokes number indicates if the particles are tracers. The Stokes number (St) corresponding to the behaviour of the red blood cells in the plasma is defined as:

$$St = \frac{\rho_r d_r^2 u_a}{\mu_f l}, \quad (8.1)$$

where ρ_r is the red blood cell density, d_r its diameter, μ_f the plasma dynamic viscosity and l a characteristic length of the flow. Here, the red blood cell density is considered the same as the plasma density, the flow characteristic length l is set to 10^{-2} cm and red blood cell diameter is set to 7×10^{-6} m. The Stokes number is then small enough to consider the red blood cells as tracers as $St \ll 1$. Red blood cells are thus modelled thanks to massless particles. Moreover, the particles have no effect on the fluid flow and presumably do not interact with each other.

The velocity $u(\mathbf{x}_p)$ of each particle is computed thanks to an interpolation from the Eulerian velocity field. A classical inverse distance weighting interpolation method is used to this respect. The particle position at the next time step is then given by,

$$x_p(t + \Delta t) = x_p(t) + \int_t^{t+\Delta t} u(x_p) dt, \quad (8.2)$$

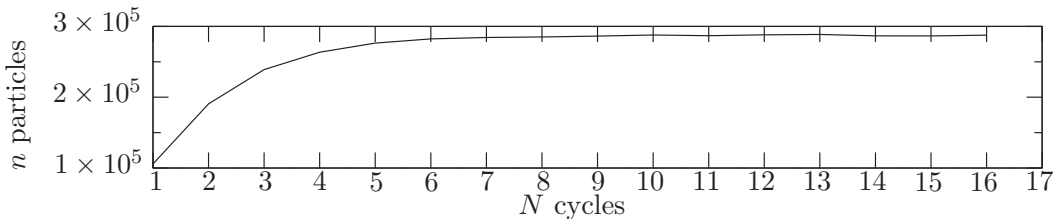


Figure 8.2: Convergence of the number of particles at the end of the diastole in the *heart A* for each computed cycle.

where Δt is the numerical time step and where the time integration is performed by a three-stage Runge-Kutta method. Particles are introduced in the heart flow through the numerical domain inlets. A color flag from 1 to 4 distinguishes where the particles come from. Figure 8.1A shows these numerical flags traduced by different colors. the flag is 1 for particles from LSPV, 2 for RIPV, 3 for LIPV and 4 for RSPV. The number of particles injected depends on the flow rate imposed at the inlet patch. The injection rate is fixed at 10^5 particles per second, but is scaled by the ratio between the flow rate imposed at the pulmonary veins and its maximum: Q_{pv}/Q_{pv}^{max} . During flow reversal at the pulmonary veins, no particles are injected and they are deleted from the domain if they leave it.

Particles data are saved when particles pass predefined planes: the first plane is the elliptical mitral open area and the second plane is the aortic plane (see chapter 4 for details on valve models). This procedure enables to obtain separate statistics for the atrium and for the ventricle. The counting at the mitral is effective only during diastole, as the mitral valve is closed the rest of the time. Similarly, for the aortic plane, the particles statistics are gathered only during systole. Particles passing through the aortic plane during systole are then removed from the numerical domain. For each particle, the life time, integrated kinetic energy, path length and the color flag between 1 and 4 are saved first when passing through the mitral plane, then passing the AV plane. In addition, at the aortic plane, the minimum level reached in the ventricle (z coordinate) and the simulation total time are also stored. Mean and root mean square velocity along the trajectory can be computed from these data. From the stored information, particles entering in the LV during the E wave can be easily identified.

To ensure accurate statistics, several heart cycles were computed, until the number of particles within the ventricle and the atrium is stabilized. Figure 8.2 shows the convergence for *heart A*. Around six cycles were necessary to reach an almost constant number of particles in the domain. Ten more cycles have been computed and statistics have been gathered over the last three cycles. Thus, statistics cannot be computed for particles with a life time greater than seven heart cycles. The stabilized number of particles in the heart is close to 3×10^5 .

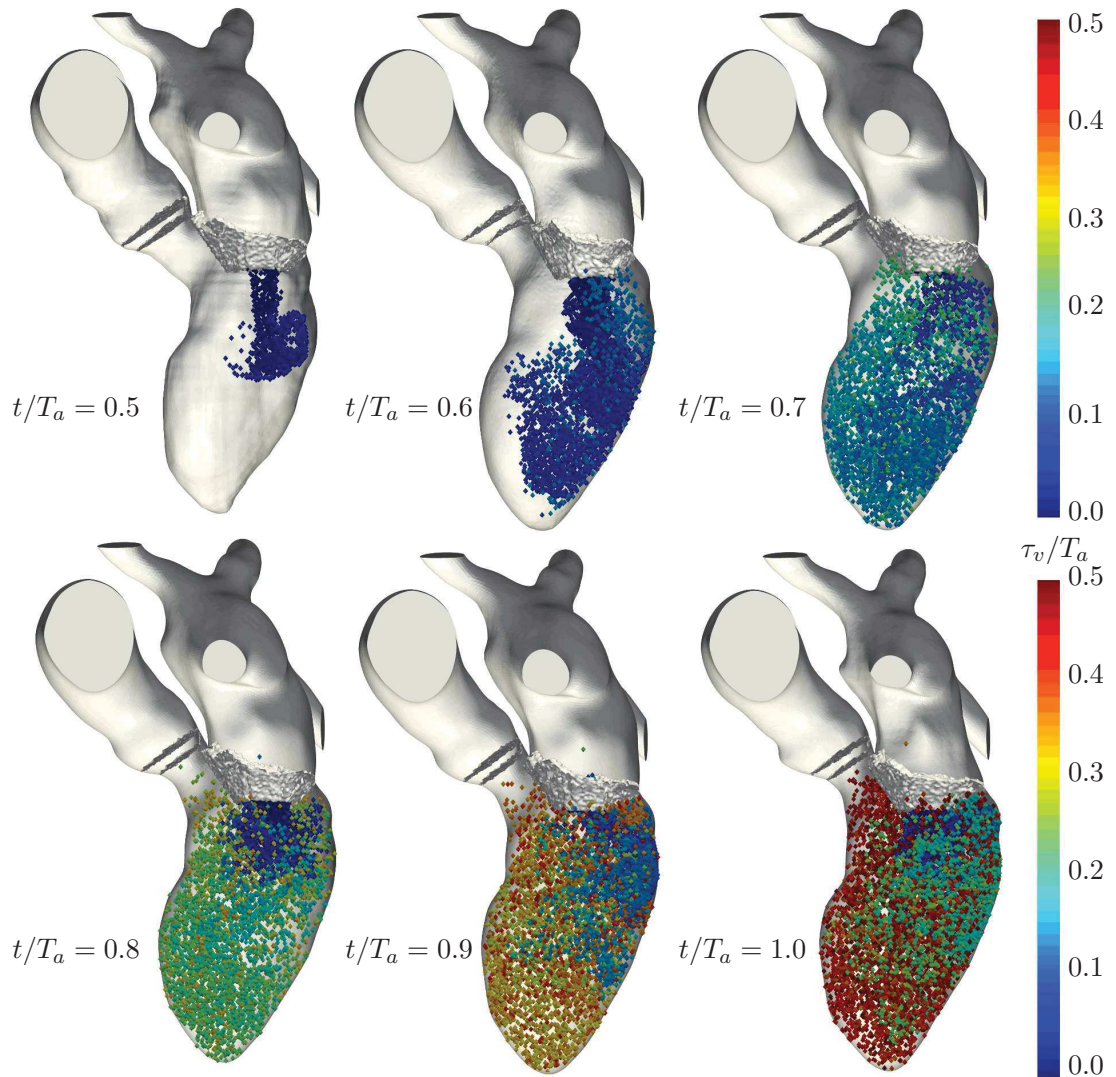


Figure 8.3: Particle residence time is shown for *heart A*. Six times during diastole are shown. Only 50 000 particles are displayed for a better visualization.

8.3 Results for the *heart A*

8.3.1 Ventricle global behaviour

The time for a red blood cell to travel from the mitral opening plane to the aortic plane is defined as $\tau_v = t_{ao} - t_{mv}$ where t_{mv} (resp. t_{ao}) is the time when the particle passes through the mitral plane (resp. aortic plane). Figure 8.3 shows the ventricle residence time for 50 000 particles in *heart A*. The number of particles was deliberately limited in order to have a better visualization. Six different times are displayed, all of them during diastole. Interestingly the particles issued from the RSPV follow the atrium wall

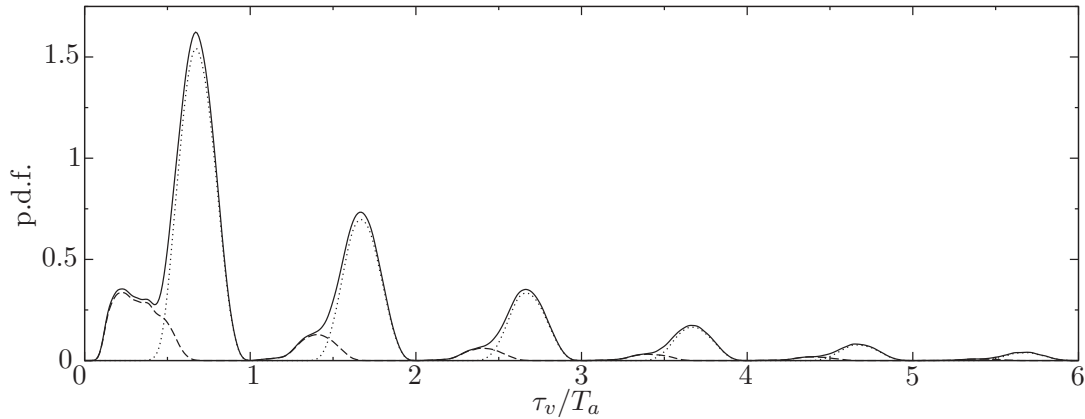


Figure 8.4: Probability density function of residential time in the left ventricle (solid line). The E wave contribution is plotted with a dotted line, the remaining contribution (L and A wave) with a dashed line.

resulting in a direct pathway toward the mitral plane. This behaviour is in fact coherent with the flow features discussed in chapter 5.

At $t/T_a = 0.5$, the E wave vortex ring is clearly bounded by the fresh particles entering the ventricle. At $t/T_a = 0.6$ after the vortex ring hits the lateral wall, the flow momentum redirection has an important effect on the particles. While a part of the particles go toward the apex, a non negligible amount of particles are entrained toward the mitral valve. What this means is that the particles repartition is strongly influenced by the vortex ring, its interaction with the lateral wall and its velocity as well. Between $t/T_a = 0.7$ and 0.9 , the L and the A waves enter the ventricle. Older particles are entrained from the base to the apex and from the apex to the septum wall of the ventricle. Differentiation between lateral wall and septum wall is clearly seen in term of residence time here. However a lot of fresh particles stays in the top half of the ventricle.

8.3.2 Left ventricle: residence time

Particle residence times were gathered and a probability density function (p.d.f), shown in Fig. 8.4, is computed to provide quantitative data. The probability density function (in solid line) shows distinct peaks which individually look similar to normal distributions. Interestingly, there is finite time windows where the E wave particles have their residence time as *new* particles can only enter during the diastole. For this heart, the median residence time in the ventricle is $0.8 T_a$. Half of the particles are hence ejected through the aorta in less than one heart cycle. The term "*direct flow*", first introduced by Bolger *et al.* [20], defines the particles ejected from the ventricle in one heart cycle. Here, the *direct flow* represents 55 % of the particles. In the same spirit, 79 % of the particles are ejected in two cycles, 90 % in less than three and 96 % in less than four

heart cycles. These figures are way higher than the ones found in the rare literature on this subject. Thanks to MRI methods, Bolger *et al.* [20] found a *direct flow* of 21 ± 6 %, and Eriksson [51] 38 ± 5 %. Hendabadi *et al.* [79] obtained a direct flow of 43 ± 11 % using echocardiography, which is closer of our value of 55 %. Through numerical simulation of left ventricles, Seo and Mittal [156] found a *direct flow* between 48 and 54 % by changing the E/A ratio between 0.5 and 2, for normal haemodynamics. Through simulation study of realistic left heart, Doenst *et al.* [42] computed the *direct flow* using the ejection fraction. Doenst *et al.* *direct flow* is then computed by assuming that the blood is perfectly mixed in the ventricle. The presented results shows that this estimation is acceptable as the fraction ejection for this patient is 58 %, which is really close of the measured *direct flow* of 55 % for *heart A*.

The residence time p.d.f. is now decomposed in two parts: an E wave contribution (dotted line) and the remaining part (dashed line), composed by the L wave and A wave contributions (see Fig. 8.4). Results show that the particles from the A wave follow almost a normal distributions as well. This p.d.f. contribution can be read as a sum of normal distributions with very similar standard deviations ($\sigma \sim 0.1$) and similar shifted means (~ 68 % of the considered cycle).

However, the remaining contributions deform these distribution (mainly visible in the firsts cycles): for each cycle, the particles from the remaining contributions are ejected first. Particles from the L and A wave contributions have a median residence time of $0.44 T_a$. Half of these particles are ejected in less than a half of heart cycle, and 65% of the particles in one cycle, 90% in less three cycles.

Note that the idea first introduced by Watanabe *et al.* [178] of "first-in, first-out" is not respected here. In this hypothesis, the ejection should remove the residual blood before the blood freshly injected in the ventricle. Here on the contrary, a "last-in, first-out" is observed, as particles entering the LV during the L wave and the A wave are located close to the aortic root at the beginning of the systole and a thus rapidly exiting the LV.

8.3.3 Left ventricle: penetration

The study of the penetration of the particles within the heart can explain this "last-in, first-out" phenomenon. The penetration is defined as z_{min}/l_d where the quantity z_{min} for a particle is the minimum depth reached by this particle during its lifetime. l_d is the ventricle maximum length during diastole. The p.d.f. of the penetration z_{min}/l_d is plotted in Fig. 8.5. A particle reaching the apex at one moment along its trajectory has the value of 0. In the contrary, a particle staying at the mitral valve level and exiting the ventricle has the value 0. The p.d.f shows that particles can travel through the entire ventricle. The p.d.f shows two distinct peaks, one around $0.1 l_d$ and another around $0.75 l_d$. The median value of the penetration is 0.71 and about 90% of the particles go deeper than 40% of the ventricle length. Decomposition of the p.d.f. between the particles coming from the E wave and the others (see Fig. 8.5) shows that the E wave

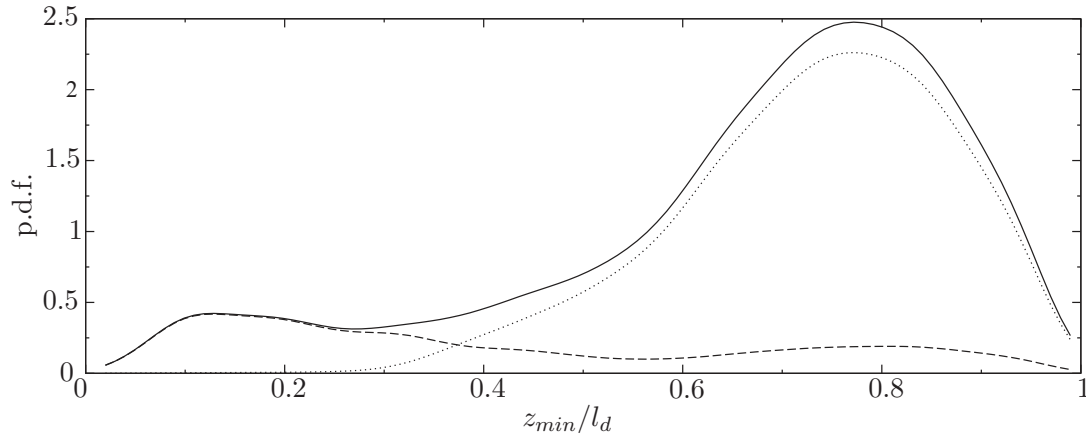


Figure 8.5: Penetration within the left ventricle is given by the particle minimum level in the cavity. Here in solid line, the probability density function of the minimum level z_{min} nondimensionalised by the maximum length of the ventricle l_d is plotted. 0 being the mitral valve level, 1 the apex. The E wave contribution is plotted with a dotted line, the remaining contribution with a dashed line.

particles travel deeper in the ventricle. The median value of the E waves particles penetration is 74% while the L and A waves particles have a median value of 33%. Hence, because the L and A waves particles stay in the upper part of the ventricle, they are ejected first. The reason why these particles do not travel deeper in the ventricle because of the weak A wave for *heart A*. Anticipating on the results of section 8.4.3, we can state that this low penetration is related to the weakness of the A wave in this heart. *Heart B*, has a more intense A wave has also particles from the A wave reaching deeper positions in the ventricle. Results for the E wave particles penetration are concentrated mainly between $0.3 l_d$ and $1 l_d$ while the other particles can be found at every depth in the ventricle. This can be explained by the fact that the particles from the L and A wave stay in the ventricle for more than a cycle, and are dragged deeper in the heart during the next diastole thanks to the E wave.

The two variables z_{min}/l_d and τ_v/T_a can be observed through a bivariate distribution (see Fig. 8.6). The upper plot is the bivariate p.d.f. of the particles only coming from the E wave. The bottom plot shows the same distribution but for all the particles. When looking at the p.d.f. for the E wave particles, the narrow time windows where the "close to normal" p.d.f. were observed (see Fig. 8.4) is visible; note also that the median penetration in the ventricle does not show high variations with respect to the residence time. In addition, residence time and penetration in the left ventricle have a weak correlation ($r = 0.52$) suggesting that there is no stagnation zone.

When the L and A waves contributions are added (bottom plot), their contribution is visible mainly in the upper left of the plot, expressing a low penetration and an associated low residence time of these particles. For particles with a residence time

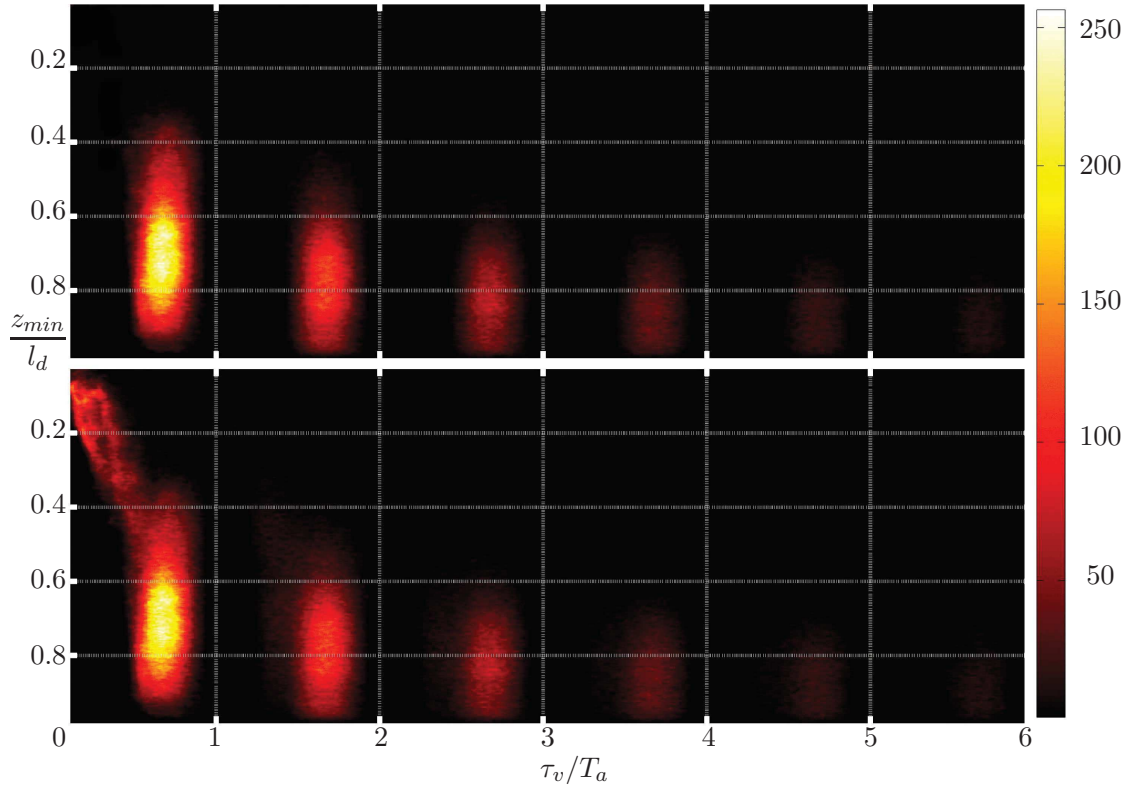


Figure 8.6: Bivariate distributions of variables z_{min}/l_d and τ_v/T_a . Top plot is the distribution of the E wave contribution only while the bottom plot is the total p.d.f.

greater than $1T_a$, the L and A waves contribution is more subtle. The particles mainly go deeper than 60% of the ventricle, as the E wave particles. However, L and A waves particles are ejected through the aorta earlier than the others, explaining why there is a contribution visible in the left of the total distribution for each cycle.

These bivariate distribution of the residence time versus the penetration of the particles is a bio-marker of a weak A wave and a strong E wave. This information is another way of observing the E/A wave ratio which is classically used in clinical routine [125]. This distribution could give more information than a simple velocity ratio. Indeed the weak penetration is a consequence of the high E/A ratio for this patient but it could give also an indication of a pathology. A patient with a normal E/A ratio could have a pathological distribution if the intracardiac flow is not normal. In pathological state a non-uniformity of the ventricle relaxation for example could affect the A wave filling.

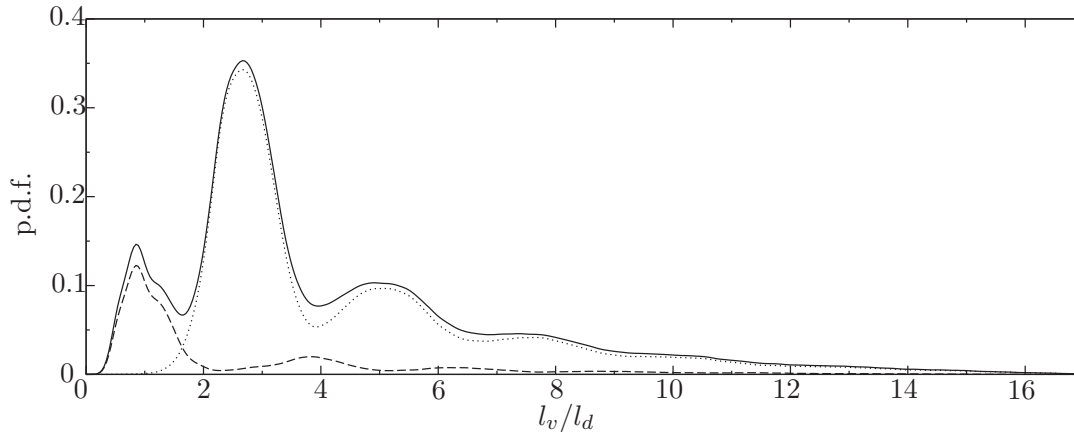


Figure 8.7: Probability density function of path length in the left ventricle (solid line). The E wave contribution is plotted with a dotted line, the remaining contribution with a dashed line.

8.3.4 Left ventricle: path length travelled

The particles path length in the ventricle is measured. Figure 8.7 shows the p.d.f. of the path length l_v nondimensionalized by the length of the ventricle l_d . The distribution shows different peaks. Peaks are visible at roughly 0.9 , 2.5 , 5 and $7.5l_d$. After $10l_d$ the distribution decreases linearly. The median value is 3.15 and surprisingly, particles can travel more than ten times the ventricle length.

Decomposition between the contributions of E and L-A waves show that the first peak at $l_v/l_d = 0.9$ of the p.d.f. is due to the L-A waves particles. 65% of the L-A waves particles travel less than $2l_d$. This L-A waves contribution shows lower peak at around $3.9l_d$ and another one at $6.4l_d$. The same differences of $2.5l_d$ is visible between peaks of the E wave contribution at 2.5 , 5 and $7.5l_d$. These peaks are certainly the consequence of the recirculating cell in the ventricle, $2.5l_d$ being roughly the distance travelled from the mitral valve plus the travel to the apex and back to the base of the ventricle plus the velocity fluctuations. The L-A waves particles with a longer residence time are 'trapped' in the same mechanism as the E wave particles, explaining the deeper penetration of the L-A waves with a residence time higher than $1T_a$ as discussed in the former section. Interestingly, the percentage of L-A waves particles travelling less than $2l_d$ and the ones which have a residence time smaller than $1T_a$ is the same.

The study of the path length by subclasses of residence time (not shown here) shows that particles with a residence time of less than $1T_a$ travel less than $4l_d$. Apart from this *direct flow*, other residence time subclasses correspond to normal distribution and peak of each of the distribution corresponds to the peaks evoked before, reinforcing the idea that for each heart cycle, the particles travel roughly $2.5l_d$ in the ventricle.

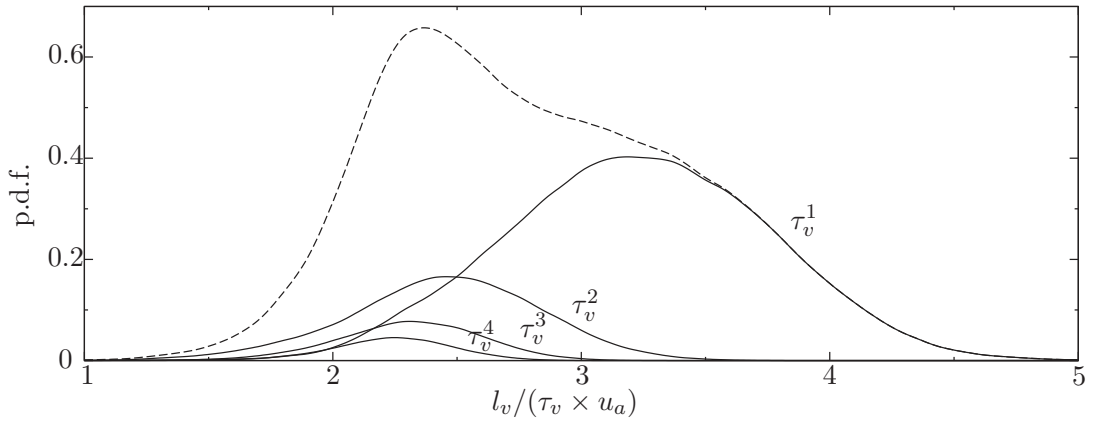


Figure 8.8: Probability density function of the mean particle velocity within the left ventricle is plotted in dashed line. Each residence time subclass is defined as $\tau_v^k = \{\tau_v | k - 1 < \tau_v/T \leq k\}$.

8.3.5 Left ventricle: mean particle velocity

The probability density of the mean particle velocity defined has l_v/τ_v , and nondimensionalized by u_a (as a reminder, $u_a = 0.1 \text{ m.s}^{-1}$), is plotted in Fig. 8.8. Here, the velocity has not been decomposed in E and L-A contribution as the differences between the two contributions is mainly due to their magnitude differences. The median velocity is $2.8 u_a$. This p.d.f. is decomposed in residence time subclasses defined has $\tau_v^k = \{\tau_v | k - 1 < \tau_v/T \leq k\}$. The four first subclasses are plotted in Fig. 8.8. All the subclasses p.d.f. remarkably follow normal distributions, the mean being smaller and smaller with larger residence time. The τ_v^1 subclass represents 55 % of the particles and have a mean velocity of $3.2u_a$, the upper subclasses having a mean velocity decreasing toward $2.25 u_a$. The higher velocity of the first τ_v^1 subclass can be explained by its quick ejection through the aorta. These particles keep the high velocity of the E wave which made them enter the ventricle. They stay for only one diastasis and leave before systole, which feature both low velocity. Note that mean velocity and penetration z_{min} are not correlated; the difference of velocities is not a consequence of penetration.

8.3.6 Left atrium: residence time

In order to provide an analysis of the atrial flow from the Lagrangian point of view, we now detail the results for the atrium only. The particle residence time is gathered and the probability density function is reported in Fig. 8.9. The probability density function (in solid line) distinctly shows four peaks. Contrary to what happens in the ventricle, the particles enter continuously in the atrium, which changes the general aspect of the p.d.f. (compared to Fig. 8.4). However, no particle is measured with a residence time smaller than $0.21 T_a$, which must be the lowest time needed from the veins to the mitral

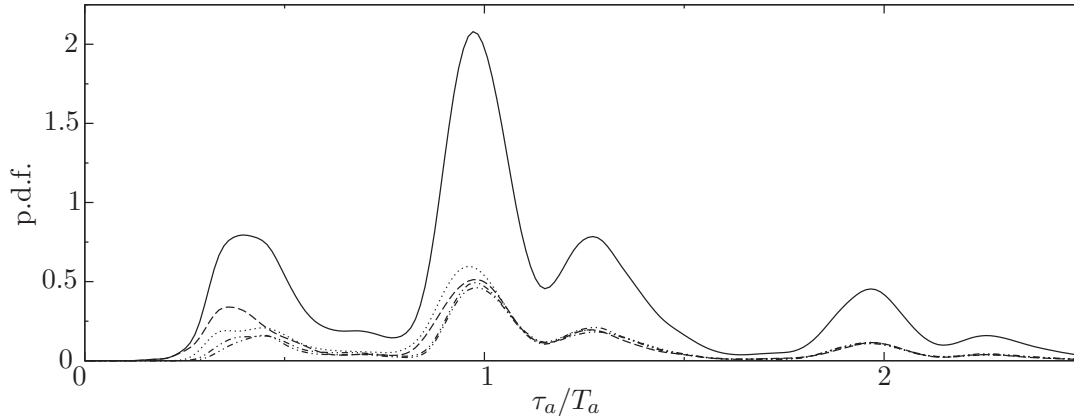


Figure 8.9: Probability density function of residence time in the left atrium (solid line). Each pulmonary vein contribution is plotted as well: RSPV (dashed line), RIPV (dotted line), LIPV and LSPV contributions are plotted using the same line as differences between the two are small.

valve. For this heart, the median residence time to travel in the atrium is $1T_a$. Half of the particles are hence ejected through the mitral valve in one heart cycle which is less than in the ventricle.

The decomposition of the residence time p.d.f. into four contributions from the four pulmonary veins show similar values. However, particles coming from the RSPV and from the RIPV pass from the atrium to the ventricle in less time than the others. The particles coming from the RSPV follow the atrial wall in a swirled trajectory and reach the mitral valve fast. A part of particles coming from the RIPV passes 'under' the point of impact of the atrial jets. As first observed by Fyrenius [62], this result seems paradoxical, given that the left lower pulmonary venous jet enters in closer proximity to the mitral valve. Instead of exiting the atrium, the particles issuing the left sided inflows are trapped and recirculate in vortices before finally moving toward the mitral valve. This disparate behaviour between left and right venous particles can be anticipated from the flow description from chapter 5. However, the particles remaining more than one cycle lose memory of where they come from, as shown by the similar behaviour observed for the the four PV for residence time superior to T_a .

8.3.7 Left atrium: mean particle velocity

The probability density of the mean particle velocity, defined has l_a/τ_a and nondimensionalized by u_a , is plotted in Fig. 8.10. Here, the velocity has been decomposed in the fourth first subclasses of residence time defined has $\tau_a^k = \{\tau_a | k - 1 < \tau_a/T \leq k\}$. This p.d.f. has the appearance of a gamma distribution instead of the normal distribution aspect seen in the ventricle. Using a common gamma distribution parametrization with a shape parameter k and a scale parameter θ , one can observe that the scale parameter

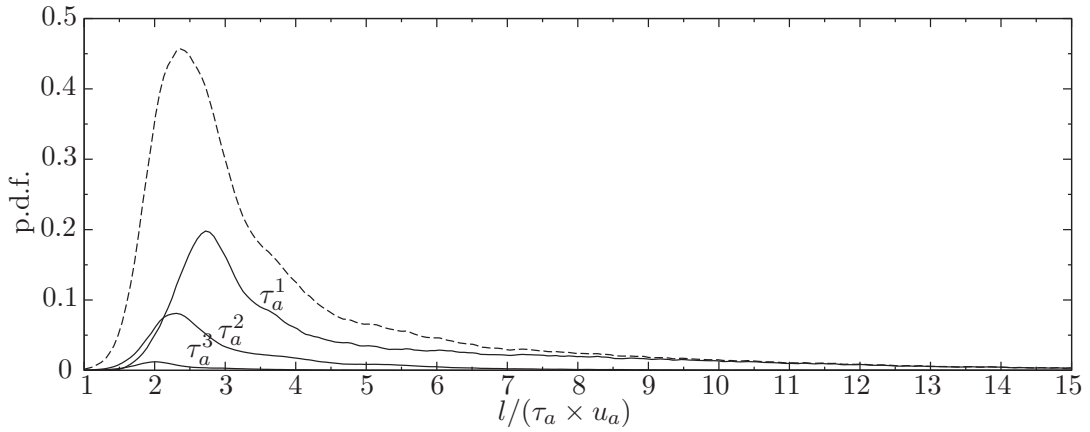


Figure 8.10: Probability density function of the mean particle velocity within the left atrium is plotted in dashed line. Each residence time subclass (defined as $\tau_a^k = \{\tau_a | k - 1 < \tau_a/T \leq k\}$) contribution is plotted.

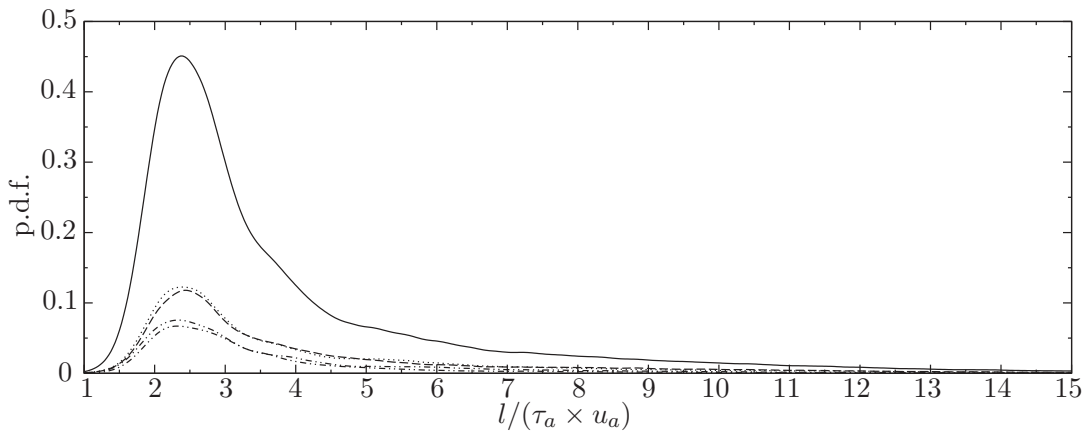


Figure 8.11: Probability density function of the mean particle velocity within the left atrium is plotted in solid line. Each pulmonary veins contribution is plotted. The RSPV in dashed line, RIPV in dotted line. The LIPV and LSPV contribution are both in dashed dotted dotted line as differences between the two are small.

remains similar, while the shape parameter decreases as higher residence time subclasses are observed. The τ_a^1 subclass represents 45 % of the particles and have a median velocity value of $4.9u_a$. The upper subclasses have a mean velocity decreasing to reach $2.1u_a$ for the subclass τ_a^6 .

The higher velocity of the first τ_v^1 subclass can be explained by its quick ejection through the aorta. These particles rapidly acquire high velocity of the E wave, during which they enter the ventricle.

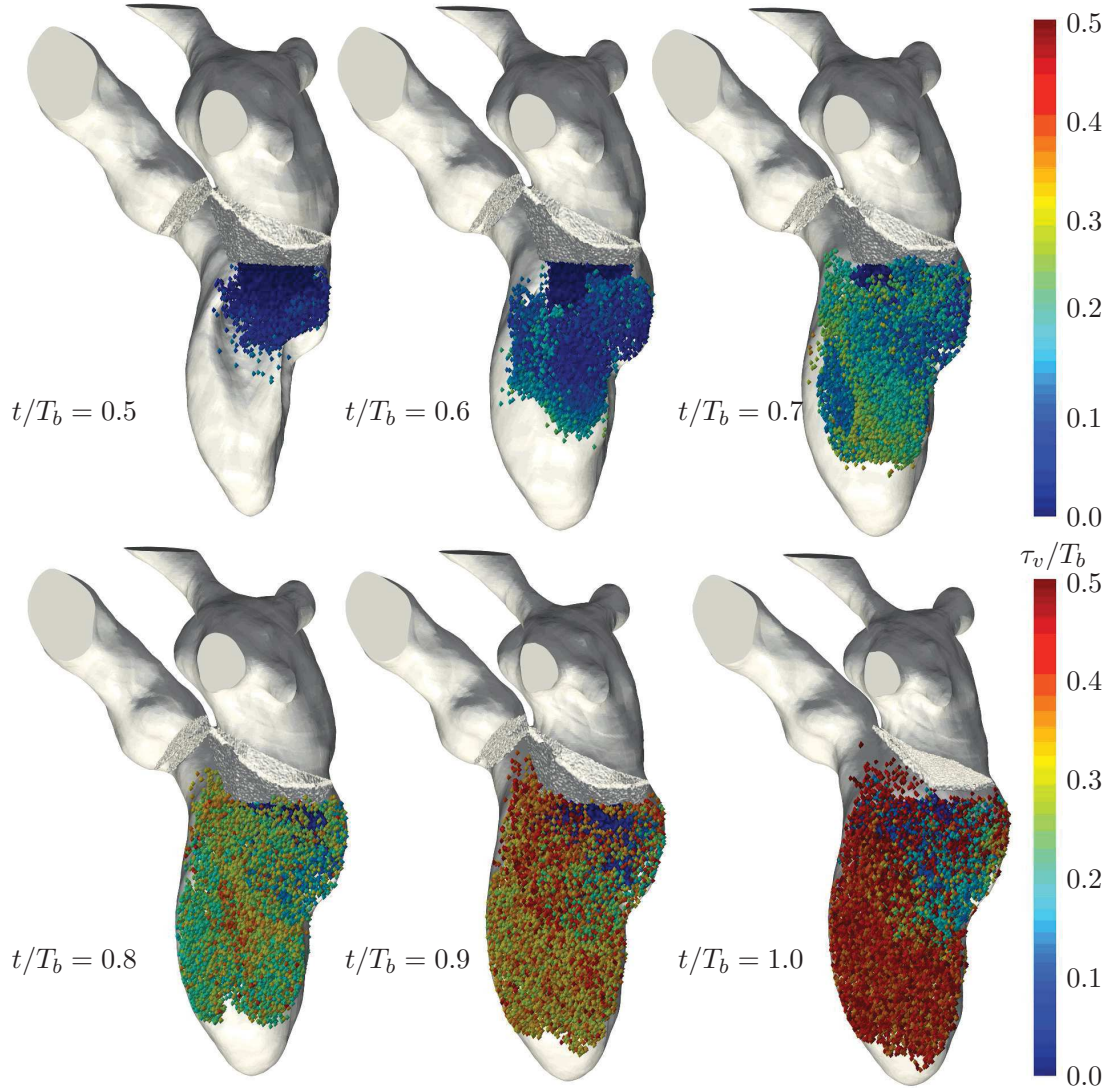


Figure 8.12: Residence time is shown for the healthy subject: *heart B*. Six instants during the diastole are shown. Only 50 000 particles are shown for a better visualization.

8.4 Results for the *heart B*

Results in *heart A* are specific to heart having a high E/A ratio. *Heart B*, which is a healthy heart, presents more classic characteristics. The particle analysis is thus reported here to highlight the common and distinct features in the two hearts.

8.4.1 Global behaviour

As for *heart A*, the ventricular residence time is calculated between the mitral opening plane and the aortic plane. Figure 8.12 shows the particle residence time for 50 000

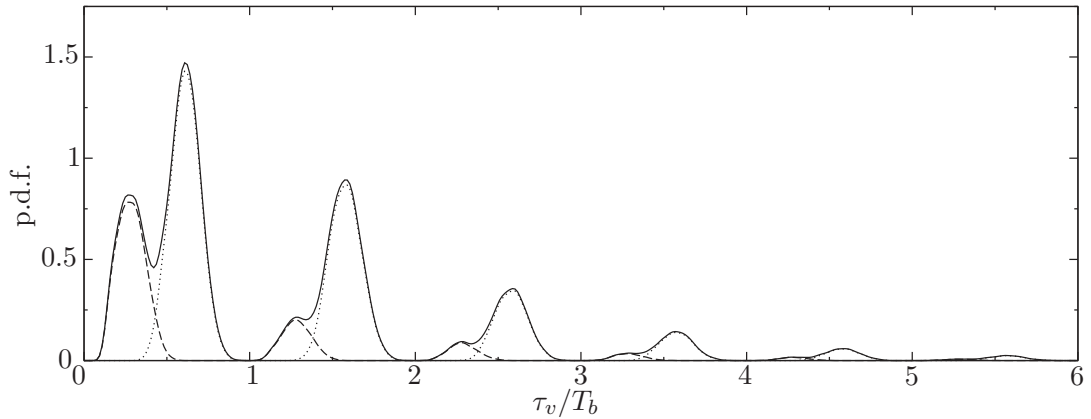


Figure 8.13: Probability density function of residence time in the left ventricle (solid line). The E wave contribution is plotted with a dotted line, the A wave contribution with a dashed line.

particles in *heart B*. The number of particles was limited for a better visualization.

At $t/T_b = 0.5$, the E wave vortex ring transports fresh particles in the ventricle. At $t/T_b = 0.6$ the vortex ring hits the lateral wall and the papillary muscles. Particles do not go all the way down to the ventricle compared to *heart A*, the vortex ring travelling not as far. Instead of scattering particles vertically, along the lateral wall as in *heart A*, the jet impact makes particles fill the heart mostly laterally. Between $t/T_b = 0.7$ and 0.9 , A wave enters the ventricle. Older particles are entrained from the base to the apex and from the apex to the septum wall of the ventricle. This movement is less evident here. However, differentiation between lateral wall and septum wall is also observable in term of residence time. A lot of fresh particles stay in the top half of the ventricle as for *heart A*, showing that the weak A wave of *heart A* does not seem to be the explanation. Also, it seems that a significant quantity of particles stays near the apex, compared to *heart A*.

8.4.2 Left ventricle: residence time

Figure 8.13 shows the residence time probability density function (in solid line) for *heart B*. As for *heart A*, the plot shows distinct peaks, similar to normal distributions. For this heart, the median residence time in the ventricle is $0.72 T_b$ against $0.8 T_b$ for *heart A*. This is explained by the larger quantity of A wave particles entering the left heart during one cycle giving more weight to the younger particles. This is actually the main difference here between the two hearts: A wave contribution is more important as expected. Here, *direct flow* represents 54 % of the particles which is only slightly lower than for *heart A*. Moreover, 81 % of the particles are ejected in two cycles, 92 % in less than three and 0.97 % in less than four heart cycles which is only slightly higher results than for *heart A*. Overall, the E/A ratio does not seem to highly affect

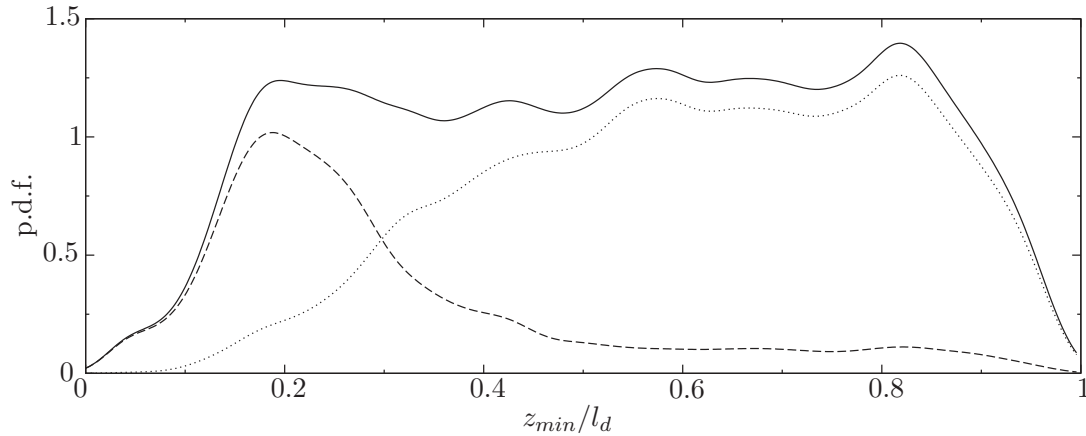


Figure 8.14: Penetration within the left ventricle is given by the particle minimum level in the cavity. Here in solid line, the probability density function of the minimum level z_{min} nondimensionalised by the maximum length of the ventricle l_d is plotted. The E wave contribution is plotted with a dotted line, the remaining contribution with a dashed line.

the residence time results. Also, the residence times are still much higher than most of the ones previously reported in the literature.

The decomposition of the residence time p.d.f. into an E wave contribution and an A wave contribution shows that the particles from each E wave follow almost perfect normal distributions, as in *heart A*. This p.d.f. contribution can be seen as a sum of normal distributions with very similar standard deviations but different means ($\sim 60\%$ of the considered cycle). However, the A wave contribution is responsible for the contribution occurring in the first half of each cycle and mainly visible in the first cycles: for each cycle, the particles from the remaining contributions are ejected first, as in the *heart A*, refuting again the idea of "first-in, first-out". A "last-in, first-out" type of behaviour is observed, irrespective of the E/A ratio.

8.4.3 Left ventricle: penetration

Figure 8.14 shows the particle penetration in the heart ventricle. The penetration is defined as in section 8.3.3. The p.d.f shows that particles can travel through the entire ventricle, until the apex. However, for this heart, the p.d.f. does not show particular peaks. It shows a wide range of possible particle penetration instead. The median value of the penetration is $0.54 l_d$ and 66% of the particles go deeper than 40% of the ventricle length. The difference between *heart A* and *B* is here notable. The particles penetration is not as high and is more homogeneous.

The decomposition of the p.d.f. between the particles coming from the E wave and the ones from the A wave shows that the E wave particles travel deeper in the ventricle than the A wave ones. However, the difference is less pronounced than in the *heart A*.

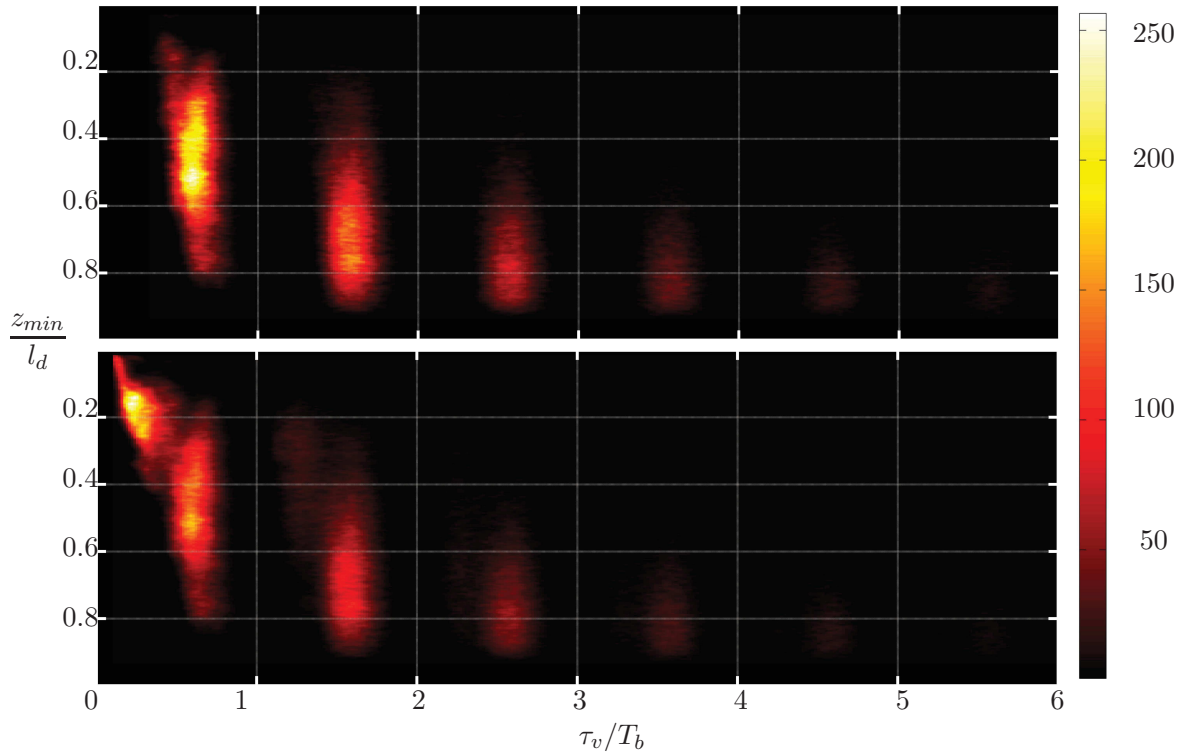


Figure 8.15: Bivariate distributions of variables z_{min}/l_d and τ_v/T_b . Top plot is the distribution of the E wave contribution only while the bottom plot is the total p.d.f.

In addition, the A wave particles do not go much deeper than in *heart A*. While the A wave is much stronger in *heart B*, the median value is of $0.25 l_d$, against $0.3 l_d$ for *heart A*. Note that for *heart A*, particles are entering the ventricle during the 'L wave'. These particles have a higher residence time than if they would enter during the A wave. They are likely to be captured in the large recirculating cell in the ventricle hence travelling deeper in the heart. The median value of penetration for the E wave particles is $0.63 l_d$, against $0.74 l_d$ in *heart A*.

Figure 8.15 shows the bivariate distribution of z_{min}/l_d and τ_v/T_b . The upper plot is the bivariate p.d.f. of the particles only coming from the E wave. The bottom plot shows the same distribution for all the particles. Here, the median penetration in the ventricle shows slight variations with the residence time. Further, residence time and penetration in this healthy left ventricle are more correlated as $r=0.67$, against 0.52 for *heart A*. This suggests that stagnation might be more present in this healthy heart than in *heart A*. Nonetheless, this result might be surprising but was already reported by Zheng *et al.* [188]. It was suggested that a decreased E/A ratio reduces the mixing level in the left ventricle. Our results suggest the same.

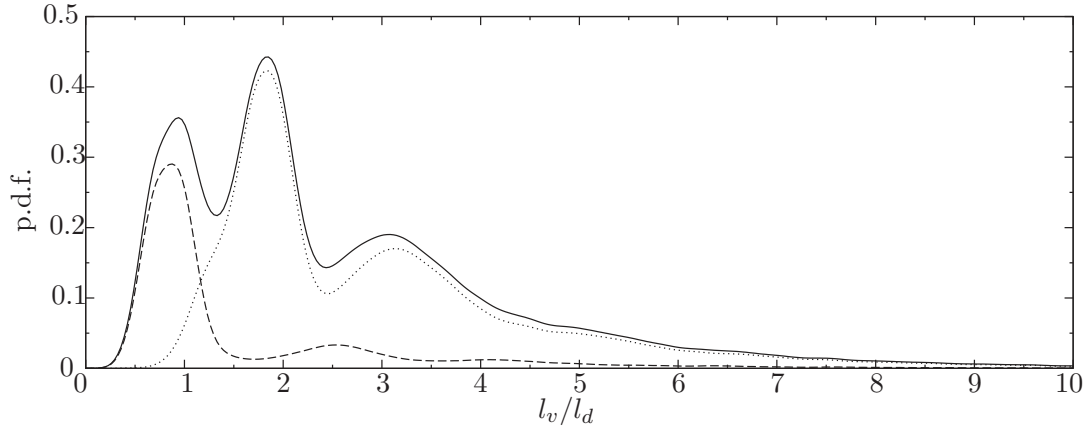


Figure 8.16: Probability density function of path length in the left ventricle (solid line). The E wave contribution is plotted with a dotted line, the remaining contribution with a dashed line.

8.4.4 Left ventricle: path length travelled

Figure 8.16 shows the p.d.f. of the path length l_v nondimensionalized by the length of the ventricle l_d . The distribution shows different modes. Peaks are visible at roughly 0.9 , 1.8 and $3.1 l_d$. After $6 l_d$ the distribution decreases linearly. The median value is $2 l_d$. For *heart A* median value is 60% higher. Path in *heart B* seems more optimized in view of path length travelled. In addition, 99% of the particles travel less than $9 l_d$ against $15 l_d$ for *heart A*, finding again the same 60% difference.

The decomposition between the contributions of the E wave and the A wave shows that the first peak at $l_v/l_d = 0.9$ of the p.d.f. is mostly due to the A wave particles. 73% of the A waves particles travel roughly $1.5 l_d$. This A waves contribution shows a smaller peak at $2.6 l_d$ and another one at $4.2 l_d$. This difference of $1.6 l_d$ is close to the measured differences of $1.3 l_d$ visible between the two peaks of the E wave contribution at 1.85 and $3.15 l_d$. In the corresponding section of *heart A*, it was inferred that these peaks are the consequence of the recirculating cell in the ventricle, measured distance being roughly the distance travelled from the mitral valve plus the travel to the apex and back to the base of the ventricle plus the velocity fluctuations. *Heart A* has a recirculating cell of roughly all the length of the ventricle, the diastasis being longer than in *heart B*. Here, the recirculating cell represents $\sim 65\%$ of the ventricle. A distance of $\sim 1.5 l_d$ is measured between each p.d.f. peak and roughly corresponds to two goes around in the ventricle.

8.4.5 Left ventricle: mean particle velocity

The probability density function of the mean particle velocity defined has l_v/τ_v and nondimensionalized by u_b is plotted in Fig. 8.17. The median velocity is $1.7 u_b$.

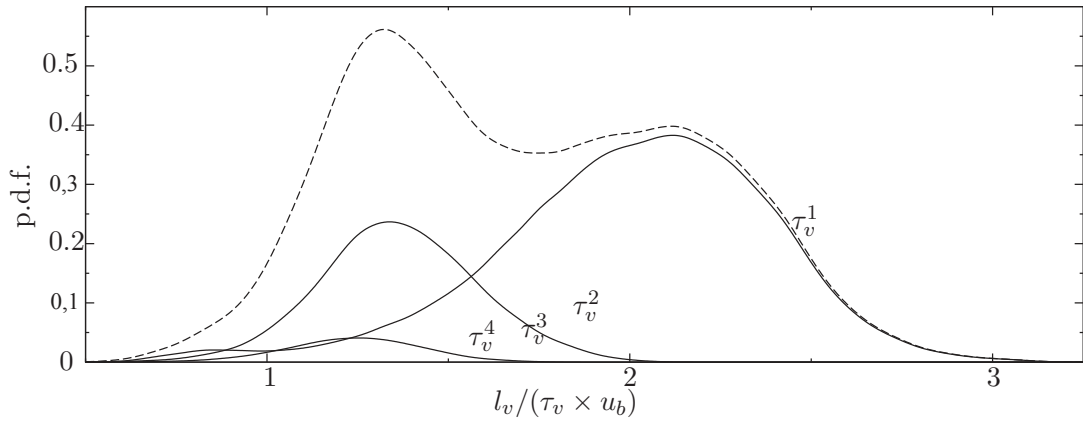


Figure 8.17: Probability density function of the mean particle velocity within the left ventricle is plotted in dashed line. Each residence time subclass is defined as $\tau_v^k = \{\tau_v | k - 1 < \tau_v/T \leq k\}$.

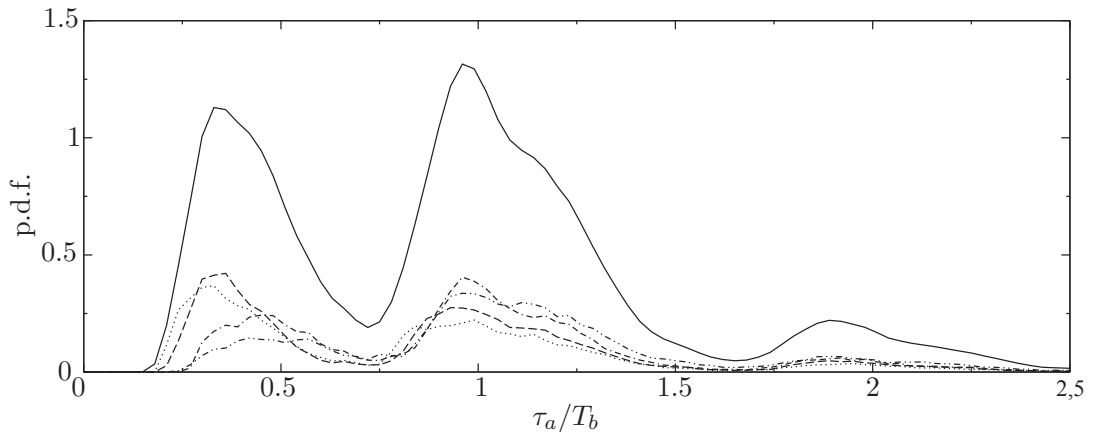


Figure 8.18: Probability density function of residence time in the left atrium (solid line). Each pulmonary vein contribution is plotted as well: RSPV (dashed line), RIPV (dotted line), LIPV (dashed dotted dotted line) and LSPV (dashed dashed dotted line).

This p.d.f. is decomposed in residence time subclasses as well, corresponding to the first four cycles (see Fig. 8.17). All the subclasses p.d.f. follow remarkably normal distributions, the mean being smaller and smaller as the residence time increases. The τ_v^1 subclass has a mean velocity of $2.0 u_b$.

8.4.6 Left atrium: residence time

Figure 8.9 shows the probability density function (in solid line) of residence time in the left atrium. The p.d.f. is similar to the corresponding one in the *heart A*. Three peaks are clearly visible at $\tau_a/T_b = 0.33, 0.97$ and 1.9 . For *heart A*, a fourth peak was visible.

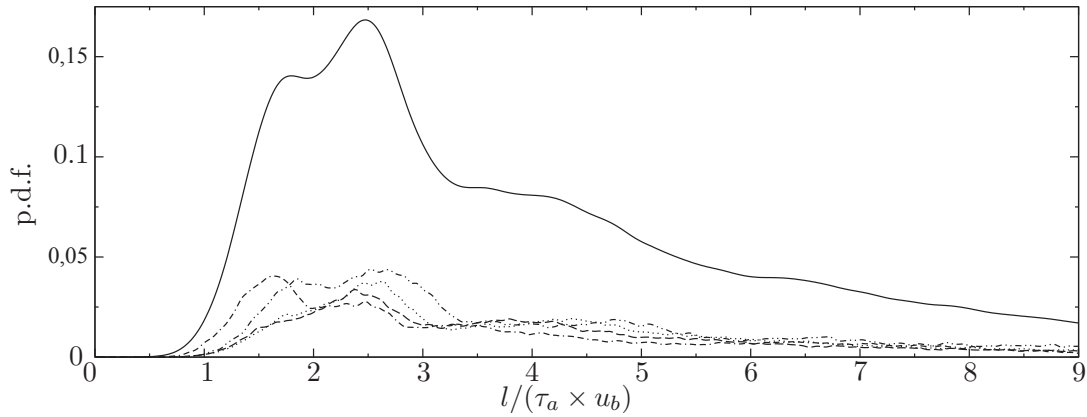


Figure 8.19: Probability density function of the mean particle velocity within the left atrium (solid line). Each pulmonary vein contribution is plotted as well. Contribution of particles from the the RSPV is plotted with a dashed line and ones from the RIPV in dotted line. The LIPV is plotted with a dashed dotted dotted line and the LSPV contribution in dashed dashed dotted line.

The corresponding one here can be guessed at $1.14 T_b$. No particle has been measured with residence time lower than $0.2 T_b$. the median residence time in this atrium is $0.95 T_b$. 94% of the particles are ejected within two cycles, and 99 % in three. These values are very similar to the ones found for *heart A*.

The decomposition of the residence time p.d.f. in the four contributions from the four pulmonary veins shows similar behaviours as in *heart A*. The particles coming from the RSPV and from the RIPV pass from the atrium to the ventricle in less time. The LIPV particles behaviour is more distinct than the LSPV in this heart. The LSPV particles are ejected faster from the atrium than the LIPV while this behaviour, although present, was hardly visible in *heart A*.

8.4.7 Left atrium: mean particle velocity

Figure 8.10 shows the probability density of the mean particle velocity in the atrium. Unlikely in the *heart A* atrium, this p.d.f. has not the aspect of a gamma distribution. The p.d.f. has a peak at $2.5 u_b$, but this peak is not unique. Another peak at $1.75 u_b$ is visible. Although the minimum mean velocity is the same (with $0.6 u_b$), the median velocity is higher with $3.7 u_b$. The p.d.f. decomposition by pulmonary vein shows a behaviour very different from *heart A*. Here, the particles from the LSPV have the lowest velocity values with a median value of $3.0 u_b$, while the LIPV particles have a median velocity of $3.6 u_b$. The RSPV and RIPV particles have the higher velocities with respectively 4.0 and $4.2 u_b$.

	<i>Heart A</i>	<i>Heart B</i>
Cardiac cycle (s)	$T_a = 1.0$	$T_b = 0.75$
EF	58	62
Ref. velocity (m.s ⁻¹)	$u_a = 0.10$	$u_b = 0.16$
Median residence time	$0.8T_a$	$0.72T_b$
Direct flow	55 %	54 %
Median z_{min}	$0.71 l_d$	$0.54 l_d$
Median z_{min} for the E wave particles	$0.74 l_d$	$0.63 l_d$
Median z_{min} for the other particles	$0.33 l_d$	$0.25 l_d$
Median path length	$3.1 l_d$	$2.0 l_d$
Median velocity	$2.8 u_a$	$1.7 u_b$

Table 8.1: Main results for *heart A* and *heart B*.

8.5 Conclusion

Using the developed methodology in this thesis, numerical simulations are employed to investigate the blood transport in left hearts. Thanks to Lagrangian particles this chapter compares the red blood cells transport in one heart with a restrictive filling (*heart A*) and one healthy heart (*heart B*). Qualitatively, it seems that no stagnation zone is present in both hearts. Particles pass quickly from the atrium to the ventricle. In the ventricle, the three dimensional flow basically transport particle to the apex. The E wave vortex ring carries blood from the atrium to the apex of the ventricle in both hearts. However, the restrictive filling implies that the E wave is more powerful for *heart A*. The result is that the E wave particles penetrate deeper in the unhealthy subject. This transport mechanism takes place on the lateral wall side of the ventricle. Then, particles reach the top of the ventricle along the septal wall. However, a large part of particles stays near the mitral valve, especially for the healthy heart. This can be explained by the fact that the A wave is weaker than the E wave. Table 8.1 summarizes some results of *heart B* accompanied with the counterpart results of *heart A* for comparison.

It has been supposed in the literature that the healthy ventricle works as a mixing chamber. In fact, the diseased heart shows more mixing thanks to its powerful E wave, its direct flow being more closer to its ejection fraction. This observation was also made by Zheng *et al.* zheng2014computational. In addition, the supposed "first-in first-out mode" assumption by Watanabe *et al.* [178] to describe the blood transport is not verified here.

It has to be remarked that the presented results are close to Zheng *et al.* [188] while they only use a prolate-spheroidal geometry. This point gives confidence in simple academic geometry, allowing multiple cases simulation whilst avoiding complex patient-specific model construction for particles transport. Information extracted from these studies and the present should provide information on the normal behaviour of the

human left heart and thus could help VAD design [61, 75, 99, 100]. Knowing the normal residence time in the heart could help to tighten up the design requirements of blood pumps. In addition, the present work opens possibilities of including hemolysis models [8, 61, 168].

Finally, recall that strong hypotheses have been made to mimic blood transport. Particles do not interact each others and are considered as tracers in a Newtonian fluid flow. This cannot take into account the complex real blood rheology. In addition, walls are modelled as boundaries generating elastic rebounds of the cells, a very simple view of a very complex reality. In the physiological configuration, the endocardium of the left ventricle is not smooth, trabeculae are present. These structure are not modelled here, but might have a strong influence on the red blood cells behaviour. Mixing and residence time could be affected as the interstitial regions within the trabeculae might be prone to flow stasis.

Chapter key points:

- Measured *direct flows* are about 55 % in this study (close to ejection fraction).
- No stagnation zone is visible.
- Main differences between hearts: the ventricle penetration (due to strong difference in the A wave intensity) and mean velocity in the atrium.

Conclusion

Main results, discussions & perspectives

Chapter contents

9.1	Global conclusion	183
9.2	Discussions	185
9.2.1	Morphological modelling	185
9.2.2	Blood modelling	186
9.3	Perspectives	187

In this last chapter, the main findings and conclusions drawn from this thesis are recalled. Then, the physical modelling choices and their consequences are discussed. Finally, possible directions for future research are proposed.

9.1 Global conclusion

This thesis has been the occasion to develop and use a methodology allowing numerical computations of blood flow in left hearts. The large eddy simulations have demonstrated how computational fluid dynamics can provide an opportunity to study intracardiac flow and to shed light on its turbulent nature.

We were able to provide results consistent with the current knowledge in terms of left heart flow for each of the presented hearts. In the left atrium, the flow showed a clear swirling structure that maintains blood in motion. In the ventricle, the well-known mitral jets during the E and the A wave, preceded by a vortex ring, are also observed. The classical large recirculating cell, characteristic of the flow during diastasis, is also seen in the phased-averaged velocity fields. All these features have been reported several times in the literature using medical imaging, numerical studies and experimental studies. Additionally, the presented results underline the fact that over-simplified geometries cannot fully reproduce certain physical events as the blood swirling motion

visible at the mitral tips.

The presented results also show that the use of a fluid numerical method well adapted to turbulent flows is necessary. The intracardiac flow has been explored for many decades but no consensus on whether or not there is significant turbulence within a normal heart was established. In the majority of the past numerical studies, simulations mainly used solvers with low-order stabilizations terms, artificial viscosity or dissipative schemes. In addition, in most of the cases the grid were insufficiently refined, annihilating the possibility of capturing hypothetical instabilities. In this work, the use of sufficiently refined numerical grid and of non-dissipative numerical schemes, in conjunction with appropriate SGS model, enabled the observation of cycle-to-cycle variations in the cardiac flow field. A disturbed and transitional flow nature is revealed, accompanied by well identified mechanisms of turbulence production. Such variations were expected in the present flow, due to the high Reynolds numbers encountered and the unsteadiness of the flow coming from the pulmonary veins. The present results show that in spite of rigorously identical contraction and boundary conditions, fluid inertia makes the flow differ from one cycle to another.

In the left ventricle, velocity fluctuations are reported mainly in late diastole. Between the impact of the E wave jet on the lateral wall and the end of diastole, the flows display non-negligible levels of cycle-to-cycle fluctuations for both presented subjects. Indeed, both the vortex ring impact and the E wave jet deceleration occur approximately at the same time, and both are features promoting turbulence. The resulting transient turbulent fields are examined through the invariant map of the turbulent stress anisotropy. It reveals that turbulence, when present, is close to an axisymmetric state most of the time, and never reaches an isotropic state. We also show that the late diastole large recirculation cell is most probably perturbed by small vortices. The flow field relaminarizes when the systolic phase begins, thanks to the stabilizing effect of the acceleration provoked by the ventricle contraction. The entire process of vortex structure undergoing turbulent breakdown and subsequent relaminarization occurs at each cycle, although significant cycle-to-cycle differences are observed. In the atrium, velocity fluctuations are reported mainly when the inflowing flow decelerates and when inflowing jets interact with each other or impinge the atrial wall.

Finally, this thesis demonstrates how computer simulations can provide an opportunity to obtain data currently unobtainable by other modalities and with essentially no risk for patients. In addition, the present work shows that turbulence must be considered for the heart and that *haemo-turbulence* might be a normal feature even for healthy hearts.

9.2 Discussions

9.2.1 Morphological modelling

Heart deformations

As exposed in chapter 2, section 2.1, the left heart is a complex biological object. In this work, the heart deformations are computed thanks to medical images. Hence, the spatio-temporal resolution of these images constitutes a limitation. The heart deformations between each medical image is unknown and thus makes it difficult to accurately account for short phases, as the isovolumic contraction and relaxation. Although the ten images per cardiac cycle used for *heart A* enabled a convincing flow prediction, specific tests should be performed to precisely assess the impact of the temporal resolution of the medical images on the computed flow field.

Similarly, the tangential deformations of the endocardium may not be well captured. However, as discussed in chapter 4, section 4.8, the captured tangential velocity is coherent with the usual reported values. In addition, with respect to the flow velocity magnitude, the obtained tangential velocity is negligible.

Another hypothesis is made about deformations: each computed heart cycle uses rigorously the same deformations in this work. However, differences exist between each heart beat in-vivo because of the heart rate variability. Variations in the time interval between heartbeats probably have an influence on the flow and its cycle-to-cycle variations and are not accounted for here.

Heart geometry

Besides the deformations, the level of modelling of the heart geometry depends on the segmentation. For each presented heart, the simulations included the entire ventricle, the atrium, the aorta root and the pulmonary veins. The *heart B* has also papillary muscles. The left atrial appendage has not been modelled. Valves were included through models which assume only two positions: open or close. This valve modelling is one of the main drawbacks of the presented method.

In addition to the global geometry of the heart cavities, the human ventricle has two additional features which were omitted in the presented simulations: the cordae tendinae and the trabeculations. The cordae tendinae, between the papillary muscles and the mitral valve, certainly disturb the intra-ventricular flow. Given their small thickness, they could not be segmented in this work. This structure could only be accounted for through a hypothetical model. Another omitted feature here is that the endocardium of the human left ventricle is not smooth. As shown in chapter 2, section 2.1, the trabeculations give a "ridged" aspect to the endocardial surface. Here, a smooth endocardial surface has been implicitly supposed. However, in real heart flow, the roughness of the wall surface could play a role in the measured turbulence level. In addition, the interstitial regions within the trabeculations could provoke flow stasis.

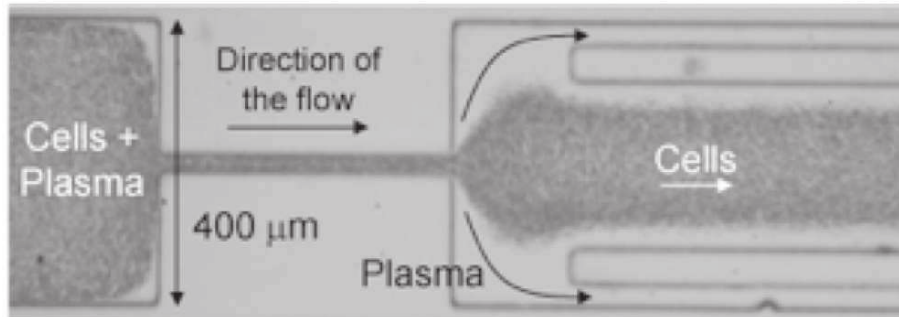


Figure 9.1: Microfluidic experiments with a constriction. The blood cells are separated from plasma (from [53]).

9.2.2 Blood modelling

Finally, the simulated fluid in this work is not blood but may be considered as "viscous plasma". Plasma, which is the blood's liquid medium, is essentially an aqueous solution. However, whole blood (plasma plus cells) exhibits complex non-Newtonian fluid dynamics.

It has been shown in this work (chapter 5, section 5.4.1) that using a Carreau-Yasuda fluid does not change drastically the intracardiac flow. However, the Carreau-Yasuda model only takes into account a shear-thinning behaviour for a blood analogue fluid. It is of course a poor model for full blood, for which the shear-thinning effect is the results of the formation of "rouleaux". In addition, viscoelastic and thixotropic effects are neglected. These blood properties are closely related to the blood structure and how red blood cells suspension is distributed in the heart. The red blood cells determine the rheological behaviour of blood depending on their aggregation, deformation and alignment in the flow.

The complex movement of the red blood cells plays a role in the cells distribution, especially in complex geometry. For example, red blood cells channel flows passing through stenosis have a complex behaviour [2, 53]. Figure 9.1 displays a direct visualization of a flow of red blood cells (from Faivre *et al.* [53]). The cell suspension is not uniformly filling the left cavity in the figure. It is even more shrinking in the right cavity, where a non-negligible percentage of the cavity is only filled by plasma. The cellular content in the middle channel was reported to be enriched by 24%. What is the exact rheological consequence? Another example is the red blood cells near-wall behaviour. The natural tendency of sheared deformable cells to move away from boundaries [73] creates cell-free layer adjacent to the vascular walls of size comparable to the size of a single cell. Due to the drift of the deformable red cells away from the channel boundaries, the near-wall region is occupied by the plasma. How can this phenomenon be properly modelled remembering that the ventricle endocardium is not smooth? Consequences on the intracardiac flow are not known today and it seems illusory to think

that basic blood model could handle these complex behaviours.

The blood nature raises other questions. Blood is considered as a continuum, meaning the "blood material" is continuously distributed and fills the entire heart cavities. When the flow is the most turbulent, space averaged Kolmogorov length scale is of the order of $100 \mu\text{m}$ in our computations, giving credit to the continuum model validity. However locally, the Kolmogorov length scale reaches values of the order of $20 \mu\text{m}$ which is only a few times the size of a red blood cell. Then locally, one could suppose that the continuum model fails [7]. There are no appropriate models capable of describing flow in deformable cells suspensions today, even less in turbulent flow. Further research must be conducted in this direction in order to develop a proper model.

9.3 Perspectives

Some possibilities for further research directions and future work are indicated in this section. This thesis raises new questions that can be (hopefully) addressed in the future. Here is a list of further researches which should be or are considered using the tool developed along this thesis.

- The heart rate is continually changing. These changes occur naturally as a result of internal body changes, environment stresses or physical activity. The changes in heart rate is expressed as changes of the E wave and the A wave duration during diastole [21, 37]. This phenomenon could be modelled, thereby providing information on the intracardiac flow under high heart beat rate. Is the flow mapping is drastically modified? What about the turbulence?
- Transit of red blood cells as presented in chapter 9 has been conducted using instantaneous flows. Does turbulence and the subsequent flow fluctuations have a noticeable influence on the simulated tracers and their statistics? A comparison between tracers convected by the phase-averaged flow and by the instantaneous flow could answer this question. Additionally, this study could give information on the relevance of the use of MRI for this type of studies.
- Very few numerical studies have been conducted on the right heart [108]. The presented method can handle it. Figure 9.2 displays a rough segmentation of an entire heart and its deformations during a heart cycle (deformations are extracted from MRI images).
- A collaboration with Dr. Stephane Nottin and Claire Maufrais (EA4278 - Laboratoire de Pharm-écologie cardiovasculaire, Avignon, France) has been initiated to compare the intra-ventricular flow in high-level athlete hearts and in sedentary subjects.
- A collaboration with Dr. Damien Garcia (RUBIC - Research Unit of Biomechanics and Imaging in Cardiology, Montreal, Canada) has been initiated. The objective

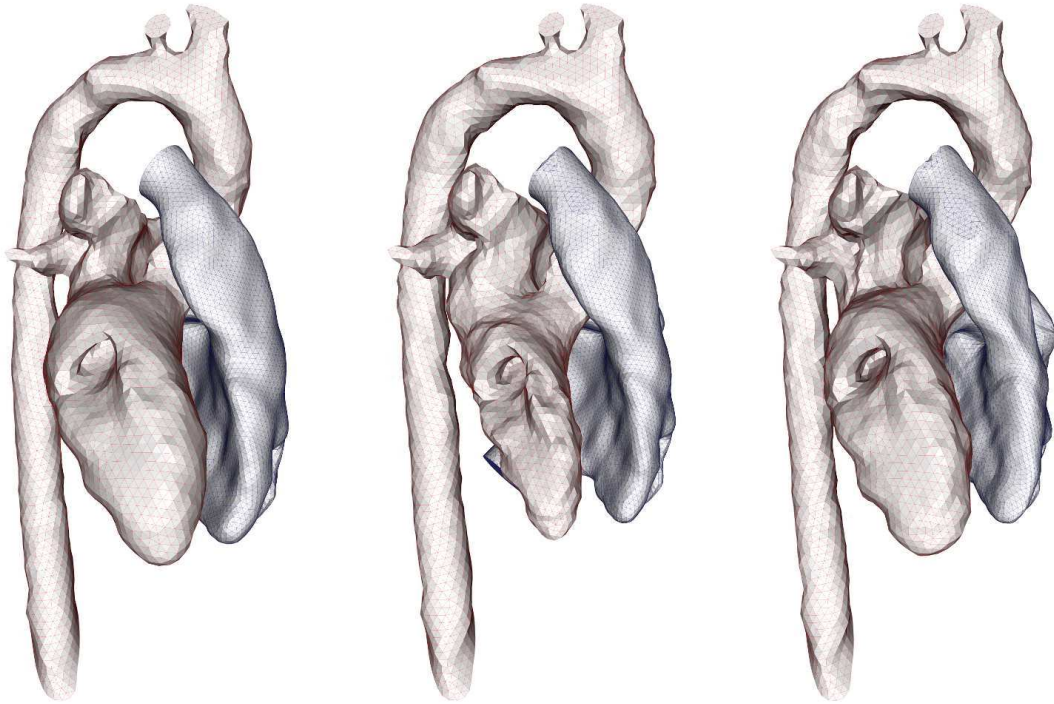


Figure 9.2: Full human heart during diastole. In light red, the left heart and the aorta. In light blue, the right heart.

is to use our simulations as a database in order to participate to the validation of an Echo-Doppler pressure mapping method [63].

Nomenclature

η	The Kolmogorov length scale.
λ	Penalty parameter for deformations.
λ_c	Relaxation time used by the Carreau-Yasuda model.
\mathcal{G}^σ	Gaussian smoothing convolution kernel of width σ .
\mathcal{P}_k^V	Volumetric production of turbulent kinetic energy.
ν_c	Kinematic viscosity computed by the Carreau-Yasuda model.
ν_n	Constant kinematic viscosity for Newtonian assumption.
ν_t	Turbulent kinematic viscosity.
ν_0	Kinematic viscosity at zero shear rate used by the Carreau-Yasuda model.
ν_{inf}	Kinematic viscosity at infinite shear rate used by the Carreau-Yasuda model.
ρ	Fluid density.
σ	Kernel width of Gaussian smoothing.
a_c	A dimensionless parameter used by the Carreau-Yasuda model.
K^V	Volumetric mean flow kinetic energy.
k^V	Volumetric turbulent kinetic energy.
l_d	Ventricle length at the end of diastole.
l_s	Ventricle length at the end of systole.
n_c	Power index coefficient used by the Carreau-Yasuda model.
R_a	Mean radius of the open mitral surface.
T_a	The total duration of the cardiac cycle of <i>heart A</i> .
T_b	The total duration of the cardiac cycle of <i>heart B</i> .
u_a	Reference velocity used for <i>heart A</i> ($u_a=0.10\text{m.s}^{-1}$).
u_b	Reference velocity used for <i>heart B</i> ($u_b=0.16\text{m.s}^{-1}$).

List of Figures

1.1	Visualization of blood flow in a left heart. (a) Phase-contrast magnetic resonance imaging (from [109]) and (b) Echo-PIV (from [84]).	4
1.2	Velocity measurements on healthy human subject from [165]: high-frequency disturbances were observed above the aortic valve (a) and in mid-ascending aorta (b). (c) and (d) shows blood flow velocity records in a canine ascending aorta. (c) from [181] and (d) from [153].	8
2.1	Sketch of the circulatory system (from [17]).	14
2.2	Cardiac events occurring in the cardiac cycle (from [17]).	15
2.3	Sketch of the human heart. Blue components indicate de-oxygenated blood pathways and red components indicate oxygenated pathways. from [158]	17
2.4	Trabeculae carneae on the inner surface of a left ventricle (from [1]).	18
3.1	Representation of a transformed material domain Ω and <i>observation domain</i> ω at times t and t' thanks to a material and a ALE mappings for the general case.	25
3.2	Scheme illustrating where the body-force is applied in the body Ω , immersed in the fluid domain Ω_f	31
3.3	Visualization of the mesh deformation. From left to right, mesh at $t = 0$, $t = \tau/3$, $t = 2\tau/3$	33
3.4	Uniform flow case. Explicit Euler (left) and RK4 method (right). \circ 2nd-order; \times 4th-order scheme in space.	33
3.5	Uniform flow case. RK4, 4th-order scheme in space. Non-respecting DGCL scheme.	34
3.6	Principle of the test case. The fluid outlet is on the right.	34
3.7	Simulation at $t = T/4$ (top figure) and $t = 3T/4$ (bottom plot). Outlet is on the left, moving piston on the top.	36
3.8	Grid convergence study. Left L_{inf} , right L_2 norms of the error.	36
3.9	Analytical (symbols) and numerical (lines) streamwise (right) and normal wise (left) velocity profiles at $x = 5$ mm and at times $+ t = 0$; $\times t = T/4$; $\square t = T/2$; $\circ t = 3T/4$. Dotted lines, 4th order in space; solid lines, 2nd.	37
3.10	Principle of the 3D test case. Left, beginning of the cycle. Right, half-cycle.	38
3.11	Analytical (lines) and numerical (symbols) streamwise (left) and normal wise (right) velocity profiles at $z = 0.05$ m and at times $\diamond t = 0$; $\square t = T/4$; $\nabla t = T/2$; $\circ t = 3T/4$. Filled symbols, 4th order in space ; open symbols, 2nd.	41
3.12	Measured data on the simulations.	42

4.1	Flowchart representing the preparation to the intensity-based image registration process (see section 4.1.2) and the CFD preparation see section 4.1.3. 4D medical images (given as input data) are segmented, measured and treated providing the process outputs.	47
4.2	Flowchart representing the image registration process fore each couple constituted of the <i>template</i> and one <i>reference</i> image. 3D deformation field between the two images (given as input data) is computed, providing the output of the process.	49
4.3	Heart image from a MRI scan. Down-sampling is applied to the image (a). Images (b) and (c) represent image (a) with a reduced resolution by scaling 0.25 and 0.5 respectively. The voxel-centred image grid is shown in image (d) for a sub-part of image (c).	51
4.4	Chosen <i>template</i> image from a MRI scan (a). Images (b) represents the threshold applied to image (a) to the <i>grey values</i> . The threshold is represented by the histogram (<i>grey values</i> versus number of voxels n_p) and allow to keep the voxels with a <i>grey values</i> between 60 and 255 here. The corresponding <i>mask</i> is then created and depicted in red on the heart image. . . .	52
4.5	Segmentation from a CT scan. Slice of the volumetric image is depicted in transparency. Image (a) represents a segmentation only based on the <i>grey values</i> of the 3D image. Image (b) represents the same 3D model after manual treatments and image (c) the chosen area of interest for the blood computation.	53
4.6	Heart image from a CT scan. Gaussian kernels applied from left to right: 3mm^3 , 1.5mm^3 and 0mm	56
4.7	Mesh deformation procedure applied to a left human heart. The <i>template</i> mesh segmented from the image at time t_0 is deformed thanks to ψ_i to obtain the mesh at time t_i . This procedure is done for each image in the cardiac cycle in order to obtain the corresponding meshes.	59
4.8	Skewness histograms for a left heart grid at end diastole (top figure) and mid-systole (bottom figure). Each left heart cavity is color tagged.	60
4.9	Top left: annulus markers and modelled MV leaflets. Parameters a, b of the ellipse ϵ are indicated. Top right: full MV model included in the numerical domain (the AV is represented as well). Bottom: MV scheme.	63
4.10	Manual measure of the open mitral area for a healthy subject (in red). The right and left ventricles are indicated for information.	64
4.11	Measures (cross symbols) of the open mitral area during the diastole t_{dia} . The median of the measures is indicated by a dotted line at 520mm^2 . . .	65
4.12	Volumes obtained for a ventricle from a set of 4D medical images. Solid line, deformation (i), dashed line, deformation (ii).	67

- 4.13 Average ventricle rotation obtained for from a set of 4D medical images. Full line, tangential velocity kinetic energy K_t , dashed line, normal velocity kinetic energy K_n 68
- 4.14 Averaged LV rotational and torsional velocity profiles in 20 subjects. Blue, light green, dark green, and violet lines indicate apical, middle, and basal rotations and LV torsion, respectively. MC indicates mitral valve closure; AO, aortic valve opening; Ej, peak ejection flow velocity in the outflow tract; AC, aortic valve closure (ie, end systole); MO, mitral valve opening; Pk-E, peak early filling velocity; and En-E, end of E wave. From [135]. 69
- 5.1 *Template* computational domain extracted from a 3D medical image. The same domain is represented for four different points of view and the left ventricle (LV), left atrium (LA) and Aorta (AO) are indicated. Black line passing through the left heart indicates the position of slices used to describe the flow in section 5.3. 74
- 5.2 Left: left atrium with its four pulmonary veins labelled. Right: sketch of inflow angles and the four pulmonary veins projected on a plane (the plane is displayed in the left picture). The dashed line indicates that the flow coming from the RSPV is directed toward the MV compared to the others. 76
- 5.3 Flow rates at the aortic valve (top plot), mitral valve (middle plot) and the total heart inflow (bottom plot) imposed at the pulmonary veins during the heart cycle. Vertical dotted lines mark the limit between the systolic phase (t/T_a between 0.015 and 0.375) and the diastolic phase. The E wave, L wave and A wave are indicated on the mitral flow. 77
- 5.4 Left: left heart with probes p_1 and p_2 indicated. Right: solid lines represent the phase averaged velocity magnitude at probes locations using n_c cycles. The dots represent the instantaneous velocity magnitude for the n -ith cycle. The first column of plots represents the data at $t/T_a = 0.20$, the second column at $t/T_a = 0.65$. Top plots represent data from probe p_1 while the bottom plots represent data from probe p_2 81
- 5.5 Volume rendering of non-dimensional vorticity magnitude of the phase-averaged velocity fields at different times of the simulation. First row, left plot: $t/T_a=0.25$. Center plot: $t/T_a=0.35$. Right plot: $t/T_a=0.45$. Second row, left plot: $t/T_a=0.55$. Center plot: $t/T_a=0.65$. Right plot: $t/T_a=0.99$. Sketch of the inflow flow rate presented in Fig. 5.3 is reported with a time indication. The mapping relating vorticity magnitude with opacity is linear. Heart wall is made partially transparent to allow observation of the flow behaviour. . . 82

- 5.6 Phase-averaged non-dimensional velocity field (\mathbf{u}_f/u_a) projected on a slice of the heart. Velocity vector scale is not constant though the heart cycle and is indicated for each plot. First row, left plot: $t/T_a=0.25$. Center plot: $t/T_a=0.35$. Right plot: $t/T_a=0.45$. Second row, left plot: $t/T_a=0.55$. Center plot: $t/T_a=0.65$. Right plot: $t/T_a=0.99$. Sketch of the inflow flow rate presented in Fig. 5.3 is reported with a time indication. 84
- 5.7 Phase-averaged non-dimensional velocity (\mathbf{u}_f/u_a) vectors field projected on planes and velocity magnitude. Planes are indicated on the heart sketches and are viewed from the top of the heart in the apex direction (plane's orientation is indicated). The MV leaflets are visible in the right bottom plots and are coloured in gray. Left: $t/T_a=0.35$. Right: $t/T_a=0.65$. Sketch of the inflow flow rate presented in Fig. 5.3 is reported with a time indication. 86
- 5.8 Evolution of Q criterion isosurface ($Q = 30u_a^2/R_a^2$) showing the structures present in the instantaneous field, through the heart cycle. First row, left plot: $t/T_a=0.25$. Center plot: $t/T_a=0.35$. Right plot: $t/T_a=0.45$. Second row, left plot: $t/T_a=0.55$. Center plot: $t/T_a=0.65$. Right plot: $t/T_a=0.99$. Sketch of the inflow flow rate presented in Fig. 5.3 is reported with a time indication. 87
- 5.9 Left: streamlines in the atrium at $0.75T_a$. Right, isosurface of Q-criterion ($5\frac{u_a^2}{R_a^2}$) showing the structures present in the instantaneous field at $0.51T_a$. Vortex rings are indicated by the two red arrows. 89
- 5.10 Nondimensional fluctuating kinetic energy E_k/u_a^2 . First row, left plot: $t/T_a=0.25$. Center plot: $t/T_a=0.35$. Right plot: $t/T_a=0.45$. Second row, left plot: $t/T_a=0.55$. Center plot: $t/T_a=0.65$. Right plot: $t/T_a=0.99$. Sketch of the inflow flow rate presented in Fig. 5.3 is reported with a time indication. . . 90
- 5.11 Comparison of viscosity ν_c and shear rate $\dot{\gamma}$ relationship as predicted by the Carreau-Yasuda model (solid line). The constant viscosity ν_n used in the Newtonian hypothesis is indicated using the red dashed line. 93
- 5.12 Ratio between viscosity ν_c computed with Carreau-Yasuda model and constant viscosity ν_n . First row, left plot: $t/T_a=0.25$. Center plot: $t/T_a=0.35$. Right plot: $t/T_a=0.45$. Second row, left plot: $t/T_a=0.55$. Center plot: $t/T_a=0.65$. Right plot: $t/T_a=0.99$ 94
- 5.13 Maps of ratio of the SGS viscosity ν_t to molecular viscosity ν_n . Plot (a) and (c) display the ratio for the dynamic Smagorinsky model. Plot (b) and (d) are maps of the σ -model SGS viscosity ratio. Left plots (a and b) are maps of the ratio at $t/T_a = 0.55$ while the right plots (c and d) are maps at $t/T_a = 0.65$ 96
- 5.14 Velocity (left plots) and TKE maps (right plots) obtained with the dynamic Smagorinsky and with the σ -model. For each plots couple, the left is the results of simulation with dynamic Smagorinsky model, the right with σ -model. The displayed maps correspond to $t/T_a = 0.65$ 97

- 6.1 *Template* computational domain extracted from a 3D medical image. The same domain is represented from four different points of view and the left ventricle (LV), left atrium (LA), Aorta (AO) and two pulmonary veins are indicated. Black line passing through the left heart indicates the position of slices used to describe the flow in section 6.3. Probes locations and outflow patch are also indicated. 102
- 6.2 Flow rates (in mL.s⁻¹) at the aortic valve (top plot), mitral valve (middle plot) and the total heart inflow (bottom plot) imposed at the pulmonary veins during the heart cycle. Vertical dotted lines mark the limit between the systolic phase (t/T_a between 0.015 and 0.375) and the diastolic phase. The E wave and the A wave are indicated on the mitral flow. 104
- 6.3 Solid lines represent the phase averaged velocity magnitude at probes locations using n_c cycles. The dots represent the instantaneous velocity magnitude for the n^{th} cycle. Top, middle, bottom plots represent data from probe p_3 at $0.65T_a$, p_5 at $0.90T_a$ and p_7 at $0.65T_a$ respectively. 106
- 6.4 Solid lines represent the turbulent kinetic energy at probes locations using n_c cycles. The dots represent the instantaneous fluctuating energy for the n^{th} cycle. Top and bottom plots represent data from probe p_5 and p_7 at $0.65T_a$ respectively. 107
- 6.5 Phase-averaged non-dimensional velocity field ($\langle U_i \rangle / u_a$) over a cutting-plane through the left heart (see Fig. 6.1 for the position of the plane). The velocity vector scale is not constant through the heart cycle and is indicated for each plot. The mitral valve is depicted in light grey and the aortic valve in dark grey. 108
- 6.6 Phase-averaged non-dimensional velocity field ($\langle U_i \rangle / u_a$) over cutting-planes through the left atrium. The velocity fields are projected through the plane indicated in the left figure. The scale is fixed row by row. 109
- 6.7 Left: time history of normalized vertical velocity U_3/u_a over 10 of the 50 cycles used for phase-averaging for the 10 probes studied. Right: phase-averaged of normalized vertical velocity $\langle U_3 \rangle / u_a$ at the same 10 points. The vertical dotted line delimits the systolic phase from the diastolic phase at $t/T_a = 0.375$ 110
- 6.8 Left and middle plot: instantaneous non-dimensional velocity fields at $t/T = 0.65$. Right plot: phase-averaged non-dimensional velocity field at $t/T = 0.65$. Mitral valve is depicted in light grey and the aortic one in dark grey and scale is the same for all three images. 113
- 6.9 Volumetric mean flow kinetic energy K^V (full line) and five times the turbulent kinetic energy k^V (dashed line) in the left ventricle (top plot), and in the left atrium (bottom plot). The energies are nondimensionalised by u_a^2 . The vertical dotted lines delimit the systolic phase and the diastolic phase. 113

6.10	Left, kinetic energy measurements in healthy left ventricles using MRI (from [25]). Right, kinetic energy measurements in healthy left atria using MRI (from [9]).	114
6.11	TKE (blue solid line) and LV volume change (red dashed line) over diastole (mean \pm SD) for 11 healthy subjects using MRI (from [185]).	115
6.12	Nondimensional turbulent kinetic energy k/u_a^2 at three different times: t/T_a $= 0.25$ (a), $t/T_a = 0.55$ (b) and $t/T_a = 0.65$ (c).	116
6.13	Left plots: time evolution of the r.m.s. of the 3 velocities components, nondimensionalised by u_a . Right plot: turbulent kinetic energy nondimen- sionalised by u_a^2 over the cardiac cycle at the ten probes p_1 to p_{10} . The vertical dotted line marks the limit between the systolic phase and the dias- tolic phase at $t/T_a = 0.375$	118
6.14	Volume-averaged production of turbulent kinetic energy \mathcal{P}_k^V in the ventri- cle (solid line) and in the left atrium (dashed line). Productions are both nondimensionalised by u_a^3/l_s . Vertical dotted lines mark the limit between the systolic phase (t/T_a between 0.015 and 0.375) and the diastolic phase. .	119
6.15	Production of turbulent kinetic energy \mathcal{P}_k nondimensionalised by u_a^3/l_s at $t/T_a = 0.55$. Left plot: production \mathcal{P}_k in the same plane in Fig. 6.1. Center and right plots: volume rendering of the non-dimensional TKE production \mathcal{P}_k on two different views. The mapping relating production magnitude with opacity is linear. Heart wall is made partially transparent to allow observation and the aorta was deleted as focus is on the LA and LV. On all plots, the three areas where $\mathcal{P}_k < 0$ are indicated by the letters A, B and C.	120
6.16	Lumley triangles at times $t/T_a = 0.5$ (left plots) and 0.7 (right plots) for the ventricle (top plots) and for the atrium (bottom plots).	122
6.17	Evolution of the mean isotropy parameter I during the heart cycle for the atrium cavity (dashed line) and the ventricle cavity (solid line). The data are calculated every $T_a/10$ for the atrium and the ventricle cavities are displayed respectively as triangles and circles.	124
6.18	Power spectral density (PSD) of vertical velocity fluctuations u_3 at the 10 studied points.	125
6.19	Time-frequency representation of the Power Spectral Density (PSD) of the vertical fluctuating velocity u_3 at the 10 probes locations. PSD is color coded (scale on the left) with the same range as Fig. 6.18.	127
7.1	Full human left heart extracted from MRI images. The same domain is shown from four different points of view. The left ventricle (LV), left atrium (LA), Aorta (AO), Anterio Lateral (A-L) and Postero Medial (P-M) pap- illary muscles are indicated. A black line passing through the left heart indicates the position of the slice which will be used to describe the flow in the remainder of the chapter.	132

7.2	Volume of the ventricle (V_1 solid line) and of the left atrium (V_2 dashed line). The vertical black line marks the limit between the systolic phase and the diastolic phase at $t/T_b = 0.34$	133
7.3	Flow rates in $\text{mL}\cdot\text{s}^{-1}$ at the aortic valve (top plot), mitral valve (middle plot) and the total heart inflow imposed at the pulmonary veins during the heart cycle (bottom plot). The vertical line delimits the systolic phase from the diastolic phase at $t/T_b = 0.34$	135
7.4	Positions of the seven probes in <i>heart B</i>	137
7.5	Solid lines represent the phase-averaged velocity magnitude at 2 probes locations using n_c cycles. The dots represent the instantaneous velocity magnitude for the n_c -ith cycle. Top and bottom plots display data from probe p_1 at $0.7T_b$ and p_5 at $0.7T_b$, respectively.	137
7.6	Solid lines represent the phase averaged TKE magnitude at 2 probes locations using n_c cycles. The dots represent the instantaneous TKE magnitude for the n_c -ith cycle. Top and bottom plots display data from probe p_1 at $0.7T_b$ and p_5 at $0.7T_b$, respectively.	138
7.7	Volume rendering of non-dimensional vorticity magnitude of the phase-averaged velocity fields at different times of the simulation. First row, left plot: $t/T_b=0.15$. Center plot: $t/T_b=0.50$. Right plot: $t/T_b=0.57$. Second row, left plot: $t/T_b=0.65$. Center plot: $t/T_b=0.75$. Right plot: $t/T_b=0.90$. The mapping relating vorticity magnitude with opacity is linear. The heart wall is made partially transparent to allow a better observation of the flow behaviour.	139
7.8	Evolution of Q criterion isosurface ($Q = 70u_b^2/R_a^2$) showing the vortical structures present in a typical instantaneous velocity field.	141
7.9	Phase-averaged non-dimensional velocity field over a cutting plane through the left heart (see Fig. 7.1 for the position of the plane). The velocity vector scale is not constant and is indicated for each plot. The mitral valve is depicted in light grey and the aortic valve in dark grey.	143
7.10	Left: time history of normalized vertical velocity U_3/u_b over 6 cardiac cycles of the 30 cycles used for phase-averaging at the 7 studied points. Right: phase-averaged of normalized vertical velocity $\langle U_3 \rangle / u_b$ at the same 7 points. The vertical dotted line delimits the systolic phase from the diastolic phase at $t/T_b = 0.34$	144
7.11	3D velocity vectors in the atrium at $0.6T_b$ and $0.7T_b$. The velocity field is only shown in the atrium. Pulmonary veins are indicated. The black arrow in the bottom figure is pointing the plane where kinetic energy is computed in Fig. 7.13.	146
7.12	3D velocity vectors in the atrium during systole at $0.3T_b$. The velocity field is only shown in the atrium. A plane passing through the four veins is included. Pulmonary veins are indicated.	147

7.13	Kinetic energy of the axial flow velocity K_3 (solid line) and of tangential velocity component (dashed line) above the mitral valve. Figure 7.11 shows the location of the plane where K_3 and $K_{1,2}$ are calculated. Energies are nondimensionalised by u_b^2 . The vertical dotted line delimits the systolic phase from the diastolic phase at $t/T_b = 0.34$	147
7.14	Volumetric mean flow kinetic energy K^V (full line) and five times the turbulent kinetic energy k^V (dashed line) in the left ventricle (top plot), and in the left atrium (bottom plot). The energies are nondimensionalised by u_b^2 . The vertical dotted line delimits the systolic phase from the diastolic phase at $t/T_b = 0.34$	148
7.15	Nondimensional turbulent kinetic energy k/u_b^2 during the heart cycle.	150
7.16	Volumetric production of turbulent kinetic energy \mathcal{P}_k^V in the ventricle (solid line) and in the left atrium (dashed line). Productions are both nondimensionalised by u_b^3/l_s . The vertical dashed line marks the limit between the systolic phase and the diastolic phase at $t/T_b = 0.34$	151
7.17	Volume rendering of the production of turbulent kinetic energy \mathcal{P}_k nondimensionalised by u_b^3/l_s at $t/T_b = 0.65$. The mapping relating production magnitude with opacity is linear. Heart wall is made partially transparent to allow observation.	152
7.18	Time-frequency representation of the Power Spectral Density (PSD) of the vertical fluctuating velocity u_3 at the 7 probes locations. PSD is color coded (scale on the bottom right).	154
8.1	Scheme of <i>heart A</i> . The names of the four pulmonary veins are indicated. Statistics are saved first when the particles pass through the mitral valve (coloured in green in the right figure to indicate that they are accounted for in statistics) and then when the particles pass through the aortic valve.	161
8.2	Convergence of the number of particles at the end of the diastole in the <i>heart A</i> for each computed cycle.	162
8.3	Particle residence time is shown for <i>heart A</i> . Six times during diastole are shown. Only 50 000 particles are displayed for a better visualization.	163
8.4	Probability density function of residential time in the left ventricle (solid line). The E wave contribution is plotted with a dotted line, the remaining contribution (L and A wave) with a dashed line.	164
8.5	Penetration within the left ventricle is given by the particle minimum level in the cavity. Here in solid line, the probability density function of the minimum level z_{min} nondimensionalised by the maximum length of the ventricle l_d is plotted. 0 being the mitral valve level, 1 the apex. The E wave contribution is plotted with a dotted line, the remaining contribution with a dashed line.	166
8.6	Bivariate distributions of variables z_{min}/l_d and τ_v/T_a . Top plot is the distribution of the E wave contribution only while the bottom plot is the total p.d.f.	167

8.7	Probability density function of path length in the left ventricle (solid line). The E wave contribution is plotted with a dotted line, the remaining contribution with a dashed line.	168
8.8	Probability density function of the mean particle velocity within the left ventricle is plotted in dashed line. Each residence time subclass is defined as $\tau_v^k = \{\tau_v k - 1 < \tau_v/T \leq k\}$	169
8.9	Probability density function of residence time in the left atrium (solid line). Each pulmonary vein contribution is plotted as well: RSPV (dashed line), RIPV (dotted line), LIPV and LSPV contributions are plotted using the same line as differences between the two are small.	170
8.10	Probability density function of the mean particle velocity within the left atrium is plotted in dashed line. Each residence time subclass (defined as $\tau_a^k = \{\tau_a k - 1 < \tau_a/T \leq k\}$) contribution is plotted.	171
8.11	Probability density function of the mean particle velocity within the left atrium is plotted in solid line. Each pulmonary veins contribution is plotted. The RSPV in dashed line, RIPV in dotted line. The LIPV and LSPV contribution are both in dashed dotted dotted line as differences between the two are small.	171
8.12	Residence time is shown for the healthy subject: <i>heart B</i> . Six instants during the diastole are shown. Only 50 000 particles are shown for a better visualization.	172
8.13	Probability density function of residence time in the left ventricle (solid line). The E wave contribution is plotted with a dotted line, the A wave contribution with a dashed line.	173
8.14	Penetration within the left ventricle is given by the particle minimum level in the cavity. Here in solid line, the probability density function of the minimum level z_{min} nondimensionalised by the maximum length of the ventricle l_d is plotted. The E wave contribution is plotted with a dotted line, the remaining contribution with a dashed line.	174
8.15	Bivariate distributions of variables z_{min}/l_d and τ_v/T_b . Top plot is the distribution of the E wave contribution only while the bottom plot is the total p.d.f.	175
8.16	Probability density function of path length in the left ventricle (solid line). The E wave contribution is plotted with a dotted line, the remaining contribution with a dashed line.	176
8.17	Probability density function of the mean particle velocity within the left ventricle is plotted in dashed line. Each residence time subclass is defined as $\tau_v^k = \{\tau_v k - 1 < \tau_v/T \leq k\}$	177

8.18	Probability density function of residence time in the left atrium (solid line). Each pulmonary vein contribution is plotted as well: RSPV (dashed line), RIPV(dotted line), LIPV (dashed dotted dotted line) and LSPV (dashed dashed dotted line).	177
8.19	Probability density function of the mean particle velocity within the left atrium (solid line). Each pulmonary vein contribution is plotted as well. Contribution of particles from the the RSPV is plotted with a dashed line and ones from the RIPV in dotted line. The LIPV is plotted with a dashed dotted dotted line and the LSPV contribution in dashed dashed dotted line.	178
9.1	Microfluidic experiments with a constriction. The blood cells are separated from plasma (from [53]).	186
9.2	Full human heart during diastole. In light red, the left heart and the aorta. In light blue, the right heart.	188

List of Tables

3.1	Comparison of wake parameters for steady-state flow around a cylinder at $Re_D = 30$ with experimental and numerical data.	42
5.1	Geometric characteristics of the ostia. Ostia are oval in shape. The areas reported are obtained by assuming elliptic shapes.	75
5.2	Main characteristics for <i>heart A</i>	78
5.3	Set of parameters used in the Carreau-Yasuda model. Data fitted from work by Thurston [170].	93
6.1	Main flow characteristics describing the simulation. The section-averaged maximum velocity over the cardiac cycle is indicated as U_{max} . The maximum Reynolds number Re_{max} is based on the mean diameter D ($D = 2R_a = 2\sqrt{ab}$) and maximum velocity U_{max} . Time when the Re_{max} is reached is reported as t_m/T_a	104
7.1	Main characteristics for <i>heart A</i> and <i>heart B</i>	136
7.2	Main results for <i>heart A</i> and <i>heart B</i>	155
8.1	Main results for <i>heart A</i> and <i>heart B</i>	179

Bibliography

- [1] Supplement to the Dennis Daniel's course (Stony Brook University, New York, USA). www.thebodyonline.net. Accessed: 2014-08-21.
- [2] Abkarian, M., Faivre, M., Horton, R., Smistrup, K., Best-Popescu, C., and Stone, H. Cellular-scale hydrodynamics. *Biom. Mat.* 3, 3 (2008), 034011.
- [3] Adelson, E., Anderson, C., Bergen, J., Burt, P., and Ogden, J. Pyramid methods in image processing. *RCA Engng* 29 (1984), 33–41.
- [4] Adrian, R. Particle-imaging techniques for experimental fluid mechanics. *Annual review of fluid mechanics* 23, 1 (1991), 261–304.
- [5] Alfakih, K., Plein, S., Thiele, H., Jones, T., Ridgway, J., and Sivananthan, M. Normal human left and right ventricular dimensions for MRI as assessed by turbo gradient echo and steady-state free precession imaging sequences. *J. Mag. Res. Imag.* 17, 3 (2003), 323–329.
- [6] Allender, S., Scarborough, P., Peto, V., Rayner, M., Leal, J., Luengo-Fernandez, R., and Gray, A. European cardiovascular disease statistics.
- [7] Antiga, L., and Steinman, D. Rethinking turbulence in blood. *Biorheology* 46, 2 (2009), 77–81.
- [8] Arora, D., Behr, M., and Pasquali, M. Hemolysis estimation in a centrifugal blood pump using a tensor-based measure. *Artif. Organs* 30, 7 (2006), 539–547.
- [9] Arvidsson, P., Töger, J., Heiberg, E., Carlsson, M., and Arheden, H. Quantification of left and right atrial kinetic energy using four-dimensional intracardiac magnetic resonance imaging flow measurements. *J. App. Physiol.* 114 (2013), 1472–1481.
- [10] Ashburner, J., Andersson, J. L. R., and Friston, K. J. High-dimensional image registration using symmetric priors. *NeuroImage* 9 (1999), 619–628.
- [11] Ashburner, J., Neelin, P., Collins, D. L., Evans, A., and Friston, K. J. Incorporating prior knowledge into image registration. *NeuroImage* 6 (1997), 344–352.
- [12] Baccani, B., Domenichini, F., Pedrizzetti, G., and Tonti, G. Fluid dynamics of the left ventricular filling in dilated cardiomyopathy. *J. Biomech.* 35 (2002), 665–671.

- [13] Baumgartner, H., Hung, J., Bermejo, J., Chambers, J., Evangelista, A., Griffin, B., Iung, B., Otto, C., Pellikka, P., and Quiñones, M. Echocardiographic assessment of valve stenosis: Eae/ase recommendations for clinical practice. *Eu. J. Echo.* (2008).
- [14] Baya Toda, H., Cabrit, O., Balarac, G., Bose, S., Lee, J., Choi, H., and Nicoud, F. A subgrid-scale model based on singular values for les in complex geometries. In *Proceedings of the Summer Program* (2010), p. 193.
- [15] Baya Toda, H., Cabrit, O., Truffin, K., Bruneaux, G., and Nicoud, F. Assessment of subgrid-scale models with a large-eddy simulation-dedicated experimental database: The pulsatile impinging jet in turbulent cross-flow. *Phys. Fluids* 26, 7 (2014), 5108.
- [16] Becker, R., Eisenberg, P., and Turpie, A. Pathobiologic features and prevention of thrombotic complications associated with prosthetic heart valves: fundamental principles and the contribution of platelets and thrombin. *Am Heart J.* 141, 6 (2001), 1025–1037.
- [17] Betts, J. *Anatomy and Physiology.* 2013.
- [18] Bird, R. B., Armstrong, R. C., and Hassager, O. Dynamics of polymeric liquids. vol. 1: Fluid mechanics.
- [19] Boffi, D., and Gastaldi, L. Stability and geometric conservation laws for ale formulations. *Comput. Meth. Appl. Mech. Engng* 193 (2004), 4717–4739.
- [20] Bolger, A., E., H., M., K., L., W., J., E., A., S., T., E., J.P., K., C.J., C., and B., W. Transit of blood flow through the human left ventricle mapped by cardiovascular magnetic resonance. *J. Cardiovasc. Magn. Reson.* 9 (2007), 741–747.
- [21] Bombardini, T., Gemignani, V., Bianchini, E., Venneri, L., Petersen, C., Pasanisi, E., Pratali, L., Alonso-Rodriguez, D., Pianelli, M., and Faita, F. Diastolic time–frequency relation in the stress echo lab: filling timing and flow at different heart rates. *Cardiovascular ultrasound* 6, 1 (2008), 15.
- [22] Bronzino, J. *Biomedical engineering handbook*, vol. 2. CRC press, 1999.
- [23] Carlhäll, C., and Bolger, A. Passing strange flow in the failing ventricle. *Circulation: Heart Failure* 3, 2 (2010), 326–331.
- [24] Carlsson, M., Heiberg, E., Toger, J., and Arheden, H. Quantification of left and right ventricular kinetic energy using four-dimensional intracardiac magnetic resonance imaging flow measurements. *Am. J. Physiol. Heart Circ. Physiol.* 302 (2012), 893–900.

- [25] Carlsson, M., Heiberg, E., Toger, J., and Arheden, H. Quantification of left and right ventricular kinetic energy using four-dimensional intracardiac magnetic resonance imaging flow measurements. *Am. J. Physiol. Heart. Circ. Physiol.* 302 (2012), 893–900.
- [26] Carpy, S., and Manceau, R. Turbulence modelling of statistically periodic flows: synthetic jet into quiescent air. *Int. j. of heat and fluid flow* 27, 5 (2006), 756–767.
- [27] Cenedese, A., Del Prete, Z., Miozzi, M., and Querzoli, G. A laboratory investigation of the flow in the left ventricle of a human heart with prosthetic, tilting-disk valves. *Expe. Fluids* 39, 2 (2005), 322–335.
- [28] Chen, J., Lu, X., and Wang, W. Non-newtonian effects of blood flow on hemodynamics in distal vascular graft anastomoses. *J. of biomech.* 39, 11 (2006), 1983–1995.
- [29] Cheng, C., Tempel, D., van Haperen, R., van der Baan, A., Grosveld, F., Daemen, M., Krams, R., and de Crom, R. Atherosclerotic lesion size and vulnerability are determined by patterns of fluid shear stress. *Circulation* 113, 23 (2006), 2744–2753.
- [30] Cheng, M., Lou, J., and Luo, L. Numerical study of a vortex ring impacting a flat wall. *J. Fluid Mech.* 660 (2010), 430–455.
- [31] Cheng, Y., Oertel, H., and Schenkel, T. Fluid-structure coupled CFD simulation of the left ventricular flow during filling phase. *Ann. Biomed. Engng* 33 (2005), 567–576.
- [32] Chien, S. Shear dependence of effective cell volume as a determinant of blood viscosity. *Science* 168, 3934 (1970), 977–979.
- [33] Chien, S. Mechanotransduction and endothelial cell homeostasis: the wisdom of the cell. *Am. J. Physiol. Heart Circ. Physiol.* 292 (2007), 1209–1224.
- [34] Chnafa, C., Mendez, S., Moreno, R., and Nicoud, F. *The Cardio-Circulatory System: from Modeling to Clinical Applications*, vol. 1 of *Modeling, Simulation and Applications*. Springer, 2014, ch. Using image-based CFD to investigate the intracardiac turbulence.
- [35] Chnafa, C., Mendez, S., and Nicoud, F. Image-based large-eddy simulation in a realistic left heart. *Comput. Fluids* 94 (2014), 173 – 187.
- [36] Chorin, A. Numerical solution of the Navier-Stokes equations. *Math. Comput.* 22 (1968), 745–762.

- [37] Chung, C., Karamanoglu, M., and Kovács, S. Duration of diastole and its phases as a function of heart rate during supine bicycle exercise. *Am. J. of Physiology-Heart and Circ. Physio.* 287, 5 (2004), H2003–H2008.
- [38] Cimino, S., Pedrizzetti, G., Tonti, G., Canali, E., Petronilli, V., De Luca, L., Iacoboni, C., and Agati, L. In vivo analysis of intraventricular fluid dynamics in healthy hearts. *Eu. J. Mech. - B/Fluids* 35 (2012), 40–46.
- [39] Coutanceau, M., and Bouard, R. Experimental determination of the main features of the viscous flow in the wake of a circular cylinder in uniform translation. part 1. steady flow. *J. Fluid Mech.* 79, 02 (1977), 231–256.
- [40] Dahl, S. K., Thomassen, E., Hellevik, L. R., and Skallerud, B. Impact of pulmonary venous locations on the intra-atrial flow and the mitral valve plane velocity profile. *Cardiovasc. Engng Tech.* 3 (2012), 269–281.
- [41] Dapogny, C., Dobrzynski, C., and Frey, P. Three-dimensional adaptive domain remeshing, implicit domain meshing, and applications to free and moving boundary problems. *J. Comput. Phys.* 262 (2014), 358–378.
- [42] Doenst, T., Spiegel, K., Reik, M., Markl, M., Hennig, J., Nitzsche, S., Beyersdorf, F., and Oertel, H. Fluid-dynamic modeling of the human left ventricle: Methodology and application to surgical ventricular reconstruction. *Ann. Thor. Surg.* 87 (2009), 1187–1195.
- [43] Domenichini, F., Pedrizzetti, G., and Baccani, B. Three-dimensional filling flow into a model left ventricle. *J. Fluid Mech.* 539 (2005), 179–198.
- [44] Domenichini, F., Querzoli, G., Cenedese, A., and Pedrizzetti, G. Combined experimental and numerical analysis of the flow structure into the left ventricle. *J. Biomech.* 40 (2007), 1988–1994.
- [45] Donea, J., Huerta, A., Ponthot, J., and Rodriguez-Ferran, A. Arbitrary Lagrangian-Eulerian methods. *Encyclo. Comput. Mech.* (2004).
- [46] Druault, P., Guibert, P., and Alizon, F. Use of proper orthogonal decomposition for time interpolation from PIV data. *Expe. Fluids* 39 (2005), 1009–1023.
- [47] Dyverfeldt, P., Kvitting, J., Sigfridsson, A., Engvall, J., Bolger, A., and Ebbers, T. Assessment of fluctuating velocities in disturbed cardiovascular blood flow: In vivo feasibility of generalized phase-contrast MRI. *J. Mag. Reso. Imag.* 28 (2008), 655–663.
- [48] Dyverfeldt, P., Kvittingand, J., C.J., C., Boano, G., Sigfridsson, A., Hermansson, U., Bolger, A., Engvall, J., and Ebbers, T. Hemodynamic aspects of mitral regurgitation assessed by generalized phase-contrast MRI. *J. Mag. Reso. Imag.* 33 (2011), 582–588.

- [49] Einstein, D., Pin, F. D., Jiao, X., Kuprat, A., Carson, J., Kunzelman, K., Cochran, R., Guccione, J., and Ratcliffe, M. Fluid-structure interactions of the mitral valve and left heart: comprehensive strategies, past, present and future. *Int. J. Numer. Meth. Biomed. Engng* 26 (2010), 348–380.
- [50] Epstein, F. MRI of left ventricular function. *J. of nuc. cardio.* 14, 5 (2007), 729–744.
- [51] Eriksson, J., Bolger, A., Ebbers, T., and Carlhall, C. Four-dimensional blood flow-specific markers of LV dysfunction in dilated cardiomyopathy. *Eu. Heart J. - Cardio. Imag.* 14 (2013), 417–424.
- [52] Fadlun, E., Verzicco, R., Orlandi, P., and Mohd-Yusof, J. Combined immersed-boundary finite-difference methods for three-dimensional complex flow simulations. *J. Comput. Phys.* 161 (2000), 35–60.
- [53] Faivre, M., Abkarian, M., Bickraj, K., and Stone, H. Geometrical focusing of cells in a microfluidic device: an approach to separate blood plasma. *Biorheology* 43, 2 (2006), 147–159.
- [54] Falahatpisheh, A., and Kheradvar, A. High-speed particle image velocimetry to assess cardiac fluid dynamics in vitro: From performance to validation. *Eu. J. Mech. - B/Fluids* 35 (2012), 2–8.
- [55] Faludi, R., Szulik, M., D’hooge, J., Herijgers, P., Rademakers, F., Pedrizzetti, G., and Voigt, J.-U. Left ventricular flow patterns in healthy subjects and patients with prosthetic mitral valves: an in vivo study using echocardiographic particle image velocimetry. *The J. of thor. and cardio. surg.* 139, 6 (2010), 1501–1510.
- [56] Farhat, C., Geuzaine, P., and Grandmont, C. The discrete geometric conservation law and the nonlinear stability of ALE schemes for the solution of flow problems on moving grids. *J. Comput. Phys.* 174 (2001), 669–694.
- [57] Ferguson, G. Turbulence in human intracranial saccular aneurysms. *J. Neuro.* 33 (1970), 485–497.
- [58] Fernández, M., Formaggia, L., Gerbeau, J.-F., and Quarteroni, A. The derivation of the equations for fluids and structure. In *Cardiovascular mathematics*. Springer, 2009, pp. 77–121.
- [59] Formaggia, L., Quarteroni, A., and Veneziani, A. *Cardiovascular Mathematics: Modeling and simulation of the circulatory system*, vol. 1. Springer, 2009.
- [60] Fortini, S., Querzoli, G., Espa, S., and Cenedese, A. Three-dimensional structure of the flow inside the left ventricle of the human heart. *Expe. Fluids* 54, 11 (2013), 1–9.

- [61] Fraser, K., Taskin, M., Griffith, B., and Wu, Z. The use of computational fluid dynamics in the development of ventricular assist devices. *Medical engineering & physics* 33, 3 (2011), 263–280.
- [62] Fyrenius, A., Wigstrom, L., Ebbers, T., Karlsson, M., Engvall, J., and Bolger, A. Three dimensional flow in the human left atrium. *Heart* 86 (2001), 448–455.
- [63] Garcia, D., del Alamo, J. C., Tanne, D., Yotti, R. L., Cortina, C., Bertrand, E., Antoranz, J. C., Perez-David, E., Rieu, R., Fernandez-Aviles, F., and Bermejo, J. Two-dimensional intraventricular flow mapping by digital processing conventional color-doppler echocardiography images. *IEEE Trans. Med. Imag.* 29 (2010), 1701–1713.
- [64] Garimella, R., and Swartz, B. Curvature estimation for unstructured triangulations of surfaces. *Los Alamos National Laboratory* (2003).
- [65] Geers, L., Tummers, M., and Hanjalić, K. Experimental investigation of impinging jet arrays. *Exps. Fluids* 36 (2004), 946–958.
- [66] Gence, J., and Mathieu, J. The return to isotropy of an homogeneous turbulence having been submitted to two successive plane strains. *J. Fluid Mech.* 101 (1980), 555–566.
- [67] Gerbeau, J. F., Vidrascu, M., and Frey, P. Fluid-structure interaction in blood flows on geometries based on medical imaging. *Comput. Struct.* 83 (2005), 155–165.
- [68] Germano, M., Piomelli, U., Moin, P., and Cabot, W. H. A dynamic subgrid-scale eddy viscosity model. *Phys. Fluids* 3 (1991), 1760–1765.
- [69] Gharib, M., Rambod, E., Kheradvar, A., Sahn, D., and Dabiri, J. Optimal vortex formation as an index of cardiac health. *Proc. Natl. Acad. Sci. U.S.A.* 103 (2006), 6305–6308.
- [70] Gijssen, F., Van de Vosse, F., and Janssen, J. The influence of the non-Newtonian properties of blood on the flow in large arteries: steady flow in a carotid bifurcation model. *J. Biomech.* 32, 6 (1999), 601–608.
- [71] Gijssen, F., Van de Vosse, F., and Janssen, J. The influence of the non-Newtonian properties of blood on the flow in large arteries: unsteady flow in a 90 curved tube. *J. Biomech.* 32, 7 (1999), 705–713.
- [72] Gilardi, M., Rizzo, G., Savi, A., and Fazio, F. Registration of multi-modal biomedical images of the heart. *Int. Assoc. of Radiopharma.* 40, 1 (1996), 142–150.
- [73] Goldsmith, H. Microscopic flow properties of red cells. In *Federation proceedings* (1966), vol. 26, pp. 1813–1820.

- [74] Goldstein, D., Handler, R., and Sirovich, L. Modeling a no-slip flow boundary with an external force field. *J. Comput. Phys.* 105, 2 (1993), 354–366.
- [75] Goubergrits, L., and Affeld, K. Numerical estimation of blood damage in artificial organs. *Artif. organs* 28, 5 (2004), 499–507.
- [76] Grundestam, O., Wallin, S., and Johansson, A. Direct numerical simulations of rotating turbulent channel flow. *J. Fluid Mech.* 598 (2008), 177–200.
- [77] Ha, J. W., Oh, J. K., Redfield, M. M., Ujino, K., Seward, J. B., and Tajik, A. J. Triphasic mitral inflow velocity with middiastolic filling: clinical implications and associated echocardiographic findings. *J. Am. Soc. Echo.* 17 (2004), 428–431.
- [78] Haugen, B. O., Berg, S., Brecke, K. M., Samstad, S. O., Slørdahl, S. A., Skjærpe, T., and Torp, H. Velocity profiles in mitral blood flow based on three-dimensional freehand colour flow imaging acquired at high frame rate. *Eu. J. Echo.* 1 (2000), 252–256.
- [79] Hendabadi, S., Bermejo, J., Benito, Y., Yotti, R., Fernández-Avilés, F., del Álamo, J., and Shadden, S. Topology of blood transport in the human left ventricle by novel processing of doppler echocardiography. *Ann. Biomed. Engng* 41, 12 (2013), 2603–2616.
- [80] Hill, D., Studholme, C., and Hawkes, D. Voxel similarity measures for automated image registration. In *Visualization in Biomedical Computing* (1994), International Society for Optics and Photonics, pp. 205–216.
- [81] Hirt, C., Amsden, A., and Cook, J. An arbitrary lagrangian-eulerian computing method for all flow speeds. *J. Comput. Phys.* 14, 3 (1974), 227–253.
- [82] Hirt, C., Amsden, A., and Cook, J. An arbitrary lagrangian–eulerian computing method for all flow speeds. *J. Comput. Phys.* 135, 2 (1997), 203–216.
- [83] Hollnagel, D. I., Summers, P. E., Poulidakos, D., and Kollias, S. S. Comparative velocity investigations in cerebral arteries and aneurysms: 3D phase-contrast MR angiography, laser doppler velocimetry and computational fluid dynamics. *NMR in Biomed.* 22 (2009), 795–808.
- [84] Hong, G. R., Pedrizzetti, G., Tonti, G., Li, P., Wei, Z., Kim, J., Baweja, A., Liu, S., Chung, N., Houle, H., Narula, J., and Vannan, M. Characterization and quantification of vortex flow in the human left ventricle by contrast echocardiography using vector particle image velocimetry. *J. Am. Coll. Cardiol.* 1 (2008), 705–717.
- [85] Hunt, J. C. R., Wray, A. A., and Moin, P. Eddies, stream, and convergence zones in turbulent flows. In *Center for Turbulence Research Report CTR-S88* (1988).

- [86] Jacquin, L., Leuchter, O., Cambonxs, C., and Mathieu, J. Homogeneous turbulence in the presence of rotation. *J. Fluid Mech.* 220 (1990), 1–52.
- [87] Kameneva, M., Burgreen, G., Kono, K., Repko, B., Antaki, J., and Umezu, M. Effects of turbulent stresses upon mechanical hemolysis: experimental and computational analysis. *ASAIO j.* 50, 5 (2004), 418–423.
- [88] Kheradvar, A., Houle, H., Pedrizzetti, G., Tonti, G., Belcik, T., Ashraf, M., Lindner, J. R., Gharib, M., and Sahn, D. Echocardiographic particle image velocimetry: a novel technique for quantification of left ventricular blood vorticity pattern. *J. of the Am. Soc. of Echocardio.* 23, 1 (2010), 86–94.
- [89] Kilner, P., Yang, G., Mohiaddin, R., Firmin, D., and Longmore, D. Helical and retrograde secondary flow patterns in the aortic arch studied by three-directional magnetic resonance velocity mapping. *Circulation* 88 (1993), 2235–2247.
- [90] Kilner, P., Yang, G. Z., Wilkes, A., Mohiaddin, R. H., Firmin, D. N., and Yacoub, M. H. Asymmetric redirection of flow through the heart. *Nature* 404 (2000), 759–761.
- [91] Kim, H., Hertzberg, J., and Shandas, R. Development and validation of echo PIV. *Expe. Fluids* 36 (2004), 455–462.
- [92] Kim, H.-K., Sohn, D.-W., Lee, S.-E., Choi, S.-Y., Park, J.-S., Kim, Y.-J., Oh, B.-H., Park, Y.-B., and Choi, Y.-S. Assessment of left ventricular rotation and torsion with two-dimensional speckle tracking echocardiography. *J. of the Am. Soc. of Echocardio.* 20, 1 (2007), 45–53.
- [93] Kim, W. Y., Walker, P. G., Pedersen, E. M., Poulsen, J. K., Oyre, S., Houliind, K., and Yoganathan, A. P. Left ventricular blood flow patterns in normal subjects: A quantitative analysis by three-dimensional magnetic resonance velocity mapping. *J. Am. Coll. Cardiol.* 26 (1995), 224–238.
- [94] Ku, J., Elkins, C., and Taylor, C. Comparison of CFD and MRI flow and velocities in an in vitro large artery bypass graft model. *Ann. Biomed. Engng* 33, 3 (2005), 257–269.
- [95] Le, T. B., and Sotiropoulos, F. On the three-dimensional vortical structure of early diastolic flow in a patient-specific left ventricle. *Eu. J. Mech. - B/Fluids* 35 (2012), 20–24.
- [96] Les, A. S., Shadden, S. C., Figueroa, C. A., Park, J. M., Tedesco, M. M., Herfkens, R. J., Dalman, R. L., and Taylor, C. A. Quantification of hemodynamics in abdominal aortic aneurysms during rest and exercise using magnetic resonance imaging and computational fluid dynamics. *Ann. Biomed. Engng* 38 (2010), 1288–1313.

- [97] Lilly, D. A proposed modification of the germano subgrid-scale closure method. *Phys. Fluids A* 4 (1992), 633–635.
- [98] Lilly, L. *Braunwald's heart disease: a textbook of cardiovascular medicine*, vol. 1. Elsevier Health Sciences, 2012.
- [99] Long, C., Esmaily-Moghadam, M., Marsden, A., and Bazilevs, Y. Computation of residence time in the simulation of pulsatile ventricular assist devices. *Comput. Mech.* (2013), 1–9.
- [100] Long, C., Marsden, A., and Bazilevs, Y. Shape optimization of pulsatile ventricular assist devices using fsi to minimize thrombotic risk. *Comput. Mech.* (2014), 1–12.
- [101] Long, Q. Subject-specific computational simulation of left ventricular flow based on magnetic resonance imaging. *Proceedings of the Institution of Mechanical Engineers, Part H* 222 (2008), 475–485.
- [102] Lumley, J. Computational modeling of turbulent flows. *Adv. Appl. Mech.* 18 (1978), 213.
- [103] Lumley, J., and Newman, G. The return to isotropy of homogeneous turbulence. *J. Fluid Mech.* 82 (1977), 161–178.
- [104] Macosko, C. *Rheology: Principles, measurements, and applications*. 1994. VCH, New York.
- [105] Maintz, J. B. A., and Viergever, M. A. A survey of medical image registration. *Med. Image Ana.* 2 (1998), 1–36.
- [106] Makela, T., Clarysse, P., Sipila, O., Pauna, N., Pham, Q. C., Katila, T., and Magnin, I. E. A review of cardiac image registration methods. *Med. Imaging, IEEE Transactions on* 21 (2002), 1011–1021.
- [107] Malandin, M., Maheu, N., and Moureau, V. Optimization of the deflated conjugate gradient algorithm for the solving of elliptic equations on massively parallel machines. *J. Comput. Phys.* 238 (2013), 32–47.
- [108] Mangual, J., Domenichini, F., and Pedrizzetti, G. Describing the highly three dimensional right ventricle flow. *Annals of biomedical engineering* 40, 8 (2012), 1790–1801.
- [109] Markl, M., Kilner, P., and Ebbers, T. Comprehensive 4D velocity mapping of the heart and great vessels by cardiovascular magnetic resonance. *J. Cardiovasc. Magn. Reson.* 13 (2011), 1–22.

- [110] Masud, A., Bhanabhagvanwala, M., and Khurram, R. A. An adaptive mesh rezoning scheme for moving boundary flows and fluid-structure interaction. *Comput. Fluids* 36 (2007), 77–91.
- [111] Mathers, C., Fat, D., and Boerma, J. *The global burden of disease: 2004 update*. World Health Organization, 2008.
- [112] Mathieu, J. G. J. On the application of successive plane strains to grid-generated turbulence. *J. Fluid Mech.* 93 (1979), 501–513.
- [113] Mendez, S., Gibaud, E., and Nicoud, F. An unstructured solver for simulations of deformable particles in flows at arbitrary reynolds numbers. *JCP* 256 (2014), 465–483.
- [114] Merrifield, R., Long, Q., Xu, X. Y., Kilner, P. J., Firmin, D. N., and Yang, G. Z. Combined CFD/MRI analysis of left ventricular flow. *Med. Im. Aug. Reality* 3150 (2004), 229–236.
- [115] Midulla, M., Moreno, R., Baali, A., Chau, M., Negre-Salvayre, A., Nicoud, F., Pruvo, J. P., Haulon, S., and Rousseau, H. Haemodynamic imaging of thoracic stent-grafts by computational fluid dynamics (CFD): presentation of a patient-specific method combining magnetic resonance imaging and numerical simulations. *Eu. Radiol.* 22 (2012), 2094–2102.
- [116] Mihalef, V., Ionasec, R. I., Sharma, P., Georgescu, B., Voigt, I., Suehling, M., and Comaniciu, D. Patient-specific modelling of whole heart anatomy, dynamics and haemodynamics from four-dimensional cardiac CT images. *Interface Focus* 1 (2011), 286–296.
- [117] Mikhal, J., and Geurts, B. Immersed boundary method for pulsatile transitional flow in realistic cerebral aneurysms. *Comput. Fluids* 91 (2014), 144–163.
- [118] Mittal, R., Simmons, S., and Najjar, F. Numerical study of pulsatile flow in a constricted channel. *J. Fluid Mech.* 485 (2003), 337–378.
- [119] Modersitzki, J. *Numerical Methods for Image Registration (Numerical Mathematics and Scientific Computation)*. 2004.
- [120] Mohd-Yusof, J. Combined immersed-boundary/B-spline methods for simulations of flow in complex geometries. *Ann. Research Briefs, Center for Turbulence Research* (1997).
- [121] Moran, P. A flow velocity zeugmatographic interlace for nmr imaging in humans. *Mag. reso. im.* 1, 4 (1982), 197–203.

- [122] Moreno, R., Nicoud, F., Veunac, L., and Rousseau, H. Non-linear transformation field to build moving meshes for patient specific blood flow simulations. *Eu. Conf. Comp. Fluid Dyna.* (2006).
- [123] Moureau, V., Domingo, P., and Vervisch, L. Design of a massively parallel CFD code for complex geometries. *Comptes Rendus Mécanique 339* (2011), 141–148.
- [124] Moureau, V., Domingo, P., and Vervisch, L. From large-eddy simulation to direct numerical simulation of a lean premixed swirl flame: Filtered laminar flame-PDF modeling. *Comb. Flame 158* (2011), 1340–1357.
- [125] Nagueh, S., Appleton, C., Gillebert, T., Marino, P., Oh, J., Smiseth, O., Waggoner, A., Flachskampf, F., Pellikka, P., and Evangelisa, A. Recommendations for the evaluation of left ventricular diastolic function by echocardiography. *Eu. J. Echo. 10*, 2 (2009), 165–193.
- [126] Nakatani, S. Left ventricular rotation and twist: why should we learn? *J. of cardio. ultrasound 19*, 1 (2011), 1–6.
- [127] Nerem, R., Seed, W., and Wood, N. An experimental study of the velocity distribution and transition to turbulence in the aorta. *J. Fluid Mech. 52*, 01 (1972), 137–160.
- [128] Nicoud, F. Hemodynamic changes induced by stenting in elastic arteries. *Center for turbulence research annual research biefs* (2002).
- [129] Nicoud, F., Moreno, R., Tayllamin, B., Chau, M., and Rousseau, H. Computational hemodynamics in moving geometries without solving the fluid-structure interaction problem. In *Conference on Modelling Fluid Flow* (2009).
- [130] Nicoud, F., Toda, H. B., O. Cabrit, S. B., and Lee, J. Using singular values to build a subgrid-scale model for large eddy simulations. *Phys. Fluids 23* (2011), 085106.
- [131] Nishino, K., Samada, M., Kasuya, K., and Torii, K. Turbulence statistics in the stagnation region of an axisymmetric impinging jet flow. *Int. J. heat fluid flow 17* (1996), 193–201.
- [132] Nordsletten, D., McCormick, M., Kilner, P., Hunter, P., Kay, D., and Smith, N. Fluid–solid coupling for the investigation of diastolic and systolic human left ventricular function. *Int. J. for Num. Meth. in Biomed. Eng. 27*, 7 (2011), 1017–1039.
- [133] Nordsletten, D. A., Niederer, S. A., Nash, M. P., Hunter, P. J., and Smith, N. P. Coupling multi-physics models to cardiac mechanics. *Prog. Biophys. Mol. Biol. 104* (2011), 77–88.

- [134] Notomi, Y., Martin-Miklovic, M., Oryszak, S., Shiota, T., Deserranno, D., Popovic, Z., Garcia, M., Greenberg, N., and Thomas, J. Enhanced ventricular untwisting during exercise a mechanistic manifestation of elastic recoil described by doppler tissue imaging. *Circulation* 113, 21 (2006), 2524–2533.
- [135] Notomi, Y., Setser, R., Shiota, T., Martin-Miklovic, M., Weaver, J., Popović, Z., Yamada, H., Greenberg, N., White, R., and Thomas, J. Assessment of left ventricular torsional deformation by doppler tissue imaging validation study with tagged magnetic resonance imaging. *Circulation* 111, 9 (2005), 1141–1147.
- [136] Peacock, J., Jones, T., Tock, C., and Lutz, R. The onset of turbulence in physiological pulsatile flow in a straight tube. *Exps. Fluids* 24 (1998), 1–9.
- [137] Pedrizzetti, G., and Domenichini, F. Nature optimizes the swirling flow in the human left ventricle. *Phys. Rev. Let.* 95 (2005), 108101.
- [138] Peskin, C. Flow patterns around heart valves: a numerical method. *J. Comput. Phys.* 10, 2 (1972), 252–271.
- [139] Pham, D. L., Xu, C., and Prince, J. L. Current methods in medical image segmentation. *Annu. Rev. Biomed. Engng* 2 (2000), 315–337.
- [140] Pinelli, A., Naqavi, I., Piomelli, U., and Favier, J. Immersed-boundary methods for general finite-difference and finite-volume navier–stokes solvers. *J. Comput. Phys.* 229, 24 (2010), 9073–9091.
- [141] Pope, S. *Turbulent flows*. Cambridge university press, 2000.
- [142] Pope, S. B. Ten questions concerning the large-eddy simulation of turbulent flows. *New J. Phys.* 6 (2004), 35.
- [143] Querzoli, G., Fortini, S., and Cenedese, A. Effect of the prosthetic mitral valve on vortex dynamics and turbulence of the left ventricular flow. *Phys. Fluids* 22 (2010), 041901.
- [144] R., M. *Simulations Numériques Vasculaires, Spécifiques et Réalistes*. PhD thesis, Université Toulouse III, 2007.
- [145] Rieth, M., Proch, F., Stein, O., Pettit, M., and Kempf, A. Comparison of the sigma and smagorinsky les models for grid generated turbulence and a channel flow. *Comput. Fluids* (2014).
- [146] Saber, N. R., Gosman, A. D., Wood, N. B., Kilner, P. J., Charrier, C. L., and Firmin, D. N. Computational flow modeling of the left ventricle based on in vivo MRI data: initial experience. *Ann. Biomed. Engng* 29 (2001), 275–83.

- [147] Saber, N. R., Wood, N. B., Gosman, A. B., Merrifield, R. D., Yang, G. Z., Charrier, C. L., Gatehouse, P. D., and Firmin, D. N. Progress towards patient-specific computational flow modeling of the left heart via combination of magnetic resonance imaging with computational fluid dynamics. *Ann. Biomed. Engng* 31 (2003), 42–52.
- [148] Sagaut, P. *Large eddy simulation for incompressible flows*, vol. 3. Springer Berlin, 2000.
- [149] Saiki, E., and Biringen, S. Numerical simulation of a cylinder in uniform flow: application of a virtual boundary method. *J. Comput. Phys.* 123, 2 (1996), 450–465.
- [150] Savi, A., Gilardi, M., Rizzo, G., Pepi, M., Landoni, C., Rossetti, C., Lucignani, G., Bartorelli, A., and Fazio, F. Spatial registration of echocardiographic and positron emission tomographic heart studies. *Eu. j. of nuc. med.* 22, 3 (1995), 243–247.
- [151] Schenkel, T., Malve, M., Reik, M., Markl, M., Jung, B., and Oertel, H. MRI-based CFD analysis of flow in a human left ventricle: Methodology and application to a healthy heart. *Ann. Biomed. Engng* 37 (2009), 503–515.
- [152] Scotti, A., and Piomelli, U. Turbulence models in pulsating flows. *AIAA J.* 40 (2002), 537–544.
- [153] Seed, W., and Wood, N. Velocity patterns in the aorta. *Cardiovasc. research* 5, 3 (1971), 319–330.
- [154] Sengupta, P., Pedrizzetti, G., Kilner, P., Kheradvar, A., Ebbers, T., Tonti, G., Fraser, A., and Narula, J. Emerging trends in cv flow visualization. *JACC: Cardiovascular Imaging* 5, 3 (2012), 305–316.
- [155] Sengupta, P., Tajik, A., Chandrasekaran, K., and Khandheria, B. Twist mechanics of the left ventricle: principles and application. *JACC: Cardio. Im.* 1, 3 (2008), 366–376.
- [156] Seo, J., and Mittal, R. Effect of diastolic flow patterns on the function of the left ventricle. *Phys. Fluids* 25, 11 (2013), 110801.
- [157] Sforza, D. M., Putman, C. M., and Cebal, J. R. Hemodynamics of cerebral aneurysms. *Annu. Rev. Fluid Mech.* 41 (2009), 91–107.
- [158] Shier, D., Butler, J., and Lewis, R. *Hole’s Human Anatomy*. McGraw-Hill, 1996.
- [159] Simonsen, A., Krogstad, P., et al. Turbulent stress invariant analysis: clarification of existing terminology. *Phys. Fluids* 17 (2005), 88103–88103.

- [160] Sinha, S., Sinha, U., Czernin, J., Porenta, G., and Schelbert, H. Noninvasive assessment of myocardial perfusion and metabolism: feasibility of registering gated MR and PET images. *Am. j. of roentgenology* 164, 2 (1995), 301–307.
- [161] Smiseth, O. A., and Tendera, M. *Diastolic heart failure*. Springer, 2008.
- [162] Smith, N., de Vecchi, A., McCormick, M., Nordsletten, D., Camara, O., Frangi, A., Delingette, H., Sermesant, M., Relan, J., Ayache, N., et al. euheart: personalized and integrated cardiac care using patient-specific cardiovascular modelling. *Interface focus* 1 (2011), 349–364.
- [163] Stalder, A., Frydrychowicz, A., Russe, M., Korvink, J., Hennig, J., Li, K., and Markl, M. Assessment of flow instabilities in the healthy aorta using flow-sensitive MRI. *J. Mag. Reso. Imag.* 33 (2011), 839–846.
- [164] Stein, P., and Sabbah, H. Measured turbulence and its effect on thrombus formation. *Circulation Research* 35, 4 (1974), 608–614.
- [165] Stein, P., and Sabbah, H. Turbulent blood flow in the ascending aorta of humans with normal and diseased aortic valves. *Circ. Res.* 39 (1976), 58–65.
- [166] Tang, D., Yang, C., Geva, T., and del Nido, P. J. Patient-specific MRI-based 3D FSI RV/LV/patch models for pulmonary valve replacement surgery and patch optimization. *J. Biomech. Engng* 130 (2008), 041010.
- [167] Tanné, D., Bertrand, E., Kadem, L., Pibarot, P., and Rieu, R. Assessment of left heart and pulmonary circulation flow dynamics by a new pulsed mock circulatory system. *Expe. Fluids* 48 (2010), 837–850.
- [168] Taskin, M. E., Fraser, K., Zhang, T., Wu, C., Griffith, B., and Wu, Z. Evaluation of eulerian and lagrangian models for hemolysis estimation. *ASAIO Journal* 58, 4 (2012), 363–372.
- [169] Taylor, C. A., and Figueroa, C. A. Patient-specific modeling of cardiovascular mechanics. *Annu. Rev. Biomed. Engng* 11 (2009), 109–134.
- [170] Thurston, G. Rheological parameters for the viscosity viscoelasticity and thixotropy of blood. *Biorheo.* 16, 3 (1978), 149–162.
- [171] Vadakkumpadan, F., Arevalo, H., Ceritoglu, C., Miller, M., and Trayanova, N. Image-based estimation of ventricular fiber orientations for personalized modeling of cardiac electrophysiology. *IEEE Trans. Med. Imag.* 31 (2012), 1051–1060.
- [172] Valen-Sendstad, K., Mardal, K. A., Mortensen, M., Reif, B. A., and Langtangen, H. Direct numerical simulation of transitional flow in a patient-specific intracranial aneurysm. *J. Biomech.* 44 (2011), 2826–2832.

- [173] Valen-Sendstad, K., Piccinelli, M., and Steinman, D. High-resolution computational fluid dynamics detects flow instabilities in the carotid siphon: Implications for aneurysm initiation and rupture? *J. of Biomech.* (2014).
- [174] Valen-Sendstad, K., and Steinman, D. Mind the gap: Impact of computational fluid dynamics solution strategy on prediction of intracranial aneurysm hemodynamics and rupture status indicators. *Am. J. Neuro.* (2013).
- [175] Varghese, S., Frankel, S., and Fischer, P. Direct numerical simulation of stenotic flows. part 2. pulsatile flow. *J. Fluid Mech.* 582 (2007), 281–318.
- [176] Vedula, V., Fortini, S., Seo, J.-H., Querzoli, G., and Mittal, R. Computational modeling and validation of intraventricular flow in a simple model of the left ventricle. *Theo. and Comput. Fluid Dynamics* (2014), 1–16.
- [177] Verzicco, R., Mohd-Yusof, J., Orlandi, P., and Haworth, D. Les in complex geometries using boundary body forces. *Center for Turbulence Research Proceedings of the Summer Program, NASA Ames - Stanford University* (1998), 171–186.
- [178] Watanabe, H., Sugiura, S., Kafuku, H., and Hisada, T. Multiphysics simulation of left ventricular filling dynamics using fluid-structure interaction finite element method. *Biophys. J.* 87 (2004), 2074–2085.
- [179] Welch, P. The use of fast fourier transform for the estimation of power spectra: a method based on time averaging over short, modified periodograms. *IEEE Trans. Audio Electroacoust.* AU 15 (1967), 70–73.
- [180] Williamson, J. Low-storage runge-kutta schemes. *J. Comput. Phys.* 35 (1980), 48–56.
- [181] Yamaguchi, T., Kikkawa, S., Tanishita, K., and Sugawara, M. Spectrum analysis of turbulence in the canine ascending aorta measured with a hot-film anemometer. *J. of biomech.* 21, 6 (1988), 489–495.
- [182] Yamaguchi, T., Kikkawa, S., Yoshikawa, T., Tanishita, K., and Sugawara, M. Measurement of turbulence intensity in the center of the canine ascending aorta with a hot-film anemometer. *J. of biomech. eng.* 105, 2 (1983), 177–187.
- [183] Yilmaz, F., and Gundogdu, M. A critical review on blood flow in large arteries; relevance to blood rheology, viscosity models, and physiologic conditions. *Korea-Australia Rheo. J.* 20, 4 (2008), 197–211.
- [184] Yoganathan, A. P., He, Z., and Casey, J. S. Fluid mechanics of heart valves. *Annu. Rev. Biomed. Engng* 6 (2004), 331–362.

- [185] Zajac, J., Eriksson, J., Dyverfeldt, P., Bolger, A., Ebbers, T., and Carlhall, C. Turbulent kinetic energy in normal and myopathic left ventricles. *J. Mag. Reso. Imag.* (2014), n/a–n/a.
- [186] Zhao, S. Z., Papathanasopoulou, P., Long, Q., Marshall, I., and Xu, X. Y. Comparative study of magnetic resonance imaging and image-based computational fluid dynamics for quantification of pulsatile flow in a carotid bifurcation phantom. *Ann. Biomed. Engng* 31 (2003), 962–971.
- [187] Zheng, X., Seo, J. H., Vedula, V., Abraham, T., and Mittal, R. Computational modeling and analysis of intracardiac flows in simple models of the left ventricle. *Eu. J. Mech. - B/Fluids* 35 (2012), 31–39.
- [188] Zheng, X., Xue, Q., and Mittal, R. Computational study of hemodynamic effects of abnormal E/A ratio on left ventricular filling. *J. Biomech. Engng* 136, 6 (2014), 061005.